**TECHNISCHE
UNIVERSITÄT
WIEN**
Vienna University of Technology

DISSERTATION

Beam Dynamics Studies for High-Intensity Beams in the CERN Proton Synchrotron

ausgeführt zum Zwecke der Erlangung des akademischen Grades eines Doktors der technischen Wissenschaften unter der Leitung von

Privatdoz. Dipl.-Ing. Dr.techn. Michael Benedikt
Atominstitut, E141

Dr. Simone Gilardoni
CERN EN-STI

eingereicht an der Technischen Universität Wien
Fakultät für Physik von

Dipl.-Ing. Alexander Huschauer
Matrikelnummer: 0625514

Genf, Mai 2016

Abstract

With the discovery of the Higgs boson, the existence of the last missing piece of the Standard Model of particle physics (SM) was confirmed. However, even though very elegant, this theory is unable to explain, for example, the generation of neutrino masses, nor does it account for dark energy or dark matter.

To shed light on some of these open questions, research in fundamental particle physics pursues two complimentary approaches. On the one hand, particle colliders working at the high-energy frontier, such as the Large Hadron Collider (LHC) at the European Organization for Nuclear Research (CERN), located in Geneva, Switzerland, are utilized to investigate the fundamental laws of nature. Alternatively, fixed target facilities require high-intensity beams to create a large flux of secondary particles to investigate, for example, rare particle decay processes, or to create neutrino beams.

This thesis investigates limitations arising during the acceleration of high-intensity beams at the CERN Proton Synchrotron (PS). The studies presented are aimed at reducing beam loss occurring during the injection and extraction processes, which cause high radioactive activation of the PS ring. The minimization of beam loss is essential to allow maintenance, repair or exchange of crucial accelerator equipment, especially for the production of more intense proton beams, which will eventually be required by future experimental facilities.

The first part of this thesis focuses on an intra-bunch oscillation phenomenon, which is observed immediately after injection of high-intensity beams and causes undesirable beam loss. The oscillations are experimentally characterized, detailed simulation studies are presented and the underlying mechanism, namely the interaction between the beam and the self-induced electromagnetic fields in the surrounding vacuum chamber, is explained.

The second part of this thesis sets out the way to making the Multi-Turn Extraction (MTE), a novel scheme based on advanced concepts of non-linear beam dynamics, an operational replacement of the Continuous Transfer (CT) process. Experimental studies stressing the susceptibility of the MTE technique to fluctuations of the magnetic field are discussed, and the results of 6D time-dependent simulations are explained. Furthermore, a redesign of the extraction process itself is presented. The design of a new extraction bump, which is required by the installation of a passive absorber to protect the magnetic extraction septum, is set out. In addition, improved non-linear extraction optics are presented, which allow the reduction of beam loss at extraction to the expected design values of less than 2%. The entirety of the presented studies played a crucial role in concluding the MTE commissioning process. Since September 2015, the MTE scheme has successfully replaced the CT extraction, leading to a significant reduction of the activation of the PS ring.

Kurzfassung

Mit der Entdeckung des Higgs-Bosons wurde die Existenz des letzten fehlenden Teils des Standardmodells der Elementarteilchenphysik (SM) bestätigt. Obwohl sehr elegant, ist diese Theorie nicht im Stande Phänomene, wie die Erzeugung der Masse von Neutrinos oder die Existenz von Dunkler Materie und Dunkler Energie, zu erklären.

Um Antworten auf diese offenen Fragen zu finden, bedient sich die Grundlagenforschung im Bereich der Teilchenphysik zweier sich gegenseitig ergänzender Herangehensweisen. Einerseits werden hochenergetische Teilchenbeschleuniger, wie der Large Hadron Collider (LHC) an der Europäischen Organisation für Kernforschung (CERN) in Genf in der Schweiz, verwendet, um die fundamentalen Naturgesetze zu untersuchen. Eine Alternative stellen Anlagen dar, welche durch Wechselwirkung zwischen Teilchenstrahlen hoher Intensität und einem speziellen Target, einen hohen Fluss an Sekundärteilchen erzeugen. Diese können dann verwendet werden um, zum Beispiel, seltene Zerfallsprozess zu untersuchen oder Neutrinostrahlen zu erzeugen.

Diese Dissertation befasst sich mit der Beschleunigung von Teilchenstrahlen hoher Intensität im CERN Proton Synchrotron (PS) und den dabei auftretenden Limitierungen der Leistungsfähigkeit. Die präsentierten Studien zielen darauf ab, Strahlverluste während der Injektions- und Extraktionsprozesse, welche zu hoher radioaktiver Aktivierung des PS Tunnels führen, zu verringern. Die Minimierung solcher Verluste ist unerlässlich, um die Wartung, die Reparatur oder den Austausch von kritischen Elementen des Beschleunigers zu ermöglichen. Dies ist insbesondere im Hinblick auf zukünftige experimentelle Anlagen, welche Protonenstrahlen mit höheren Intensitäten im Vergleich zu heute benötigen werden, von Bedeutung.

Im ersten Teil dieser Dissertation wird ein Phänomen beschrieben, welches unmittelbar nach der Injektion von Strahlen hoher Intensität beobachtet wird. Es handelt sich dabei um Oszillationen innerhalb der Teilchenpakete, die zu ungewollten Strahlverlusten führen. Die Eigenschaften dieser Oszillationen werden experimentell charakterisiert und der zugrundeliegende Mechanismus, nämlich die Wechselwirkung zwischen dem Strahl und den selbstinduzierten elektromagnetischen Feldern in der umliegenden Vakuumkammer, wird anhand von detaillierten Simulation erklärt.

Im zweiten Teil dieser Arbeit werden die verschiedenen Schritte dargelegt, welche dazu geführt haben, dass die Multi-Turn Extraction (MTE), ein neuartiger Extraktionsmechanismus basierend auf fortgeschrittenen Konzepten der nichtlinearen Strahldynamik, den Continuous Transfer (CT) Prozess erfolgreich ersetzen konnte. Experimentelle Studien, welche die Empfindlichkeit des MTE-Verfahrens gegenüber Fluktuationen des Magnetfeldes zeigen, werden behandelt und die Resultate von zeitabhängigen Simulation in 6D werden erklärt. Darüber hinaus wird die Neugestaltung des Extraktionsprozesses präsentiert. Dies betrifft einerseits das Design eines neuen Extraktionsbumps, welcher aufgrund der Installation eines passiven Absorbers zum Schutz

des magnetischen Septums benötigt wurde. Weiters wird eine neue, nichtlineare, Extraktionsoptik gezeigt, deren Einsatz zu der Reduktion der Extraktionsverluste auf die erwarteten Werte von unter 2% führt. Die Vielzahl der durchgeführten Studien hat wesentlich zu der erfolgreichen Inbetriebnahme des MTE-Prozesses beigetragen. Im September 2015 konnte das MTE-Verfahren den CT-Prozess ersetzten, was in der Folge zu einer wesentlichen Reduktion der Aktivierung des PS Tunnels geführt hat.

Acknowledgments

The past years as a doctoral student at CERN have been an exceptional experience for me. From the beginning of my undergraduate studies, it has always been my dream to pursue a career in high-energy physics. Today, it is my pleasure to thank those, who encouraged, inspired and accompanied me along this journey to eventually make this dream come true.

First and foremost, I would like to express my gratitude to my brilliant supervisor at CERN, Simone Gilardoni. Thanks for all your guidance and support, your curiosity and endless imagination, and the multitude of enlightening discussions, which have made working with you such a pleasure. I wish you all the best in your new role.

Furthermore, I am indebted to my university supervisor Michael Benedikt, who made it possible for me to work at CERN in the first place, and for his support during the studies for my master's degree and the period as doctoral student.

I have had the great pleasure to work with my fellow students and friends, Cédric Hernalsteens and Raymond Wasef. I will always remember our discussions over lunch and coffee, and the seemingly endless hours, days and nights we spent together either in the control room or in the offices to analyse data. *Bonne continuation à vous deux!*

I would like to express my gratitude to the remaining members of the MTE core team, Massimo Giovannozzi and Guido Sterbini. To Massimo, for giving me the opportunity to work on this unique project, for the various explanations on non-linear beam dynamics, your constructive criticism and the multitude of ideas arising out of discussions. To Guido, for the unforgettable months spent together in the control room trying to understand what we did not at the time, for sharing your scientific and systematic attitude with me, and for your invaluable contribution to the work presented in this thesis.

I owe my sincere gratitude to Giovanni Rumolo, Elias Métral, Kevin Li and Nicolas Mounet for fruitful discussions and explanations concerning collective effects. Their theoretical knowledge together with their experience in experimental and simulation studies provided valuable insight, which allowed me to progress with my work.

I am extremely grateful to the operations crew of the PS and the PSB. Without your continuous support, all the experimental studies I have conducted over the last years would not have been possible. Thank you for making me feel a part of the *équipe*!

I owe my gratitude to the different section leaders I had the pleasure to work with over the years: Rende Steerenberg, Gianluigi Arduini, E.Métral and Yannis Papaphilippou. I highly appreciate our discussions and your many constructive suggestions.

Furthermore, I would like to thank Alfred Blas, Alan Findlay, Bettina Mikulec and Jocelyn Tan for their assistance and for useful discussions during the dedicated measurements at the PSB. I would also like to acknowledge the excellent collaboration with colleagues from the TE-EPC

group, and especially mention Karsten Kahle, Gilles Le Godec and Olivier Michels.

I am also thankful to Sandra Aumon, Hannes Bartosik, Elena Benedetto, Heiko Damerau, Vincenzo Forte, Steven Hancock, Tobias Persson and Benoit Salvant for a multitude of fruitful discussions, critical comments and useful suggestions.

For proofreading the manuscript and providing many invaluable comments, I would like to express my gratitude to Simone Gilardoni, Massimo Giovannozzi, Alan Findlay, Elias Métral, China Irwin and Hannes Bartosik.

I am very grateful to my friends in the Geneva region and in Austria, who make me feel home in either place. Mein spezieller Dank gilt jenen zu Hause in Österreich, die, trotz dem wir uns leider viel zu selten sehen, großartige Freunde bleiben.

Der größte Dank gebührt meiner Familie. Insbesondere meinen Eltern, die mich bei jeder Entscheidung unterstützt, mir jedoch nie etwas vorgeschrieben und mir immer die freie Wahl gelassen haben. Euch, meinem Bruder und meinen Schwiegereltern möchte ich besonders dafür danken, dass ihr uns immer ein herzliches Willkommen bereitet, auch wenn wir nur ein paar Mal im Jahr für kurze Zeit nach Hause kommen.

Zum Schluss möchte ich mich bei dem wichtigsten Menschen in meinem Leben, meiner Frau Tanja, bedanken. Für die vielen gemeinsamen Jahre, die uns immer mehr zusammengeschweißt haben, für deine uneingeschränkte Unterstützung jeglicher Art, und dafür, dass du vermutlich die einzige Person, neben mir selbst, bist, die es sich angetan hat diese Dissertation komplett Korrektur zu lesen.

Table of Contents

List of Abbreviations and Acronyms

ACEM Aluminium Cathode Electron Multiplier

AD Antiproton Decelerator

BBQ Base Band Tune measurement system

BCT beam current transformer

BLM beam loss monitor

BOSS beam offset signal suppressor

BP basic period

BSW horizontal dipole magnet to create the slow bump

BWS beam wire scanner

CERN European Organization for Nuclear Research

CNGS CERN Neutrinos to Gran Sasso

CT Continuous Transfer

DFA242 fast dipole 242

DFA254 fast dipole 254

DHZ15 horizontal dipole magnet in SS15

DHZ18 horizontal dipole magnet in SS18

DR design report

EPC Electrical Power Converters Group of the TE Department

F8L Figure-of-Eight Loop

FFT Fast Fourier Transform

ISOLDE On-Line Isotope Separator facility

ISR Intersecting Storage Rings

KFA04 fast kicker in SS04

KFA13 fast kicker in SS13

KFA21 fast kicker in SS21

KFA71 fast kicker in SS71

LEIR Low Energy Ion Ring

LEP Large Electron Positron

LEQ Low Energy Quadrupoles

LHC Large Hadron Collider

Linac2 Linear Accelerator 2

LS1 Long Shutdown 1

MAD Methodical Accelerator Design

MTE Multi-Turn Extraction

MU magnet unit

MU101 reference magnet installed outside the PS tunnel

nTOF neutron Time-Of-Flight facility

ODN normal defocusing octupoles

ONO39 normal octupole in SS39

ONO55 normal octupole in SS55

ORBIT Objective Ring Beam Injection and Tracking code

ORM orbit response matrix

PC power converter

PFW Pole Face Windings

ppm parts per million

ppp protons per pulse

PS Proton Synchrotron

PSB Proton Synchrotron Booster

PTC Polymorphic Tracking Code

PU pick-up

QKE kick enhancement quadrupoles

RF radio frequency

RMS root mean square

RP radio protection

SBEND sector bending magnet

SC super-cycle

SEH31 electrostatic septum in SS31

SFP stable fixed point

SHiP Search for Hidden Particles

SM Standard Model of particle physics

SMH16 magnetic septum in SS16

Spp̄S Super Proton Antiproton Synchrotron

SPS Super Proton Synchrotron

SS straight section

SVD singular value decomposition

TFB transverse feedback

TMCI Transverse Mode Coupling Instability

TPS15 dummy septum: a passive absorber to protect SMH16

UFP unstable fixed point

WBPU wide band pick-up

WCM wall current monitor

XNO39 normal sextupoles in SS39

XNO55 normal sextupoles in SS55

1 Introduction

In the course of the last years, tremendous progress has been made in fundamental particle physics research. This has been especially driven by the physics programme at the Large Hadron Collider (LHC) [1], a particle accelerator designed to store and collide proton or lead ion beams at centre-of-mass energies of several TeV per nucleon pair, located at the European Organization for Nuclear Research (CERN) [2] in Geneva, Switzerland. Thirty years after the first ideas concerning this machine were put on paper, the extremely successful first LHC physics run culminated in the discovery of a new particle with a mass of roughly 125 GeV/c^2 [3, 4]. Soon after this announcement it became clear that this particle was indeed consistent with a Higgs boson, which was theoretically predicted in 1964 [5–7]. With this milestone, the existence of the last missing piece of the Standard Model of particle physics (SM), a theory describing the interactions of elementary particles, was confirmed. Furthermore, precise verification of various well-known processes, which are intrinsic to the SM, became possible due to the vast amount of recorded data.

However, the SM is unable to provide explanations for several mysteries which have been puzzling physicists for decades. For example, why is our universe, or the part we know of today, mainly composed of matter instead of antimatter? How are neutrino masses generated?

At the LHC, the search for physics beyond the SM has been rather unsuccessful so far. A complementary approach to the LHC research programme at the high-energy frontier concentrates on high-intensity machines. Experimental facilities operating in this regime require the impact of a high-intensity beam on a target to create a large flux of secondary particles, which can then be used to investigate, for example, rare particle decay processes, or to create neutrino beams. A variety of experimental facilities at CERN require intense proton beams for fixed target physics. The On-Line Isotope Separator (ISOLDE) experimental area [8] at the Proton Synchrotron Booster (PSB) is intended to study the properties of radioactive nuclei. At the Proton

Synchrotron (PS), proton beams have been delivered to the neutron Time-Of-Flight (nTOF) facility [9] to study neutron-nucleus interactions since 2001. In the framework of the CERN Neutrinos to Gran Sasso (CNGS) project [10], protons extracted from the Super Proton Synchrotron (SPS) were used to create a beam of muon-type neutrinos.

Additional facilities, which are currently in the design phase, are intended to profit from the unique infrastructure provided by the CERN accelerator complex. For example, the Search for Hidden Particles (SHiP) experiment [11], which is aimed at finding new particles with masses of only a few GeV/c^2, has been recently proposed to explore physics beyond the SM. SHiP intends to receive a proton beam from the SPS and, therefore, the particles produced in the Duoplasmatron source located at the beginning of the accelerator chain have to be transferred to the SPS via the Linear Accelerator 2 (Linac2), the PSB and the PS. However, to match the requirements in terms of beam characteristics, the maximum intensity produced by the CERN accelerators will have to be increased compared to the present performance, which will not be possible without overcoming certain limitations.

The research presented in this thesis is focused on studying the limitations for high-intensity beam operation in the PS. At present, these issues appear at injection of the beams from the PSB, during the process of crossing the transition energy, and at extraction to either the experimental facilities, which are directly linked to the PS, or the SPS [12]. The limitations result in significant losses along the PS ring, which become especially critical for devices located in the injection and the extraction regions, as these elements suffer from high radioactive activation. Given that the requests of proposed fixed target facilities can only be met by further increasing the PS beam intensity, the breakdown of any crucial element in these regions would require an extremely long waiting time before any possible intervention.

Therefore, the emphasis of the studies performed in the framework of this thesis is put on the investigation of two different topics, with the aim of reducing beam loss during these processes. In the first part of this thesis, vertical intra-bunch oscillations occurring immediately after injection into the PS are discussed. Based on extensive experimental and simulation studies, this phenomenon, which was first observed about twenty years ago and has remained unexplained ever since, is shown to behave different from an instability. It is rather the injection error and the subsequent interaction of the beam with the self-induced fields in the vacuum chamber, which induces an intra-bunch motion. The simple reduction of the injection error is found to be sufficient to reduce beam loss due to this oscillation. Furthermore, it is concluded that, on the basis of the planned upgrade of the PS injection energy [13], future high-intensity beams will be even less affected than today's operational beams.

The second part of this thesis is then dedicated to optimization of the extraction losses. Due to the special requirements of the SPS for high-intensity beams, the Continuous Transfer (CT) technique was proposed in the nineteen-seventies [14]. However, high beam losses, which are intrinsic to this technique, require an alternative extraction scheme in the future. Therefore, the Multi-Turn Extraction (MTE) was proposed in 2001 [15]. This resonant extraction mechanism

exploits advanced concepts of non-linear dynamics and applies a fourth order stable resonance to perform beam splitting in the transverse phase space. The resulting beamlets are then extracted over multiple turns. After several years of commissioning of this novel concept, the milestone of replacing CT with MTE was achieved in September 2015. In this thesis, crucial steps to achieve this goal are set out. Simulations to substantiate and explain the susceptibility of the MTE process to magnetic perturbations, which had already been experimentally observed in the past, are discussed. Furthermore, benchmarking of simulation results with experimental data is performed and extremely good agreement is concluded. Concerning the extraction process itself, a passive absorber to protect the magnetic extraction septum by reducing beam loss at its location was installed in 2014 [16]. To overcome the additional aperture restriction presented by this device, a new extraction bump was developed, and the corresponding simulations and experimental results are presented. The usually simple concept of an extraction bump is significantly complicated by the peculiar phase space structure of the MTE beam. In addition, the design of new non-linear extraction optics is discussed, and the experimental implementation showing a loss reduction of 5% is presented. Moreover, the experimental studies to properly align the magnetic septum with respect to the passive absorber are described. Based on the implementation of all aforementioned improvements, less than 2% of beam loss during the MTE process was achieved, compared to the typical CT values of $5 - 7\%$.

This thesis is structured as follows. After this introduction, Chapter 2 presents a general theoretical overview of accelerator physics and defines the main terminology. Chapter 3 sets out the working principle of the PS and defines its main elements. Chapter 4 gives a brief explanation of the simulation codes used for the injection and extraction studies. Chapter 5 concentrates on the injection oscillations and describes the experimental and simulation studies in great detail. Lastly, Chapter 6 introduces the MTE principle, discusses its advantages, and presents studies leading to its operational implementation by overcoming issues, which significantly hampered the progress of this complex technique in the past.

2 Concepts used in accelerator physics

The motion of an electrically charged particle moving with velocity $\boldsymbol{v}$ under the influence of electric and magnetic fields $\boldsymbol{E}$ and $\boldsymbol{B}$, respectively, is governed by the Lorentz force

$$\frac{d\boldsymbol{p}}{dt} = e(\boldsymbol{E} + \boldsymbol{v} \times \boldsymbol{B}), \tag{2.1}$$

where $\boldsymbol{p}$ is the particle's momentum. Based on this equation, various linear and circular particle accelerators have been developed over the last century. In order to explore the fundamental properties of matter, the requirements in terms of maximum particle energy have significantly increased over the years and led to the invention of the synchrotron. Currently, it is mostly this type of circular accelerator which is applied for research in the field of high-energy physics due to its efficiency in increasing the energy of particles. Its main components are dipole and quadrupole magnets, which ensure transversely stable particle motion around a circular orbit. The arrangement of these elements is commonly described as lattice of the accelerator. In addition, oscillating electric fields, which are confined within radio frequency (RF) cavities, are applied to accelerate the particles by increasing their energy on a turn-by-turn basis. In order to keep the particles on the design orbit, which passes through the centre of all magnets, the energy gain provided has to be synchronously accompanied by a rise of the magnetic field of the dipoles.

An ensemble of single particles inside an accelerator, which is referred to as a particle beam, is guided along the machine circumference by these external electromagnetic fields. Once the number of circulating particles, i.e. the beam intensity, becomes large, the interaction between themselves and the induced fields in the surrounding environment such as the vacuum chambers has to be considered as well. Therefore, a differentiation must be made between single-particle and collective effects.

A brief and non-exhaustive introduction to both fields is set out in the following sections, which

is in large part based on the excellent available literature [17–23]. The interested reader is referred to these texts for more in-depth treatment of the subjects.

2.1 Transverse motion and resonances

Given the circular geometry of a synchrotron, a curvilinear coordinate system as illustrated in Fig. 2.1, is the appropriate choice to describe the motion of particles. The vectors x and y span the transverse plane, which is perpendicular to the motion of a particle on the ideal design orbit. The longitudinal distance of an arbitrary point along this orbit is defined by the coordinate s. To keep a reference particle with momentum p_0 on the design orbit of a synchrotron the equality

$$\frac{p_0}{e} = B_0(s)\rho(s) \tag{2.2}$$

needs to be satisfied. B_0 and ρ denote the dipole field and the local radius of curvature, respectively, and the product of these terms is called magnetic rigidity. In accelerator physics it is common to use s instead of the time t as the independent variable, and the system can be described in terms of the Hamiltonian

$$\mathcal{H} = -\left(1 + \frac{x}{\rho}\right)\left[p^2 - p_x^2 - p_y^2\right]^{\frac{1}{2}} - eA_s, \tag{2.3}$$

where A_s refers to the third component of the vector potential, which, however, is not equal to the $s-$projection of $\boldsymbol{A}$.

Usually the transverse momenta are small compared to the total momentum, i.e. $p_{x,y} << p$, which allows the expansion of the square root. Considering only linear magnetic fields, i.e.
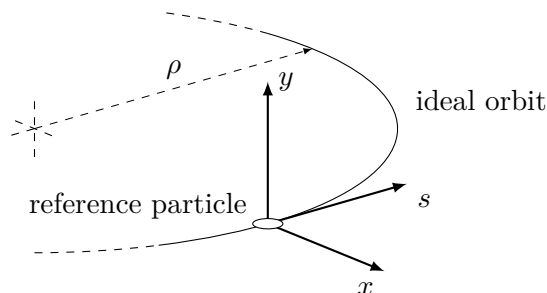

Figure 2.1. Curvilinear coordinate system applied in synchrotrons. x and y specify the transverse distance from the design orbit and s measures the longitudinal distance along it.

dipolar and quadrupolar contributions, the transverse magnetic components read

$$
\begin{aligned}
B_x &= \frac{\partial B_y(s)}{\partial x} y, \\
B_y &= B_0(s) + \frac{\partial B_y(s)}{\partial x} x,
\end{aligned}
\tag{2.4}
$$

and with the definition of the normalized quadrupole gradient

$$
k(s) = \frac{\partial B_y(s)}{\partial x} \frac{1}{B_0(s)\rho(s)},
\tag{2.5}
$$

the linearized transverse Hamiltonian becomes

$$
\mathcal{H}_{\mathrm{tr}}^{\mathrm{lin}} = (p - p_0)\frac{x}{\rho} + p_0 \left[\left(\frac{1}{\rho^2} - k \right) \frac{x^2}{2} + k\frac{y^2}{2} \right] + \frac{p_x^2}{2p_0} + \frac{p_y^2}{2p_0}.
\tag{2.6}
$$

By applying Hamilton's equations

$$
z' = \frac{dz}{ds} = \frac{\partial \mathcal{H}_{\mathrm{tr}}^{\mathrm{lin}}}{\partial p_z} \qquad \text{and} \qquad p_z' = \frac{dp_z}{ds} = -\frac{\partial \mathcal{H}_{\mathrm{tr}}^{\mathrm{lin}}}{\partial z},
\tag{2.7}
$$

where z refers to either x or y, the inhomogeneous differential equations of motion are obtained:

$$
\begin{aligned}
x'' + K_x(s)x &= \frac{\delta}{\rho}, \\
y'' + K_y(s)y &= 0,
\end{aligned}
\tag{2.8}
$$

which are known as Hill's equations. The functions $K_x(s) = \left(\frac{1}{\rho^2} - k \right)$ and $K_y(s) = k$ describe the focusing properties of the lattice and satisfy the periodicity condition $K_z(s) = K_z(s+C)$, where C is the accelerator circumference. Furthermore, the relative momentum deviation $\delta = \Delta p / p_0$ was introduced. The general solution of Eqs. (2.8) can be written as

$$
z(s) = \sqrt{\varepsilon_z \beta_z(s)} \cos(\varphi_z(s) + \varphi_{z,0}) + \delta D_z(s).
\tag{2.9}
$$

The emittance ε_z is a measure of the area enclosed by the particle trajectory in the respective phase space spanned by (z, z'), $\beta_z(s)$ denotes the periodic betatron amplitude function, $\varphi_z(s)$ and $\varphi_{z,0}$ the betatron phase and its initial condition, respectively, and $D_z(s)$ the dispersion function. An on-momentum particle ($\delta = 0$) performs betatron oscillations around the design orbit, whereas these oscillations take place around a different, dispersive, orbit for particles with $\delta \neq 0$. Moreover, vertical dipoles are usually only installed in transfer lines between two accelerators, but not inside synchrotrons themselves, and, therefore, the vertical dispersion function is zero. In general, the term 'optics functions' is used to describe both $\beta_z(s)$ and $D_z(s)$. An important parameter for the stability of the motion is the betatron tune Q_z. It describes the accumulated phase advance over one turn or, more intuitively, the number of transverse

oscillations a particle performs per revolution:

$$Q_z = \frac{1}{2\pi} \, \varphi_z(s) = \frac{1}{2\pi} \oint \frac{ds}{\beta_z(s)}. \tag{2.10}$$

The fractional part of the tune is often referred to as q_z.

The above considerations are valid for ideal accelerators. In reality, however, the motion is influenced by unavoidable magnetic imperfections arising from fabrication tolerances or misalignments with respect to the ideal orbit. Therefore, a single particle will no longer pass through the centre of all magnets, but rather follow a different closed orbit, which is determined by the magnetic perturbations. For the purpose of illustration, an ideal machine with only a single dipolar perturbation $\Delta z'$ at a location s_0 is considered, and the resulting distortion of the orbit can be expressed as

$$z_{\mathrm{co}}(s) = \Delta z' \, \frac{\sqrt{\beta_z(s)\beta_z(s_0)}}{2\sin(\pi Q_z)} \cos(\pi Q_z - |\varphi_z(s) - \varphi_z(s_0)|). \tag{2.11}$$

Only for non-integer values of Q_z an infinite growth of the motion can be avoided. Accordingly, dipolar perturbations excite integer resonances. Likewise, magnetic errors of higher order, such as quadrupolar, sextupolar, octupolar, etc., excite additional resonances. To avoid such resonant phenomena and to assure stable motion in general, it is important to choose the working point, i.e. the transverse tunes, of an accelerator such that the resonance condition

$$kQ_x + lQ_y = m, \tag{2.12}$$

where k, l and m are integers, is not satisfied.

Misalignments of magnetic elements also lead to additional important, so-called feed-down, effects. A particle passing off-centre through such a device does not only experience the type of multipolar field the magnet was designed for, but also fields of any lower order. Considering a particle travelling through a quadrupole with an offset Δx, the vertical magnetic field becomes

$$B_y = \frac{\partial B_y(s)}{\partial x}(x + \Delta x) = \underbrace{\frac{\partial B_y(s)}{\partial x}\Delta x}_{\text{dipole (const.)}} + \underbrace{\frac{\partial B_y(s)}{\partial x}x}_{\text{quadrupole}}, \tag{2.13}$$

including also a dipolar contribution in addition to the quadrupolar one.

Furthermore, the concept of chromaticity requires some explanation. As the focusing properties of the lattice depend on the particle momentum, which can be represented by including gradient errors $\Delta K_z \approx K_z \delta$ in the equations of motion, the betatron tune depends on the relative momentum offset. The result is a chromatic, i.e. energy dependent, tune shift, and Q_z can be developed in terms of δ:

$$Q_z(\delta) = Q_{z,0} + Q_z' \delta + Q_z'' \delta^2 + \dots. \tag{2.14}$$

$Q_{z,0}$ refers to the tune of an on-momentum particle and the terms Q'_z and Q''_z denote the linear and the second order chromaticity, respectively. Chromaticity introduces a coupling between the transverse and the longitudinal planes and needs to be carefully controlled during machine operation. It is also often common to define the normalized linear chromaticity as

$$\xi_z = \frac{Q_z - Q_{z,0}}{Q_{z,0}} \frac{1}{\delta}. \tag{2.15}$$

So far, only the motion of single particles has been treated. By considering a particle beam, the aforementioned emittance ε_z adopts a statistical relevance. For such a multi-particle system it is impossible to evaluate all single-particle emittances, and, instead, ε_z is defined as phase space area, which contains a certain percentage of all particles. Real beam distributions are usually Gaussian in the transverse planes, and the root mean square (RMS) beam size can be expressed as

$$\sigma_z(s) = \sqrt{\varepsilon_z \beta_z(s) + D_z(s)^2 \delta^2}, \tag{2.16}$$

where also ε_z and δ are RMS quantities.

2.2   Longitudinal dynamics

In contrast to the transverse magnetic guiding forces, oscillating electric fields are applied in the longitudinal direction to accelerate the particles. For the so-called synchronous particle, the energy gain remains constant every time it traverses an RF cavity. To keep it on the design orbit, synchronization between the oscillation frequency f_{RF} of the electric field and the particle's revolution frequency f_0 is required. However, this does not necessarily imply equality of the two frequencies, and RF cavities are usually operated at multiples of the revolution frequency according to

$$f_{\mathrm{RF}} = h f_0, \tag{2.17}$$

where h is referred to as the harmonic number. This relation shows that, actually, h synchronous particles can be accelerated at the same time. In practice, a beam is accelerated and the RF system groups the particles inside the beam into bunches (see also Fig. 2.3). In such a multi-particle system, a certain spread in momentum or energy between the different particles is unavoidable. The fact that the path length covered by a particle crucially depends on its momentum, leads to a frequency spread, which can be expressed as

$$\frac{\Delta f}{f_0} = -\left(\alpha_c - \frac{1}{\gamma_0^2} \right) \delta = -\eta\delta. \tag{2.18}$$

In the above relation, γ_0 denotes the relativistic parameter, α_c the momentum compaction factor, which is a property of the lattice and describes the dependency of the path length on the

relative momentum offset δ, and η the slip factor. One observes that at the so-called transition energy, for which $\gamma_0 = \gamma_{\mathrm{tr}} = \frac{1}{\sqrt{\alpha_c}}$ holds true, η becomes zero and, therefore, the revolution frequency is independent of the particle momentum. For $\gamma_0 \neq \gamma_{\mathrm{tr}}$, two different regimes can be identified: below and above the transition energy, corresponding to negative and positive values of η, respectively. For $\eta < 0$, an increase of the particle momentum leads to an increased revolution frequency, as the gain in velocity overcompensates for the longer path length. Above the transition energy, the opposite is true and a particle behaves as if it would have negative mass.

In the absence of longitudinal focusing forces, the momentum difference between synchronous and non-synchronous particles leads to a continuous increase of their distance. Therefore, the principle of phase stability [24, 25] is exploited in the longitudinal plane to keep the particles together and to form the already mentioned bunches. In Fig. 2.2, the concept is illustrated: below the transition energy, a low-momentum particle arrives late at the RF cavity with respect to the synchronous particle. It experiences a higher electric field, which is usually of sinusoidal form, and, therefore, higher acceleration. In turn, its revolution frequency increases and it approaches the phase of the synchronous particle ϕ_s. As soon as the particle arrives earlier than the synchronous one, it will be decelerated so that it again closes the gap. This process leads to an oscillation of all particles around the phase ϕ_s, and these synchrotron oscillations are the basis for longitudinal stability. Due to the different dynamics above the transition energy, the phase of the cavity voltage has to be changed from ϕ_s to $\pi - \phi_s$.

In order to derive the longitudinal equations of motion, the synchrotron Hamiltonian

$$\mathcal{H}_{\mathrm{sy}}(\phi, \delta) = \frac{\omega_0 e V}{2\pi \beta_0^2 E_0} \left(\cos\phi - \cos\phi_s + (\phi - \phi_s)\sin\phi_s \right) + \frac{1}{2} h \eta \omega_0 \delta^2, \qquad (2.19)$$
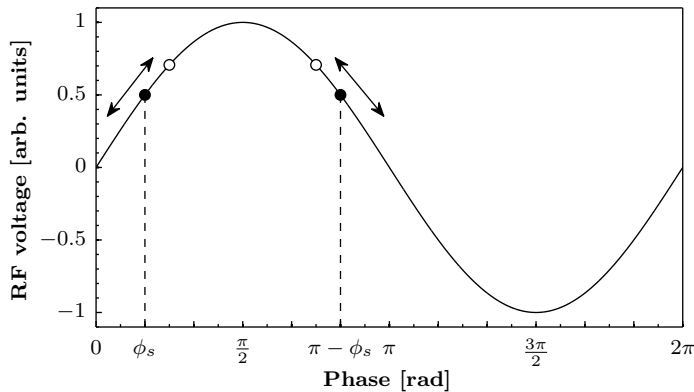

Figure 2.2. Illustration of the principle of longitudinal phase stability in a synchrotron. The solid line represents the sinusoidal wave of the electric field and the black circles represent the synchronous particle below (left) and above (right) the transition energy. All other particles (indicated by the white circles) carry out synchrotron oscillations around the synchronous one.

is considered as starting point. In this expression ω_0 denotes the angular revolution frequency, e the electric charge, V the peak RF voltage, β_0 the relativistic factor, E_0 the total particle energy and ϕ the phase of the particle. In contrast to transverse motion, time t is considered as independent variable, and using the Hamilton formalism leads to the following equations describing the variation of ϕ and δ:

$$
\begin{aligned}
\dot{\phi} &= \quad\frac{\partial \mathcal{H}_{\text{sy}}}{\partial \delta} = h\omega_0\eta\delta, \\
\dot{\delta} &= -\frac{\partial \mathcal{H}_{\text{sy}}}{\partial \phi} = \frac{\omega_0}{2\pi\beta_0^2 E_0}eV(\sin\phi - \sin\phi_s).
\end{aligned}
\tag{2.20}
$$

For constant or slowly varying RF parameters, $\mathcal{H}_{\text{sy}}$ is quasi-static and, therefore, time-independent. This results in the existence of two fixed points, for which

$$
\dot{\delta} = 0 \qquad \text{and} \qquad \dot{\phi} = 0
$$

holds true. They are located at

$$
\begin{aligned}
(\phi_s, 0)/(\pi - \phi_s, 0) &\qquad \text{stable fixed point (SFP)}, \\
(\pi - \phi_s, 0)/(\phi_s, 0) &\qquad \text{unstable fixed point (UFP)},
\end{aligned}
$$

where the first pairs of values correspond to the situation below the transition energy, and the others to the one above it. An example of the longitudinal phase space above the transition energy is shown in Fig. 2.3 (a). The motion around the SFP is elliptic, whereas the trajectories adopt a hyperbolic shape close to the UFP. The phase space trajectory going through the UFP separates the regimes of bound and unbound motion, and is therefore called separatrix. The area contained within the separatrix is referred to as longitudinal acceptance or bucket, and represents the maximum phase space area, which can be covered by a bunch. In Fig. 2.3 (b), accelerating buckets for different values of ϕ_s are compared to the stationary bucket, and one realizes that the available acceptance is significantly reduced during acceleration. Therefore, typical values of ϕ_s are around 30°.

Particles inside the separatrix perform synchrotron oscillations around the SFP, and for small oscillation amplitude, the synchrotron Hamiltonian can be linearized to

$$
\mathcal{H}_{\text{sy}}^{\text{lin}}(\phi,\,\delta) = \frac{1}{2}h\eta\omega_0\delta^2 - \frac{\omega_0 eV}{4\pi\beta_0^2 E_0}\phi^2,
\tag{2.21}
$$

which is valid for the case of a stationary bucket and was obtained by using the small angle approximation $\cos\phi \approx 1 - \frac{\phi^2}{2}$. The equation of motion for the phase is then obtained as

$$
\ddot{\phi} - \frac{\omega_0^2 eVh\eta}{2\pi\beta_0^2 E_0}\phi = \ddot{\phi} - \omega_s^2\phi = 0,
\tag{2.22}
$$

and the linear synchrotron tune Q_s is defined as the number of longitudinal oscillations a particle performs per revolution:

$$Q_s = \frac{\omega_s}{\omega_0} = \sqrt{\frac{eVh|\eta|}{2\pi\beta_0^2 E_0}}. \tag{2.23}$$

2.3 Collective effects

In the previous two sections, single-particle effects were addressed, and their collective interactions were not considered. However, this approach is only admissible as long as the self-generated fields constitute only small perturbations to the external guiding forces. In general, this does not apply to high-intensity beams and, therefore, multi-particle effects have to be carefully studied, as they usually limit the intensity reach of an accelerator.

A differentiation should be made between collective effects in free space, which essentially refers to direct space charge phenomena, and beam interaction with the self-induced electromagnetic fields in the surrounding environment. These effects lead to either incoherent or coherent phenomena, causing a change of the single particle motion or affecting the movement of the beam as a whole. If the induced fields are sufficiently strong, instabilities, which are characterized by an exponential growth of one or several statistical moments of the beam distribution, can develop. Eventually, this will result in emittance blow-up and beam loss, causing significant degradation
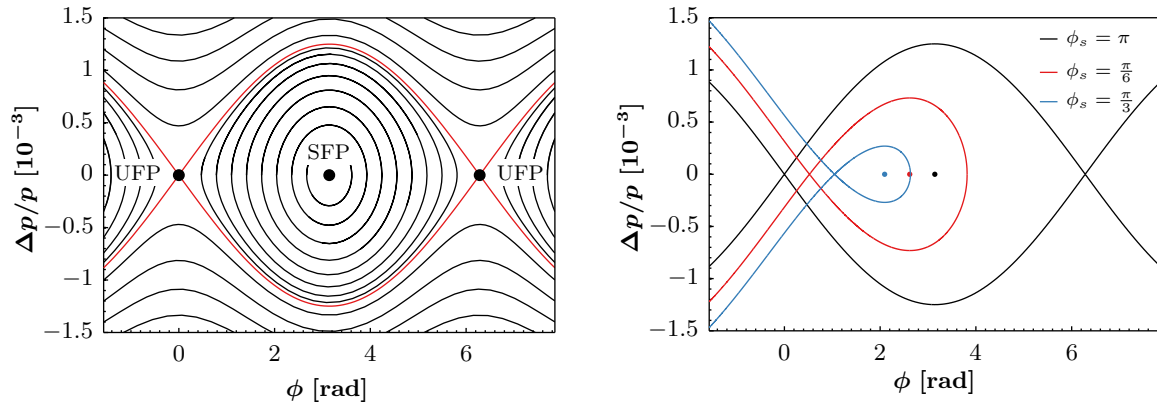
(a) Phase space portrait of a stationary bucket. Inside the separatrix (red line), the motion is stable and particles perform synchrotron oscillations around the SFP. Particle motion outside this bucket area is unbound.

(b) The SFPs of accelerating buckets above the transition energy are located at $\phi = \pi - \phi_s$. The acceptance is clearly reduced with respect to a stationary bucket.

Figure 2.3. Longitudinal phase space for stationary and accelerating buckets above the transition energy.

of the beam quality.

An ensemble of identically charged particles experiences a Coulomb repulsion, which is commonly known as direct space charge effect. However, if the particles are non-stationary, their movement also constitutes an electric current, which is accompanied by a magnetic field. The repulsion is then partially compensated by the magnetic attraction and, if $\beta = 1$, both contributions cancel out completely.

The transverse repulsion affects the focusing properties of the accelerator. A common approach to evaluate the effect of direct space charge forces on the beam distribution is to include a space charge driven focusing error in the equations of motion presented in Eq. (2.8). Consequently, the particles experience a tune shift, which, for a transversely Gaussian distribution, can be expressed as

$$\Delta Q_z = -\frac{r_0 R}{2e\beta_0\gamma_0^2\varepsilon_z^n}\lambda, \tag{2.24}$$

with r_0 the classical radius of a proton, R the average radius of the machine, $\varepsilon_z^n = \varepsilon_z\beta_0\gamma_0$ the transverse normalized emittance and λ the longitudinal line density of the beam. One remarks that the direct space charge tune shift is always defocusing, and that it induces an incoherent tune spread inside the beam, which depends on the longitudinal particle position. This spread results in a modification of the low-intensity working point and in a potential overlap with resonances if the condition in Eq. (2.12) is fulfilled. Due to the inverse dependency on $\beta_0\gamma_0^2$, the tune spread is most important in low-energy machines.

In the above considerations, the electromagnetic interaction between the beam and the surrounding environment was not taken into account. If particles circulating off-centre in a perfectly conducting and smooth vacuum chamber are assumed, a ring of induced charges travels at identical speed with the beam. Depending on the frequency of the induced fields, they are either non-penetrating or penetrating. Only the latter can eventually reach the magnet poles. With the effect depending on the vacuum chamber geometries, these fields act back on the circulating distribution, and cause incoherent and coherent tune shifts.

Furthermore, space charge effects are also present in the longitudinal plane, where they depend on the derivative of the line density λ', and change from being defocusing below to focusing above the transition energy.

In reality, however, vacuum pipes have finite conductivity and their geometry varies along the accelerator circumference to accommodate, e.g. injection, extraction and measurement systems. In contrast to the previously explained space charge effects, which lead to a real tune shift, these non-ideal geometries induce a complex tune shift and the imaginary part characterizes the growth rate of instabilities.

For the purpose of illustration, a simple model containing only two particles travelling a distance ds apart from each other on the ideal orbit can be considered. In a real chamber, the leading particle leaves behind the so-called wake field, which can perturb the motion of the trailing one. In the longitudinal plane, this results either in energy loss of the second particle or in heating

of the accelerator equipment. The force experienced by a particle when traversing a certain element can be expressed as

$$W_{\parallel}(ds) = -\frac{\Delta E_2}{q_1 q_2}, \tag{2.25}$$

where $W_{\parallel}(ds)$ is the longitudinal wake function, and q_1 and q_2 the electric charges of the source and the trailing particle, respectively.

In order to affect the transverse dynamics, an offset of at least one particle is required. This gives rise to the definition of the dipolar and quadrupolar wake functions

$$
\begin{aligned}
W_{Dz}(ds) &= -\frac{\Delta E_{z,2}}{q_1 q_2 \Delta z_1}, \\
W_{Qz}(ds) &= -\frac{\Delta E_{z,2}}{q_1 q_2 \Delta z_2},
\end{aligned}
\tag{2.26}
$$

where the normalization by the respective transverse offset $\Delta z_{1,2}$ was introduced. This formalism is especially useful for simulation codes, as it can be applied to derive the kicks experienced by the trailing particles according to

$$\Delta z_2'(ds) = -\frac{q_1 q_2}{E_0}[W_{D,z}(ds)\Delta z_1 + W_{Q,z}(ds)\Delta z_2]. \tag{2.27}$$

A different, but equivalent, approach of describing the beam-environment interaction is based on the fact that the material characteristics depend on the frequency of the fields. Therefore, it is natural to describe the accelerator elements in the frequency domain, leading to the concept of impedance, which is obtained by computing the Fourier transform of the wake function:

$$
\begin{aligned}
Z_{\parallel}(\omega) &= \int_{-\infty}^{\infty} W_{\parallel}(s)e^{-i\omega s/c}\frac{ds}{c}, \\
Z_{D,Q,z}(\omega) &= i\int_{-\infty}^{\infty} W_{D,Q,z}(s)e^{-i\omega s/c}\frac{ds}{c},
\end{aligned}
\tag{2.28}
$$

with c the speed of light. The real and imaginary parts of the impedance then describe the effect on the motion. For example, the indirect space charge impedance, which is purely imaginary, does not cause any instability. Application of an inverse Fourier transform to the impedance, yields again the wake function of the respective element.

3 The CERN Proton Synchrotron

It was a milestone when proton beams in the PS reached the design top energy of 26 GeV in November 1959. For the first time in the history of accelerator physics, an accelerator based on the alternating-gradient focusing principle had been successfully commissioned.

In addition to protons, various other particle species have been accelerated since then, namely deuterons for the Intersecting Storage Rings (ISR), antiprotons for the Super Proton Antiproton Synchrotron (Sp$\bar{\text{p}}$S) collider, and electrons and positrons for the Large Electron Positron (LEP) collider. Today, the PS holds a key position within the injector chain of the LHC, where it receives beams from the PSB and the Low Energy Ion Ring (LEIR), and transfers them to the SPS. It either accelerates protons or heavy ions for the LHC physics programme or provides those beams to different fixed target experiments.

The following pages give an overview of the main elements making up the PS [26, 27], as well as of the devices used to perform the measurements presented in this thesis.

3.1 The main components of the PS

The accelerator is composed of 100 combined function magnet units (MUs), which are interleaved by 100 straight sections (SSs), leading to a total circumference of $2\pi \times 100$ m. Each MU is divided into two half-units, a focusing and a defocusing structure, respectively, providing the alternation of the gradient. Overall, this arrangement results in a FOFDOD lattice and additional elements, such as devices for injection and extraction, accelerating cavities and auxiliary magnets, are located in the drift spaces between the MUs. In addition to the 100 main magnets installed in the PS tunnel, one reference magnet (MU101), which is electrically connected in series with the other elements, is accessible during machine operation to perform magnetic measurements.

Figure 3.1 shows a cross section of one MU. The main excitation is provided by the main coils, and additional circuits, the Pole Face Windings (PFW), are located on top of the hyperbolically shaped magnetic poles. These special elements are divided into narrow and wide windings for each half-unit, and the naming convention refers to the width of the air gap at the position of the respective circuit. Together with the Figure-of-Eight Loop (F8L), which is an additional winding that crosses between the two half units giving the corresponding shape, the PFW allow the control of betatron tunes and linear chromaticities. However, depending on their settings, the PFW can induce highly non-linear fields, which may lead to beam instabilities. Therefore, extensive measurements were conducted in the past to determine the 5×5 working point matrix, which expresses the relationship between the currents of the five circuits and the beam dynamics observables tune and linear chromaticity [29]. In theory, the second order chromaticity in one plane could also be controlled using this approach; however, this was shown to be rather unreliable [30] and, therefore, a reduced 4×4 matrix is usually used during operation.

In contrast to these smoothly distributed elements, 40 Low Energy Quadrupoles (LEQ) are installed to control both transverse tunes from injection kinetic energy at 1.4 GeV up to a kinetic energy of about 3.5 GeV. Due to the limited strength of the LEQ, the PFW and the F8L take over the control of the working point above this energy. The LEQ, the F8L and the individual circuits of the PFW are independently powered, offering high flexibility during machine operation.

Among the LHC injectors, the PS is the accelerator used to define the longitudinal structure of the beams. Different types of RF cavities, installed in various SSs, allow the carrying out of different manipulations in the longitudinal phase space. This includes bunch splitting or merging, but also rotations in order to provide short bunches. The main accelerating system comprises eleven 10 MHz cavities, with one of them being a spare, and additional 20, 40, 80 and 200 MHz cavities are available as well.
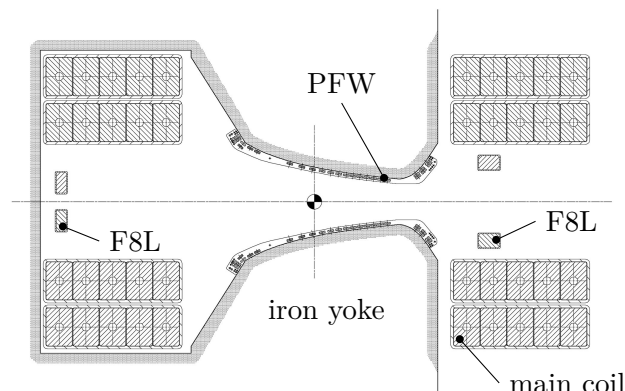

Figure 3.1. Cross section of one MU of the PS. The reference point between the two poles corresponds to the location of the closed orbit. The circuits of the PFW, which are encapsulated by an epoxy resin, are situated directly on top of the poles. Furthermore, the main coils and the F8L are visible [28].

The remaining SSs are, on the one hand, occupied by additional auxiliary magnets such as dipole correctors, sextupoles and octupoles, but also by devices used to measure different beam characteristics as presented in the next section.

Furthermore, the definition of some terminology, which will be frequently used throughout this thesis, is in order. First, this concerns the naming convention applied in the PS. Every element installed in the tunnel is characterized by two or three letters followed by two numbers. Choosing one of the extraction kickers, namely KFA04, for the purpose of illustration, this can be understood in the following way: KFA stands for Kicker FAst, whereas 04 identifies SS04 as its location. Additional important terms are described using Fig. 3.2. The PS is a cycling machine and, therefore, the magnetic field rises to a certain value to keep the beam on the closed orbit during the process of acceleration and decreases back to zero after extraction. This occurs within a given time frame, which has the length of either one or multiple basic periods (BPs), each lasting 1.2 s. The sequence of all processes, including injection, acceleration, extraction and possible additional beam manipulations is referred to as cycle, and the characteristics of each cycle depend on the specific requirements of the user, for whom the beam is intended. To deliver beam to multiple facilities almost simultaneously, different cycles are grouped together to the so-called super-cycle (SC), which is usually around 30 BPs long, but can be reprogrammed within minutes.
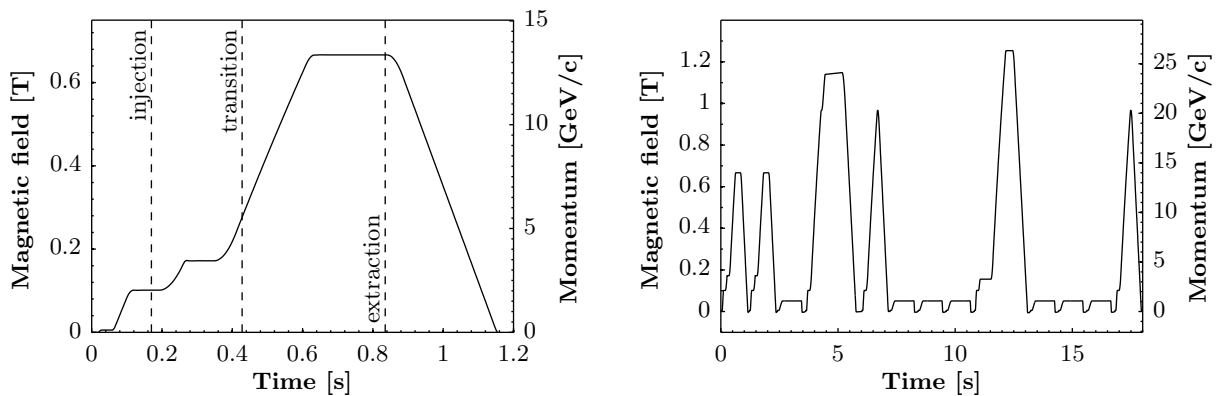
(a) Typical PS magnetic cycle used to produce the SPS fixed target beam (see also Chapter 6). Injection occurs at 170 ms, transition energy is crossed at 428 ms and the beam is extracted at 835 ms.

(b) PS SC with two fixed target and a zero cycle in front, followed by cycles dedicated to physics in the EAST area and the nTOF facility. The cycle reaching 26 GeV/c corresponds to one for the LHC.

Figure 3.2. Illustration of a cycle and a SC in the PS.

3.2 Beam instrumentation

In order to properly study the evolution of a beam distribution in a given time frame, which can range from a few turns up to seconds, a set of adequate measurement systems is indispensable. The main parameters of interest are usually the beam intensity, the betatron tunes, and the transverse and longitudinal distributions. Furthermore, it is important to closely monitor beam loss along the accelerator, which allows early detection of equipment failure and is an important ingredient to keeping the radiation levels low. In small and low-energy machines the damage potential of the beam is usually small; however, especially for a collider such as the LHC, with an enormous amount of energy stored in the circulating beam, accurate beam loss measurements become part of the machine protection system. The various types of beam instrumentation installed in the PS, which are suited to measure the aforementioned parameters, are briefly discussed below.

Beam intensity measurements are performed with rather simple devices, so-called beam current transformers (BCTs). The circulating beam induces a certain magnetic flux in dedicated measurement coils, and the measured signal can then be related to the beam intensity [31]. In the PS, a measurement is provided every millisecond.

Control of the betatron tunes during the acceleration cycle is important to assure beam stability. Therefore, it has to be possible to measure these parameters with high precision. The common approach is to kick the beam in the transverse planes, and to record the subsequent oscillations of the beam centroid with position sensitive electrostatic pick-up (PU) electrodes for consecutive turns. The tune is then obtained by performing a Fast Fourier Transform (FFT) on the oscillating signal. The intrinsic error of this procedure is proportional to $1/N_{\mathrm{turns}}$, with N_{turns} being the number of recorded turns. By performing either an interpolation on the obtained magnitude spectrum or applying a windowed FFT, the error can be further reduced [32, 33].

At CERN, the especially sensitive Base Band Tune (BBQ) measurement system has been developed, which can detect oscillation amplitudes of only a few nanometres [34]. At the moment, the BBQ system is applied throughout the LHC injector chain and at the LHC itself, but also at other laboratories.

Fundamental information about the beam requires accurate knowledge of the transverse and longitudinal phase space distribution. However, a direct measurement of these quantities is not possible. Usually, the projections of the distributions on the x, y and s axes are obtained.

To measure the transverse profiles in the PS, beam wire scanners (BWSs) are installed at multiple locations in the ring. These devices flip a thin carbon wire through the circulating beam to create secondary particles, which are then detected by an arrangement of scintillators and photomultipliers. Subsequently, correlation of the position of the wire and the signals coming from the photomultipliers makes it possible to obtain a projection of the beam distribution and, if the optics functions at the respective location are known, the transverse emittance can be deduced [35]. Currently three horizontal (in SS54, SS65 and SS68) and two vertical (in SS54

and SS85) devices are installed in the PS. One has to note that these devices do not provide an instantaneous measurement of the distribution, as the wire takes about 2 ms to traverse the beam (see also Section 6.2.1.2).

In the longitudinal plane, the signal from a PU or a wall current monitor (WCM) provides a measurement of the bunch profile. As it performs synchrotron oscillations, the distribution slightly rotates every turn and each profile corresponds to a projection at a different angle. Applying a tomographic reconstruction algorithm, it is then possible to accurately reconstruct the longitudinal phase space [36].

To understand the distribution of beam loss along the ring, two different systems are currently in use. On the one hand, the ageing system based on Aluminium Cathode Electron Multiplier (ACEM) detectors is the one mainly applied during machine operation [37, 38]; however, a new system has already been designed and will be installed in the coming years [13]. These beam loss monitors (BLMs) are glass vacuum tubes installed on top of each main magnet, and every lost particle, which impacts on the aluminium cathode, causes electron emission. Signal amplification is achieved via multiplication of the electron current using dynodes. As the subsequent electronics modules integrate the signal over 1 ms, losses cannot be resolved on a turn-by-turn basis. Therefore, the system is usually referred to as slow BLMs.

Certain applications require a loss measurement with a time resolution better than one revolution period, i.e. smaller than 2 μs. Therefore, new types of BLMs have been installed at critical locations, namely on the main magnets after the injection and extraction septa as well as on MU15 (see also Section 6.2.4). The active elements are diamond detectors, providing a time resolution of a few nanoseconds. Eventually, 16 of these fast BLMs will be installed in the PS.

4 Beam dynamics simulation codes

In the scope of this thesis, several beam dynamics studies have been performed, which required a close interplay of experimental and numerical approaches. The work presented in Chapters 5 and 6 relies essentially on three different well-known and benchmarked simulation codes. This chapter serves as an introduction to these tools and as a justification for their suitability for the studies presented in the following. Code development itself was not pursued as part of this thesis and, therefore, extensive discussions on the applied models and the actual implementation of the codes are omitted. For further details, the interested reader is referred to the cited references.

4.1 MAD-X/PTC

Initially developed at CERN to design the optics of the LHC, the Methodical Accelerator Design (MAD)-X program has become the quasi-standard to design, study and optimize lattices for circular accelerators and beam lines over the last decade [39].

In order to investigate the optics parameters of a certain structure, the sequence of the elements representing its lattice has to be specified. This includes the definition of the element's type (bending magnet, quadrupole, RF cavity, etc.), its geometrical properties, i.e. the dimensions and the positioning, as well as the strengths of active elements. After importing all required information, it is, among other things, possible to compute the optics parameters, match the properties of the machine to desired values and evaluate the effect of magnetic errors on the particle motion [40, 41].

Moreover, a tracking module is included in MAD-X, which propagates a particle's phase space coordinates over an arbitrary number of turns around the accelerator. However, it comes with the disadvantage of being non-symplectic when considering thick elements, i.e. the phase space volume is not preserved during this process. To overcome this drawback, the Polymorphic Track-

ing Code (PTC) library, which provides symplectic integration methods and allows the user to determine the required precision, was embedded into MAD-X [42]. In addition, matching of non-linear chromaticity, the computation of anharmonicities, i.e. the detuning with amplitude, and the determination of the optics functions around any SFP are possible with PTC. As this is a fully integrated library, MAD-X basically acts as the interface to PTC and the aforementioned element definitions are taken over accordingly. Based on these features, PTC is ideally suited to account for the complexity of the PS main magnets, and especially to study the Multi-Turn Extraction (MTE) (see also Chapter 6).

Modelling the lattice in a realistic way in simulations is a rather difficult task, which is a consequence of the complexity of the PS MUs. To construct the combined function magnet, each MU is made up of two sector bending magnets (SBENDs), as shown in Fig. 4.1. In addition to the dipole component, each SBEND is assigned with either a focusing or a defocusing quadrupolar component. Moreover, two thin multipoles are inserted in every half-unit, which are used to build an effective non-linear model of the machine. Based on non-linear chromaticity measurements, quadrupolar, sextupolar and octupolar kicks are then introduced into the lattice via these multipoles [43].

At the time of the construction of the PS, the magnetic errors of the different MUs were not measured. Therefore, no random components are currently included in the simulations. However, magnetic measurements of spare magnets as well as 3D simulation studies of the MUs have been started, which will allow further improvement of the modelled lattice.
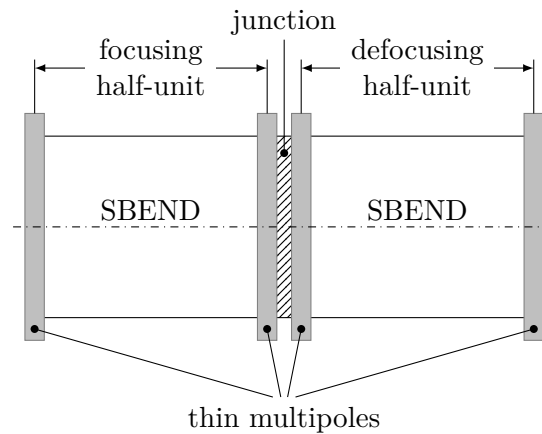
Figure 4.1. Modelling of the PS MU. The thin multipoles are inserted to match non-linear chromaticity up to the octupolar component.

4.2 PyORBIT

To model and understand space charge effects in the LHC injector complex, the symplectic tracking provided by PTC and the object-oriented Objective Ring Beam Injection and Tracking (ORBIT) code [44] were interlinked to form the code PTC-ORBIT and, more recently, its successor PyORBIT [45]. The latter provides a Python interface, is parallelized and can also be extended by the user, if desired. Several space charge solvers (particle-in-cell and frozen [46]) are implemented. Furthermore, time-dependent variation of the strengths of the magnetic elements as well as acceleration using single or double harmonic RF systems can be achieved via input tables for each individual element [47].

The usual approach to set up simulations with PyORBIT (or PTC-ORBIT in the past) is to create a flat file within MAD-X/PTC, which contains the full description of the lattice. In addition, the aforementioned table files, describing the elements' variation in time, are required. Particle distributions can be either initialized using PyORBIT itself or external input files. Particles are then tracked with PTC using the integration method specified in the flat file. At certain interaction nodes, the coordinates are handed over to the C++ routines, which perform the space charge calculations. Subsequently, the coordinates are handed back to PTC and tracking continues until the next node is reached.

Even though usually applied for space charge studies at CERN, PyORBIT was used as a single-particle tracking code only for the work presented in the following. The feature of programming time-dependent magnetic strengths allowed to investigate the transverse beam splitting in the framework of MTE. The corresponding simulation results are presented in Chapter 6.

4.3 PyHEADTAIL

In contrast to the two previously described codes, which have been applied to perform studies of the single-particle dynamics, the PyHEADTAIL code [23] is exclusively dedicated to investigate collective effects in circular accelerators. Developed in order to restructure and increase the flexibility of its predecessor HEADTAIL [48], PyHEADTAIL provides the tools to simulate the effect of wake fields and impedances, space charge, and electron clouds on the particle motion. The physical concepts of the code are based on [20] and, following a common approach in simulations, a beam is described using so-called macroparticles, each of which representing a multitude of particles. The implemented tracking algorithm transports these macroparticles using linear transfer matrices in the transverse planes, while the longitudinal equations of motion are integrated every turn. To study the interaction with the surrounding environment, which is represented in terms of wake fields or impedances, the contributions of different elements such as vacuum chambers or kickers, are usually weighted by the $\beta-$function at the respective locations to compute and apply an effective kick to the macroparticles once per turn. In contrast to this

approach, the study of space charge effects requires, just as described in the case of PyORBIT above, numerous interaction points per turn. Based on the rather simple tracking algorithm, simulations with PyHEADTAIL are significantly less demanding in terms of time compared to PyORBIT; however, this comes with the drawback of being unable to properly model complex lattices and non-linear dynamics.

This code is perfectly suited for the investigations presented in Chapter 5, where the interaction of the injected beam with the wake fields based on the PS vacuum chamber is studied. In addition to PyHEADTAIL, the analytic code Impedance-Wake2D [49] was applied to compute the wake functions from the beam coupling impedance of a cylindric structure. This code adopts a piecewise polynomial interpolation, which allows the computation of the Fourier transform for a set of non-equidistant points.

5 Intra-bunch injection oscillations

In this chapter, intra-bunch oscillations observed in the vertical plane at injection into the PS, which contribute to beam loss for high-intensity beams, are described and explained. These oscillations were perhaps first observed in 1997 [50] and first reported in 2001 [51]; however, the depicted observations were not further investigated and the necessity for detailed studies was pointed out.

Following an introduction about the injection process per se, the results of several measurements that were carried out in the PS at the end of 2012 are presented in Section 5.2.1. These measurements show that different parts along a bunch start to vertically oscillate at different frequencies immediately after entering into the PS. The eccentric motion of the beam, which is due to the closed orbit in combination with injection errors, is understood to trigger these oscillations. In Section 5.3, simulations with the PyHEADTAIL code are presented, whose results are in very good agreement with the observations in the machine.

Currently, the intra-bunch transverse damper system of the PS [52] allows to damp these oscillations. However, a detailed understanding of the underlying mechanism is indispensable in order to predict the efficiency of the system for future high-intensity beams.

5.1 The injection process

Prior to injection into the PS, proton beams are accelerated in the PSB. This synchrotron consists of four identical and almost independent synchrotrons stacked on top of each other. It was constructed to mitigate space charge issues in the PS by increasing the injection energy from 50 MeV to 800 MeV in the first place. By means of two additional upgrades, today's injection energy of 1.4 GeV has been established. After extraction of the bunches produced in these rings, they are vertically recombined in order to send them to a common transfer line towards the

PS [53].

In the PS, a single-turn injection process is adopted. Around the injection septum, located in SS42, four dipole magnets create a horizontal injection bump, which brings the orbit of the circulating particles close to the blade of this magnetic septum. Subsequently, the injection kicker in SS45 puts the beam on the closed orbit. This process is schematically illustrated in Fig. 5.1.

In Fig. 5.2, measurements of the horizontal and vertical trajectories at injection of the beam sent to the nTOF facility, i.e. the TOF beam, are shown. The impact of the injection bump, whose strength reduces to zero within approximately 1 ms, is clearly visible and the large negative
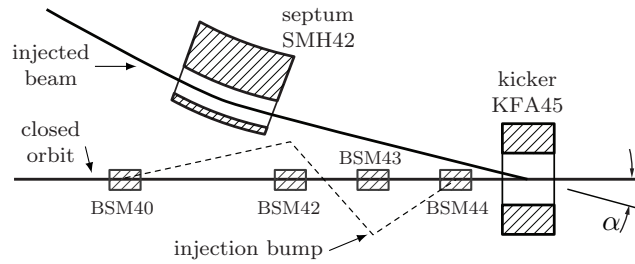
Figure 5.1. Schematic representation of the PS injection region. The dashed line indicates the deviation from the design closed orbit due to the horizontal injection bump, which is created by the dipoles BSM40 - 44 (adapted from [54]).

(a) Horizontal plane.   **(b)** Vertical plane.
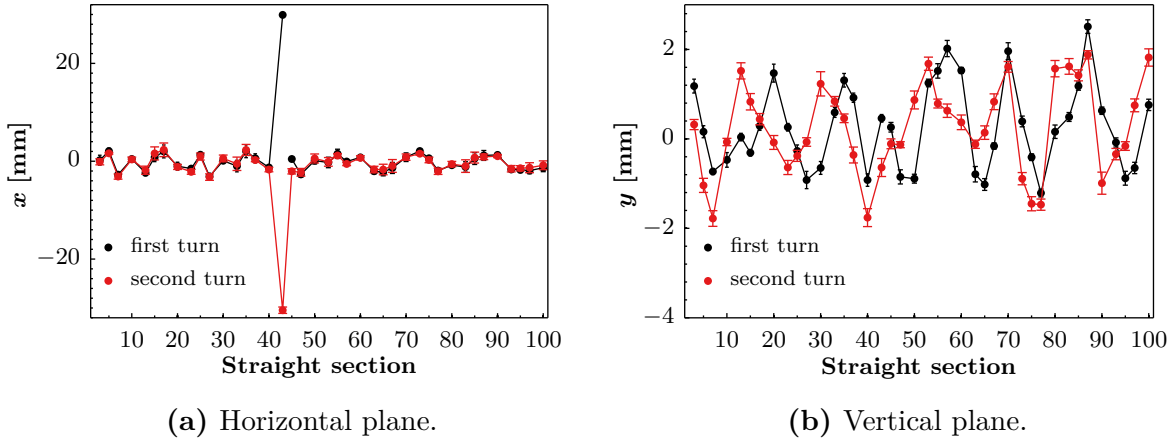
Figure 5.2. Measured transverse trajectories of the TOF beam for the first two turns after injection. Each data point represents an average value over ten measurements and the error bars correspond to the standard deviation. Due to the injection process, the beam enters into the PS with a positive position value in the horizontal plane, which is indicated in SS43. However, on subsequent turns the circulating beam follows the orbit imposed by the injection bump. The positive horizontal excursion of the beam in SS42 is not shown because of the absence of a PU in this location.

excursion of the beam in SS43 constitutes the major horizontal aperture restriction in the PS. A more detailed description of the horizontal aperture depending on the longitudinal position s along the machine is depicted in Fig. 5.3. According to the simulation studies presented in [55], the 3σ envelope of the circulating beam almost touches the mechanical aperture at the beginning of MU43.

Due to the elliptic geometry of the vacuum chamber in MU43, a horizontal excursion of the beam also constitutes a vertical aperture restriction (see Fig. 5.4). Therefore, losses at injection are caused by a beam, which is, due to the vertical closed orbit and the injection error, circulating off-centre.
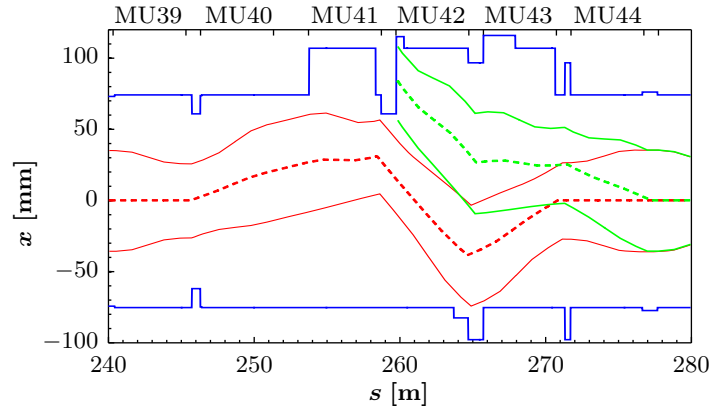
Figure 5.3. Horizontal aperture in the injection region. The dashed lines indicate the orbits of the circulating (red) and the injected (green) beam based on simulations. The solid lines indicate the respective 3σ envelopes and the mechanical aperture is shown in blue. The locations of the MUs are shown on the top. Due to the injection bump, the beam envelope closely approaches the vacuum chamber in MU43 [55].
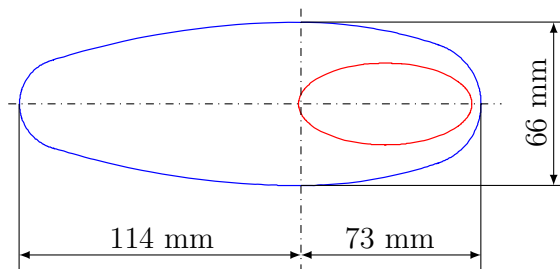
Figure 5.4. Cross section of the vacuum chamber in MU43 (blue). The origin coincides with the closed orbit in the absence of the injection bump. Additionally, the 3σ envelope of the circulating beam, whose offset is caused by the maximum of the bump, is depicted in red. The calculation of the envelope is based on the normalized RMS emittances $\varepsilon_x^n = 10$ mm mrad and $\varepsilon_y^n = 5$ mm mrad. Due to the geometry, the horizontal displacement also causes a limitation of the vertical aperture during the injection process [55].

5.2 Measurement campaign

5.2.1 Measurements at injection in the PS

The stability of particle beams in the PS can be investigated with high bandwidth instrumentation such as a WCM or a wide band pick-up (WBPU). The signals shown in the following were recorded using the WBPU installed in SS94 [56]. Its bandwidth exhibits a flat behaviour from 200 kHz to 250 MHz, which allows the measurement of high-frequency oscillations within a bunch. The WBPU provides three different output channels, i.e. the horizontal and vertical difference signals and the sum signal. The transverse signals are proportional to the bunch displacement and the line density, while the sum signal is proportional to the line density only. Measurements were performed on the high-intensity TOF and CNGS beams, which are both operated at harmonic number $h = 8$ at injection. However, the total intensities vary significantly, as only a single bunch of, at maximum, 850×10^{10} protons is sent to nTOF facility, while eight bunches, resulting in up to 2800×10^{10} protons per pulse (ppp), are accelerated for CNGS-type beams. In the PSB, the TOF bunch is created on $h = 1$ in a single ring, while two bunches per ring (operated on $h = 2$) are created for CNGS. The beam and machine parameters at injection are summarized in Tables I and II.

In Figs. 5.5 and 5.6, the horizontal and vertical difference signals measured on both beams are depicted. Horizontal oscillations, which are, due to the closed orbit in this plane, difficult to interpret are observed. In the vertical plane, oscillations of the bunches are observed as well and the signals are more pronounced than in the other plane. The beam also exhibits some longitudinal oscillations, which are shown in Fig. 5.7. The signals presented in Figs. 5.5-5.7 show non-averaged data. Moreover, it is important to remark that the observations were reproducible each time the beams were injected. In the following emphasis will be put on the vertical oscillations.

Table I. Typical measured beam parameters at injection in the PS

Parameter	CNGS	TOF
kinetic energy E_{kin} [GeV]	1.4	1.4
total intensity N_p [10^{10} p]	2500	700
normalized horizontal RMS emittance ε_x^n [mm mrad]	15	15
normalized vertical RMS emittance ε_y^n [mm mrad]	10	8
RMS bunch length σ_t [ns]	38	53
RMS bunch length σ_s [m]	10.4	14.6
RMS momentum spread δ [10^{-3}]	1.2	2
horizontal incoherent space charge tune spread $\Delta Q_{x,\mathrm{incoh}}$[1]	-0.12	-0.17
vertical incoherent space charge tune spread $\Delta Q_{y,\mathrm{incoh}}$[1]	-0.15	-0.26

[1] The tune spread was calculated according to [57].

Table II. Measured machine parameters at injection in the PS

Parameter	CNGS	TOF
horizontal tune Q_x	6.17	6.13
vertical tune Q_y	6.22	6.27
horizontal linear chromaticity ξ_x	-0.83	
vertical linear chromaticity ξ_y	-1.12	
harmonic number h	8	8
number of bunches	8	1
RF voltage V_{RF} [kV]	40	56.1
machine radius R [m]	100	

Apparently, these vertical oscillations build up rapidly after injection, in a time span which is short compared to the synchrotron period (between 400 and 600 turns at injection). By observing only a small number of consecutive turns (as shown in Figs. 5.5 and 5.6), these signals might be mistaken as head-tail instabilities, which are, in the absence of stabilizing mechanisms such as linear coupling or the transverse damper, regularly observed in the PS on direct space charge dominated high-brightness beams for the LHC [58]. However, this type of instability usually appears in the horizontal plane with a rise time of a few 100 ms, which is in contrast to the vertical oscillations described in this chapter. Figure 5.8 shows such a horizontal instability with four nodes (mode number $q = 4$), which was observed on a beam designated for the LHC [59].

Contrary to this observation, superimposition of six consecutive turns of the TOF beam does not reveal the characteristic structure one would expect from a head-tail instability (see Fig. 5.9).
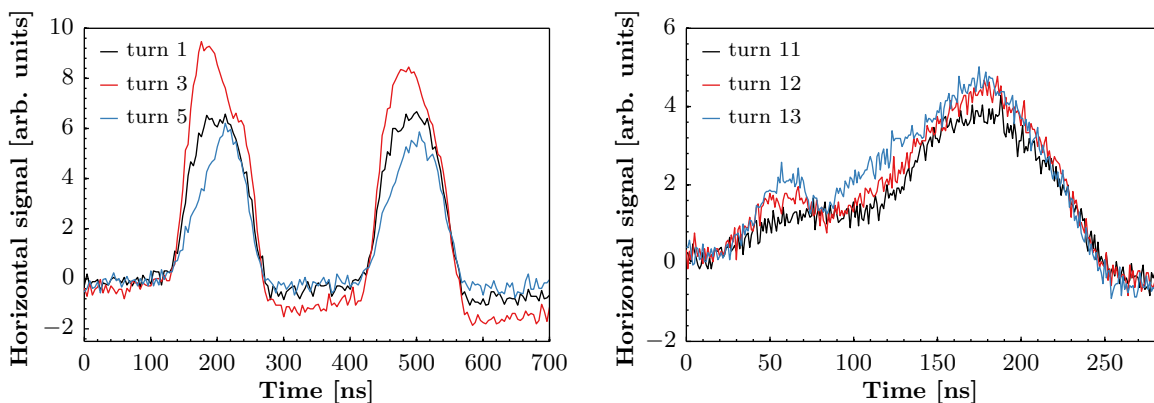
(a) Measurement on the CNGS beam. The maximum amplitude corresponds to about 23 mm.

(b) Measurement on the TOF beam. The maximum amplitude corresponds to about 10 mm.

Figure 5.5. Horizontal difference signals measured on the high-intensity beams.
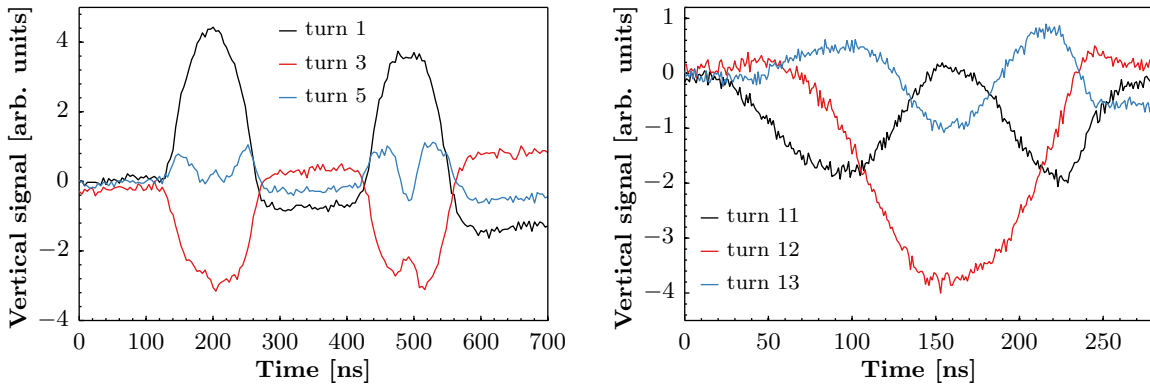
(a) Measurement on the CNGS beam. The maximum amplitude corresponds to about 9 mm.

(b) Measurement on the TOF beam. The maximum amplitude corresponds to about 7 mm.

Figure 5.6. Vertical difference signals measured on the high-intensity beams.
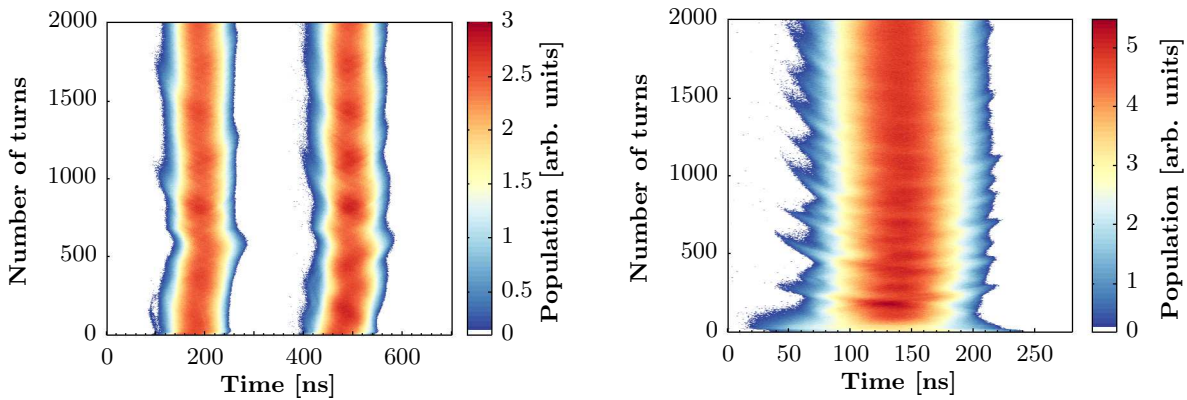
(a) Non-optimal RF-settings cause the shown oscillations on the CNGS beam.

(b) The TOF beam exhibits some quadrupolar oscillations due to its large beam loading [60].

Figure 5.7. Waterfall representation of the longitudinal signals measured on the high-intensity beams for 2000 consecutive turns after injection. The colour scheme applied to this and all subsequent figures has been adapted from [61].
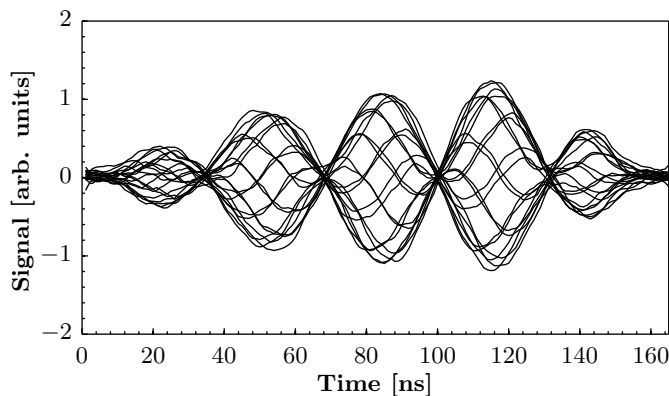
Figure 5.8. Horizontal head-tail instability ($q = 4$) measured on an LHC type beam. 20 consecutive turns of a well established instability are shown and a standing wave pattern is clearly visible [59].
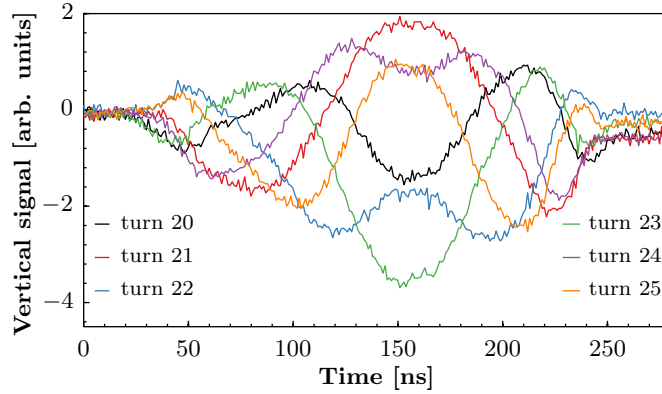
Figure 5.9. Vertical difference signals of six consecutive turns after injection of the TOF beam.

Additionally, head-tail instabilities are usually observed on a time scale longer than several synchrotron periods, as particles at the head and the tail of the longitudinal distribution have to exchange positions to drive the instability [62–64].

The transverse oscillations might also be created by coupling of several high order modes with short growth rate. This Transverse Mode Coupling Instability (TMCI) has already been observed at transition energy in the PS and is usually avoided by applying a longitudinal blow-up and a γ_{tr}−jump scheme. In Fig. 5.10, a measurement of such an instability is depicted. The vertical difference signals of two consecutive turns reveal a high-frequency travelling wave oscillation [54], which is not consistent with the oscillation pattern that is characteristic to the intra-bunch oscillations presented in this thesis. In Section 5.3.3, it will be further justified that the intra-bunch oscillations can be explained without consideration of the head-tail instability or the TMCI.
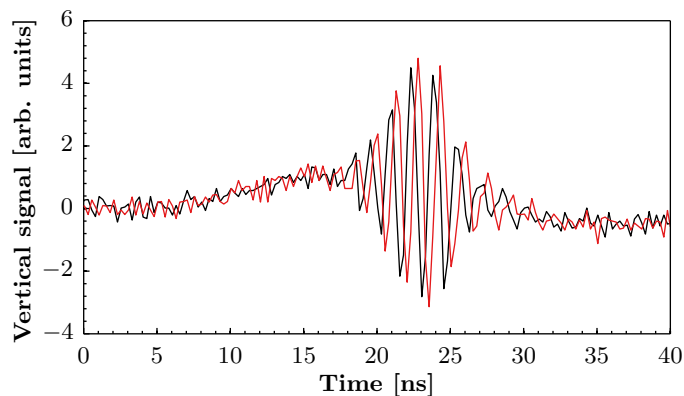
Figure 5.10. In the absence of a γ_{tr}−jump, a vertical TMCI was observed to develop on a TOF bunch when crossing transition energy. In contrast to the presented intra-bunch oscillations, this instability exhibits a travelling wave pattern with a frequency of approximately 700 MHz, which is illustrated by the measured signals of two consecutive turns [54].

In Fig. 5.11, an additional effect becomes apparent. Instead of considering consecutive turns, if one looks at every 20th turn for example, as the number of turns increases, the oscillation frequency is also found to increase. By means of an FFT, the power spectrum along the bunch of each single turn was computed, allowing the turn-by-turn evolution of the oscillation frequency to be obtained. Although this approach is limited in resolution - the recorded signals for single turns consist of only 500 data points - a trend is clearly visible: each turn the intra-bunch frequency increases.

Additional information about the local oscillation frequency could be extracted from the measured data by regarding the bunch as an accumulation of independent, coherently oscillating slices. Each slice is considered to be represented by a single bin of the measurement data and the applied procedure is explained in Fig. 5.12: looking only at the first 20 turns after injection and assuming a linear machine, as is usually the case at injection energy, the harmonic motion of each slice is obtained. Subsequent application of a sinusoidal fit allows computation of the tune of the different slices. It was decided to use this approach rather than an FFT, as the oscillation of each slice is described by only a few data points.

Apparently, these slices are subject to a tune shift depending on their position within the bunch, proportional to the line density. Furthermore, this shift causes the measured vertical tune of the coherent bunch motion to deviate from its programmed value. By means of an FFT over 1000 turns, the measured vertical tune of the TOF beam at injection varies between $Q_y = 6.27$ and $Q_y = 6.29$, while a value of $Q_y = 6.33$ is programmed. This can be explained by the tune shift presented in Fig. 5.12, where the zero intensity working point corresponds to the programmed tune. Due to the parabolic tune shift, the majority of the particles oscillate at frequencies significantly lower than this programmed value and the coherent tune computed by an FFT
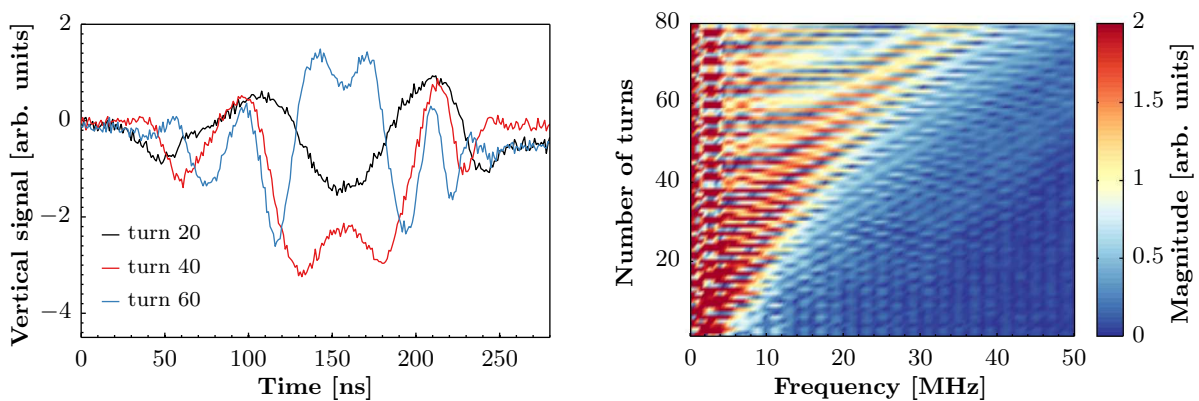
(a) Vertical signals of turns 20, 40 and 60 after injection of the TOF beam

(b) Power spectrum computed every single turn. The trend of increasing oscillation frequencies is evident.

Figure 5.11. Frequency analysis of the vertical injection oscillations.
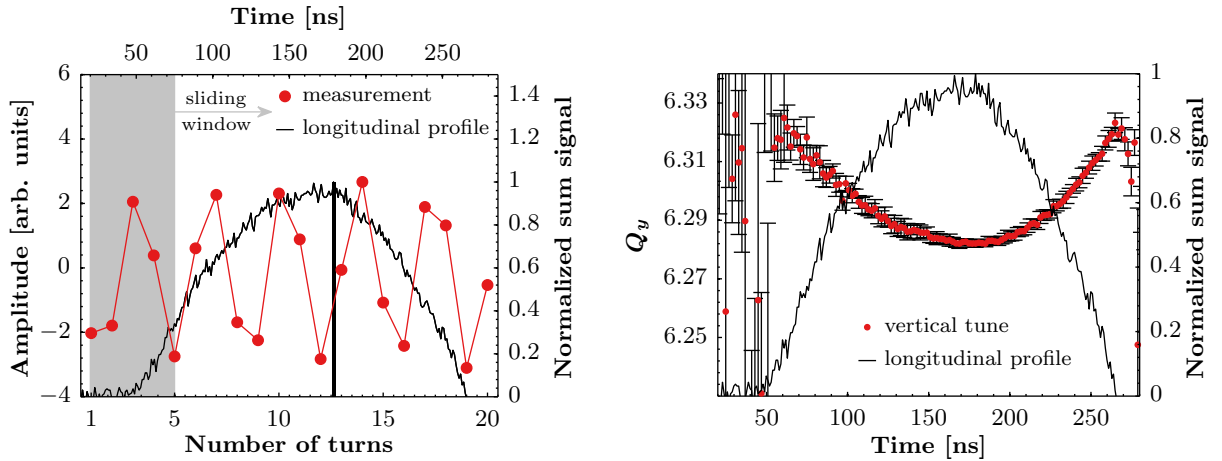
(a) The black bar indicates a single bin of the data. The vertical oscillations performed by this bin over the first 20 turns are represented by the red dots. In order to obtain the vertical tune of this respective bin, a sinusoidal fit considering a window of five turns only (indicated by the grey area) is computed. The window slides from turn 1 to turn 16 and the average over the obtained frequencies is considered as vertical tune of this bin.

(b) A detuning following the line density is revealed and the maximum tune shift is found at the peak density of the bunch. The error bars represent the standard deviation, which increases significantly at the head and the tail of the bunch as the signal is dominated by noise.

Figure 5.12. Computation of the vertical slice-by-slice tune shift along the TOF bunch, based on measured data.

demonstrates this fact.

It is important to mention that the motion of the centroid does not exhibit any growth. Therefore, the observations are described as oscillations rather than instabilities. This will be further justified by the remarks in Section 5.3.3. However, because of the restricted aperture available in MU43, any transverse oscillation of the bunches contributes to the losses in the injection region. Prior to any further investigation in the PS, measurements were carried out in the PSB to assure the stability of the beams arriving at PS injection.

5.2.2 Measurements at extraction in the PSB

In order to investigate the transverse profiles of the beams at extraction in the PSB, the high intensity ISOLDE beams were inspected first. The PUs of the transverse feedback (TFB) system were used to observe the transverse difference signals and 500 turns measured on the different rings are depicted in Fig. 5.13.

The absolute amplitude of the horizontal signal on ring 1 was found to exceed the other signals by about a factor 10, which already indicated a problem of calibration. Furthermore, the vertical signal appeared to be completely distorted and the signals measured on the remaining rings
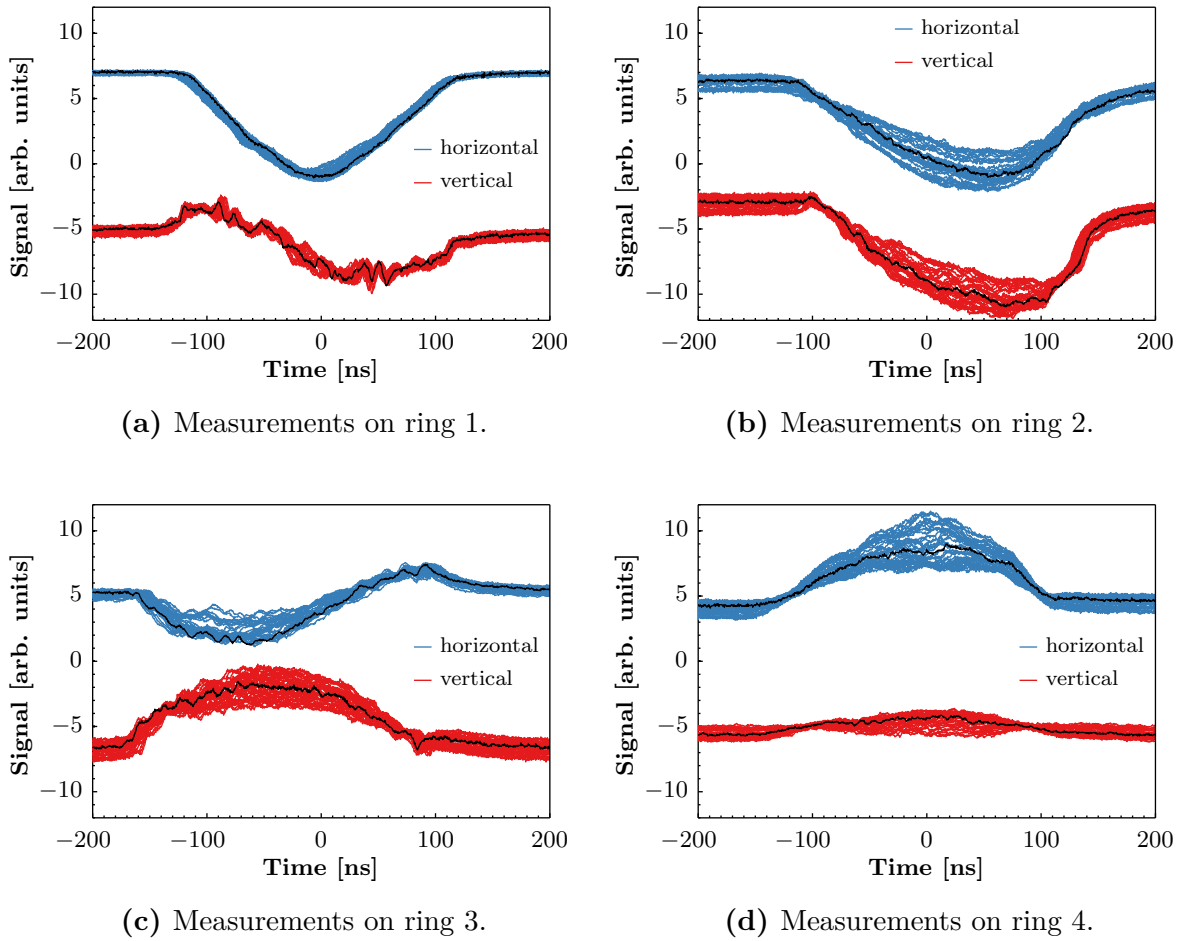
(a) Measurements on ring 1.

(b) Measurements on ring 2.

(c) Measurements on ring 3.

(d) Measurements on ring 4.

Figure 5.13. Transverse difference signals measured with the TFB PUs on all four PSB rings. Per ring, a single bunch with 700×10^{10} p, designated for the ISOLDE facility, was investigated. Measurements were started 2 ms prior to extraction and 500 turns - corresponding to 0.3 ms of data - are shown. In each case turn 250 is indicated in black. The amplitude of the horizontal signal measured on ring 1 was reduced by a factor 10 in order to be comparable to the signals on the other rings. The bunch in ring 1 appears to be distorted in the vertical plane and the horizontal signal on ring 3 indicates a bunch that is slightly skewed. Additionally, several signals show slow radial movements of the bunches.

showed some slow radial movement of the bunches. However, no transverse oscillations as in the PS were observed.

To verify these signals, measurements with a different system of PUs, the Half-Turn (HT) PUs[1], were conducted using the same beam and settings and the results are shown in Fig. 5.14. By using these PUs, no movement or distortion of the bunches in the different rings was observed and they appeared to be completely stable. However, these PUs only provide for a low bandwidth

---

[1]   These PUs were initially used to measure the betatron tunes at injection of a beam, which occupied half the circumference of the machine.

(a) Measurements on ring 1.

(b) Measurements on ring 2.

(c) Measurements on ring 4.
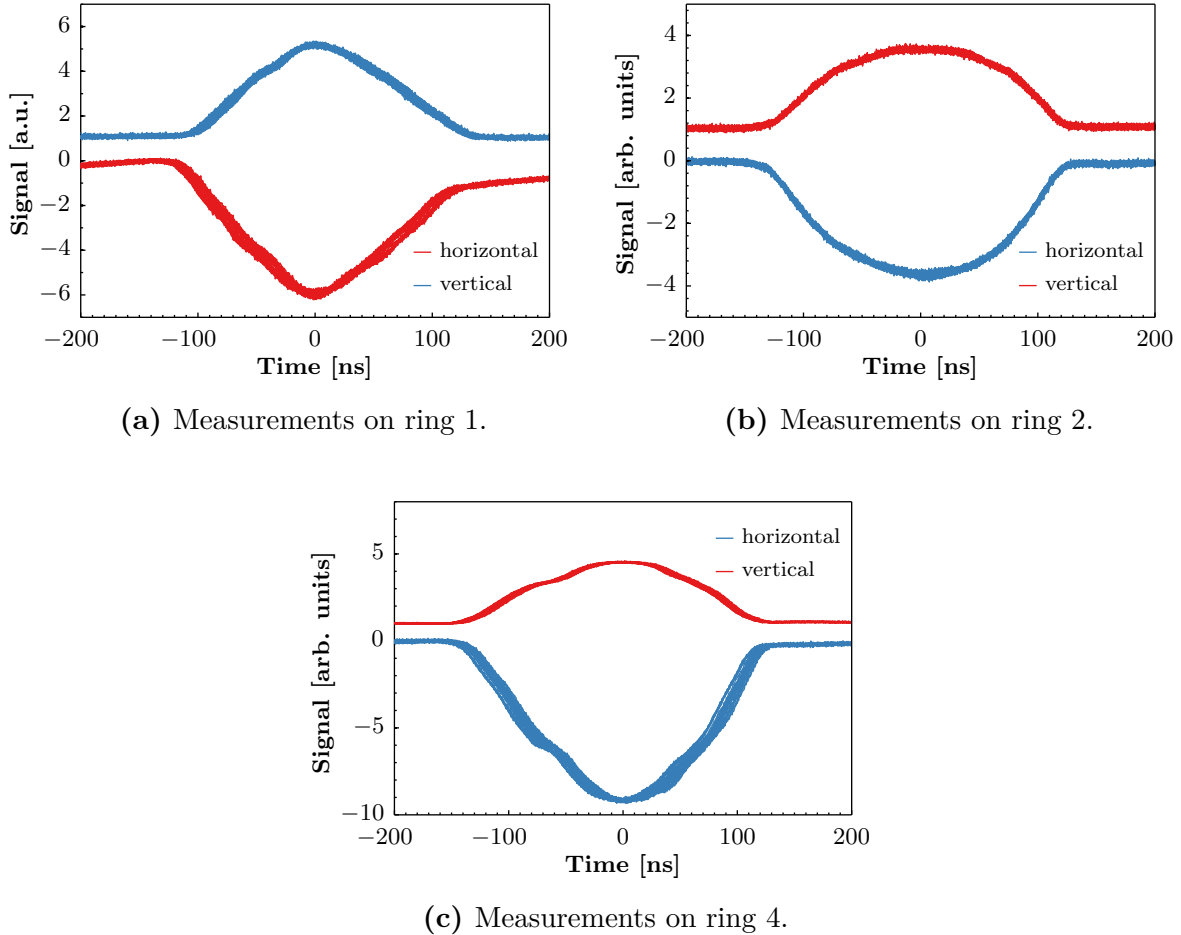
Figure 5.14. Transverse difference signals measured with the HT PUs in different PSB rings. Measurements on ring 3 are not depicted, as there is no HT PU available. The beam and the settings were identical to the ones used to obtain the data shown Fig. 5.13. The bunches appears to be completely stable over the considered 500 turns.

solution (up to approximately 20 MHz) and, therefore, it was decided to use the TFB PUs in a modified way.

As the previously discussed distortion in the vertical plane was no longer present when using the HT PUs, the beam offset signal suppressor (BOSS) unit of the TFB, which is used to remove the contribution of the closed orbit to the signal, was expected to malfunction. Adding two power splitters and one inverting combiner per ring allowed to record the difference signals on a locally connected oscilloscope, while the behaviour of the BOSS unit was excluded for further observations. Furthermore, the operational beams could still use the TFB and proceed as normal (see Fig. 5.15). With this setup, which forms a high bandwidth solution (up to 300 GHz), studies on the CNGS and TOF beams were performed (see Fig. 5.16). In addition to the transverse signals, the longitudinal ones were recorded using an available WBPU.

In both cases, CNGS and TOF, the beams were found to be completely stable, even though the intensities had been significantly increased compared to the values in Table I. Therefore, a malfunction of the BOSS unit was confirmed. This led to the understanding that the oscillations described in Section 5.2.1 are indeed generated within the PS itself.
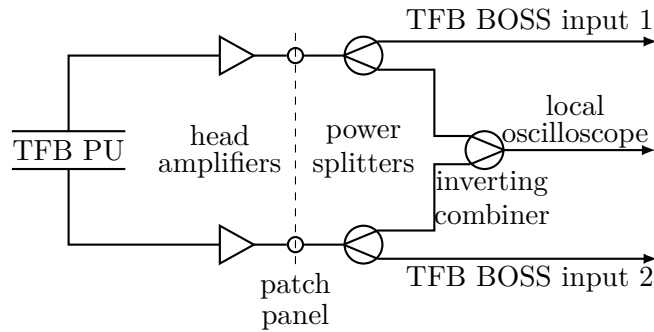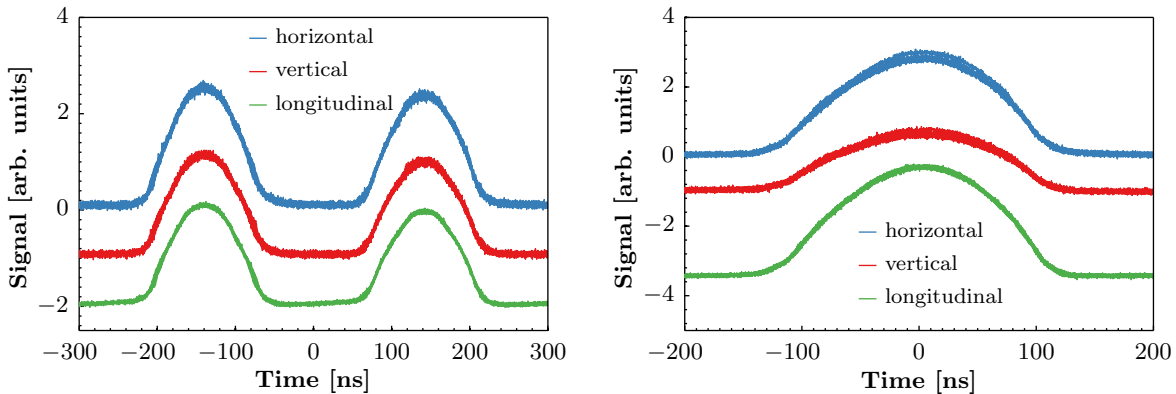

Figure 5.15. Modified setup of the TFB. The signals treated by the amplifiers were split to keep the system in the operational state, while being able to record the difference signals on a local oscilloscope.

(a) CNGS bunches on ring 3 $(N_p = 350 \times 10^{10})$.

(b) TOF bunch on ring 2 $(N_p = 850 \times 10^{10})$.

Figure 5.16. Measurements with the modified TFB setup, for a duration of 1.8 ms prior to extraction. No transverse oscillations or distortions are observed.

5.3 Simulation studies

5.3.1 General considerations and setup

The effect of the vacuum chamber on the ensemble of particles forming a bunch was simulated using the PyHEADTAIL code in combination with the analytic code ImpedanceWake2D (see also Section 4.3). With the latter, the wake functions were computed from the beam coupling impedance of a cylindric structure. The resulting dipolar and quadrupolar wake functions then served as input for the PyHEADTAIL simulations, in which the bunches are longitudinally sliced and the macroparticles within these slices experience a single kick per turn based on the provided wake functions. In principle, multiple kicks per turn and multi-bunch effects can be simulated. However, for the simulations presented in the following, one kick per turn and rapidly decaying wake functions were considered, resulting in simulations of single-bunch effects only. This approach is justified by the observations presented in Fig. 5.6: even though the number of bunches is different for the TOF and CNGS beams, the vertical oscillations are similar in both cases.

In order to determine the wall impedance of the PS vacuum chamber, a simplified model was used, consisting of a single geometry made of stainless steel (alloy 316LN) all along the $2\pi \times 100$ m circumference of the ring (see Fig. 5.17). In reality, this type of chamber accounts for about 70% of the installed vacuum chambers, while the remaining beam pipes differ in size and/or material.

The transverse wake functions W_z for this elliptic chamber were obtained by applying the respective Yokoya factors $\mathscr{Y}$ [65] to the wake functions of the cylindric chamber in the following way:

$$
\begin{aligned}
W_{x,\text{elliptic}}^{\text{dipolar}} &= \mathscr{Y}_x^{\text{dipolar}} \times W_{\text{cylindric}}^{\text{dipolar}}, \\
W_{y,\text{elliptic}}^{\text{dipolar}} &= \mathscr{Y}_y^{\text{dipolar}} \times W_{\text{cylindric}}^{\text{dipolar}}, \\
W_{x,\text{elliptic}}^{\text{quadrupolar}} &= \mathscr{Y}_x^{\text{quadrupolar}} \times W_{\text{cylindric}}^{\text{dipolar}}, \\
W_{y,\text{elliptic}}^{\text{quadrupolar}} &= \mathscr{Y}_y^{\text{quadrupolar}} \times W_{\text{cylindric}}^{\text{dipolar}}.
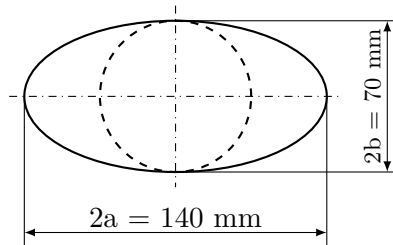\end{aligned}
\tag{5.1}
$$

Figure 5.17. Simplified model of the PS vacuum chamber. The dashed line indicates the geometry of the cylindric chamber that was used as input for ImpedanceWake2D.

The dependency of these factors on the dimensions of the elliptic geometry is shown in Fig. 5.18. For the case of the simplified PS vacuum chamber of Fig. 5.17, the following values were obtained:

$$
\begin{aligned}
\mathscr{Y}_x^{\text{dipolar}} &= 0.46, \\
\mathscr{Y}_y^{\text{dipolar}} &= 0.84, \\
\mathscr{Y}_x^{\text{quadrupolar}} &= -0.38, \\
\mathscr{Y}_y^{\text{quadrupolar}} &= 0.38.
\end{aligned}
\tag{5.2}
$$

The vertical dipolar wake function was found to be the dominating term, which could already be anticipated due to the shape of the chamber. The dipolar wake functions in both planes are shown in Fig. 5.19, where negative distances correspond to the region behind the source particle. Within a distance less than 1 m from this particle, the wake functions decrease by more than four orders of magnitude, a further justification for not taking into account multi-bunch effects. Figure 5.19 also shows the discrimination between the two contributions to the wall impedance and it is clearly visible that the indirect space charge impedance, rather than the resistive wall impedance, is the driving term for the interaction between the particles circulating in the ring and the surrounding beam pipe.

The computation of the discussed wake functions constitutes a major requirement for running the PyHEADTAIL simulation code. Additionally, the following input is necessary (see also Tables I and II):

- General beam and machine parameters such as the relativistic parameter γ_0, the beta-tron tunes Q_z, the linear chromaticities ξ_z, the RF voltage V_{RF}, the circumference of the
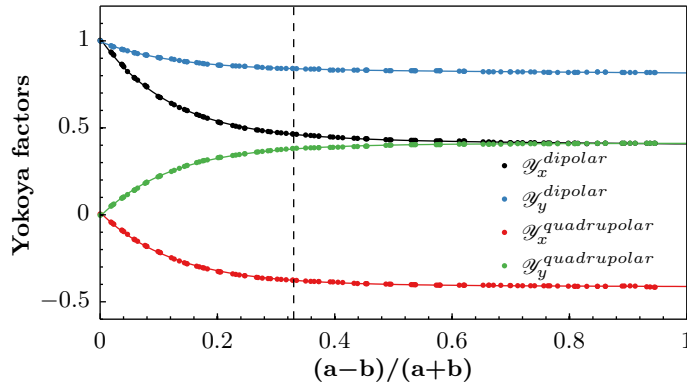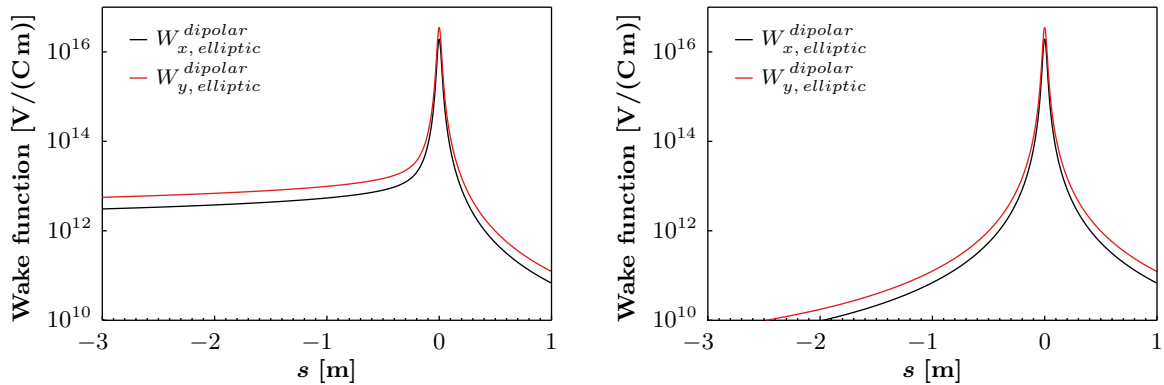

Figure 5.18. Yokoya factors for an elliptic geometry [65]. The values a and b correspond to the major and minor semi-axis, respectively, and the dashed black line indicates the ratio $\frac{a-b}{a+b}$, based on the dimensions given in Fig. 5.17.

(a) Functions based on the full wall impedance, i.e. the resistive wall and the indirect space charge impedance together.

(b) Situation when considering the indirect space charge impedance only.

Figure 5.19. Computed dipolar wake functions for the geometry shown in Fig. 5.17, at injection kinetic energy of 1.4 GeV ($\gamma_0 = 2.49$). Comparison of both figures reveals the dominating effect of the indirect space charge impedance over the contribution of the finite conductivity of the wall.

machine $2\pi R$, etc.

- According to the provided normalized transverse emittances ε_z^n and the local optics functions together with the injection errors, the macroparticles are normally distributed in the transverse planes. For the studies presented in the following, the transverse injection errors were usually implemented according to the maximum oscillation amplitudes mentioned in Figs. 5.5 and 5.6.

- The longitudinal distribution can be either initialized as a matched stationary Gaussian distribution by the code itself (requires σ_s, δ and the RF parameters) or based on a measured longitudinal phase space tomography.

- After initialization of the distributions, each bunch is longitudinally divided into slices of equal thickness, depending on the provided number of slices N_{sl}. The slicing occurs in the interval $[-3\sigma_s, 3\sigma_s]$ and by means of a convergence study the optimum value was deduced to be $N_{\text{sl}} = 1700$ for the simulations discussed in the following.

In order to perform simulation studies under realistic conditions, it was decided to use mainly a measured longitudinal distribution at PSB extraction as input. To justify this approach, distributions at two different instances are compared in Fig. 5.20, at extraction in the PSB and 5 ms after injection in the PS. In addition to the measured data, two Gaussian distributions ini-
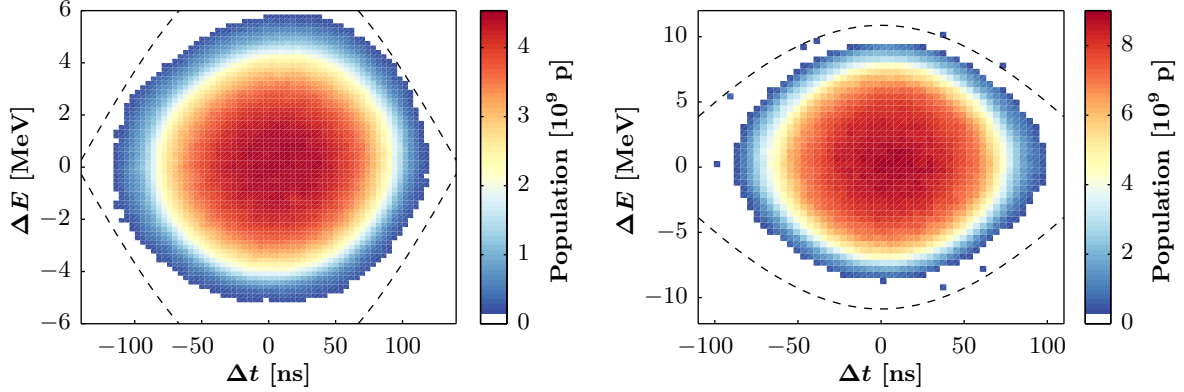
(a) Measured distribution at extraction in the PSB ($4\sigma_t = 212$ ns, $\delta = 1.2 \times 10^{-3}$, $V_{\mathrm{RF}} = 56$ kV).

(b) Measured longitudinal phase space distribution 5 ms after injection of the beam into the PS ($4\sigma_t = 172$ ns, $\delta = 1.98 \times 10^{-3}$, $V_{\mathrm{RF}} = 101$ kV). At both instances in time, injection and 5 ms later, the RF voltage is significantly different in order to prevent quadrupolar oscillations due to the high transient beam loading [60].
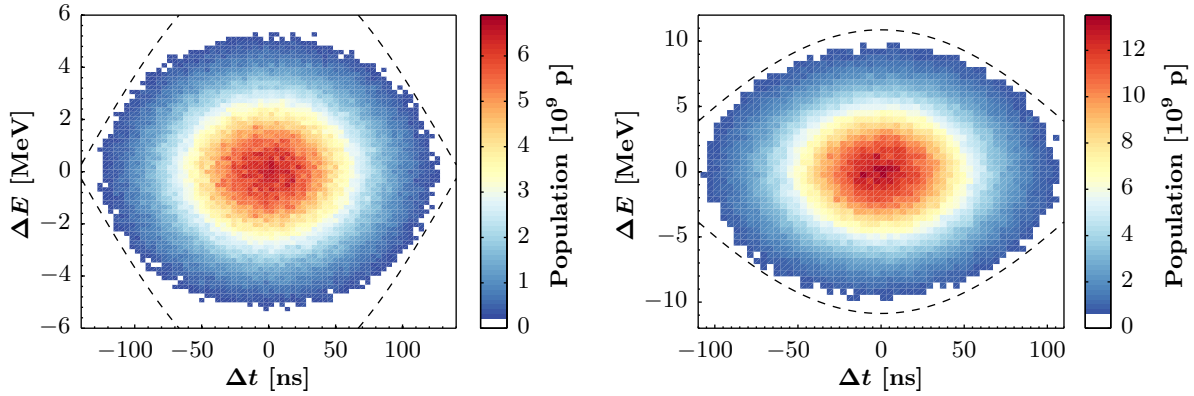
(c) Gaussian distribution initialized by the PyHEADTAIL code, based on the parameters determined by the measurement shown in (a).

(d) Gaussian distribution initialized by the PyHEADTAIL code, based on the parameters determined by the measurement shown in (b).

Figure 5.20. Density plots of different longitudinal distributions of the TOF beam, which were considered as input for the simulations. The black dashed lines describe the respective separatrices. It is important to remark that the measured data resemble more a parabolic than a Gaussian distribution and that the results of the simulations differ depending on the chosen longitudinal distribution.

tialized using the PyHEADTAIL code itself are depicted. The data clearly differ from Gaussian distributions and are considered to be parabolic. Therefore, the line densities are considerably different, which crucially influences the simulation results (see Figs. 5.27 and 5.29). Additionally, it has to be taken into account that 5 ms after injection, filamentation has occurred and the bunch is already matched to the bucket, whereas this does not apply immediately after injection. Therefore, oscillations of the bunch length are expected in the latter case.

5.3.2 Discrimination between indirect space charge and resistive wall

In general, the wake functions computed for an arbitrary vacuum chamber are based on its wall impedance and, therefore, the contributions of the resistive wall and the indirect space charge impedance cannot be distinguished.

In order to isolate the effect of the resistive wall impedance in simulations, a certain slice within the bunch is considered. All particles in front of this slice leave a wake field behind and the particles within this respective slice are subject to transverse kicks based on the summation of all fields. However, the fields created by the particles within the slice itself are not considered (see Fig. 5.21). As the strength of the wake functions is rapidly decreasing behind the source particle, the resulting tune shift is expected to be negligibly small. This is confirmed by looking at the vertical profiles in Fig. 5.22 (a). The presence of only the resistive wall impedance is not sufficient to explain the intra-bunch oscillations observed in the machine. After applying an initial injection error the amplitude of the transverse signal simply decay because of the natural chromaticity.
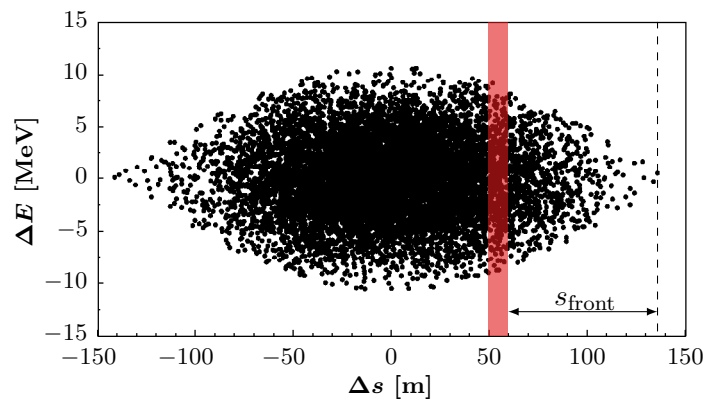

Figure 5.21. Illustration of the particles that are taken into account to compute the effect of the resistive wall impedance on the movement of the bunch. The current slice is indicated by the coloured bar and only particles within the distance s_{front} from this slice are considered. The kicks based on the wake fields created by the particles within the respective slice itself are not included.

If, instead, the effects of particles within a certain slice on themselves - and even on particles in front for $\beta_0 \neq 1$ - are taken into account, different slices along the bunch start oscillating at different frequencies, as it was measured at injection into the PS. The wake functions used as input for this simulation are the ones shown in Fig. 5.19 (b) and the corresponding vertical difference signals are presented in Fig. 5.22 (b).

The facts that the indirect space charge forces clearly dominate the wake functions and that realistic intra-bunch oscillations are immediately observed with this simple model of the machine, clearly indicate the importance of the indirect space charge effect in this case.

5.3.3   Simulations using the full wall impedance

Computing the wake fields based on the full wall impedance, and using the longitudinal distribution of the TOF beam at extraction in the PSB as input, led to simulation results which reproduce the measurements presented in Section 5.2.1 extremely well. In order to compare the results of the simulations to the measured data, the signals of the same turns as in Figs. 5.9 and 5.11 were considered to produce Figs. 5.23 and 5.24.

Applying an initial offset to this single bunch, vertical intra-bunch oscillations are obtained, as it was already expected by looking at the simulation results depicted in Fig. 5.22. However, in the horizontal plane the agreement between measurement and simulation is less, which is based on the fact that the model of the machine does not include certain conditions that are present
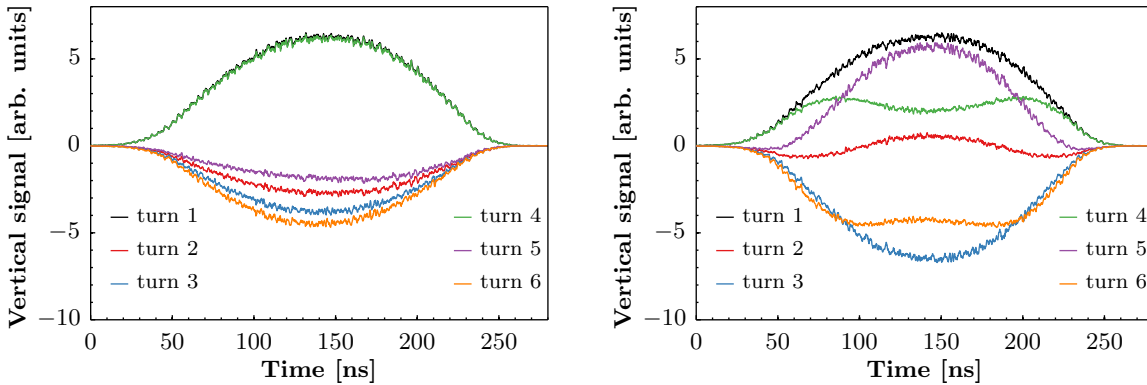
(a) Vertical difference signals when considering only the resistive wall impedance (see Fig. 5.19 (a)) and applying a vertical injection error of 7 mm. This is clearly not sufficient to reproduce the observations discussed in Section 5.2.1.

(b) Using the indirect space charge impedance (see Fig. 5.19 (b)) as input, intra-bunch oscillations, which are very similar to the measurements, are observed. A vertical injection error of 7 mm was applied.

Figure 5.22. PyHEADTAIL simulation results using the parameters of the TOF beam and different wake functions as input.

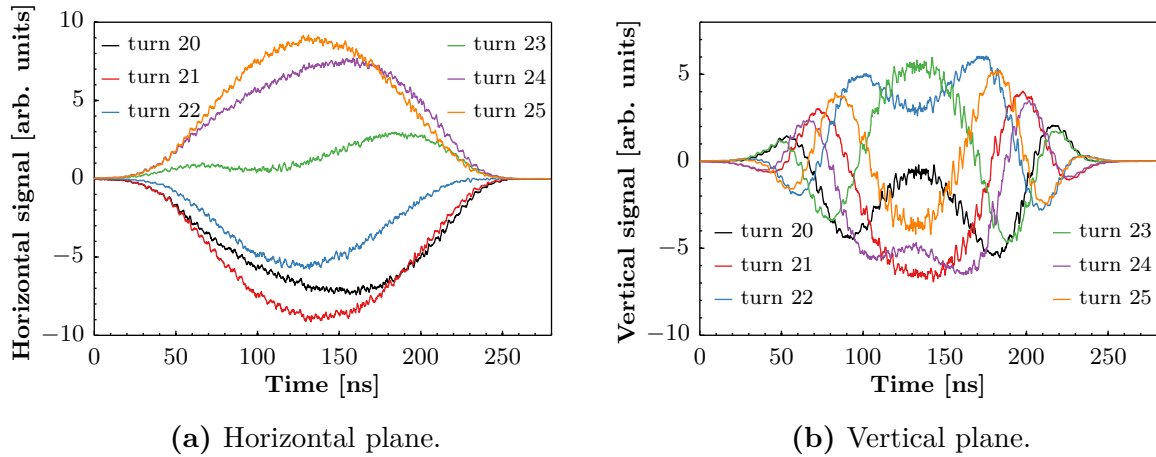**(a)** Horizontal plane.

(b) Vertical plane.

Figure 5.23. Simulated difference signals for six consecutive turns of the TOF beam. Corresponding to the values mentioned in Section 5.2.1 horizontal and vertical injection errors of 10 mm and 7 mm, respectively, were applied. Comparison with Fig. 5.9 reveals very good agreement of the vertical simulation results with the measured data. The model of the machine used in the simulations corresponds less to reality in the horizontal plane and, therefore, the simulations are not able to represent the data as well as in the other plane.

in reality. These differences arise from the modelling of the vacuum chamber on the one hand, and the absence of the injection bump on the other.

As described in Section 5.3.1, the geometry used to compute the wake fields is based on a single type of vacuum chamber, which accounts for approximately 70% of all chambers in the ring. For the remaining 30%, the major differences are the horizontal dimensions. Therefore, less agreement in this plane is expected. In addition, the closed orbit is not included in the simulations and, even though the location of the WBPU in SS94 is about half the machine circumference downstream of the septum in SS42, non-perfect closure of the horizontal injection bump is expected to influence the measurements as well.

The spectrum of these oscillations was again computed each turn. It shows an overall increase of the frequency for an increasing number of turns, which is also in agreement with the measurements. Likewise, this applies to the vertical tune shift, and the respective results are depicted in Fig. 5.24. Only minor differences between the measurements and the simulations are observed, which can be explained by the incomplete modelling of the machine and the applied longitudinal distribution. Even though a measured distribution was used, it certainly differed from the actual longitudinal distribution of the beams used for the measurements presented in Section 5.2.1, as the distributions were not recorded simultaneously.

In Fig. 5.25, the motion of the vertical centroid is shown. Compared to the measurements, the simulation results exhibit a very similar decrease of the oscillation amplitude and a slightly different tune, which results from the difference in the tune shift as visible in Fig. 5.24. Contrary
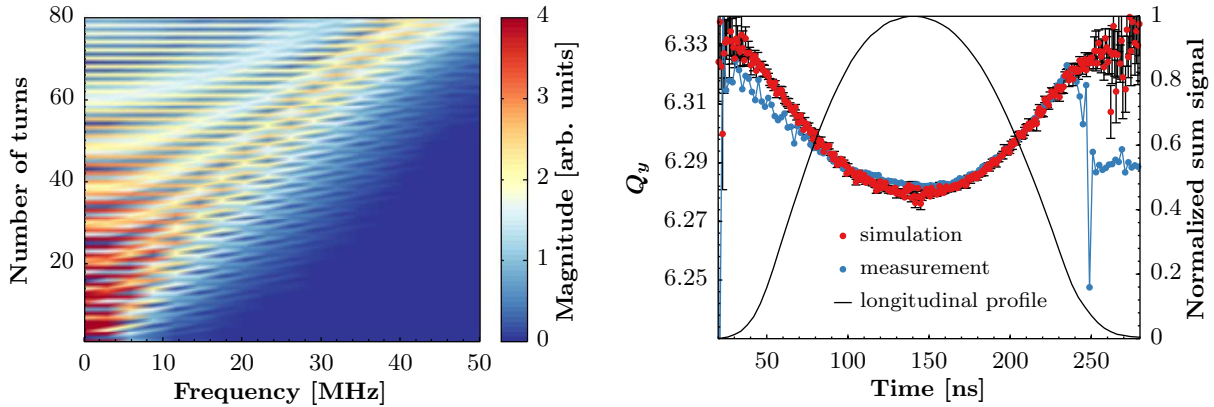
(a) Spectrum of the vertical oscillations. The overall trend is similar to the measurements of Fig. 5.11: with each turn the frequency of the oscillation increases.
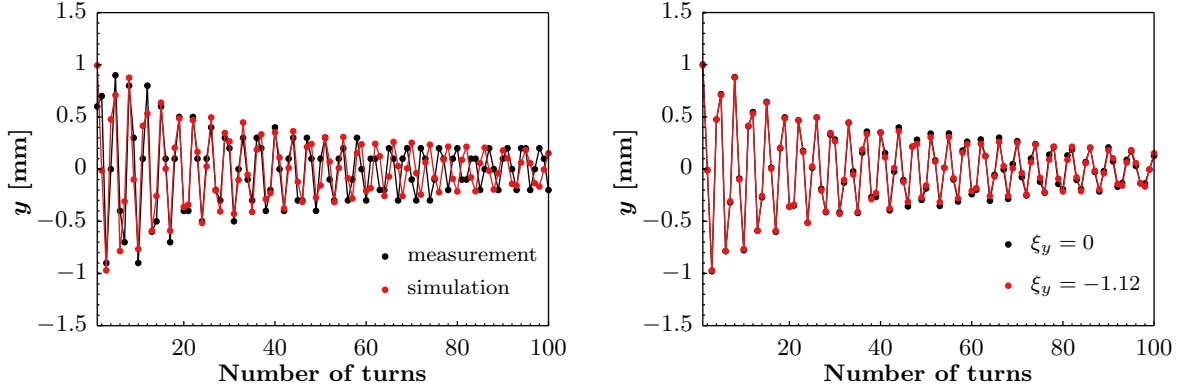
(b) Comparison between measured and simulated tune shift along the bunch. Likewise to Fig. 5.12, it depends on the local intensity. The maximum vertical tune shift $\Delta Q_{y,\text{coh}}^{\max} = 0.06$ is almost identical to what was measured in the PS.

Figure 5.24. Simulated vertical spectrum and tune shift for the TOF bunch.

to an instability, no exponential growth of the vertical amplitude is observed as the imaginary indirect space charge impedance only causes a real tune shift. Further simulations revealed that a change in linear chromaticity influences the decoherence only slightly, as the decay of the motion is dominated by the loss of phase relationship between the slices that oscillate at different frequencies. On the contrary, reducing the bunch intensity and setting the linear chromaticity again to natural values, the decay of the vertical amplitude is faster. This observation led to the understanding that the decoherence is dominated by the intra-bunch tune shift in case of high-intensity beams and by linear chromaticity for low-intensity beams.

Figure 5.26 depicts the coherent slice-by-slice tune shift for the cases $\xi_y = 0$ and $\xi_y = -3$. As already expected by looking at Fig. 5.25, almost no difference to Fig. 5.24 can be observed for zero chromaticity. However, coupling between adjacent slices is significantly increased for $\xi_y = -3$, affecting also the tune shift. The combination of this effect and the, compared to natural and zero chromaticity, faster decay of the oscillation amplitude also increases the uncertainties on the evaluation of the local tune shifts (see Fig. 5.26).

Another important point is the dependency of the oscillations on the total intensity. Considering a certain longitudinal slice within a bunch, its coherent tune shift is proportional to the intensity within the respective slice. Decreasing the total intensity, while keeping all other parameters constant, reduces the local intensity in the same way. Therefore, the tune shift decreases and, as a result, also the frequency of the intra-bunch oscillations. In several simulation runs, the maximum vertical tune shift was computed according to the procedure set out in Fig. 5.12, while

(a) Comparison between measurements and simulations of the decoherence of the vertical centroid motion, showing very good agreement. Both cases are valid for $\xi_y = -1.12$ and no exponential growth of the centroid motion is observed. Therefore, the assumption that the discussed vertical phenomenon is a pure intra-bunch oscillation rather than an instability is justified.

(b) Simulation results showing the vertical centroid motion for different chromaticities and an intensity of 700×10^{10} ppb. The decoherence differs only marginally, indicating the importance of the phenomenon described in this chapter.
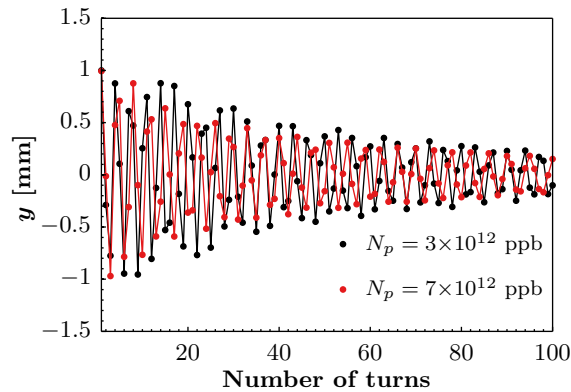
(c) Using again $\xi_y = -1.12$, and reducing the intensity, leads to a decreased tune spread along the bunch, causing slower decoherence. Therefore, the influence of the linear chromaticity on the decoherence is much more important in the low-intensity case.

Figure 5.25. Decay of the centroid's oscillation amplitude for different settings of linear chromaticity and intensity.
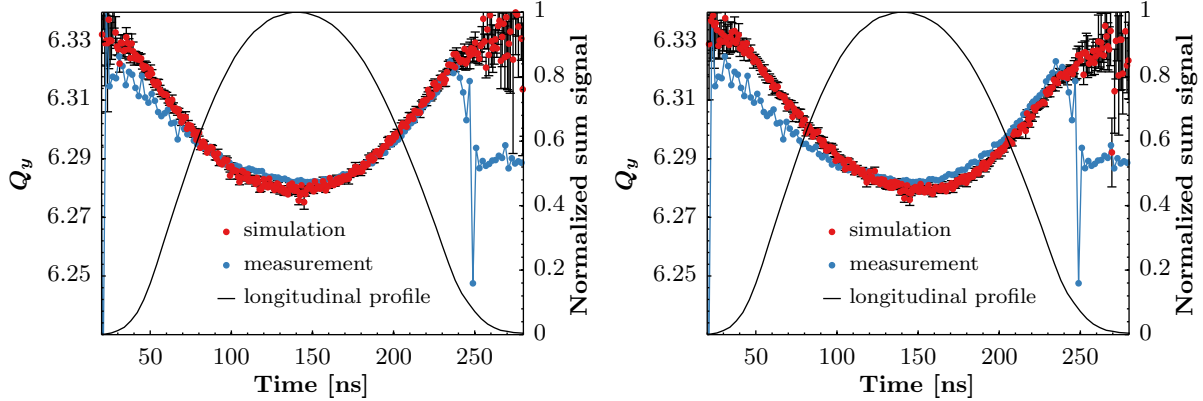
(a) Tune shift along the bunch for $\xi_y = 0$. No significant difference to the case of $\xi_y = -1.12$ (see Fig. 5.24) can be observed.

(b) Tune shift along the bunch for $\xi_y = -3$. Overall, the detuning along the bunch is slightly increased compared to natural and zero chromaticity.

Figure 5.26. Dependency of the detuning on the linear chromaticity.
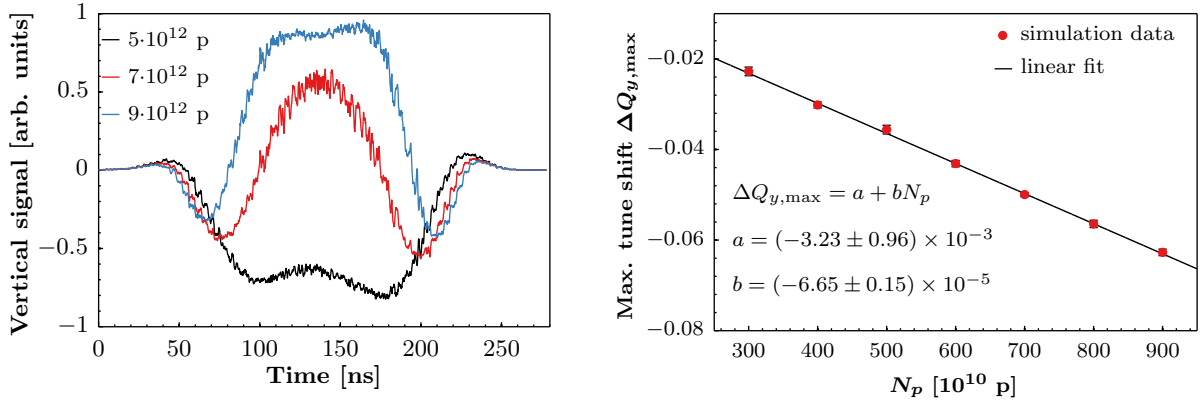
(a) Vertical difference signals for TOF bunches with different intensities. All curves were normalized to the respective maximum vertical signal of turn 1 (turn 16 is depicted). The intra-bunch frequency increases with intensity.

(b) Linear relationship between the maximum vertical tune shift and the total intensity.

Figure 5.27. Dependency of the oscillation frequency on the intensity.

the total intensity was varied. The resulting linear relationship between intensity and tune shift as well as the effect on the intra-bunch oscillations are shown in Fig. 5.27.

An important ingredient to all simulation results presented so far is that the particle distributions are initialized with a transverse displacement. Without such an injection error, and for

the beam dimensions and vacuum chamber geometry under study, the forces acting from the vacuum pipe back on the beam completely cancel out. In Fig. 5.28 (a), simulation results for different injection errors are depicted. The intra-bunch frequency is found to be independent of the magnitude of these errors, while the oscillation amplitude changes accordingly. This effect becomes especially important for beams with more than two bunches, as multiple PSB rings are required for their production. Figure 5.28 (b) illustrates this by means of a measurement of four CNGS bunches in the PS, a few turns after injection. These bunches are created in rings 3 and 4, and consecutively sent to the PS via the transfer line. There, each set of two bunches experiences a different steering, resulting in different injection errors when entering into the PS. Therefore, the vertical oscillation amplitudes differ for bunches coming from different rings.

Instead of changing the intensity to modify the line density, an identical effect can be achieved by varying the bunch length. The oscillation frequency increases for shorter bunches as it is shown in Fig. 5.29.

In the framework of the LIU project, an upgrade of the PS injection energy from 1.4 to 2 GeV is projected [66]. Due to the decrease of the indirect space charge impedance at higher energy, the vertical tune shift is also reduced (see Fig. 5.30). Therefore, the requirements in terms of bandwidth for the transverse damper system at an injection kinetic energy of 2 GeV are going to be reduced. In this respect, simulations with CNGS-type beams with a 50% increase in intensity, as it might be required for high-intensity beam production in the future, were performed. Also in this case an overall reduction of the tune shift was obtained, as the decrease of the impedance carries more weight than the increased intensity.
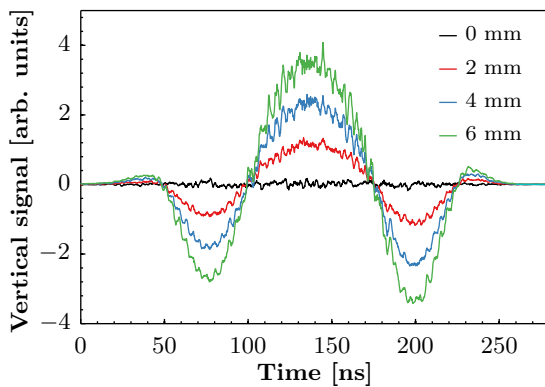
(a) Simulated dependency of the vertical oscillation on the injection error for the TOF beam. Only the amplitude of the oscillation, not the frequency, is modified by increasing the error.
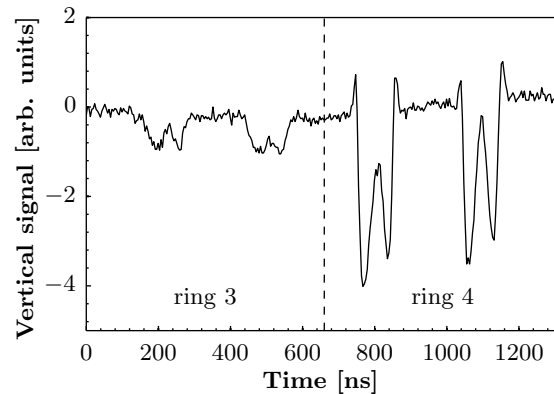
(b) Measured vertical difference signals of four CNGS bunches, 20 turns after injection. Depending on the PSB ring, the beam steering in the transfer line is different and, therefore, the injection errors differ. This results in different vertical oscillation amplitudes for bunches from different rings.

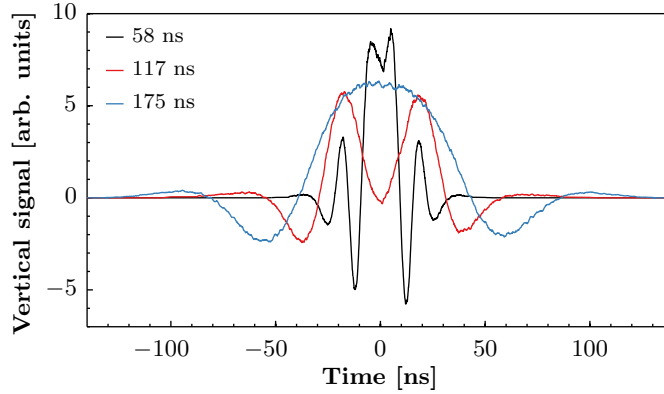**Figure 5.28.** Influence of the injection error on the intra-bunch motion.

Figure 5.29. Simulated vertical difference signals for different bunch lengths of the TOF beam. In contrast to the other simulation results, the longitudinal distributions were initialized by the PyHEADTAIL code. In both shown cases all parameters, except the full bunch length $4\sigma_t$, were kept constant. Increasing the bunch length decreases the line density and, therefore, the tune spread.
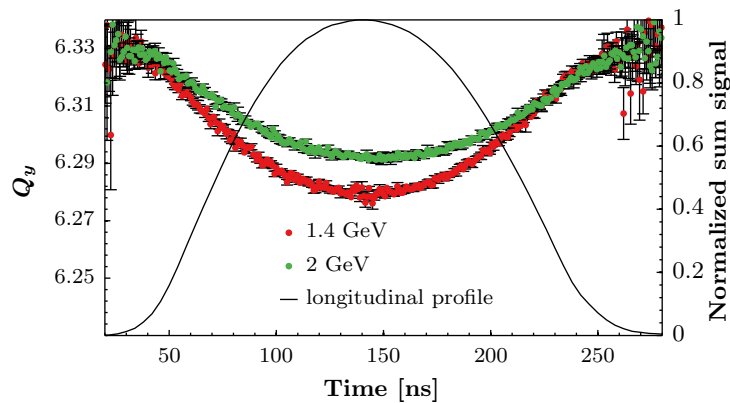

Figure 5.30. Tune shift along the bunch obtained by simulations at different injection energies. The proposed upgrade of the injection energy to 2 GeV would decrease the frequency spread along the bunch and, hence, reduce the required bandwidth of the transverse damper.

5.4   The contribution of direct space charge

In order to provide a complete study, the contribution of the incoherent space charge forces to the intra-bunch oscillations was also assessed. Therefore, an FFT particle-in-cell solver, which was initially developed to study instabilities in the LHC [67], was applied in addition to the setup described in the previous section. This approach was selected as the linearizations used for the wake computation are not applicable to the non-linear fields caused by direct space charge.

To quantify the direct space charge tune spread the following approach was used: a bunch was tracked for one turn without the contributions of the wake functions and the longitudinal motion to isolate the incoherent effect. At 120 locations along the accelerator the bunch was longitudinally divided into 200 slices - values, which were determined based on a convergence study - and the electric field of the particle distribution was numerically computed and saved. Subsequently, the bunch was tracked for another 128 turns using the previously saved electric field map to apply the incoherent space charge kicks. The field was hereby always re-centred with respect to the centroid of the bunch. For a subset of particles of this bunch, the turn-by-turn positions and angles were then processed by SUSSIX [68], providing the single particle tunes. The resulting tune distribution, also called the tune footprint, is depicted in Fig. 5.31. Comparison with the values of the maximum tune spread mentioned in Table I reveals very good agreement. Moreover, a certain fraction of the distribution appears to be locked on the horizontal integer resonance, which exhibits a rather small stop band. This is due to the fact that apart from the direct space charge kicks no other errors are present in this simplified model of the machine.

Figure 5.32 shows the result of a complete simulation including the effects of the wake fields, the longitudinal motion and the direct space charge. In this case, instead of the previously used
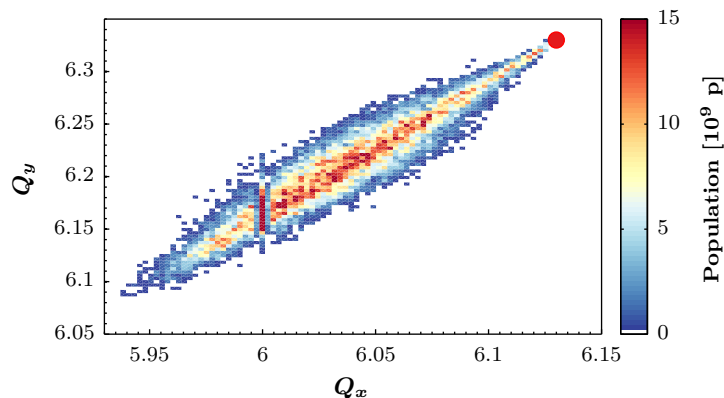

Figure 5.31. Incoherent space charge tune footprint based on the parameters of the TOF beam shown in Tables I and II. The zero intensity working point (Q_x=6.13, Q_y=6.33) is indicated by the red dot.

frozen space charge approach, the electric field was recomputed at each of the 120 locations around the ring. A clear vertical intra-bunch movement could again be observed and the signals exhibit the same behaviour as seen in Fig. 5.23, even though a significant incoherent tune spread was now included in the simulations. The insignificant contribution of direct space charge becomes even more apparent by evaluating the detuning along the bunch. Clearly, and as expected, the incoherent motion does not contribute to the obtained coherent tune shift.

Furthermore, several experimental observations support the fact that the discussed intra-bunch oscillations are not driven by direct space charge forces. First, as visible in Fig. 5.28, four bunches, which are affected by almost the same direct space charge tune spread, exhibit very different injection oscillations. Secondly, no, or only very small, intra-bunch oscillations are observed on high-brightness LHC-type beams, as the intensity per bunch is significantly smaller than for the TOF or the CNGS beam.
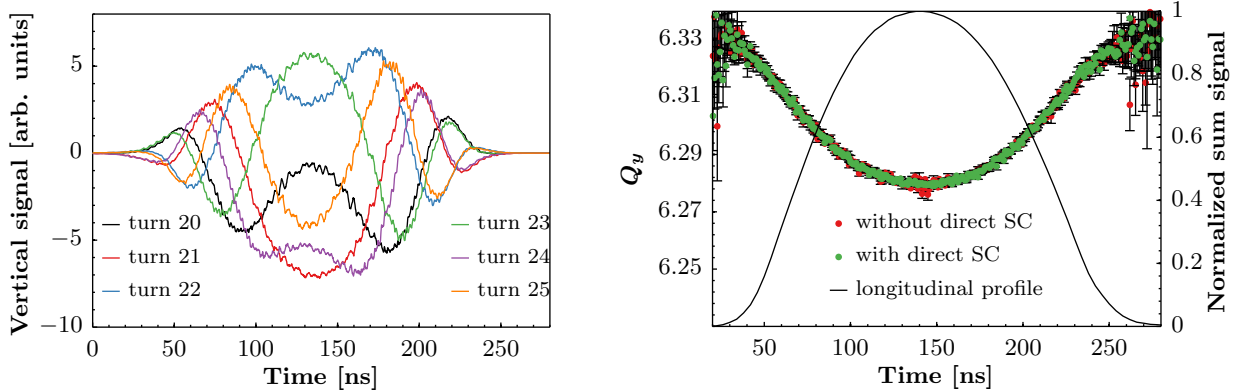
(a) Including the incoherent space charge effect in the simulations leads to vertical difference signals that are very similar to the ones shown in Fig. 5.23.

(b) Evaluation of the effect of direct space charge based on the vertical tune shift along the TOF bunch. The insignificant contribution of the incoherent space charge forces to the coherent slice-by-slice tune shift is clearly visible.

Figure 5.32. Contribution of direct space charge to the intra-bunch oscillations.

5.5 Conclusions and outlook

The injection process for proton beams into the PS constitutes one of the major limitations preventing the production of future high-intensity beams, as they will be required for proposed fixed target facilities. Given the current injection scheme, particle loss occurs as the circulating beam closely approaches the vacuum chamber in MU43 of the machine. These losses are the result of the reduced mechanical aperture in this location, which is created by the elliptic geometry of the vacuum chamber in combination with the horizontal injection bump. It is therefore unavoidable to find means to reduce beam loss, as the acceptable limits in terms of the radioactive activation of the PS ring will otherwise be exceeded.

In this chapter, measurements and simulations explaining the mechanism causing vertical intra-bunch oscillations, which are regularly observed when injecting high-intensity beams into the PS, were presented. By means of a WBPU, transverse difference signals were recorded and these oscillations were found to build up very fast compared to a synchrotron period. The analysis of the measured data revealed that the oscillation pattern is generated by a coherent vertical tune shift, which is proportional to the local longitudinal bunch density.

Based on a simplified model of the PS vacuum chamber, extensive simulation studies were performed with the PyHEADTAIL code, and the measurements could be reproduced extremely well. The vertical oscillations were understood to be induced by injection errors, which result in a transverse distribution that is not centred with respect to the beam pipe. Due to this asymmetric arrangement, the effect of the indirect space charge forces, which act back on the beam, leads to a coherent vertical tune shift causing the observed intra-bunch phenomenon. In contrast to an instability, the interaction of the beam with the imaginary space charge impedance does not drive any growth of the centroid motion, and the beam remains stable. Furthermore, it was demonstrated that the effect of direct space charge on the oscillations is negligible.

In order to mitigate the impact of the presented oscillations on the injection losses, special attention must be paid to the steering in the transfer line between the PSB and the PS. By reducing the amplitudes of transverse oscillations as far as possible, minimum beam loss can be achieved. However, due to the required vertical recombination after extracting the beams from the PSB, and inevitable shot-to-shot variations, it is impossible to completely avoid injection errors and the resulting intra-bunch phenomenon.

For the current beam intensities, the intra-bunch transverse damper system has proved to successfully reduce these injection oscillations. According to simulation results, this will also be the case for future high-intensity beams, as the injection energy of the PS will be upgraded in the near future. However, as the CERN accelerator complex is not yet capable of producing these beams, the effectiveness of the transverse damper system remains to be demonstrated experimentally.

In order to mitigate direct space charge issues at injection energy, studies concerning the transfer of long bunches with reduced line density from the PSB are currently being conducted. Based

on sophisticated manipulations in the longitudinal phase space, the production of hollow distributions, which result in flattened bunch profiles, becomes possible [69]. In addition to the mitigation of space charge issues, the decreased line density can also be exploited to reduce the presented intra-bunch oscillations.

To further improve the results of the simulation studies, and especially the agreement with the experimental data measured in the horizontal plane, several aspects could be investigated. On the one hand, this concerns the simulation code itself. The tracking routines implemented in PyHEADTAIL are rather basic, which is usually largely sufficient to study collective effects. However, as the dynamics during the injection process is complicated by the presence of the horizontal bump, a self-consistent code such as PyORBIT, where the tracking is performed by PTC, should be considered. This would allow the inclusion of either an error distribution or a measured closed orbit (see also Section 6.2.2.3). The drawback is that, so far, PyORBIT has only been used to model the effect of direct space charge and the correct treatment of wake functions or impedances still requires some minor code development. Choosing this approach would also allow the combination of the studies presented in this thesis with more recent ones, which are aimed at investigating the importance of direct space charge effects during the collapse of the bump [70].

On the other hand, the studies could be repeated at 1.4 and 2 GeV, applying a more refined impedance model of the PS, such as the one presented in [71]. This approach would overcome the disadvantage of incomplete modelling of the PS aperture, especially in the horizontal plane. Considering that the agreement between experimental and simulation studies for the vertical plane, in which the interesting phenomenon actually occurs, is already very good, the ideas mentioned above are only expected to marginally improve the results.

6 The Multi-Turn Extraction

6.1 Introduction

To provide beam for fixed target physics at the SPS, the longitudinal structure delivered by the PS has to comply with certain requirements. In order to reduce beam loading and to provide an almost continuous spill towards the experimental facilities, uniform filling of the SPS is desired. Considering that the length of the SPS is about eleven times the circumference of the PS, and that a gap for the rise time of the SPS kickers is needed, this could be achieved by ten subsequent extractions. However, to optimize the duty cycle, the so-called Continuous Transfer (CT) extraction was proposed in 1973 [14]. The advantage of this non-resonant extraction process, which occurs over five turns at 14 GeV/c, was that only two subsequent extractions from the PS are necessary. On the downside, this technique comes with one major drawback, namely significant beam loss, which occurs at multiple locations around the ring. For future high-intensity beam operation, this constitutes important constraints as personnel will be exposed to considerably elevated collective doses in case of interventions.

These issues triggered the research for an appropriate replacement of the CT process. Especially after the approval of the CNGS project, several methods were investigated to reduce beam loss at extraction in the PS and, therefore, to overcome the intensity limitations, which are intrinsic to the CT method. In this framework, a novel extraction mechanism, the Multi-Turn Extraction (MTE), was proposed in 2001 [15]. It is based on a resonant extraction mechanism, which applies non-linear transverse magnetic fields to perform advanced manipulations in the horizontal phase space.

Due to the complexity of the MTE scheme, its operational implementation has faced various difficulties. In the framework of this thesis, several experimental and simulation studies have been performed, which played a significant role in overcoming these issues. As of September

2015, the MTE process has been operationally used to deliver high-intensity beams to the SPS, and has therefore successfully replaced the CT extraction [72]. Before going into detail about the dedicated MTE studies, which contributed to this success (see Section 6.2), the principles of both CT and MTE are discussed on the following pages.

6.1.1   The CT extraction

The CT extraction is a non-resonant multi-turn extraction, which is performed by horizontally slicing the beam at the electrostatic septum in SS31 (SEH31) - a thin molybdenum foil of about 100 μm thickness - and subsequently extracting the resulting slices at the magnetic septum in SS16 (SMH16). This process occurs at 14 GeV/c, and the magnetic configurations of the cycles used in both the PS and the SPS together with typical intensity values are shown in Fig. 6.1.

In order for this process to occur over five turns, the horizontal tune is set to $Q_x = 6.25$ on the flat top, which provides a rotation of 90 degrees per PS turn in the horizontal phase space. Furthermore, a set of quadrupoles located in SS25 and SS73, the kick enhancement quadrupoles (QKE), form a local distortion of the optics to increase the β-functions and to reduce the horizontal dispersion function at SEH31 (see Fig. 6.2). Thereby, the beam density and the energy dependence in SS31 are reduced, resulting in decreased multiple scattering inside the septum blade and, therefore, less beam loss [73]. By means of slow bumps, the beam then approaches SEH31 and SMH16, and five turns before extraction a fast bump is used to kick the beam onto SEH31, in order to mechanically split it. The external particles encounter a deflecting
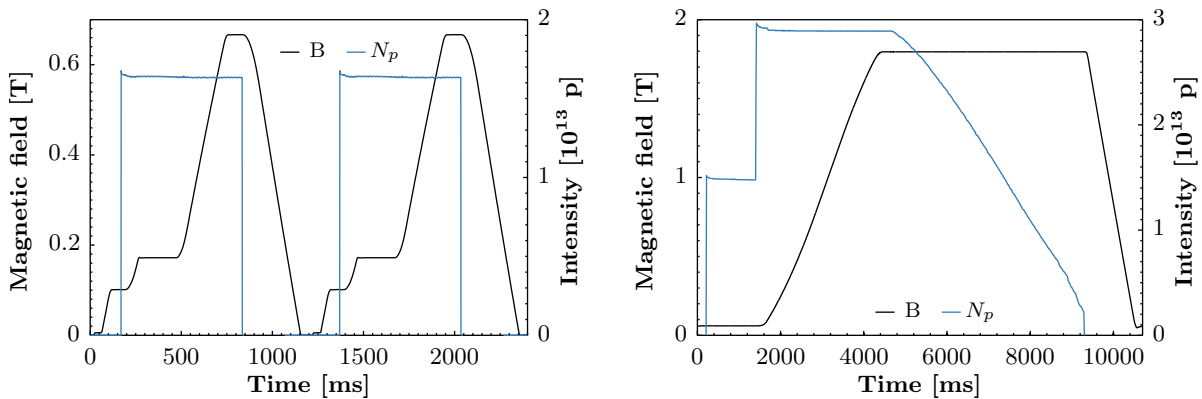
(a) In the PS, two identical magnetic cycles are used to accelerate the beam to 14 GeV/c, where it is extracted over five turns.

(b) Double injection and acceleration to 400 GeV/c in the SPS. The decrease of intensity starting on the flat top is due to the slow extraction (see also Sec. 6.1.2) towards the experimental facilities.

Figure 6.1. Magnetic field and beam intensity along the CT cycle. To fill the SPS circumference uniformly, two subsequent five-turn extractions from the PS are required.
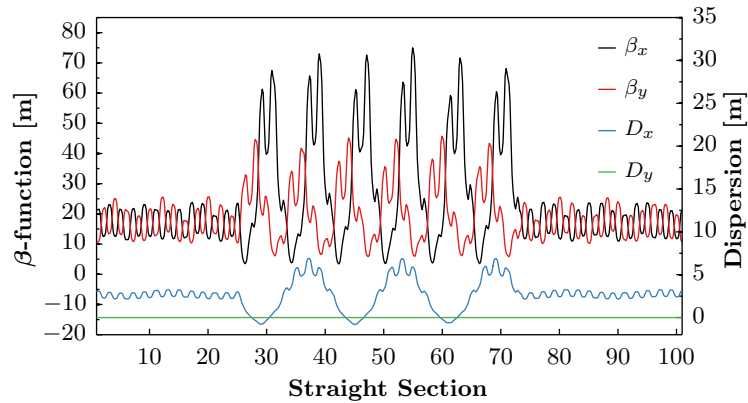
Figure 6.2. Configuration of the optics functions applied for the CT extraction. The distortion of the optics due to the QKE between SS25 and SS73 is clearly visible. To keep the beam size small at the SMH16, the functions remain unmodified in the extraction area.

kick and are extracted at SMH16. Over the subsequent turns, the fast bump, and therewith the position of the beam with respect to SEH31, is adjusted to obtain five equally populated slices. As a result of this process, the horizontal emittances and the shapes will differ significantly between the slices. It was shown theoretically that it is impossible to equalize intensity and horizontal emittance at the same time (see also Fig. 6.3) [74].
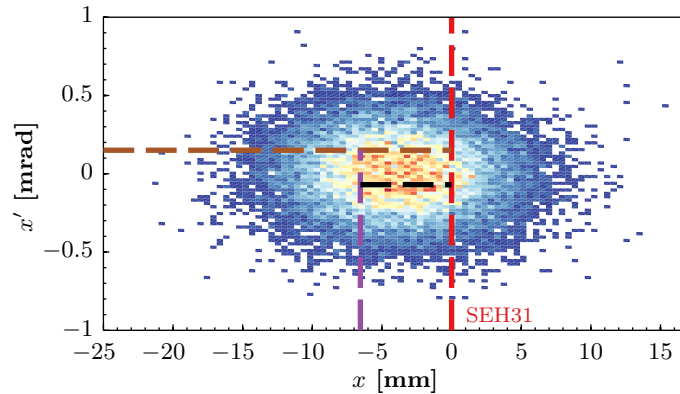
Figure 6.3. Illustration of the horizontal phase space during the CT extraction. SEH31 is represented by the red dashed line and the horizontal origin is chosen to coincide with its position. During the first turn of the extraction process, particles with positive x-values will experience an electrostatic kick and will be extracted at SMH16. One turn later, the beam will have rotated by 90 degrees and the second slice will be cut off (indicated by the brown dashed line). After two more turns, only the central slice remains and is directly kicked to the other side of SEH31. The fast bump is adjusted on a turn-by-turn basis to equalize the intensities of the five turns. A variation of the optical parameters between the five slices is inherent to this extraction process.

Once extracted from the PS, the different slices are guided through the transfer lines TT2 and TT10 until they arrive in the SPS. A certain spread between the different trajectories in the transfer line is intrinsic to the process and, therefore, two fast correctors, the fast dipole 242 (DFA242) and the fast dipole 254 (DFA254), are installed in TT2.

The small vertical acceptance of the SPS adds another complication to the CT process. To overcome this limitation, an emittance exchange insertion consisting of three skew and four normal quadrupoles is installed in TT10. Therewith, the smaller horizontal emittance and the respective trajectories are transferred to the vertical plane and vice versa [75].

The significant drawback of the CT extraction results from direct losses in SS31 and SS32, which are due to the interaction between the beam and the septum, but also from scattered particles, which continue to be transported with the beam and are lost in downstream locations (see Fig. 6.4) [73]. Furthermore, the mechanical splitting leads to a variation of the optical parameters between the five slices, causing an unavoidable blow-up at injection into the SPS.

6.1.2 The MTE principle

The basic ingredient of this novel technique is to replace the mechanical splitting of the CT extraction with a magnetic one to avoid the direct interaction of the particles with a septum blade. This can be achieved by choosing a resonant extraction mechanism, where non-linear transverse magnetic fields are applied to create multiple SFPs in the phase space. In addition,
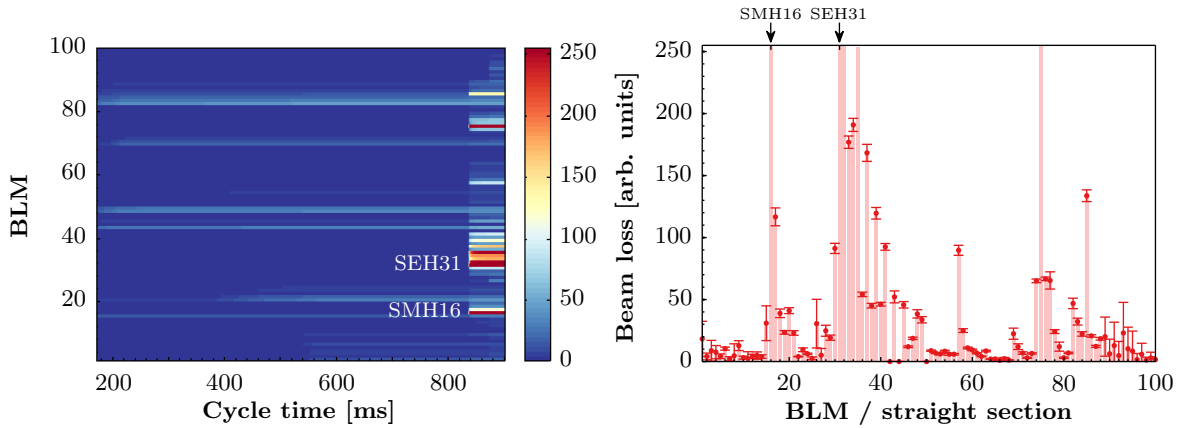
(a) Evolution of the beam losses all along the cycle. Increased loss during the extraction process is clearly visible, as well as some injection losses.

(b) Integrated beam losses after extraction. The locations of the septa are indicated on the top and error bars correspond to the standard deviation of 800 consecutive measurements.

Figure 6.4. Measured beam loss on the CT cycle in the PS ($N_p = 1.68 \times 10^{13}$ just before extraction). Values of 255 correspond to saturation of the BLMs.

the tune of the machine needs to be slowly varied to cross a certain non-linear resonance and particles can be captured inside the areas of stability around the SFPs. In general, any non-linear resonance of order n can be chosen and, depending on the stability of the resonance, n or $n + 1$ SFPs are obtained. The stability of resonances is determined by its behaviour when approaching the resonant value of the tune. In case of an unstable resonance, particles close to the origin will be repelled, leading to a depleted central part of the beam. For a stable resonance, the centre of the distribution remains populated and the beam can be separated into one core and n islands (see also Fig. 6.5). Normally, resonances with order $n > 4$ are stable [76].

An appropriate theoretical model to illustrate resonances of different orders is the area conserving Hénon map [77]. It describes the transverse motion of a particle in a simple periodic FODO lattice with a single sextupolar non-linearity. An involved treatment of the application of this map in the field of accelerator physics can be found in [78]. The transformation $\boldsymbol{x}_{n+1} = \boldsymbol{M}\,\boldsymbol{x}_n$ of the horizontal particle coordinates from turn n to $n + 1$, where $\boldsymbol{M}$ is the one-turn transfer map, explicitly reads:

$$\begin{pmatrix} x_{n+1} \\ x'_{n+1} \end{pmatrix} = \begin{pmatrix} \cos(\omega) & \sin(\omega) \\ -\sin(\omega) & \cos(\omega) \end{pmatrix} \begin{pmatrix} x_n \\ x'_n + x_n^2 \end{pmatrix}, \tag{6.1}$$

with $\omega = 2\pi q_x$. Figure 6.5 shows the topology of the horizontal phase space for different values of the fractional tune q_x. Far away from any resonant condition, the particles follow circular trajectories around the origin and the motion remains linear even at large amplitude. In the proximity of the unstable third order resonance $3q_x = 1$ a stable area, where the particle trajectories become triangular, is formed. Its extent depends on the distance to the resonance, which is defined as

$$\Delta_r = q_x - \frac{1}{m} \tag{6.2}$$

for one-dimensional resonances, with m being an integer number corresponding to the order of the resonance. Particles outside the separatrix are continuously transported to higher amplitudes, until they are eventually lost. In synchrotrons, this fact is actually exploited during the so-called slow extraction [27, and references therein]. In this process, which usually occurs over time scales of several 100,000 turns, Δ_r is continuously reduced to zero, resulting in a reduction of the stable region and repulsion of particles therein. On resonance, i.e. at $\Delta_r = 0$, the origin will be completely depleted.
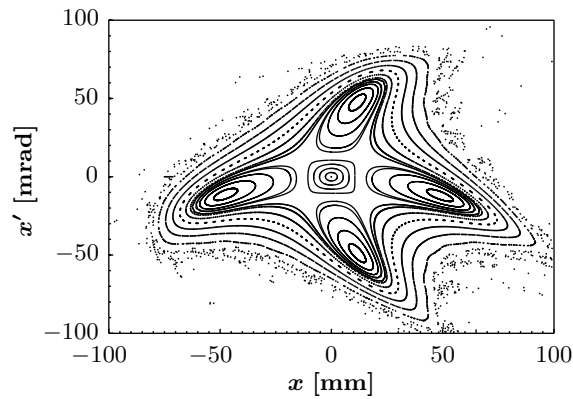
The phase space close to the stable fourth order resonance $4q_x = 1$ is depicted in Fig. 6.5. For $\Delta_r = 0.001$ four islands, clearly separated from the central core, appear. Particles that are neither captured in the core nor in the islands follow closed trajectories around the islands. The layer of chaotic motion at large amplitude determines the maximum area of stability in the phase space and is referred to as dynamical aperture.

For the extraction of high-intensity beams from the PS, the choice of the order of the resonance
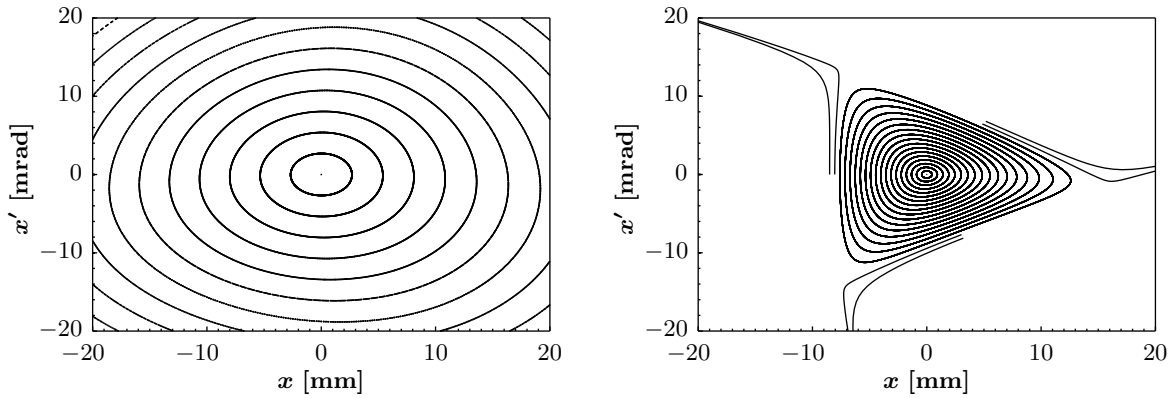
(a) Purely linear motion for the off-resonance tune $q_x = 0.22$. The particle trajectories are elliptic around the fixed point at the origin.

(b) Close to the unstable third order resonance $3q_x = 1$, the particle trajectories adopt the characteristic triangular shape. The visible area of stability around the origin is a result of setting the tune to $q_x = 0.34$. Particles outside the separatrix move to infinity.

(c) In the proximity of the stable fourth order resonance $4q_x = 1$, four islands are created around the core. Note the chaotic particle motion at large amplitude.

Figure 6.5. Horizontal phase space portraits based on the Hénon map (Eq. (6.1)) to illustrate resonances of different orders.

is dictated by the specific requirements of the SPS. In order to establish a method equivalent to the CT extraction, a stable horizontal fourth order resonance has to be applied to split the beam into one core and four islands, and to extract it over five turns to fill $^{10}/_{11}$ of the SPS circumference with two consecutive pulses. In principle, this is achievable by using only sextupolar fields, which would be an approach comparable to the Hénon map. However, precise control over several parameters, such as the size of the islands, the horizontal tune, linear and non-linear chromaticity, and detuning with amplitude, is desired, requiring additional degrees of freedom to properly adjust the splitting process. This can be achieved by adding an octupole to the lattice described by Eq. (6.1), and the corresponding one-turn map was found to be [15]:

$$
\begin{pmatrix} X_{n+1} \\ X'_{n+1} \end{pmatrix} = \begin{pmatrix} \cos(\omega) & \sin(\omega) \\ -\sin(\omega) & \cos(\omega) \end{pmatrix} \begin{pmatrix} X_n \\ X'_n + X_n^2 + \kappa\,X_n^3 \end{pmatrix},
\tag{6.3}
$$

where (X,X') are special adimensional normalized coordinates and κ depends on the ratio of the strength of the octupole K_3 to the sextupole K_2:

$$
\kappa = \frac{2}{3}\frac{K_3}{\beta_x K_2^2}.
\tag{6.4}
$$

The resulting topology of the horizontal phase space in the proximity of the resonance $4q_x = 1$ is shown in Fig. 6.6. If the separation of the islands and the core, i.e. the variation of the tune over time, occurs adiabatically, the five beamlets will be equally populated at the end of the process, with almost no beam ending up in-between. The substantial advantage of MTE over the CT extraction arises from exactly this absence of particles between the different beamlets. Instead of mechanically slicing the beam, the core and the islands are magnetically split and the magnetic extraction septum can then be placed within the emerging free space, resulting in an almost lossless extraction process (see Fig. 6.6 (c)). Due to the specific tune setting, the beam rotates by 90 degrees in the phase space and, therefore, always the outermost island is extracted. Hence, the extracted islands are also equal in terms of horizontal emittance, which significantly simplifies the optics matching to the downstream accelerator and cannot be achieved with CT. It is important to mention that the closed orbit for the islands is very different from the one of the core. As a matter of fact, the islands are one single ribbon of particles, which closes after four turns, whereas the core follows a conventional central closed orbit (see also Section 6.1.2.1 and especially Fig. 6.15).
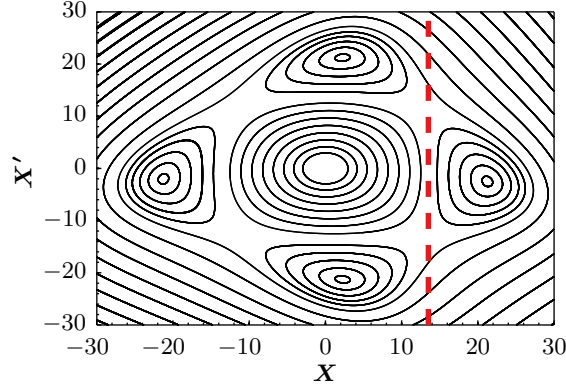
The linear FODO lattice with the single sextupolar and octupolar kick can furthermore be described by the following Hamiltonian, which was determined using the normal form approach [78, 79]:

$$
\mathcal{H}(\rho, \theta) = \Delta_r \rho + \frac{\rho^2 \Omega_2}{2} + \Delta_r \rho^2 |u_{0,3}| \cos(4\theta + \psi).
\tag{6.5}
$$
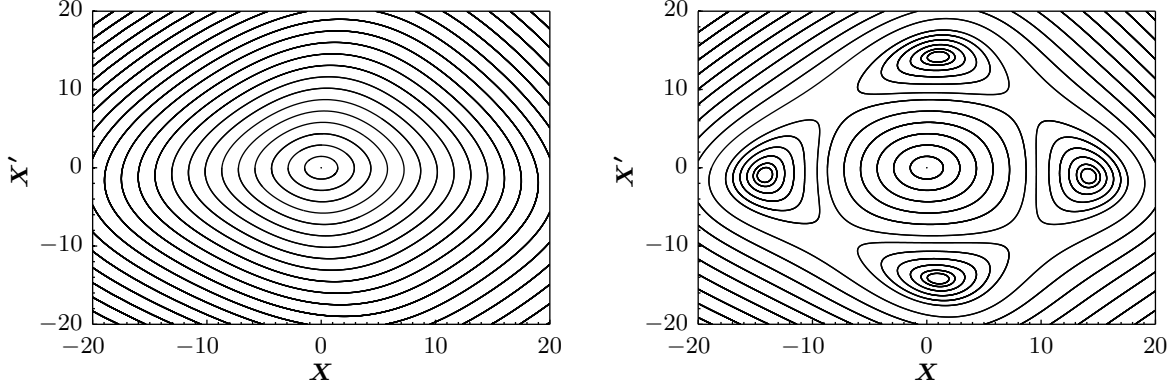
(a) At a tune of $q_x = 0.25$ the particle trajectories are no longer elliptic, but square.

(b) For $\Delta_r = 0.001$ islands are found to be clearly separated from the core.

(c) To extract a horizontally split beam, a septum blade is positioned between the core and the islands (indicated by the red dashed line). In case of the shown fourth order resonance ($\Delta_r = 0.002$), the beam rotates 90 degrees per turn and one island after the other is extracted. Extraction of the core requires an additional kick.

Figure 6.6. Horizontal phase space portraits based on Eq. (6.3) for $\kappa = 0.5$.

In this expression (ρ, θ) are action-angle coordinates, Ω_2 is a term describing the detuning with amplitude and $u_{0,3}$ is the resonant term responsible for the formation of the islands:

$$
\Omega_2 = -\frac{1}{16}\left[3\cot\left(\frac{\omega}{2}\right) - \cot\left(\frac{3\omega}{2}\right)\right] - \frac{3}{8}\kappa,
$$

$$
u_{0,3} = \frac{i}{16}\exp^{i\omega}\left[\cot\left(\frac{\omega}{2}\right) - \cot\left(\frac{3\omega}{2}\right) - 2\kappa\right].
$$

(6.6)

Fundamental parameters of the islands, such as the distance of the SFPs from the origin ρ_+ and their surface Σ, were deduced from $\mathcal{H}$ and the corresponding terms are:

$$\rho_+ = -\frac{\Delta_r}{\Omega_2 + 2\Delta_r |u_{0,3}|} \qquad \Sigma = 16\sqrt{\left|\frac{\Delta_r}{\Omega_2}\right| |u_{0,3}| \, \rho_+^2}. \tag{6.7}$$

The distance and the size of the islands increase for larger values of the tune and decrease with the octupolar component.

On the following pages the implementation of MTE in the PS is described and the actual research conducted in the framework of this thesis is motivated.

6.1.2.1 Implementation of the transverse splitting process in the PS

In 2006, the non-linear elements required to perform the horizontal splitting, i.e. sextupoles and octupoles, were installed in SS39 and SS55. These locations were chosen to provide the proper phase of the islands at SMH16 and to avoid feed-down effects during the rise of the extraction bump (see also Section 6.1.2.2). Furthermore, the increased aperture requirements of a split beam resulted in multiple modifications to the vacuum chambers. The overall implementation of the MTE scheme was rather challenging given the constraints of the layout of the PS [74]. An overview of the elements required to realize the horizontal splitting is given in Fig. 6.7 and the rationale of the process is set forth in the following:

■ Likewise to CT, the optimization of the SPS duty cycle requires the phase space manipulations
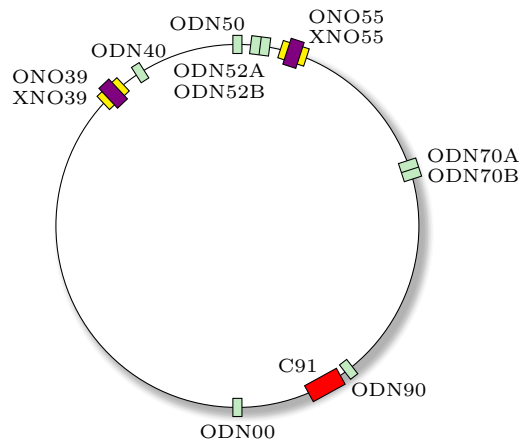

Figure 6.7. Distribution of elements along the PS, which are used to perform the transverse splitting. The LEQ are not depicted, as 40 of them are installed. Note that the dedicated sextupoles XNO are actually two separate magnets (shown in yellow). Due to the specific requirements in terms of RF voltage (see Fig. 6.11) only a single 10 MHz cavity (C91) is used.

to take place at a flat top of 14 GeV/c. Therefore, the magnetic cycle is very similar to that shown in Fig. 6.1; however, an extended flat top is required to adiabatically perform the transverse splitting (see Fig. 6.8). At high energy, the PFW determine the working point of the accelerator and, in order to cross the stable fourth order resonance $4Q_x = 25$ from below, the tunes are set to ($Q_x = 6.245$, $Q_x = 6.30$). Both linear chromaticities ξ_z are programmed to slightly positive values to (i) avoid head-tail instabilities and (ii) reduce the chromatic tune spread due to the intrinsic momentum spread of the beam. Moreover, the second order chromaticities Q_z'' are desired to be small to further reduce the modulation of the horizontal tune due to coupling to the longitudinal plane. By doing so, particles with different momenta cross the resonance almost simultaneously (see Fig 6.9).

■ The dedicated multipole magnets, i.e. the normal octupole in SS39 (ONO39), the normal octupole in SS55 (ONO55), the normal sextupoles in SS39 (XNO39), and the normal sextupoles in SS55 (XNO55), excite the stable fourth order resonance $4Q_x = 25$. Furthermore, these elements induce negative detuning with amplitude, i.e. the horizontal tune of a particle decreases as its amplitude increases, and they determine the size and shape of the islands. The sextupoles are also used to control chromaticity and account for the sextupolar feed-down created by the octupoles. Figure 6.10 (a) displays a certain configuration of the settings of the non-linear elements on the flat top of the MTE cycle.

■ The variation of the horizontal tune to cross the resonance $4Q_x = 25$ is controlled by the LEQ. At maximum octupole current, the resonant tune $Q_x = 6.25$ is reached and further increased
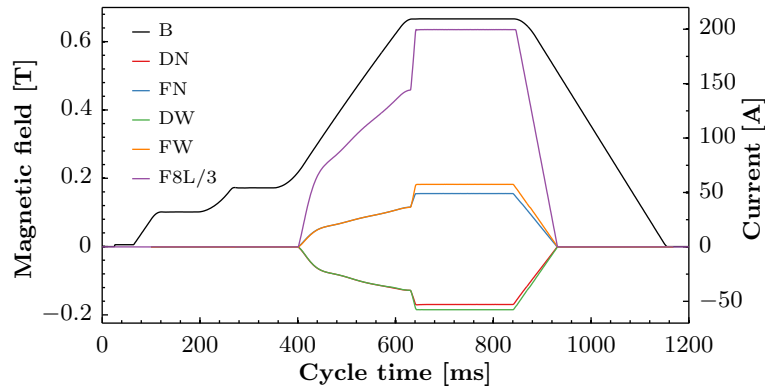

Figure 6.8. Magnetic configuration of the MTE cycle. Injection occurs at 1.4 GeV kinetic energy, the intermediate plateau is situated at 2.8 GeV kinetic energy, and the flat top, which is extended compared to CT, corresponds to a momentum of 14 GeV/c. At high energy, the working point is essentially determined by the PFW and the coloured curves represent the currents applied to these circuits. The current of the F8L was reduced by a factor three to improve readability.
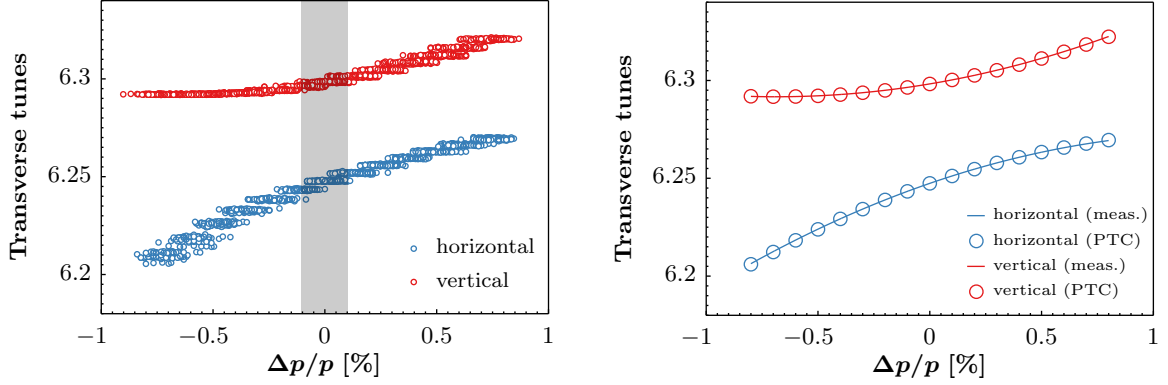
(a) 200 cycles were used to obtain statistically significant measurements of the non-linear chromaticities. The typical value of $\delta\,(4\sigma)$ during the population of the islands (see also Fig. 6.11) is displayed by the grey bar.

(b) The solid lines represent the third order polynomial fits of the measurement data and the circles the values of the model obtained after matching the quadrupolar, sextupolar and octupolar components with the thin multipoles inside the main magnets.

Figure 6.9. Chromaticity measurement on the flat top of the MTE cycle, which serves as input for simulation studies.

as the current of the octupoles is reduced. Consequently, the size of the islands as well as their separation increases.

■ The dedicated non-linear elements introduce a tune-shift, which can be expressed in terms of the Hamiltonian in the normal form space [78]:

$$h(\rho_1, \rho_2) = \sum_{k_1+k_2 \geq 2} h_{k_1,k_2}\rho_1^{k_1}\rho_2^{k_2}, \tag{6.8}$$

where $\rho_{1,2}$ are the non-linear generalizations of the linear emittances $\varepsilon_{x,y}$. The non-linear tunes to first order can then be written in the following form:

$$Q_x = Q_1 + 2h_{2,0}\rho_1 + h_{1,1}\rho_2 \qquad\qquad Q_y = Q_2 + 2h_{1,1}\rho_1 + h_{0,2}\rho_2, \tag{6.9}$$

with $h_{2,0}$ and $h_{0,2}$ describing the horizontal and vertical detuning with amplitude, respectively, and $h_{1,1}$ accounting for the non-linear coupling between the transverse planes. Minimizing $h_{1,1}$ is another effect that beneficially impacts the resonance crossing, as it reduces the modulation of the horizontal tune due to the vertical amplitude. In the PS, $h_{1,1}$ consists of two components, i.e. a constant contribution of the lattice and a dynamically changing contribution, which is

caused by the time-varying strength of ONO39 and ONO55 [80]:

$$h_{1,1} = h_{1,1,\text{lattice}} + h_{1,1,\text{dynamic}}. \tag{6.10}$$

Therefore, the strength of an additional set of eight short octupoles, the normal defocusing octupoles (ODN), is varied over time to keep $h_{1,1}$ small and almost constant. The variation of the $h_{i,j}$ and Q_x during the splitting process is illustrated in Fig. 6.10 (b).

- An important ingredient to further reduce the tune modulation is the decrease of the energy spread of the beam in the longitudinal plane. This is achieved by lowering the RF voltage of the 10 MHz cavities on the flat top as shown in Fig 6.11.

- The splitting process is extremely susceptible to fluctuations of the linear and non-linear magnetic fields. Thus, magnetic stability and reproducibility is a major concern for MTE (see also Section 6.2.1).

Corresponding to the four timings indicated by the dashed lines in Fig. 6.10, i.e. 720 ms, 730 ms, 800 ms and 835 ms, where extraction occurs at the latter, the shape of the horizontal phase space is depicted in Figs. 6.12 and 6.13. When the tune is set to $Q_x = 6.25$, the distance to the resonance is obviously zero and no islands are present. However, the phase space distortion
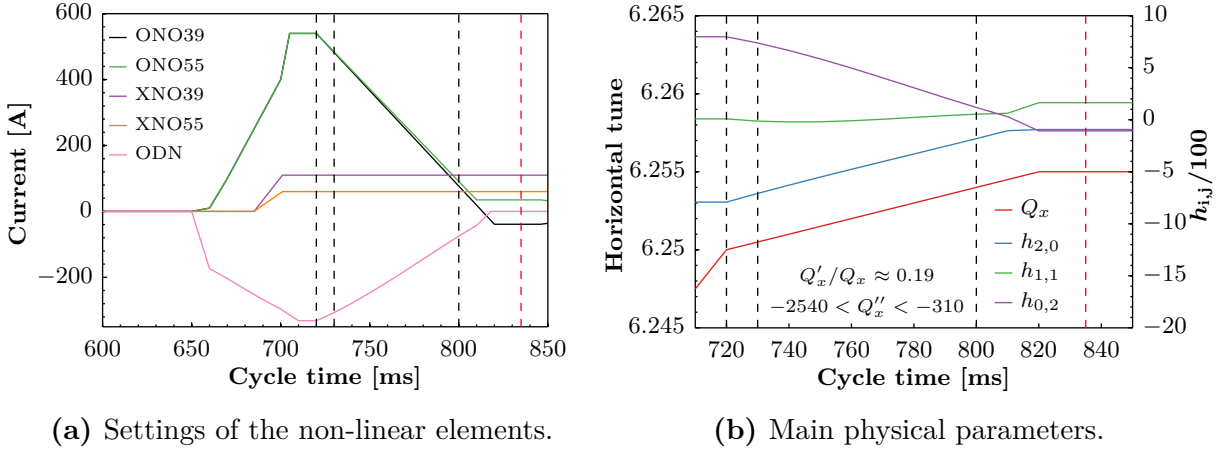

(a) Settings of the non-linear elements.   **(b)** Main physical parameters.

Figure 6.10. Configuration of the dedicated non-linear elements and variation of the main physical parameters on the flat top. The resonance is crossed at 720 ms, where the currents in the octupoles are maximum. Subsequently, the currents are reduced while the tune is increased to perform the splitting process. Once the beamlets are sufficiently separated, the beam is extracted (at 835 ms, red dashed line). During the whole process, the vertical tune is kept at $Q_y = 6.30$. The horizontal phase space configurations corresponding to the settings at the dashed lines are depicted in Figs. 6.12 and 6.13.
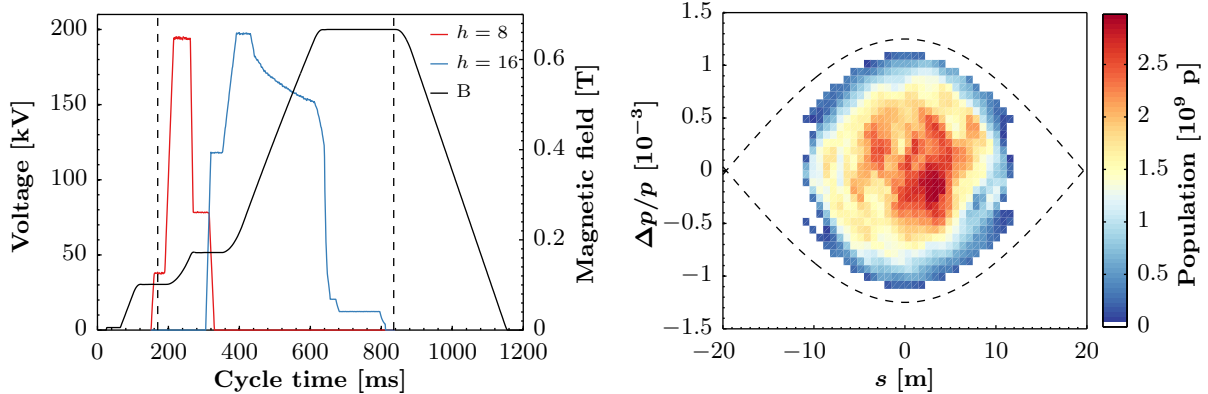
(a) RF voltage of the 10 MHz cavities along the MTE cycle. The beam from the PSB is transferred into $h = 8$ buckets and a double splitting to $h = 16$ takes place at the intermediate flat top. At 680 ms the voltage is reduced to decrease the energy spread during the transverse splitting. Afterwards, just prior to extraction, the voltage is further reduced to zero to debunch the beam. Injection and extraction timings are indicated by the dashed lines

(b) Density plot of the longitudinal distribution at 720 ms for a bunch on $h = 16$ with the following parameters: $4\sigma_s = 23.6$ m ($4\sigma_t = 79$ ns), $\delta = 4.7 \times 10^{-4}$, $V_{RF} = 12.34$ kV. Due to the low voltage the bunches experience some longitudinal coupled bunch instability [81]. The black dashed lines describe the separatrix.

Figure 6.11. Measurements of the RF voltage and the longitudinal distribution.
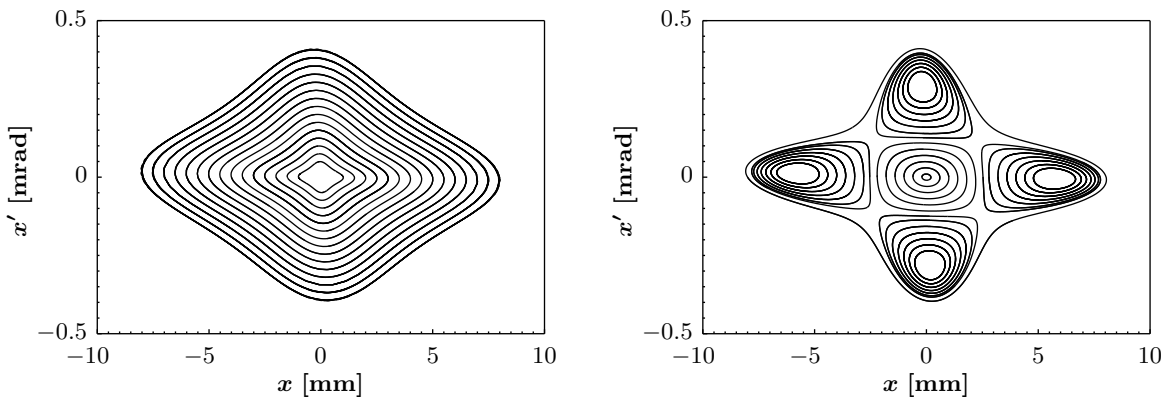
(a) 720 ms, $Q_x = 6.25$: No islands are present as the tune corresponds exactly to the resonant value.

(b) 730 ms, $Q_x = 6.2505$: The distance of the islands from the centre is already visible and their size increases.

Figure 6.12. Horizontal phase space portraits in SS01 during the splitting process at two different timings. Extremely precise control over the tune is required as small variations in the order of $\Delta Q_x = 1 \times 10^{-3}$ significantly affect the positions of the SFPs.
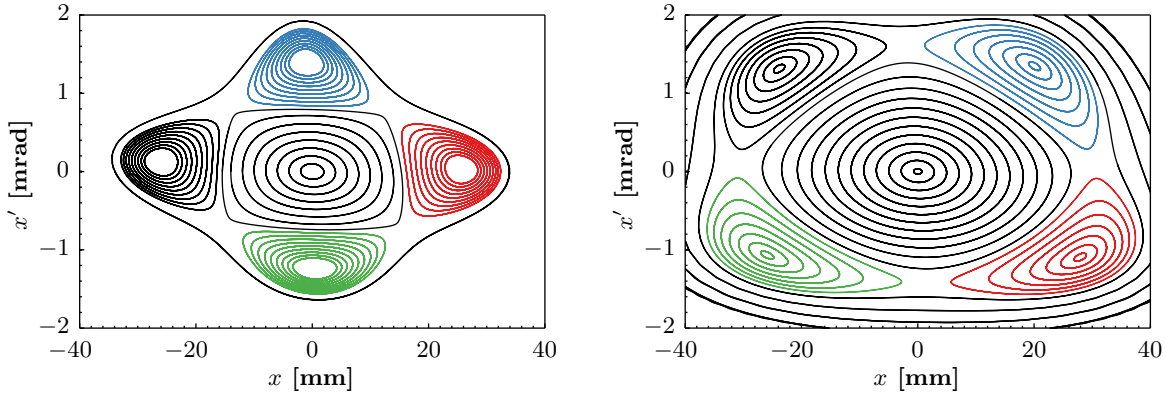
(a) 800 ms, $Q_x = 6.254$: Due to the high amplitude of the islands, they cover a significant portion of the available aperture. Careful tuning of the accelerator is required to avoid beam loss.

(b) 820 ms, $Q_x = 6.255$: Prior to extraction, a rotation of the beam in the phase space is required to extract the islands in SS16.

Figure 6.13. Horizontal phase space portraits in SS01 during the splitting process at two different timings. Extremely precise control over the tune is required as small variations in the order of $\Delta Q_x = 1 \times 10^{-3}$ significantly affect the positions of the SFPs.
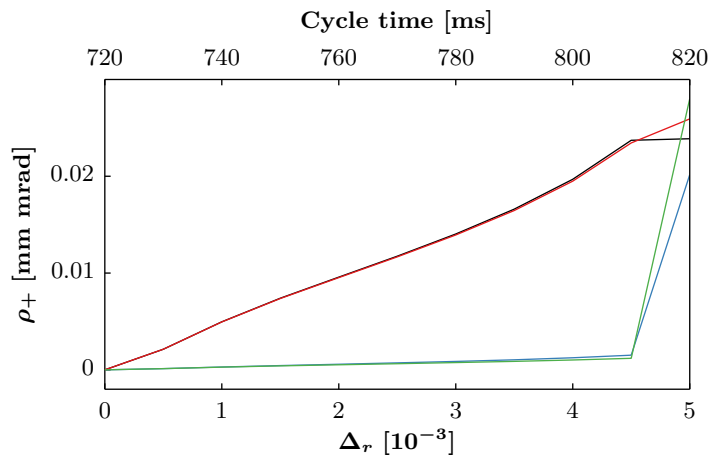

Figure 6.14. Evolution of the distance of the fixed points from the origin. The rapid change of ρ_+ after 810 ms is due to the final rotation of the beam in the phase space. In agreement with Eq. (6.7), the position of the SFPs increases almost linearly with the distance from the resonance. The colour code describes the different islands as illustrated in Fig. 6.13.

is clearly visible. Only 10 ms later, a clear separation between the central part and the area around the additional four SFPs can be observed. Towards the end of the cycle, the size of the islands and their distance from the centre have significantly increased. Once sufficiently separated, the beam has to be rotated in the phase space to properly position the islands with respect to SMH16 (see also Sec. 6.2.3). The evolution of the positions of the SFPs during the splitting is depicted in Fig. 6.14.

At this stage, the beam occupies about 100 mm of the available space and the settings of the PS have to be carefully adjusted to avoid any interaction between the beamlets and the mechanical aperture of the machine. An illustration of the horizontal and vertical closed orbits is shown in Figs. 6.15 and 6.16, and the corresponding optics functions for the core and the islands are depicted in Fig. 6.17.

Furthermore, the horizontal emittance plays a crucial role during the splitting process. In order to equally populate the islands and the core, the transverse damper is used to blow up the beam during resonance crossing, which improves the intensity distribution in the final state. The damper actually excites the beam at a certain harmonic h_d of the revolution frequency plus a fractional tune q_d ($q_d = 0.25$ is applied for MTE):

$$f_{\text{damper}} = f_{\text{rev}}\,(h_d + q_d).\tag{6.11}$$

The natural figures of merit describing the splitting efficiency are defined as

$$\eta_{\text{MTE}} = \frac{\langle N_{\text{island}}\rangle}{N_{\text{total}}} \text{ and } \eta_{\text{core}} = \frac{N_{\text{core}}}{N_{\text{total}}},\tag{6.12}$$

where $\langle N_{\text{island}}\rangle$ is the average intensity captured in the islands, N_{core} the intensity of the core and N_{total} the total intensity.

6.1.2.2 The extraction process

The transverse splitting and the extraction per se are two completely independent manipulations for MTE, whereas both processes are intrinsically connected for the CT extraction. Even though the actions required to perform the MTE splitting are very sophisticated, this is not entirely true for the proper extraction process, which can actually be simplified, as no orbit bumps around SS31 are required to approach SEH31.

In order to prepare the beam for extraction, a slow bump is applied to approach SMH16. In the framework of MTE, dedicated power supplies for the dipole magnets used to create this bump (BSW) were installed, permitting independent control of the elements in SS12, SS14, SS20 and SS22. In addition to those elements the horizontal dipole in SS15 (DHZ15) and the horizontal dipole in SS18 (DHZ18), which are usually applied for the correction of the closed orbit at high energy, were used until 2012 to properly shape the bump (see Fig. 6.18).
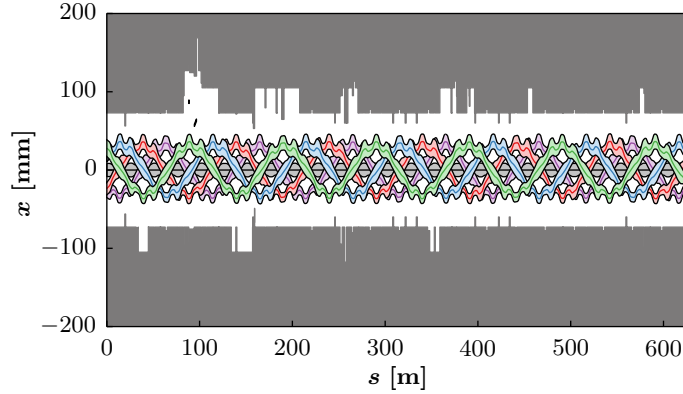
(a) The core and the islands cover a significant fraction of the available aperture at the end of the splitting process. The different islands, which are merely one single ribbon extending over four turns, are shown in different colours. The trajectory of the core, which is shown in light grey, follows a conventional orbit with one-turn periodicity.
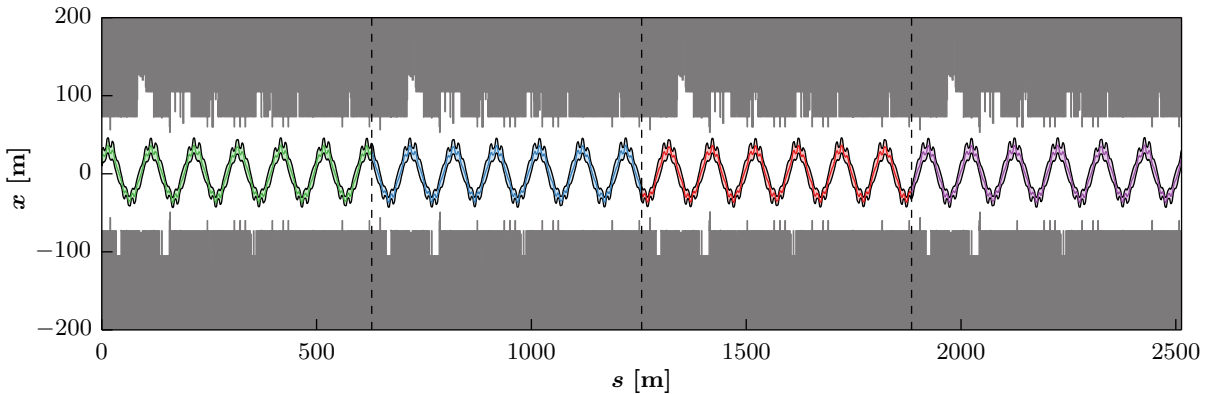
(b) Periodic trajectory of particles within one island, corresponding to four turns inside the PS. After four turns the beam reverts to its initial position. The dashed lines represent the end of the one-turn lattice and the colours are identical to those used in (a).

Figure 6.15. Horizontal closed orbits for the core and the islands in the ideal PS lattice applying the settings at extraction shown in Fig. 6.10. The difference in periodicity between the two disconnected structures is highlighted. The envelopes represent a beam size with extension of $3\sigma_x$ and $2\sigma_s$, based on Gaussian distributions in both planes ($\varepsilon_x^n = 5$ mm mrad, $\delta = 5 \times 10^{-4}$). The horizontal mechanical aperture is represented in grey. In odd sections of the accelerator, where the β_x-functions are maximum, the total beam size reaches almost 100 mm.
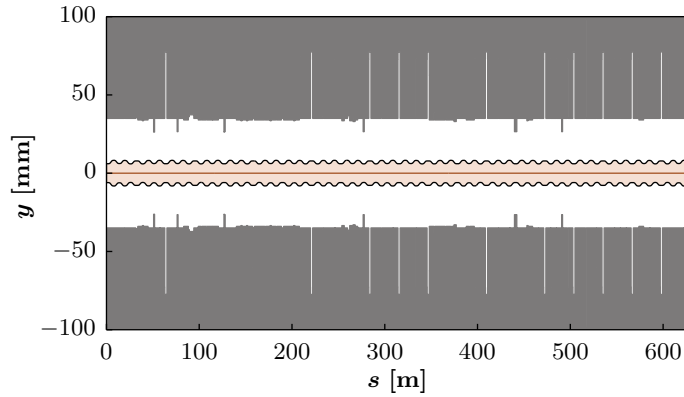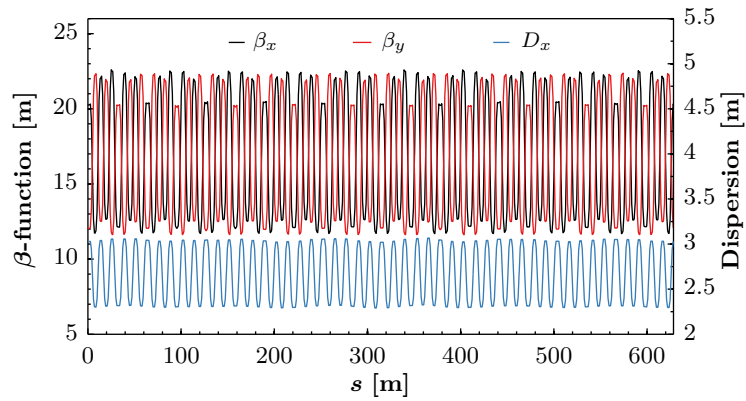
Figure 6.16. Vertical envelope for the MTE beam in the ideal PS lattice. The envelopes represent a beam size with extension of $3\sigma_y$, based on a Gaussian distribution ($\varepsilon_y^n = 5\,\mathrm{mm\,mrad}$). The beam follows a conventional closed orbit and the aperture constraints are less stringent than in the horizontal plane.


(a) The lattice functions for the core show a very regular behaviour. The vertical dispersion is zero considering the ideal lattice.
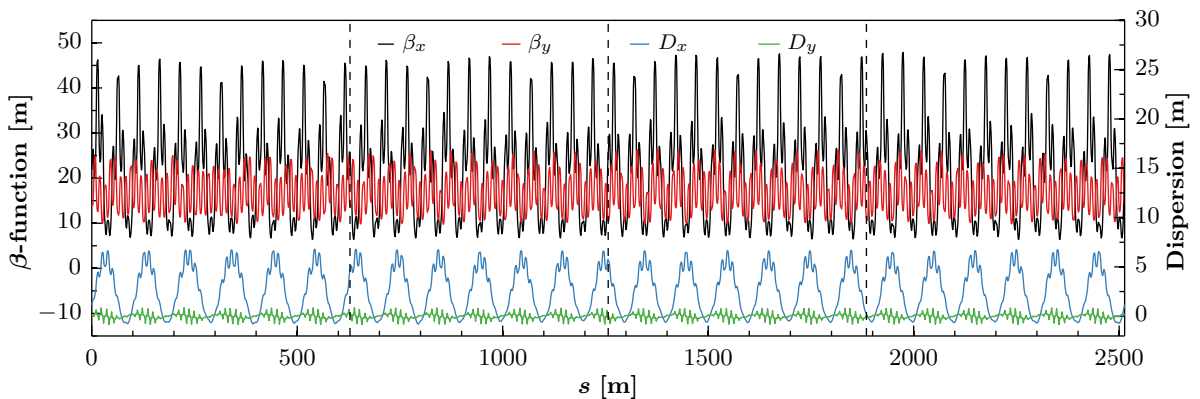
(b) The lattice functions for the islands show the previously discussed difference in periodicity as well as significant changes in the amplitudes compared to the core functions. The dashed lines represent the end of the one-turn lattice. Due to the non-zero non-linear coupling, also the vertical plane is affected.

**Figure 6.17.** Optics functions for the core and the islands.
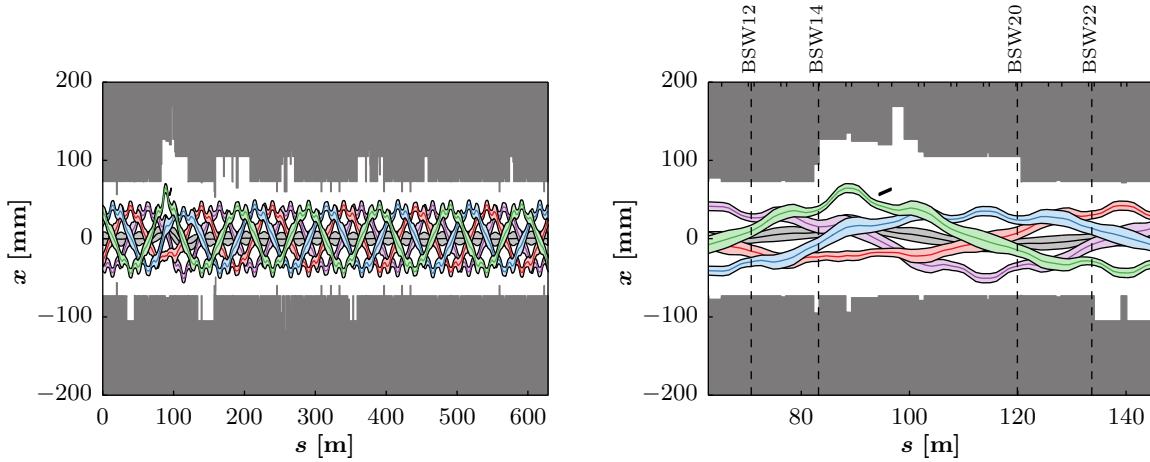
(a) The excursion of the orbit to approach SMH16 is clearly visible.

(b) Detailed view of the extraction region between SS11 and MU23. The outermost island closely approaches SMH16, which is represented by the black rectangle. The locations of the SSs are indicated by the marks on the top axis and the dashed lines describe the locations of the extraction bumpers.

Figure 6.18. Setting of the slow bump applied until 2012, using BSW12, BSW14, BSW20, BSW22 as well as DHZ15 and DHZ18.

Once the maximum of the slow bump has been reached, the fast kicker in SS13 (KFA13) and the fast kicker in SS21 (KFA21), which provide a five-turn long pulse, are applied to extract one island per turn. Subsequently, the core is extracted during the fifth turn using the single-turn fast kicker in SS04 (KFA04) and the fast kicker in SS71 (KFA71) (see Fig. 6.19).

In order to comply with the requirements of the SPS, the longitudinal structure of the beam constitutes another important point. In fact, a debunched beam with an additional modulation at 200 MHz, the frequency of the SPS RF cavities, has to be transferred to ensure proper RF capture in the SPS. Therefore, eight bunches from the PSB are injected and accelerated to the intermediate plateau (see Fig. 6.8), where each bunch is longitudinally split into two. The resulting sixteen bunches then undergo the transverse splitting process and once the islands are significantly separated and populated, the RF voltage is switched off to debunch the beam. This is a rather delicate process as, without any measurable bunch structure, the RF radial loop - a feedback loop aimed at keeping the beam in the centre of the machine by acting on its energy - stops working and the beam becomes susceptible to external effects, such as the non-reproducibility of the magnetic field. Due to the shape of the non-linear chromaticity (see Fig. 6.9), a slight change of the energy of the beam might significantly influence the position of the SFPs. Therefore, it is important to keep the beam bunched as long as possible, in order to keep the radial position under control.
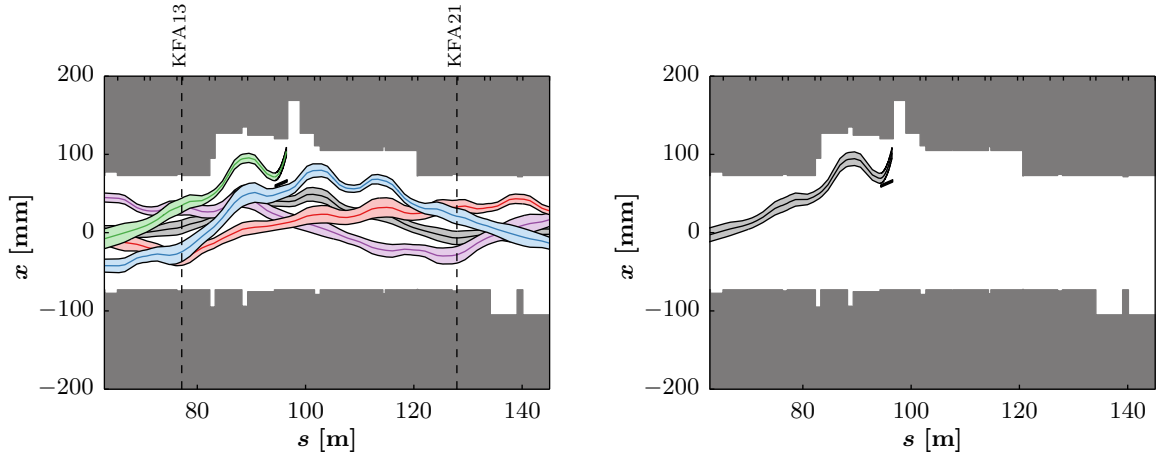
(a) Extraction of the first out of four islands. The remaining four beamlets continue to circulate on the inner side of SMH16 and will be extracted over the subsequent turns.

(b) Extraction of the core to complete the multi-turn extraction over five turns.

Figure 6.19. Fast extraction bump applied until 2012 to extract the islands and the core. Displayed is again only the fraction of the accelerator between SS11 and MU23.

6.1.2.3 Problems observed in 2010 and proposed solutions

In regard of replacing the CT extraction, a beam applying the MTE scheme with 2×10^{13} protons per pulse (ppp) was successfully sent to the SPS and used for the physics community for the first time in 2010 [82]. After about one month of operational experience, two major show-stoppers were detected [83]:

(1) significant fluctuations in the efficiency of the transverse splitting, the losses at extraction and the trajectories in the transfer lines, and

(2) unacceptably high radioactive activation of SMH16.

Figure 6.20 depicts measurement data recorded in May 2010, were a pseudo-harmonic oscillation of the splitting efficiency is apparent. The islands' intensity dropped from about 20% to 14%, which causes problems as the SPS requires an almost equal population of the five beamlets, i.e. $\eta_{\text{core}} = 20 \pm 1\%$, to avoid trips of the RF system. The source of this phenomenon was not understood at the time, even though significant effort was devoted to correlating the observed oscillations and various parameters of the machine, such as the tune and the currents of the auxiliary magnets, the PFW and the extraction dipole magnets.

A certain fraction of the losses at SMH16 is, on the other hand, intrinsic to the extraction process
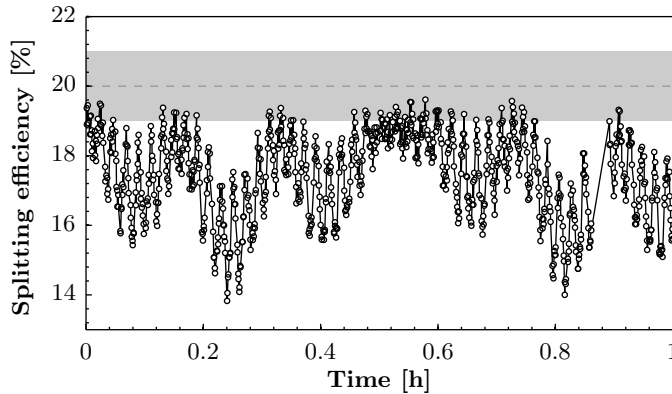
;

Figure 6.20. Oscillation of the efficiency of the transverse splitting per island based on the measurement data of 2010. The intensity is supposed to be equally distributed among the five beamlets and the grey band represents this SPS requirement (20±1%). Unacceptable oscillations of the splitting efficiency were observed.

due to the longitudinal structure of the beam. During the rise time of the fast kickers, the continuous beam is swept from the internal to the external side of SMH16, causing unavoidable beam loss. This was predicted during the design of MTE and for this reason it was initially foreseen to transfer a bunched beam at $h = 8$, which was later understood to be incompatible with the SPS. The losses in SS16 led to unacceptable activation levels inside and outside the PS tunnel and, due to the radiation cool down required prior to any intervention, failure of any device in the extraction region towards the end of the year would have caused an extremely long waiting time. Therefore, and due to the adverse effects on the LHC physics programme, it was decided to stop providing the MTE beam to the SPS.

Based on this operational experience, the coexistence of the CT and the MTE schemes was decided and, moreover, a passive absorber, the dummy septum (TPS15) [84], was proposed to be installed in SS15 to shield SMH16 during the rise time of the kickers. Therewith, beam loss can be concentrated at this location, were several concrete blocks provide additional shielding, and the downtime in case of a failure of SMH16 can be significantly reduced.

Furthermore, it is important to mention that, from a radio protection (RP) point of view, MTE appears preferable over the CT method, as the activation of all parts of the ring, with the exception of the extraction region, is significantly reduced [85].

6.1.2.4 Installation of the dummy septum in SS15

Based on the operational experience gathered with the MTE beam during the run in 2010, the decision to install TPS15 was taken. More detailed information about its design and implementation can be found in the corresponding design report (DR) [16]. This device has been

designed to absorb particles that would otherwise be lost at SMH16 during the rise time of the fast extraction kickers. These losses correspond to approximately 2% of the full beam intensity and arise due to the continuous longitudinal structure of the beam. It should be emphasized that the core and the islands are two disconnected structures in the horizontal phase space, which need to jump the blades of the septa independently. Moreover, the rise time of the fast extraction kickers is different for the islands and the core.

TPS15 allows to reduce the radioactive activation in SS16 by relocating beam loss to the well-shielded SS15 and, therefore, the waiting time for any intervention in case of an issue with
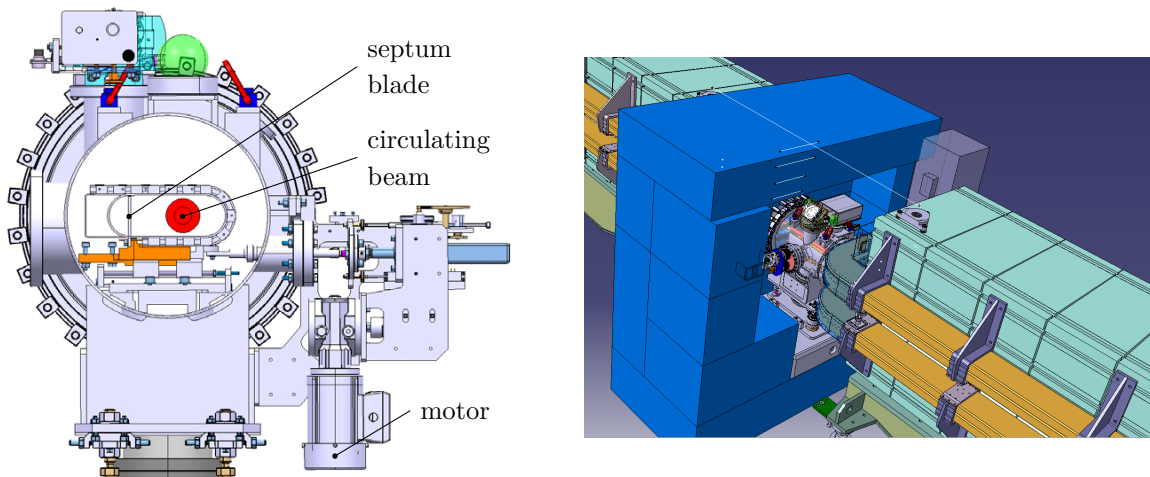
(a) Cross section of the TPS15 assembly seen from its upstream position. During the extraction process the circulating beam is moved to the external side of the blade.

(b) To locally confine the losses in SS15, an extensive concrete shielding, which is depicted by the blue blocks, has been put in place. The upstream and downstream MUs are shown as well.

(c) Photo of the installation in the tunnel.

Figure 6.21. Implementation of TPS15 in the PS.

SMH16 is significantly shortened. Obviously, the opposite would be true for an intervention in SS15; however, a failure of TPS15 would only affect the MTE beam, whereas SMH16 is required for the extraction of all proton beams.

Even though the device is designated as septum, its purpose is purely passive as the interaction with the beam is only of mechanical nature and no magnetic field to deflect the beam is applied. The main component of this passive septum is an 800 mm long and 4.4 mm thick copper blade, whose angle and position can be precisely adjusted by means of two motors to shadow the magnetic septum (see Figs. 6.21 and 6.22).

SS15 was chosen as location for the dummy septum due to its proximity to SS16. It nevertheless has to be considered that the phase advance between those two sections of the accelerator is 22.5° and the gap created downstream of TPS15 will have been slightly repopulated at the entrance of SMH16.

It is worth emphasizing that TPS15 constitutes an important aperture restriction in the extraction region. Therefore, the installation of TPS15 significantly impacted most of the other operational users as well, as the extraction trajectories had to be redesigned.
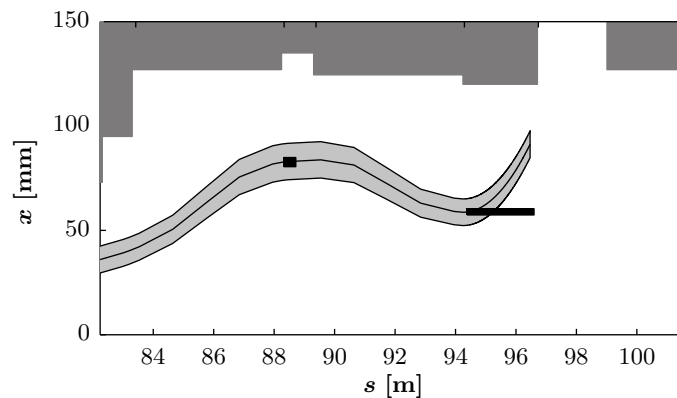

Figure 6.22. During the rise time of the fast extraction kickers, the beam is swept from the internal to the external side of both TPS15 and SMH16. Proper adjustment of the positions (and angles) of both septa allows to put SMH16 in the shadow of TPS15, and, therefore, reduce the losses in SS16. In the shown configuration the black rectangles indicate the septa at properly adjusted positions to provide shadowing. The efficiency of the shadowing might, however, be different between the core and the islands.

6.2 MTE studies after Long Shutdown 1

Between 2013 and 2014, the CERN accelerator complex was not operating for more than a year in order to perform maintenance and renovation work. During this Long Shutdown 1 (LS1), the interventions mentioned in Section 6.1.2.3 were carried out to prepare the PS for future operation with high-intensity beams. The dummy septum was put in place in SS15, while outside the tunnel, civil engineering activities were conducted to reinforce the shielding on top of the extraction region [13]. After installation of TPS15, the PS became ready for operation with the MTE beam and, therefore, the commissioning of this complex extraction technique was restarted after LS1. In this regard, the first step was to set up the transverse splitting process applying the settings that were operationally used in 2010. Significant oscillations of the splitting efficiency, which were in fact worse than observed in 2010, were soon encountered.

These oscillations constituted a substantial obstacle and hampered the progress of the commissioning. It was only after solving this issue, that the actual extraction process could be established. Due to the installation of TPS15, a complete redesign of the extraction bump was required and optimum conditions to provide shadowing had to be determined.

During the whole commissioning process, the available simulation tools played a vital role and allowed to deepen the understanding of the accelerator. In the following sections, the different aspects of the commissioning, which culminated in the operational implementation of the MTE technique, are laid out in detail.

6.2.1 Periodic oscillations of the splitting efficiency

6.2.1.1 Experimental observations

One of the challenges of working with transversely split beams is the fact that it is impossible to directly measure the locations of the various beamlets in the phase space. Using conventional PUs to provide a measurement of the beamlets' positions fails, as the system only returns the centre of the overall charge distribution. Therefore, it has to be relied on different measurement methods such as, e.g. BWSs. The horizontal scanners of the PS were extensively used to investigate the oscillations of the splitting efficiency.

In Fig. 6.23, a measured horizontal profile using BWS54 is shown together with the corresponding phase space obtained by simulations. The BWS in this straight section of the PS was chosen, as the horizontal projection reveals rather distinct beamlets. In the shown case, several parameters, such as the horizontal tune and the strength of the damper, were not optimized leading to an important population of the core in the order of about 40% and, therefore, this example was selected for the purpose of illustration only. Already from this simple comparison between the simulated phase space and its measured projection, very good agreement can be concluded. Ideally, this BWS would have been used for the measurements presented in the following; however,
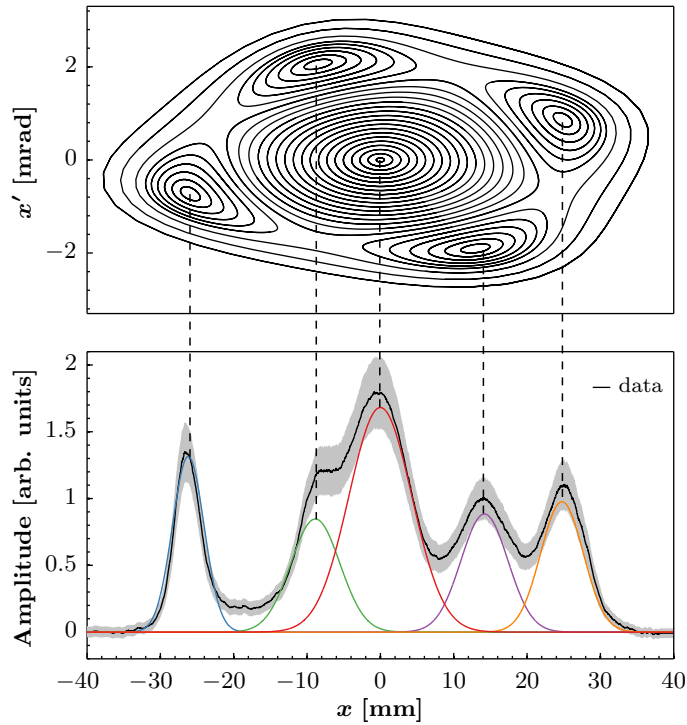
Figure 6.23. Simulated horizontal phase space at the location of BWS54 (top) and measured profile (bottom), which corresponds to an average value over 100 measurements. The grey band represents the one sigma standard deviation and the coloured lines the Gaussian fits for the different beamlets, with the only constraint being the equal integral of the functions corresponding to the four islands. The shift of the profile due to the closed orbit at BWS54 was removed. Excellent agreement between the predicted positions of the SFPs and the actual measurement is obtained, which is indicated by the dashed lines. The non-Gaussianity of the distribution in the islands together with particles remaining in-between the core and the islands during the splitting account for the difference between the data and the fits. The parameters of the splitting were set according to Sec. 6.1.2.1.

this was not possible due to a damage of the wire during the startup after LS1, and BWS68 was chosen instead.

Once the non-linear elements were set up correctly, first investigations of the transverse splitting could be started. Figure 6.24 depicts measurements of the horizontal profile recorded on fifteen different MTE cycles, which were each separated by one SC. As the beam was of rather low intensity (and consequently also low horizontal emittance), the horizontal tune was not entirely adjusted and the transverse damper was off, the efficiency of the splitting was very low. On top of this, a fluctuation of the efficiency, which occasionally led to almost no population of the islands at all, was observed. Subsequently, a significant amount of additional measurements was conducted and the impression arose that those hills and valleys of the islands' population follow indeed a periodic oscillation, as it had been observed in 2010. In Fig. 6.25, a waterfall repre-
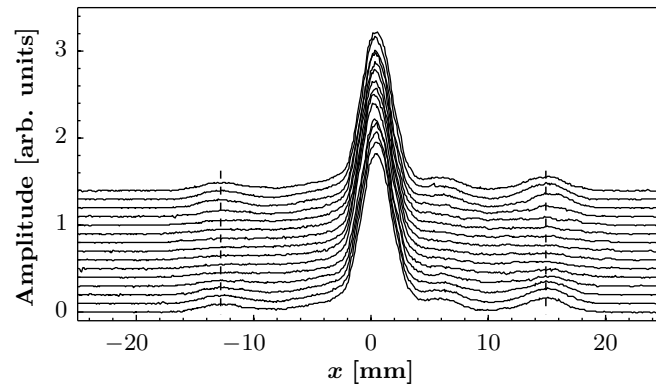
Figure 6.24. Horizontal profiles measured with BWS68 on fifteen consecutive MTE cycles. The position of the outermost islands is indicated by the dashed lines. Along them, a clear decrease of the signal after the first three measurements and an increase towards the end can be observed. The profiles were recorded at a cycle time of 820 ms.

sentation of these scans is depicted to emphasize the variation of the intensity of the islands. The period of this oscillation appears to be several SCs and, furthermore, non-constant, as the distance between the light spots is larger towards the last measurements than in the beginning.

A more detailed view of the oscillation of the intensity of the island situated at $x \approx 15$ mm is shown in Fig. 6.26, where the amplitude corresponds to the signal of BWS68. A clear change of the oscillation frequency after 39 SCs is depicted.
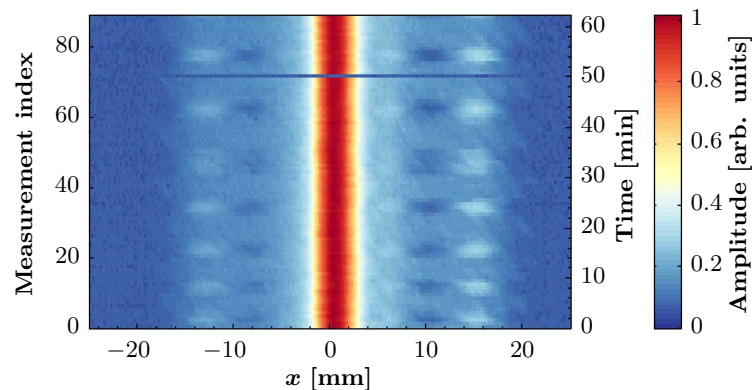

Figure 6.25. Waterfall plot of horizontal profiles measured with BWS68. The measurement index corresponds to the number of SCs and the corresponding time scale is shown as well. To improve visibility, logarithmic scaling was applied to the amplitudes of the signals. The blue line after about 70 SCs corresponds to one measurement without beam. The outermost islands are situated at the same locations as indicated in Fig. 6.24 and a modulation of their intensity is clearly observable.
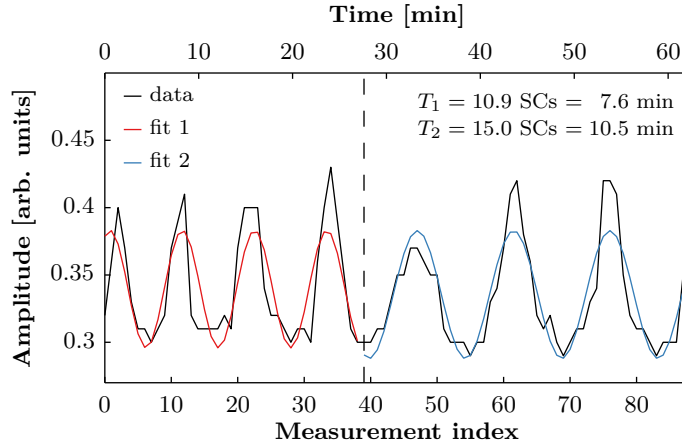
Figure 6.26. Oscillation of the amplitude measured with BWS68 corresponding to the island at $x \approx 15$ mm in Fig. 6.25. Based on sinusoidal fits, two distinct regimes with significantly different frequency are observed and the respective oscillation periods are stated on the plot.

On the basis of the observations presented in Figs. 6.24-6.26, the main physical quantities, which could significantly impact the beam during the capture process, were identified. Consequently, various measurement campaigns were initiated to correlate these properties with the variable splitting efficiency. The parameters of particular importance are mentioned in the following:

- In general, stability of the magnetic field up to the octupolar component is required, as the characteristics of the islands depend on the non-linear fields.

- Any variation of the horizontal tune, i.e. the distance from the resonance Δ_r as defined in Eq. (6.7), will affect the position of the SFPs and impact the splitting. Various effects could be the reason for this:

  - To regulate the main power supply of the PS, of the PFW, and of the F8L, only the dipolar field is considered. The sequence of cycles in the SC is known to affect the quadrupolar component of the main field [86] and, therefore, the composition of the SC could impact the MTE beam.
  - The stability of the power converters (PCs) of the elements dedicated to control the working point of the PS, i.e. the LEQ, the PFW, and the F8L.
  - The magnetic feed-down effects experienced by a beam, which passes off-axis through a non-linear element, are modified by a variation of the closed orbit and lead to a different tune.
  - Any change of the revolution frequency would indicate a change of the radial position, which, due to linear and non-linear chromaticity, results in a change of the working point.
  - Within the limits of the capabilities of the tune measurement system, all these points

should be detectable, if the resulting variation of the tune is larger than the error associated to the measurement (usually in the order of 1×10^{-3}, see also Section 3.2).

■ The momentum spread of the beam is another important parameter that influences the transverse splitting (see also Sec. 6.3.1). Therefore, stability of the RF voltage is crucial.

The measurements conducted to identify the source of the variable splitting efficiency are presented below.

Influence of the composition of the SC. The sequence of cycles in the SC as well as the position of the MTE cycle were changed while recording the BWS signals and the tune. The corresponding observations are depicted in Figs. 6.27-6.32.

The composition of the SC shown in Fig. 6.27 was kept unmodified for about two hours and the MTE cycle was placed closely after the two CT cycles in the beginning of the SC. On every MTE cycle, a measurement with BWS68 was conducted. It was important to observe such a long span of time, as the oscillations of the intensity occurred at very low frequency: the distance between two maxima was more than 15 min. During the whole measurement process this frequency was found to remain constant.

One beneficial effect of low splitting efficiency is the possibility to measure the tune of the core. If the intensity were equally shared between the core and the islands, the islands' contribution to the tune measurement would be dominant and the measured tune would be locked to $Q_x = 6.25$, corresponding to the tune of the SFPs inside the islands (see Fig. 6.28). However, with the core being significantly more populated (see e.g. Fig 6.24), the measurement system is sensitive to the tune of the central beamlet and a variation of the quadrupolar component of the magnetic field should be observed on the measured tune. In Fig. 6.29, the horizontal tune during the transverse splitting, which was measured every cycle such as the horizontal profile, is depicted. The average value over 70 measurements was subtracted to emphasize any possible variation. No regular pattern could be observed and sufficient stability of the quadrupolar fields was concluded.

In a next attempt, two MTE cycles were executed in the SC and special attention was again paid to the measurement of the horizontal profiles. The related BWS measurements, shown in Fig. 6.30, revealed the previously observed harmonic oscillation of the islands' population, but a modulation at higher frequency was observed as well. This additional phenomenon is explained in Fig. 6.31, where the data recorded on both cycles are analysed separately. In both cases, the splitting efficiency was found to oscillate at the same frequency, but the oscillations were out of phase by almost four SCs. If the effect causing the variation of the intensity in the islands were intrinsic to the magnetic configuration of the SC, a phase difference corresponding to the distance between the two cycles, i.e. less than one SC, would be expected. Therefore, an additional test with two MTE cycles was conducted. The corresponding data are depicted in Fig. 6.32.
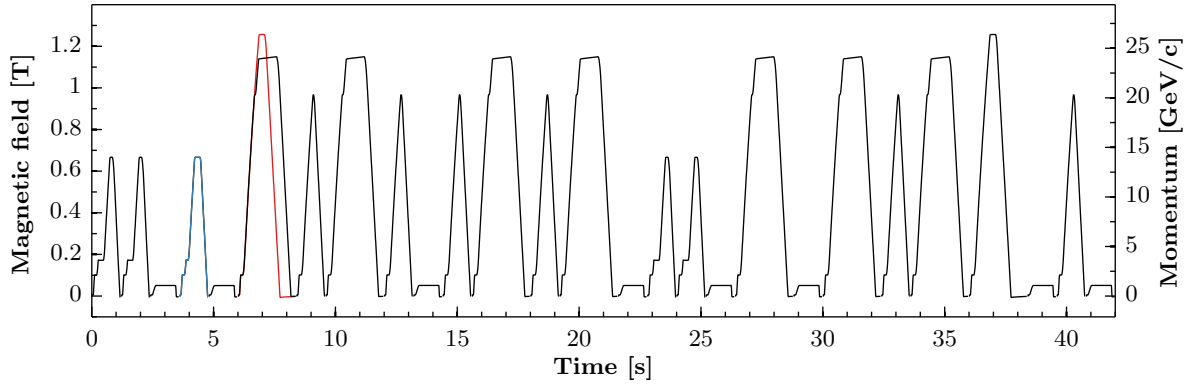
(a) Composition of the SC with four CT (14 GeV/c), one MTE (blue), one Antiproton Decelerator (AD) (red), seven EAST (25 GeV/c), six TOF (20 GeV/c) and one LHC (26 GeV/c) cycle. The AD requires beam approximately every 90 s and is therefore executed in alternation with the EAST cycle. This SC consists of 35 BPs, corresponding to a length of 42 s.
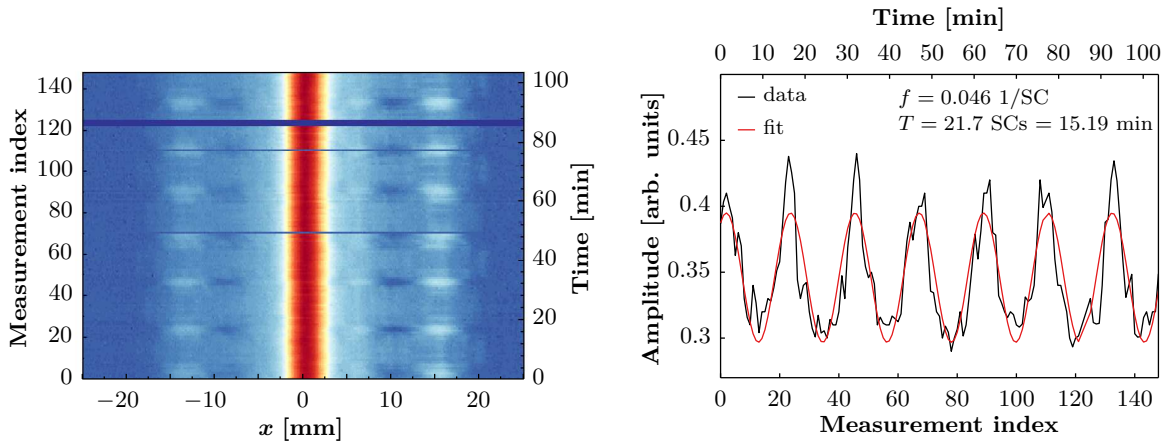
(b) Waterfall plot of horizontal profiles measured with BWS68. The maxima of the intensity modulation appear at regular intervals.

(c) Fitting of the intensity variation of the island at $x \approx 15$ mm reveals a constant period, which is noted on the plot.

Figure 6.27. The MTE cycle was executed in the beginning of the SC and an oscillation of the splitting efficiency with constant frequency was observed.
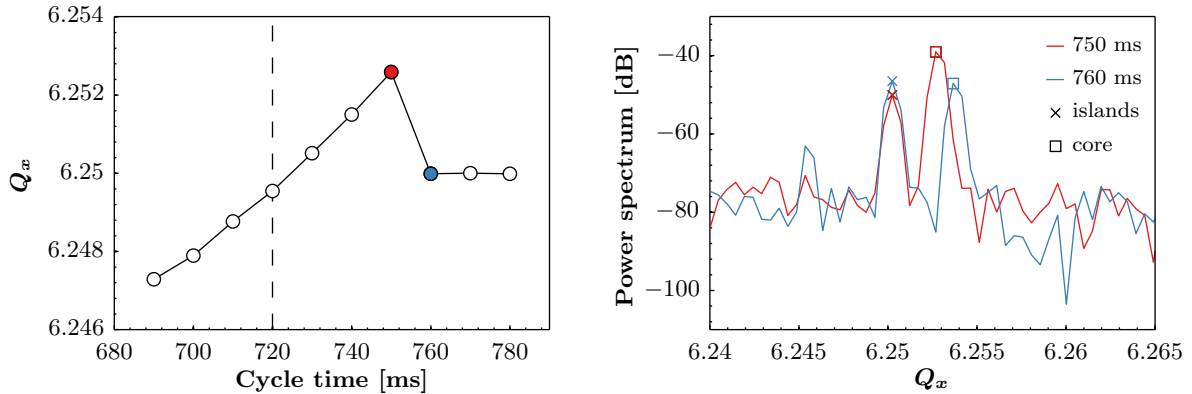
(a) Measured horizontal tune along the MTE cycle. Resonance crossing occurs at 720 ms, which is indicated by the dashed line. The data points represent the frequency at which the most prominent peak of the FFT of the turn-by-turn position signal occurs. The FFTs corresponding to the coloured markers are shown in (b).

(b) Tune spectrum for two instants of time, as indicated in (a). In both cases distinct peaks are visible: the one of the islands remains at $Q_x = 6.25$, while the tune of the core constantly increases as the islands are separated. From 760 ms onwards, the measured tune is locked to $Q_x = 6.25$, as the intensity captured inside the islands is larger than in the core.

Figure 6.28. Illustration of the effect of increasing the islands' population on the measurement of the horizontal tune. To separate the islands from the core, Q_x is increased along the cycle. Initially, i.e. as long as the intensity of the core is dominant, the main contribution to the tune spectrum comes from the central part of the beam. Once the islands are sufficiently populated and separated, the measured tune is locked to $Q_x = 6.25$.
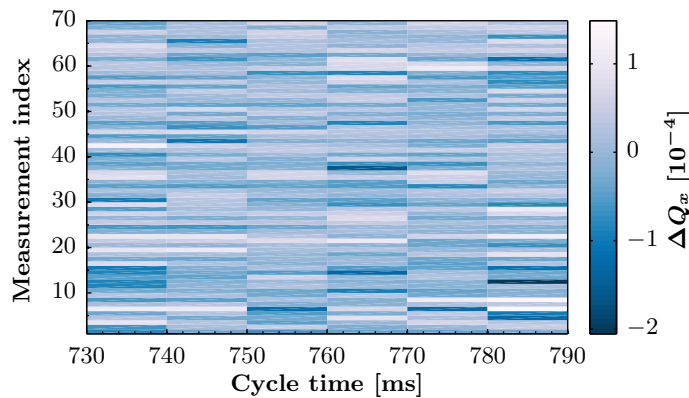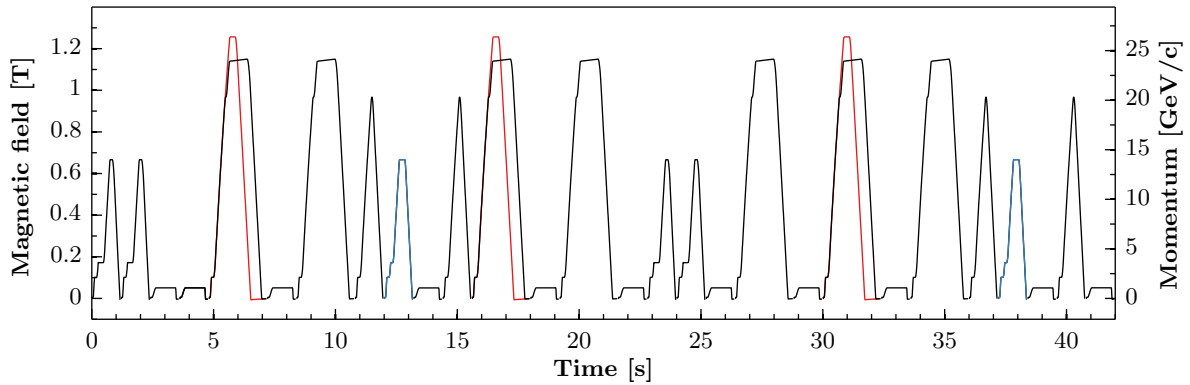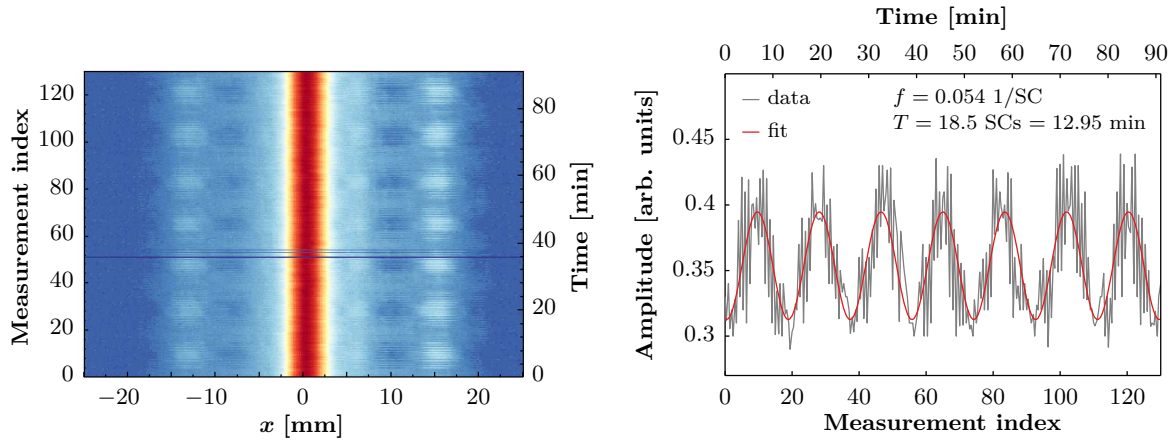

Figure 6.29. Measurement of the horizontal tune during the splitting process. The plot shows the residual signal after subtracting the average value. Noise appears to be the dominant contribution and no periodic modulation can be observed.

(a) Composition of the SC with two MTE cycles (blue).

(b) Waterfall plot of horizontal profiles measured with WS68.

(c) Intensity variation of the island at $x \approx 15$ mm based on the BWS measurements. The periodic oscillation is modulated by a high-frequency structure.

Figure 6.30. With two MTE cycles in the SC an additional high-frequency modulation of the splitting efficiency was observed. The measurement index corresponds again to the number of SCs.
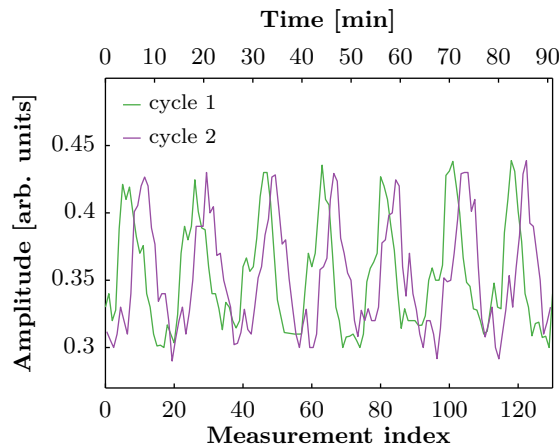
(a) Separate treatment of the measurements shown in Fig. 6.30 (c) for each cycle. A certain phase difference between two otherwise very similar signals is observed.

(b) A sinusoidal fit applied to the data of the first cycle leads to the same frequency as in Fig. 6.30 (c), where both cycles were treated together.

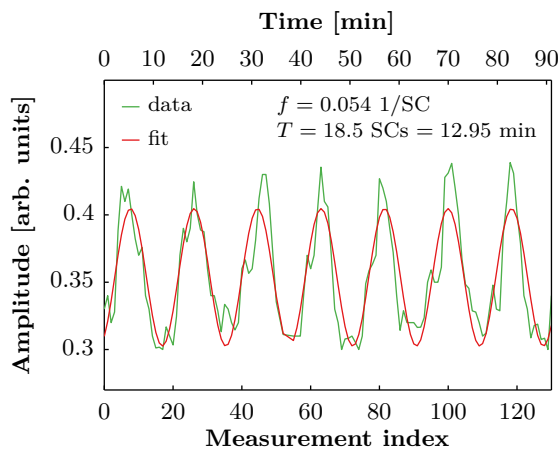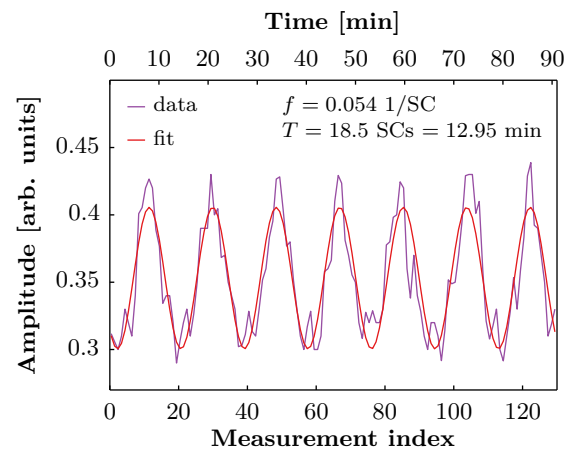**(c)** Based on the fits, the splitting efficiency oscillates at the same frequency for both cycles, but with a phase difference of 3.8 SCs.

Figure 6.31. Separate treatment of the data recorded on the two cycles shown in 6.30.
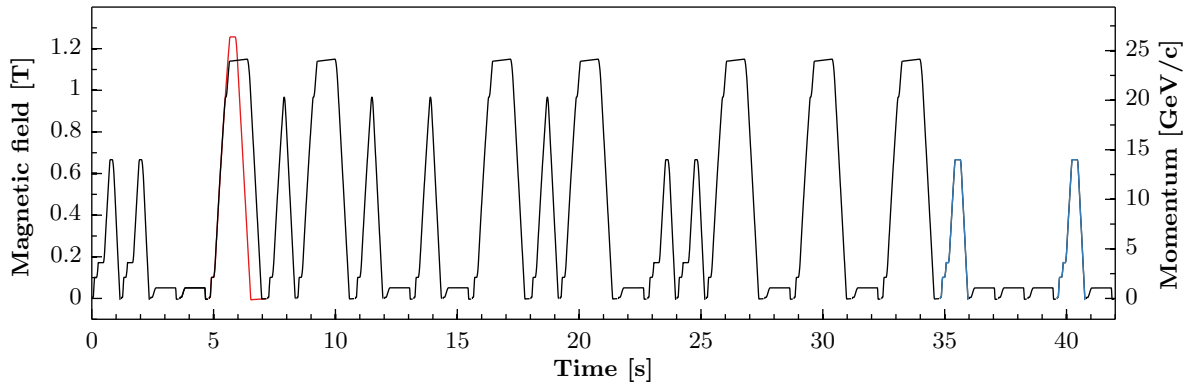
(a) Two MTE cycles (blue) were programmed at the end of the SC.
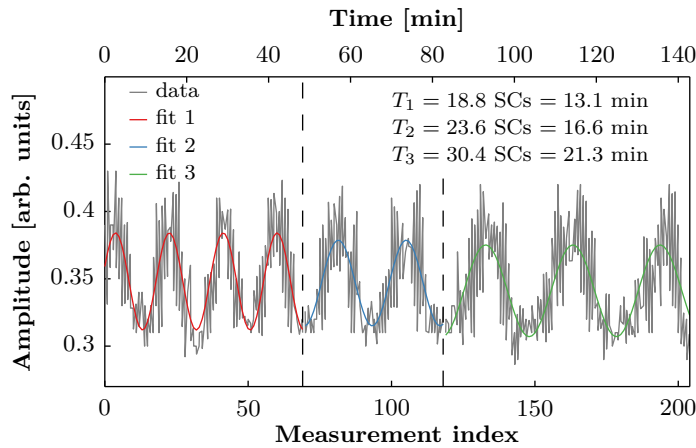
(b) The oscillation frequency changed during the measurements and a transient range is observed.

Figure 6.32. For this measurement, two MTE cycles separated by only four BPs were used. The superposition of the signals of the different cycles is again clearly visible. Furthermore, a drift of the oscillation frequency during the measurement can be deduced, even though the composition of the SC remained the same.

Even though the sequence of cycles in the SC was kept constant during the measurements, a clear change of the oscillation frequency can be deduced from the shown data. In this case the determined phase shift between the oscillations on the two different cycles corresponded to eight SCs, which exceeded by far the value expect based on the distance of the two cycles in the SC. These observations lead to the understanding that an effect, which is more complex than a pure variation of the dipolar or quadrupolar fields, impacts the quality of the splitting.

Stability of revolution frequency and RF voltage. Further investigations were conducted, and in Fig. 6.33 measurements of the revolution frequency and of the RF voltage are shown. The signals were treated in the same manner as the previously discussed measurement of the tune (see Fig 6.29) and no harmonic component could be observed.

(a) Waterfall plot of horizontal profiles measured with BWS68.

(b) An oscillation of the intensity inside the island at $x \approx 15$ mm with very short period was observed.

(c) Measurement of the revolution frequency.

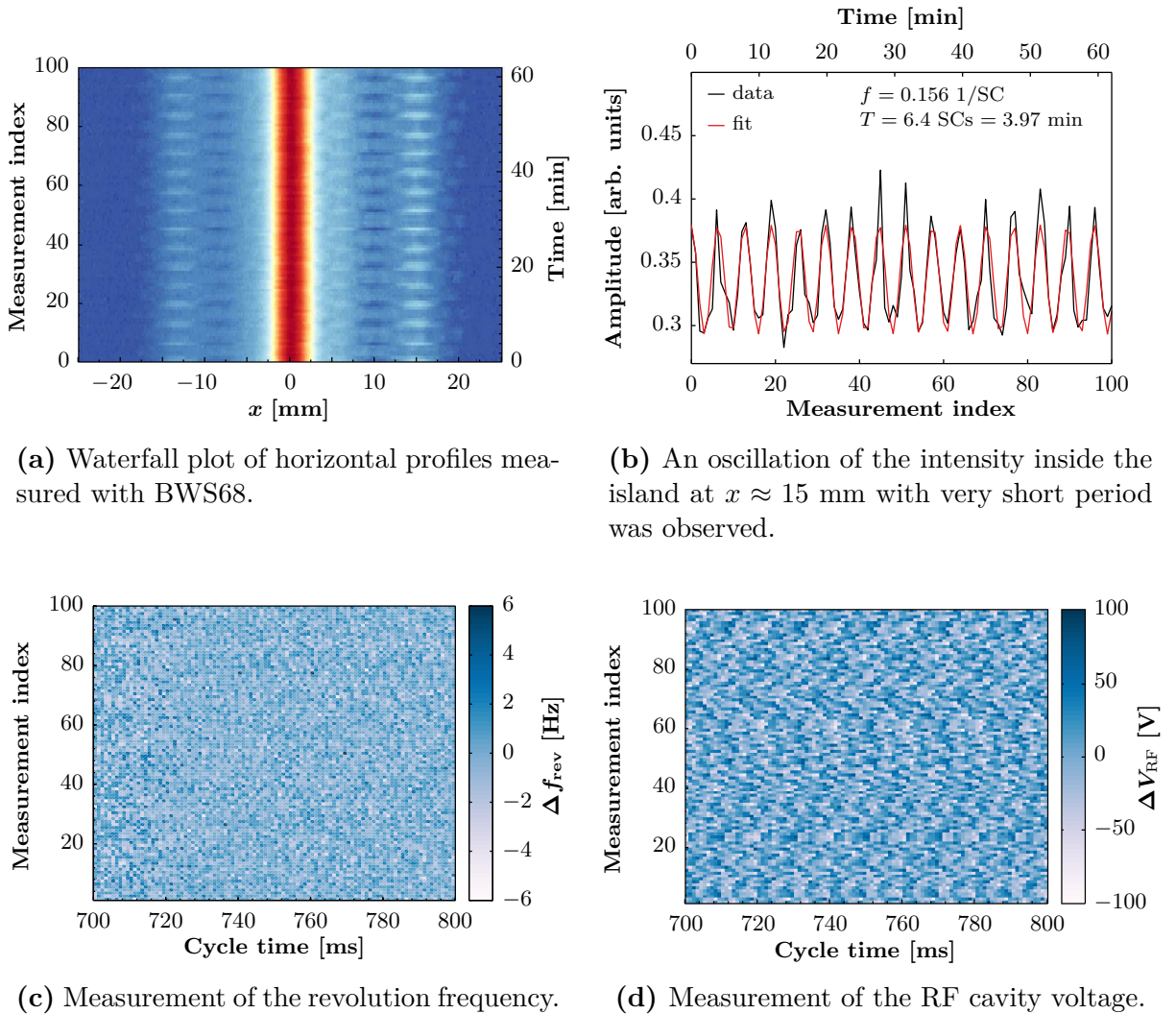

(d) Measurement of the RF cavity voltage.

Figure 6.33. For a SC with only 31 BP (corresponding to a length of 37.2 s), a significant increase of the oscillation frequency was observed. Measurements of the revolution frequency and of the cavity voltage, where the average values were subtracted, did not reveal any correlation.

Stability of the PCs of the PFW and the F8L. The currents of the PFW and the F8L were examined and the results are depicted in Fig. 6.34. On both wide circuits an oscillation was apparent; however, the frequency was not clearly correlated to the BWS signals of the islands. On the remaining circuits (DN, FN and F8L) only noise around the average value and no harmonic component was observed.

A significant impact of the wide windings of the PFW on the operation of the PS was already observed in 2007, after the installation of the new switching PCs [87]. The spill of the slow extraction of the EAST cycle was substantially degraded due to a current ripple on these circuits

(a) Measurement on the defocusing wide circuit.

(b) The cycle-by-cyle variation along 740 ms in (a) follows a periodic oscillation.

(c) Measurement on the focusing wide circuit.

(d) Similar to the DW, an oscillation is observed on the FW, but with different frequency.
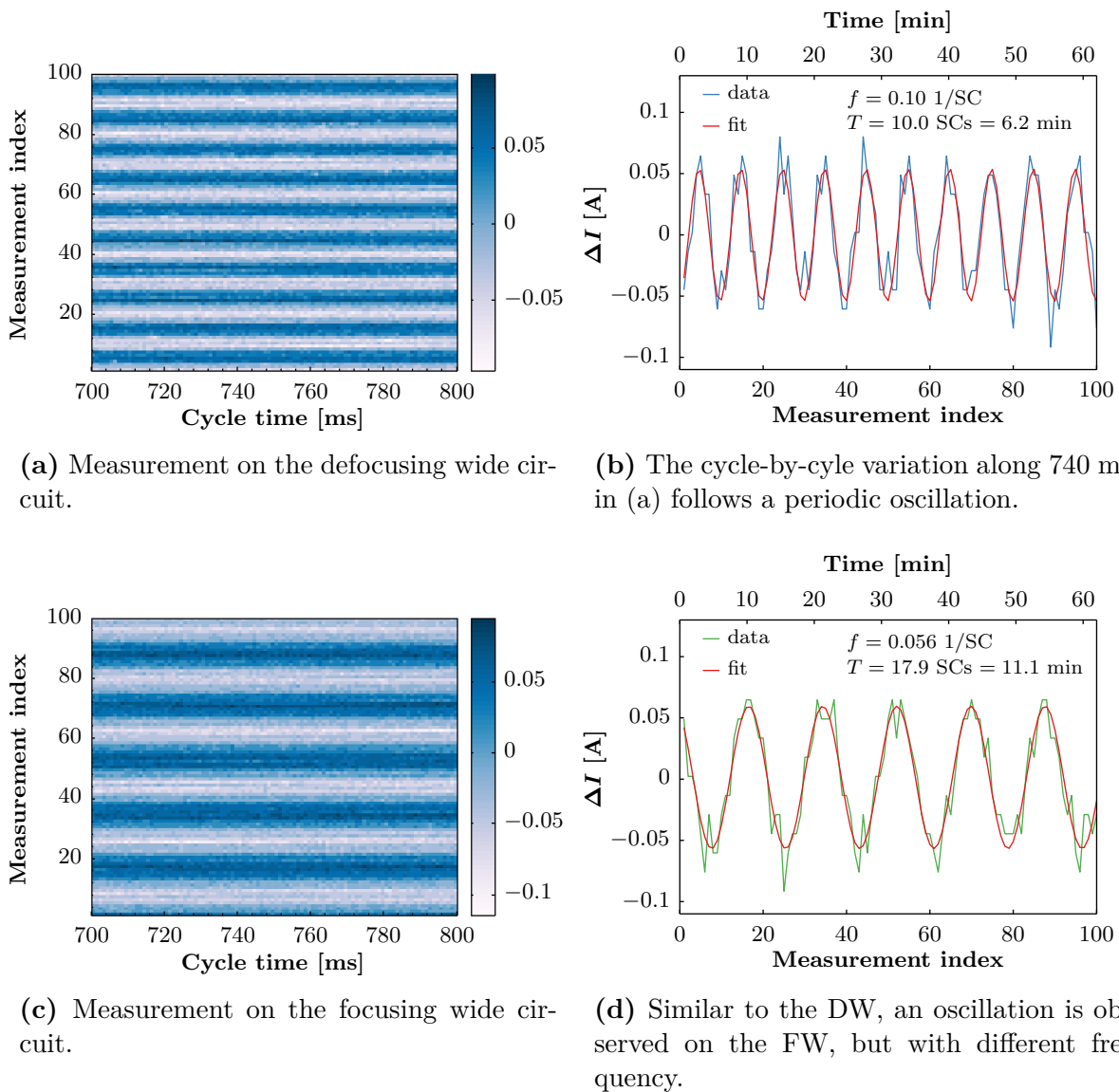
Figure 6.34. Current measurement of the wide circuits of the PFW. The average values were again subtracted and an oscillation of the current of both the DW and the FW is visible.

(see Fig. 6.35). To mitigate this effect additional inductances were installed to filter the high-frequency ripple [88].

In this framework, an interesting observation was made when measuring the transverse tunes on an argon ion cycle. Figure 6.36 shows such a measurement and, apart from the dominant horizontal and vertical tune lines, important sidebands are clearly visible. To determine the frequency f_{SB} of these sidebands, the revolution frequency f_{rev} and the distance to the main tune line ΔQ_{SB} have to be known:

$$f_{\mathrm{SB}} = \Delta Q_{\mathrm{SB}} \times f_{\mathrm{rev}}. \tag{6.13}$$

The analysis showed that ΔQ_{SB} corresponds to 5 kHz, which is equal to the switching frequency of the PCs of the PFW. The next step was to understand whether this observation could be explained by a disturbance of tune measurement system itself or if it was actually caused by a modulation of the magnetic field at 5 kHz. In the latter case, the effect would be directly transmitted to the beam.

To measure the magnetic field in the PS, PU coils are installed in the defocusing and the focusing half-units of MU101 outside the tunnel (see Fig. 6.37). The provided signals actually correspond to the time derivative of the magnetic field $\dot{B} = {}^{dB}\!/_{dt}$, and are used for longitudinal and transverse beam control as well as for the regulation of the power supplies [89]. In Fig. 6.38, measurements of the $\dot{B}$-signal on the argon cycle are depicted. An analysis of the frequency spectrum revealed an important component at 5 kHz and, therefore, it was concluded that this oscillation is indeed present on the magnetic field. More interestingly, the amplitude of the peak at 5 kHz varied over time and was observed to change at the same rate as the previously discussed amplitude of the sidebands of the measured tune.

The result of these magnetic measurements strengthened the suspicion of the effect being related
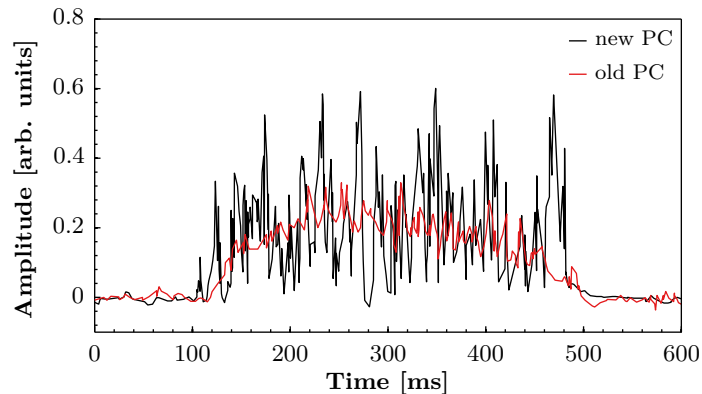

Figure 6.35. Spill of the slow extraction of the EAST cycle before and after the consolidation of the PCs of the PFW. The current ripple delivered by the new devices occasionally even led to zero extracted intensity.
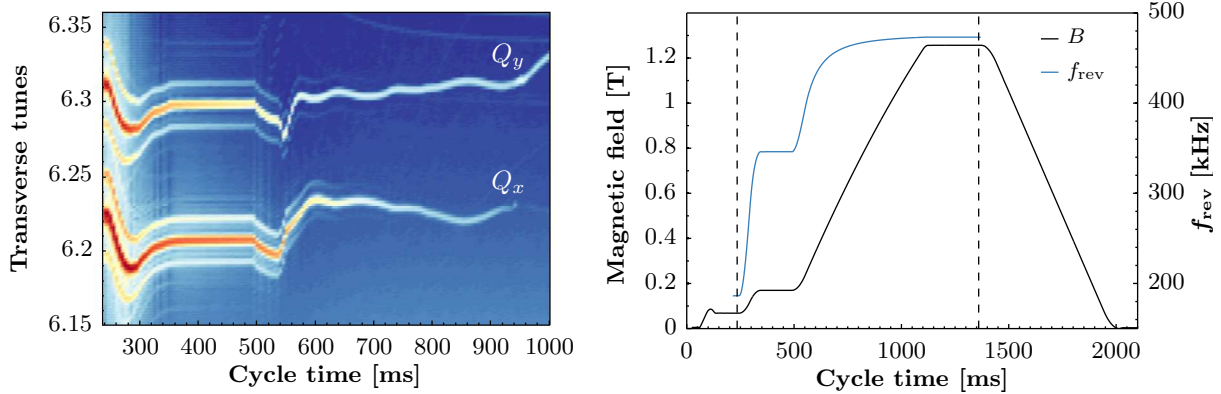
(a) Tune measurement along the ion cycle. The average value of 900 cycles is shown. Sidebands are visible in both planes.

(b) Measurement of the revolution frequency on the ion cycle. Injection and extraction are indicated by the dotted lines and occur at 235 ms and 1360 ms, respectively.
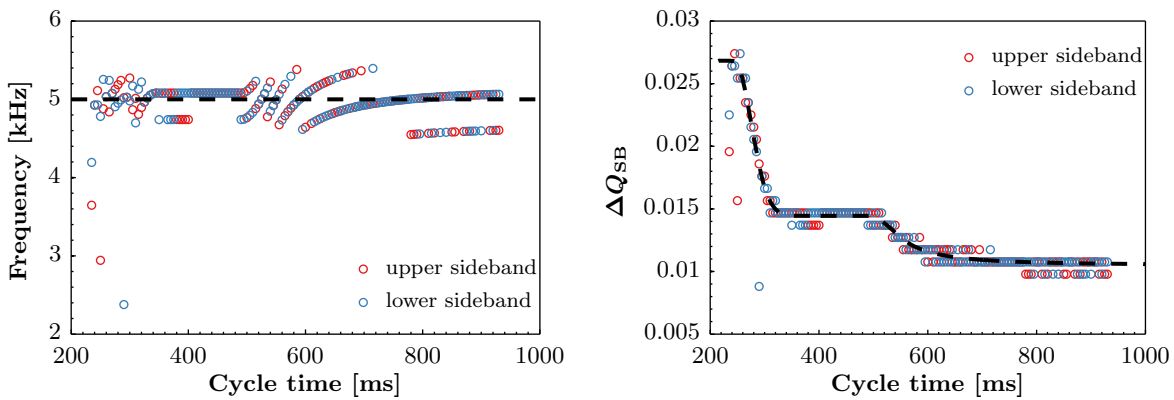
(c) The sidebands of the horizontal tune are clustered around $f_{SB} = 5$ kHz.

(d) The dashed line corresponds to the variation of the sideband frequency $f_{SB} = 5$ kHz along the cycle.

Figure 6.36. Horizontal and vertical tune measurement and determination of the sideband frequency on an argon ion cycle. The spacing between the sidebands and the main tune lines corresponds to the switching frequency of the PCs of the PFW.

(a) Installation of the coils inside the focusing half-unit of MU101. Their location is indicated by the red circle.
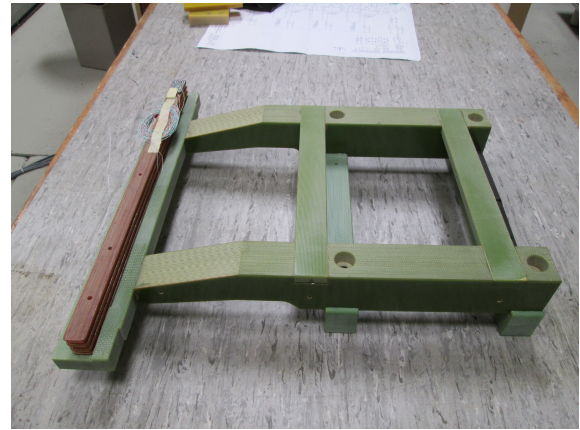
(b) Spare of the measurement coils (brown) mounted on the green support structure. Per half-unit, only one out of the three superimposed devices is operationally used.

Figure 6.37. PU coils used to measure the magnetic field in the PS. In each half-unit an assembly containing three coils and the appropriate support is installed [90].

to the PFW. Therefore, local measurements of the current, i.e. directly at the exit of the PC, were conducted, while the horizontal profiles were recorded with the repaired and hence again available BWS54 (see Fig. 6.39). A peak-to-peak current ripple of 120 mA at 5 kHz was observed on the DW and FW circuits, which corresponds to 2‰ of the operational value and is clearly exceeding the specification of ~100 parts per million (ppm) [91]. Furthermore, the oscillation of the intensity of the outermost island obtained with BWS54 was compared to the variation of the amplitude of the spectral line at 5 kHz measured on the PFW and on the magnetic field, and very good agreement of the different spectra could be concluded.

All the observations presented in this section led to the understanding that the wide circuits of the PFW were at the origin of the intensity modulation of the islands. Furthermore, it was understood that different clocks, which are not synchronized with each other, are used to control the switching of the PCs. Any minor difference in phase and frequency between the clocks will, therefore, inevitably be transmitted to the current at the output of the PC. Due to their proximity inside the main units, the different circuits are magnetically coupled and the interference of the signals results in the the variation of the magnetic field at 5 kHz. At the moment, no solution to this problem can be implemented, as the current PC hardware does not allow a synchronization of these clocks. However, an extensive measurement campaign, conducted by members of the Electrical Power Converters (EPC) Group, revealed a cabling error of the wide circuits, which enhanced the current ripple on these two elements. In Fig. 6.40, sketches of the respective cabling schemes are depicted. Actually, each wide winding consists of two individual
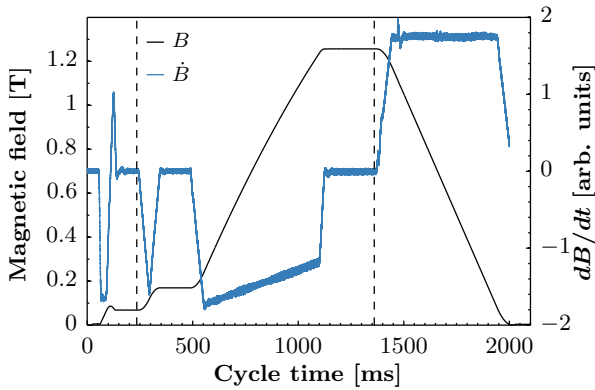
(a) Measurement of the time derivative of the magnetic field $\dot{B}$ with sampling frequency $f_s = 20$ kHz. Displayed is the sum of the D and F coils.
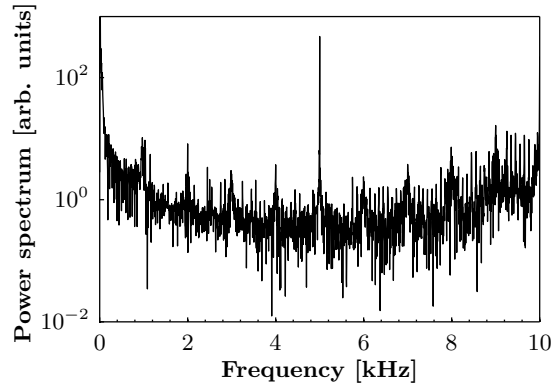
(b) The FFT of $\dot{B}$ reveals an important peak at 5 kHz.
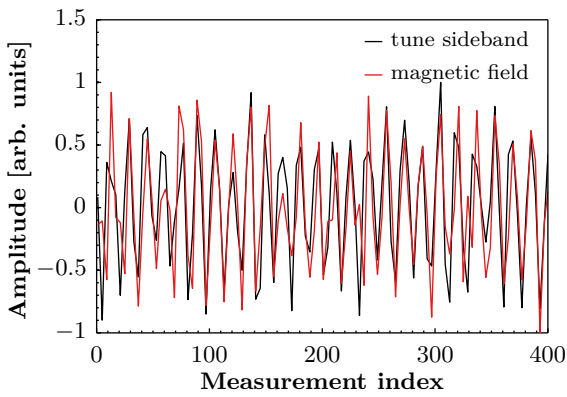
(c) The amplitude of the peak at 5 kHz shown in (b) oscillates in the same way as the amplitude of the sideband of the horizontal tune discussed in Fig. 6.36.
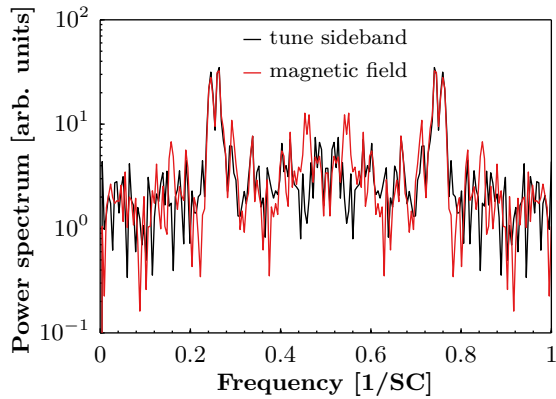
(d) Frequency analysis of the signals shown in (c). The agreement between the oscillation frequencies of the different measurements is evident.

Figure 6.38. Magnetic measurement on the argon cycle and correlation of the signals with the tune measurement.

(a) Measurement of the current of the FW circuit, conducted directly at the exit of the PC ($f_s = 20$ kHz).

(b) An important ripple at 5 kHz on the current of the FW circuit is apparent.

(c) Waterfall plot of horizontal profiles measured with BWS54.

(d) Correlation between the fluctuations observed with the BWS and the amplitude variations of the spectral lines at 5 kHz observed on the magnetic field and on the DW and FW circuits. An FFT of those three signals reveals important peaks at the same frequencies.

Figure 6.39. Comparison between the oscillation of the splitting efficiency, the amplitude variation of the 5 kHz component of the current of the wide circuits of the PFW, and the magnetic field. Very good agreement was found.

(a) Incorrect cabling of the wide circuits.   **(b)** Correct cabling of the wide circuits.
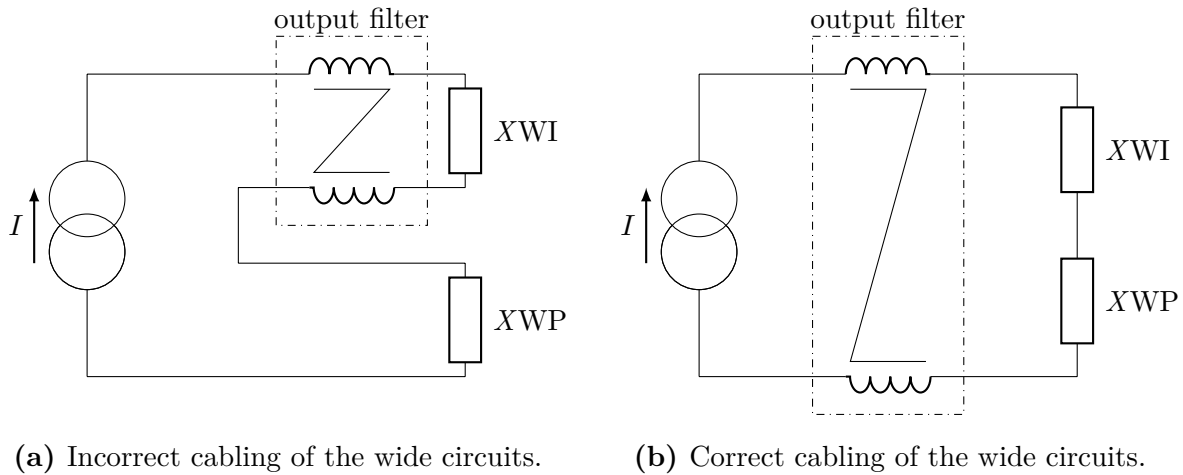
Figure 6.40. Cabling scheme of the wide circuits of the PFW before and after the intervention of EPC. *X* signifies either D or F, depending on the half-unit the winding is situated in. The output filters were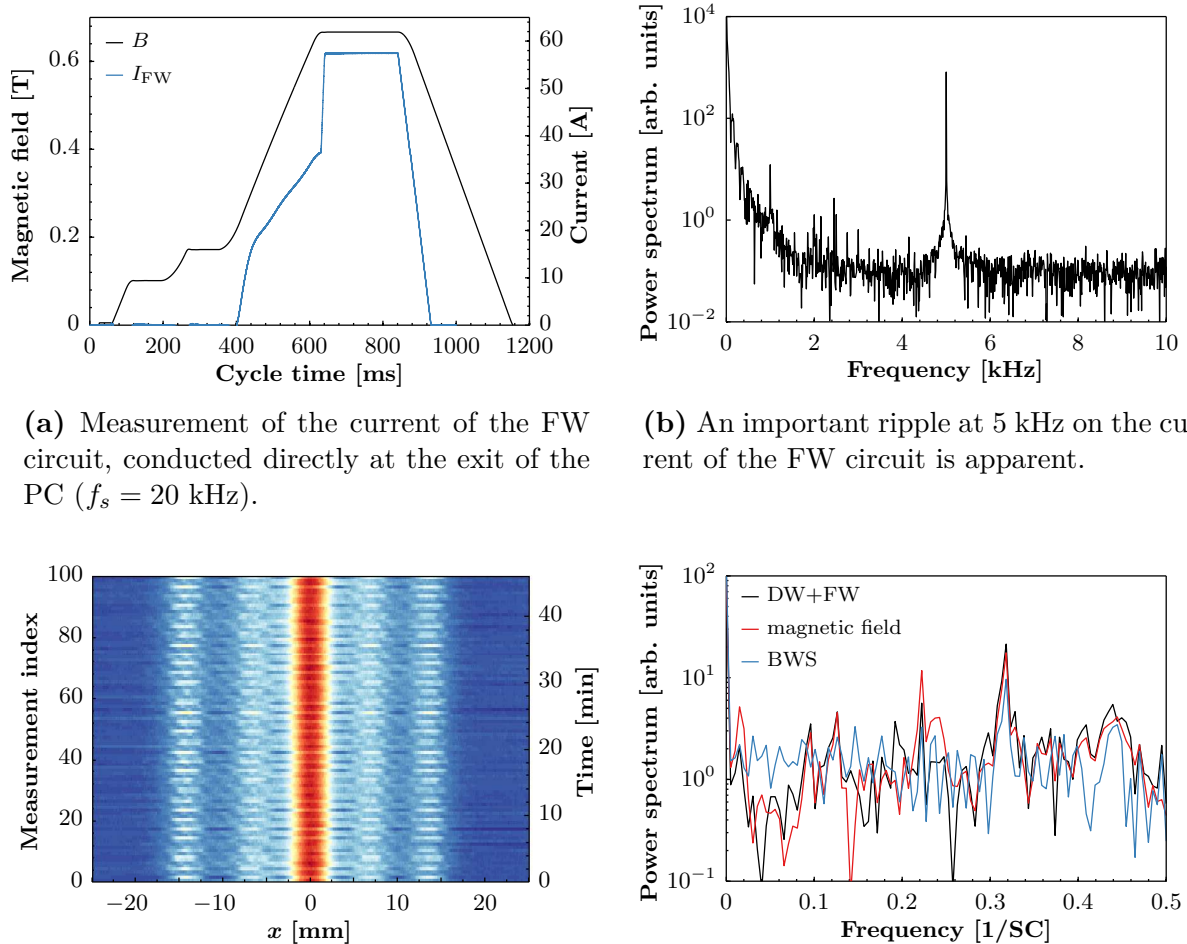 initially installed to reduce the current ripple, which was significantly affecting the slow extraction (see Fig. 6.35).

circuits, which are powered in series. These are denominated as *X*WI and *X*WP, with *X* referring to either the defocusing or the focusing half-unit, and I and P corresponding to *impair* and *pair*[1]. More detailed information about the properties of the PCs can be found in [87].

To conclude, Figs. 6.41 and 6.42 depict measurements before and after the intervention where the cabling issue was resolved. Consequently, tremendous improvement both on the stability
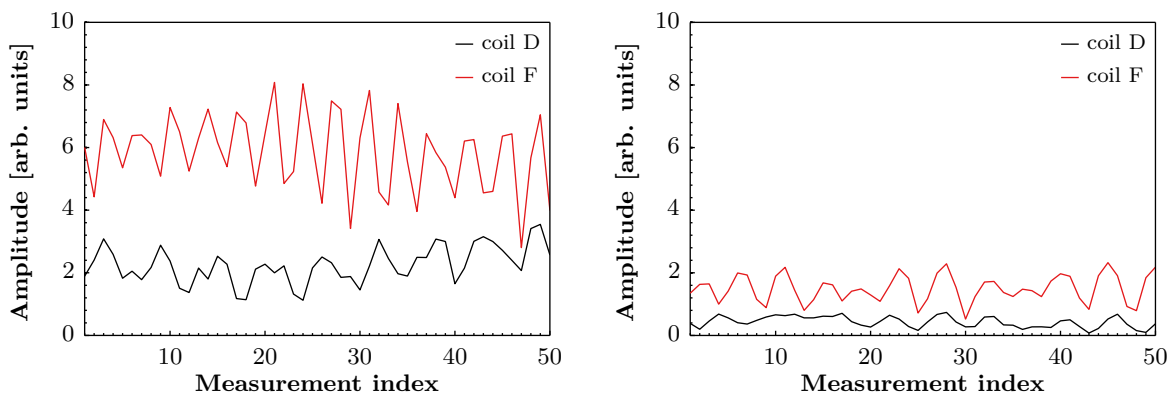
(a) Variation of the amplitude of the 5 kHz line before the intervention.

(b) After the intervention the component at 5 kHz was reduced by about a factor four.

Figure 6.41. Comparative measurement with the magnetic coils in MU101 before and after the intervention.

---

[1]   The French expressions for odd and even.
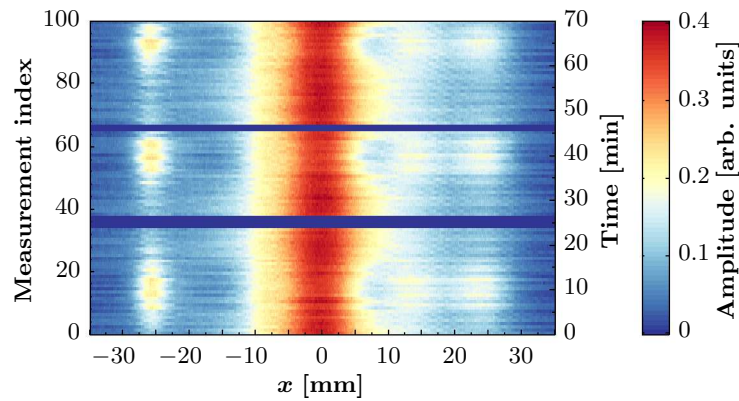
(a) Measurements before the intervention, which depict obvious intensity oscillations.
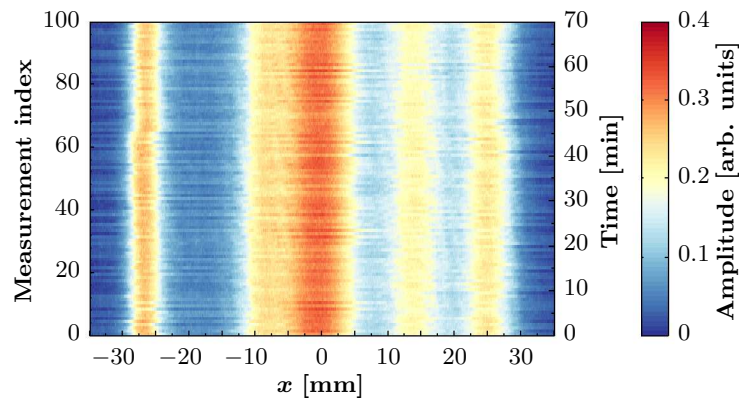
(b) Proper splitting efficiency was established after reducing the ripple at 5 kHz.

Figure 6.42. Measurements with BWS54 conducted after the intervention of EPC. Significant improvement of the stability of the transverse splitting is evident.

of the magnetic field and of the horizontal profiles was observed, which allowed to continue the commissioning of the extraction process itself as set forth in Section 6.2.2. Prior to this, benchmarking of PTC and PyORBIT simulation studies with experimental data is presented in the following section, which validated the application of the existing tools. Subsequently, simulations with these codes allowed to understand the effect of the current ripple on the dynamics of the splitting process (see Section 6.2.1.3).

6.2.1.2 Benchmarking of simulation codes

The establishment of reproducible conditions for the horizontal splitting was an important milestone to continue the experimental studies with the MTE beam. Furthermore, it allowed to benchmark the results of PTC simulations with measurements conducted with the BWSs. This was essential, as the overall complexity of MTE requires an accurate and predictive model of the accelerator to further advance the understanding of this complex technique and, in particular, to understand the observations analysed in the previous section.

Figure 6.43 depicts the evolution of the horizontal profiles during the splitting process, which is composed of seventy different measurements. For this specific setup of the non-linear elements (see Fig. 6.44), the principal population and separation of the islands occurs within 30 ms after crossing the resonance. Towards the end of the cycle, the rotation of the islands in the phase space, which is required to properly position the beamlets in the extraction region, is obvious. During the entire splitting process, the locations of the five SFPs obtained by simulations are indicated by the coloured markers on top of the measurement results. Only minor discrepancies between measurements and simulations can be observed at the start of the rotation, i.e. around a time of 810 ms: this is due to the fact that the measurement of the MTE beam with a BWS at this moment of the cycle actually takes about 5 ms and, accordingly, a time stamp of 810 ms
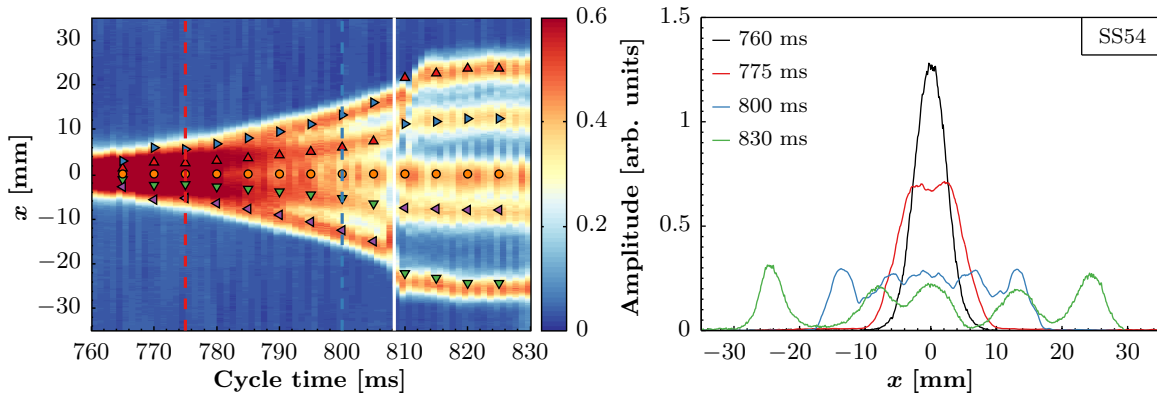
(a) Every millisecond, a measurement was performed and the formation of the islands is clearly visible. Comparison with simulations, where the circle represents the core and the triangles the islands, reveals very good agreement.

(b) Initial and final horizontal profiles, as well as intermediate measurements at timings indicated by the dashed lines in (a).

Figure 6.43. Benchmarking of the position of the fixed points obtained via PTC simulations with measurements conducted with BWS54. The evolution of the transverse splitting along the cycle is shown. In this case, the resonance was crossed at 760 ms and the rotation of the phase space started around 808 ms (white solid line in (a)).
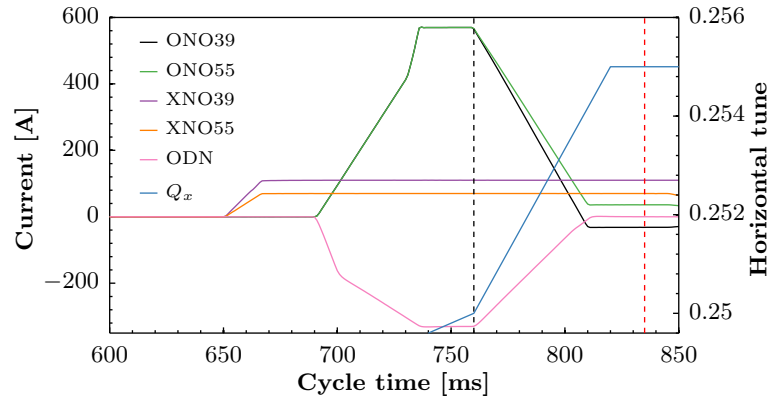
Figure 6.44. Configuration of the dedicated non-linear elements and the horizontal tune on the flat top used for the measurements depicted in Fig. 6.43. The resonance is crossed at 760 ms, which is different from the settings shown in Fig. 6.10.

corresponds to a time frame of 810 ± 2.5 ms.

Even though the measurements were not performed with statistical significance, as every wire scan could only be carried out once within the available time frame of one hour, the smooth evolution of the data presented in Fig. 6.43 indicates an extremely reproducible splitting process. The agreement between measurements and simulation results validated the ability of the model to forecast the positions of the islands.

The capabilities of PyORBIT were exploited to perform simulations of the full splitting process from resonance crossing until beam extraction. At CERN and elsewhere, this code is normally applied to investigate space charge effects; however, the simulations presented in the following clearly motivate its utility for single particle studies as well.

With the availability of this code, simulation studies taking into account the full 6D dynamics of the MTE process were conducted for the first time. As presented in Section 6.3.1, the longitudinal dynamics play an important role. This was previously experimentally studied, and the splitting efficiency η_{MTE} was reported to decrease with increasing RF voltage [92]. Therefore, the minimum possible RF voltage is applied during the splitting process (see Fig. 6.11), which reduces the energy spread of the bunches and, thereby, decreases the coupling to the horizontal plane via the chromaticity and the dispersion.

Figure 6.45 depicts the PyORBIT simulation results likewise to the measurements shown in Fig. 6.43. For this and all following PyORBIT simulations presented in this thesis, tracking of 20000 particles was determined as acceptable trade-off between computing time and sufficient particle density for the evaluation of the results. As PTC is the underlying tracking code, the evolution of the positions of the SFPs is in agreement with the experimental data. However, this is not the case for the intensity sharing among the beamlets. The splitting efficiency was found to be as low as 14.6%, which corresponds to experimental results without active transverse intra-bunch damper. During operation, the horizontal excitation provided by this element is crucial
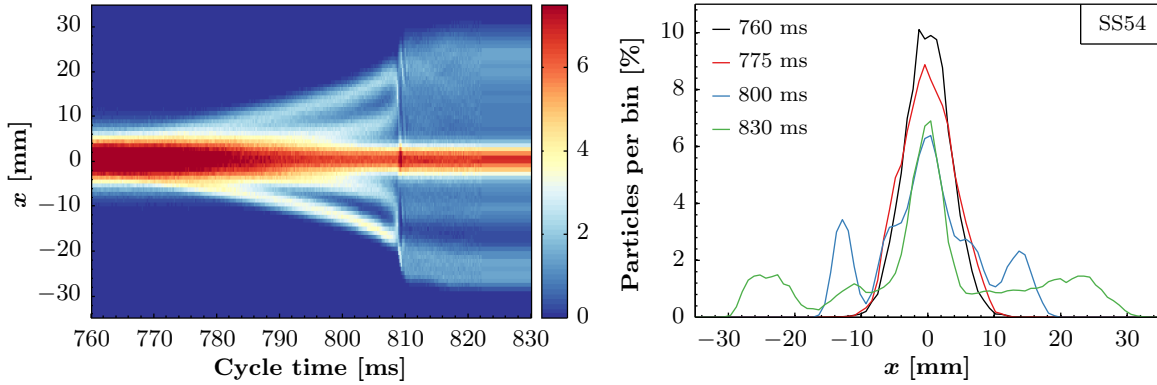
(a) Time evolution of the horizontal splitting. As a result of the projection, the islands seem to have vanished after the rotation (see also Fig. 6.46 (d)).

(b) The core of the distribution is more importantly populated compared to experimental results.

Figure 6.45. PyORBIT simulations of the full horizontal splitting process at the location of BWS54. Apart from the different population of the beamlets, the results are in very good agreement with the experimental ones shown in Fig. 6.43.

(a) 760 ms.

(b) 775 ms.

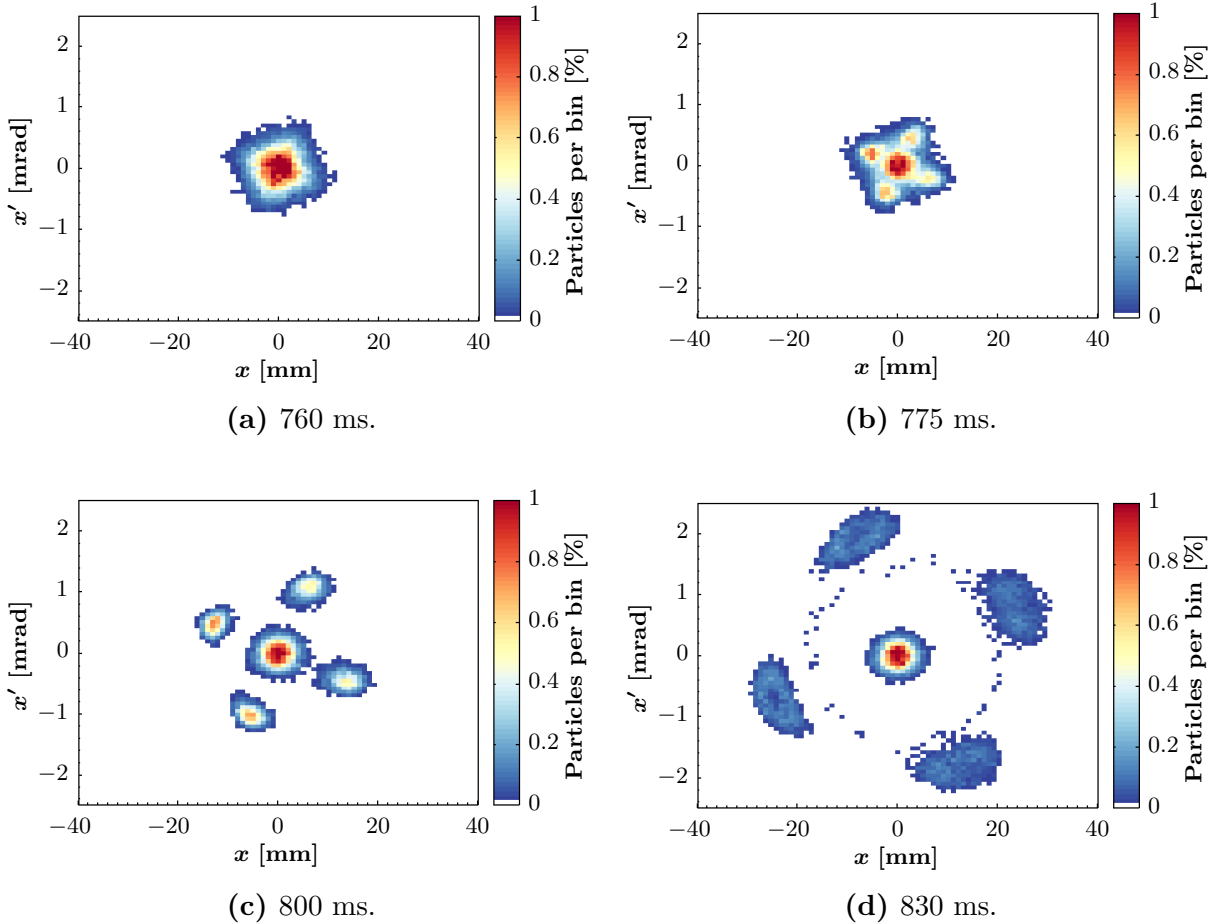**(c)** 800 ms.

(d) 830 ms.

Figure 6.46. Portraits of the horizontal phase space in SS54 during the splitting process. The rotation towards the end of the cycle is clearly non-adiabatic, causing significant emittance blow-up of the islands.

to achieving equal population of the beamlets. Such a device is currently being implemented into PTC.

The simulated horizontal phase space at several instants of time is displayed in Fig. 6.46. At resonance crossing, no islands are present and the distribution adopts the characteristic square shape. Subsequently, the beam is split and rotated before extraction. Already in Figs. 6.43 and 6.45 it became obvious that this rotation occurs very fast, i.e. within less than 5 ms. Based on the time-dependent simulation results, this process was identified to be extremely non-adiabatic, causing filamentation and hence emittance blow-up for the beam captured in the islands. In addition, a small fraction of particles is lost from the islands and remains trapped between the beamlets. At extraction, these particles will then be intercepted by the septum blade, contributing to the extraction losses. These results triggered the development of a new non-linear optics scheme to improve the rotation by significantly slowing it down and changing the optics functions around the SFPs of the islands (see Section 6.2.3).

The enormous benefit of the MTE scheme over the CT extraction becomes even more evident by looking at Fig. 6.46c. In contrast to the mechanic splitting applied for CT, which contributes extensively to the radioactive activation of a large fraction of the PS ring, the purely magnetic transverse splitting occurs fully loss-less, if performed adiabatically. Only during the rise time of the fast extraction kickers losses are created, but at a defined and well-shielded location (see also Sections 6.1.2.4 and 6.2.4).

6.2.1.3 Simulation-based explanation of the oscillation phenomenon

Time-dependent simulation studies The possibility of conducting simulations with time-varying magnet strengths with PyORBIT enables the exploration of the extremely wide MTE parameter space. However, due to the complexity of the PS lattice, this comes at the expense of significant computing time. Using the available 48 core machines to simulate the whole time span from resonance crossing to extraction, which corresponds to approximately 60000 turns, one week of computing time is required. Consequently, the most relevant studies to investigate the dynamics of the MTE process had to be wisely determined, in order to permit an efficient analysis of the problem at hand.

Based on various past simulation studies and, more importantly, on operational experience with the MTE technique, the sensitivity of the process to variations of the horizontal tune is well-known. This becomes also apparent in Figs. 6.43 and 6.44, where a variation of $\Delta Q_x = 5 \times 10^{-3}$ leads to a separation between the core and the islands of about 25 mm. As a rule of thumb, i.e. not considering the dedicated multipoles, a tune change of 1×10^{-3} leads to an increase of the islands' distance from the origin by 5 mm. Therefore, any significant modulation of the horizontal tune could influence the splitting process. Experimentally, this was investigated and ruled out as possible explanation of the oscillation phenomenon, as no periodic modulation of

the tune could be observed (see Fig. 6.29). However, it also has to be considered that a precise tune measurement usually requires to measure the beam centroid position during at least 1024 turns, which corresponds to a measurement time of more than 2 ms at 14 GeV/c in the PS. Accordingly, a modulation of the tune at the switching frequency of the PCs of 5 kHz occurs multiple times during the measurement window, and the concept of considering the tune a static quantity is actually no longer valid.

In order to evaluate the effect of the measured current ripple on the horizontal tune, the working point matrix M_{PFW} was used in the following way (see also Chapter 3):

$$M_{\mathrm{PFW}} \begin{pmatrix} \Delta I_{\mathrm{FN}} \\ \Delta I_{\mathrm{FW}} \\ \Delta I_{\mathrm{DN}} \\ \Delta I_{\mathrm{DW}} \end{pmatrix} = \begin{pmatrix} \Delta Q_x \\ \Delta Q_y \\ \Delta \xi_x \\ \Delta \xi_y \end{pmatrix}, \tag{6.14}$$

where the currents of the various PFW circuits ΔI_{i} are the input parameters. The measured ripple amplitude of 60 mA on the FW and DW circuits results in the following changes to the parameters:

$$M_{\mathrm{PFW}} \begin{pmatrix} 0 \\ 0.06 \\ 0 \\ 0 \end{pmatrix} = \begin{pmatrix} 2.85 \\ -1.88 \\ -11.4 \\ 5.46 \end{pmatrix} \times 10^{-4}$$

$$M_{\mathrm{PFW}} \begin{pmatrix} 0 \\ 0 \\ 0 \\ 0.06 \end{pmatrix} = \begin{pmatrix} -1.63 \\ 2.44 \\ -14.6 \\ 16.8 \end{pmatrix} \times 10^{-4}. \tag{6.15}$$

These values appear to be rather small; however, the various contributions might add up depending on the relative frequency and phase between the different clocks of the two PCs. Therefore, realistic assumptions of the maximum tune-shift caused by the current ripple are in the order of $\Delta Q_x \approx 5 \times 10^{-4}$ and $\Delta Q_y \approx -4 \times 10^{-4}$, which would translate into a non-negligible 2.5 mm movement of the islands.

As next step, the effect of such a tune ripple on the horizontal splitting process was investigated in detail by modulating the currents of the LEQ in time-dependent simulations. In practice, these circuits are not subject to a ripple at 5 kHz due to the different PC technology [93]; however, the ripple was distributed to these elements as they create a pure quadrupolar effect. The

amplitude of this modulation was determined with the respective tune transfer matrix:

$$M_{\text{LEQ}}^{-1} \begin{pmatrix} \Delta Q_x \\ \Delta Q_y \end{pmatrix} = \begin{pmatrix} \Delta I_{\text{F}} \\ \Delta I_{\text{D}} \end{pmatrix} \tag{6.16}$$

$$M_{\text{LEQ}}^{-1} \begin{pmatrix} 5 \\ -4 \end{pmatrix} \times 10^{-4} = \begin{pmatrix} 9.8 \\ -4.5 \end{pmatrix} \times 10^{-2}. \tag{6.17}$$

In relative terms, these values correspond to ripple amplitudes $\Delta I_{\text{F,D}}/I_{\text{F,D}}$ of 8.5% and -4.5%, respectively, based on the currents at resonance crossing ($I_{\text{F}} = 1.16$ A, $I_{\text{D}} = 1.00$ A). For the sake of simplicity, the relative modulation amplitude found for the focusing circuit was also applied to the defocusing one in all simulations shown in the following and any relative ripple amplitude quoted in the text refers to the value of I_{F}. This is justified by the fact that the horizontal dynamics is of fundamental importance to the MTE process. The vertical motion is less critical, as the non-linear coupling between the transverse planes is minimized using the ODN. All additional settings were kept unchanged with respect to those used for the simulations depicted in 6.46. The modulation of the currents at 5 kHz along the cycle is shown in Fig. 6.47. In Fig. 6.48, the effect of a 5 kHz tune ripple at various amplitudes on the horizontal distribution is depicted. The orientation of the shown phase spaces is different with respect to Fig. 6.46, as the simulation data was recorded at the beginning of the simulated lattice, i.e. in SS01. The advantage is twofold: first, the rotation is such that the islands are positioned upright and, secondly, the horizontal β-function in this section is large, leading to an increased separation between the islands and the core. This allowed to improve the determination of the splitting efficiency, which was done in the following way: particles inside the red boundary shown in
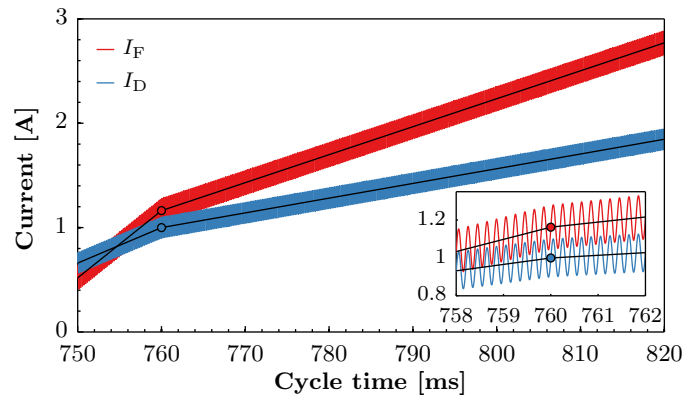

Figure 6.47. 5 kHz modulation applied to the LEQ circuits. The solid black lines correspond to the unperturbed currents and the coloured lines represent a ripple with an amplitude of 10% of the value at resonance crossing (indicated by the markers). To better visualize the oscillations, a zoom around 760 ms is shown in the bottom right corner.

Fig. 6.48 (a) were considered core particles and the remaining ones were assigned to the islands. The red lines were drawn at $\pm 3.5\,\sigma_{\text{core}}$ in x and x', based on the core size obtained in the simulations without tune ripple. This definition was applied to compare the different results presented in Figs. 6.48, 6.49 and 6.53.

These simulation results clearly confirm what was expected based on experimental data: a tune ripple, if occurring at sufficiently large amplitude, is capable of preventing a proper splitting
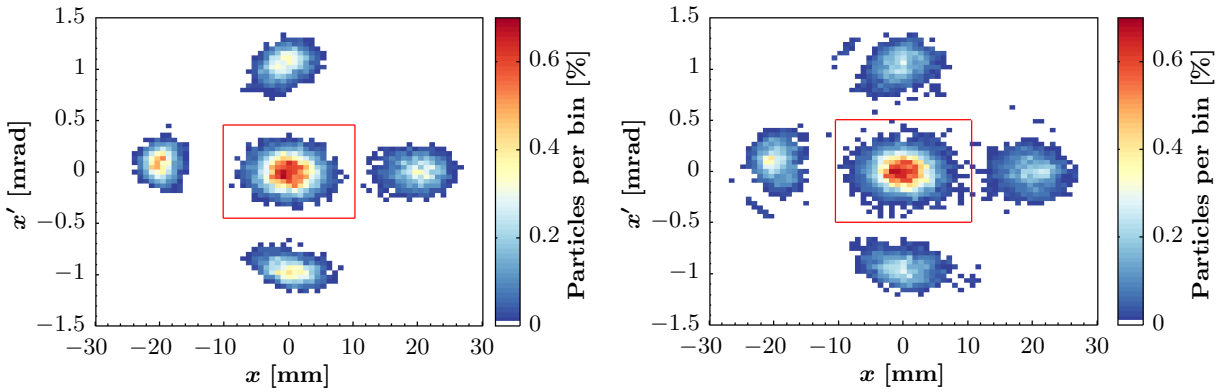
(a) The red boundary ($\pm 3.5\,\sigma_{\text{core}}$ in x and x') was chosen to contain the core particles. In the absence of any tune ripple, 42.3% of the particles remain in this region.

(b) For a ripple amplitude of 5%, the core population is slightly increased and reaches 44.4%.
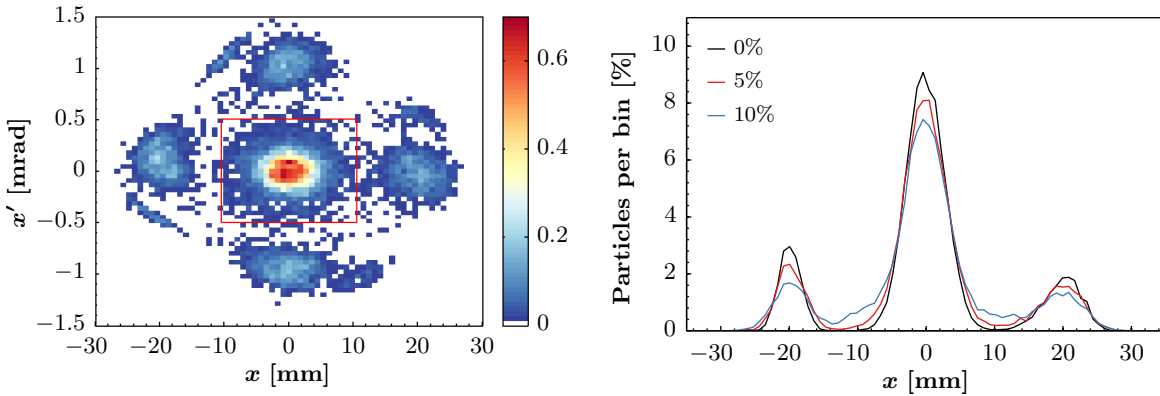
(c) At an even higher ripple amplitude of 10%, which is the same order of magnitude as calculated in Eq. (6.16), the core is populated with 47.2% of the particles and the island formation is further suppressed.

(d) Comparison of the horizontal projections of the distributions shown in (a) - (c).

Figure 6.48. Horizontal phase space portraits in SS01 for different ripple amplitudes at 5 kHz. The snapshots correspond to a cycle time of 800 ms. In agreement with experimental data, the splitting process is found to be severely affected by a tune ripple.

process. Following this conclusion, Fig. 6.49 depicts the dependency of the trapping efficiencies η_{MTE} and η_{core} on the amplitude and frequency of the ripple. At 5 kHz, the aforementioned increase of the core population for an increased ripple amplitude is visible. One should also remember that the measured spectrum of the $\dot{B}$ did not contain an important component at 2.5 kHz (see Fig. 6.38) and that, after mitigating the 5 kHz issue, proper splitting efficiency was re-established (see Fig. 6.42). Interestingly, this phenomenon is no longer observed if the ripple occurs at 10 kHz. On the other hand, the depopulation of the islands appears to be even more considerable for ripple frequencies of 2.5 kHz. This is insofar disturbing, as 2.5 kHz corresponds to the switching frequency of the PC of the F8L. However, in contrast to the various PFW circuits, only a single PC is required for the F8L. Therefore, the problem of synchronizing the different clocks does not apply and any current ripple on the F8L circuit permanently affects the splitting process in the same way as it is constant in time.

In the case of conventional beam production, where the linear motion is of principal importance, the betatronic frequencies of the particles are considerably higher than several kHz. Considering, however, the betatronic motion around the SFPs in the islands, the situation changes as the oscillation frequencies slow down significantly. Investigations were conducted to determine these so-called secondary frequencies and it was observed that particles close to the islands' centre indeed oscillate at frequencies in the low-kHz regime. The corresponding simulations and analysis are presented on the following pages.
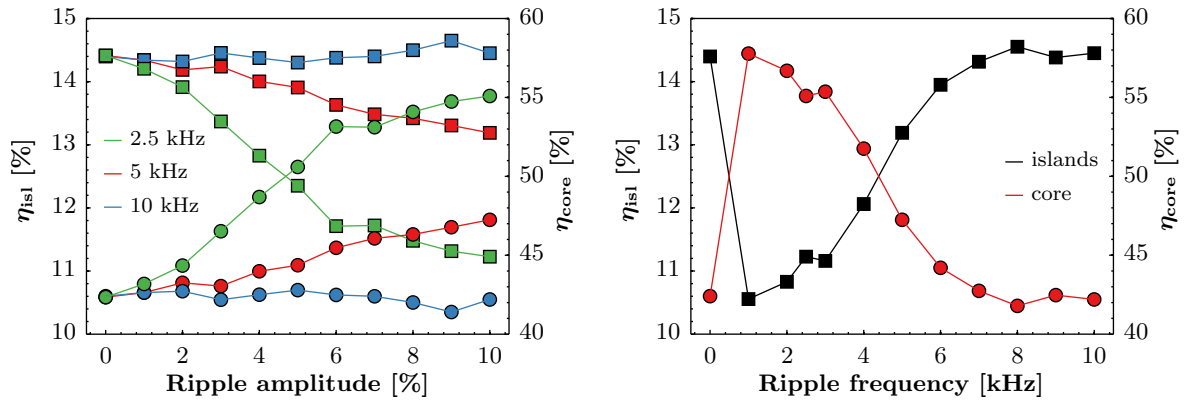
(a) At 5 kHz and large amplitudes, significantly less beam is captured in the islands, resulting in an important population of the core. Proper splitting efficiency is re-established at 10 kHz, while a ripple frequency of 2.5 kHz is even more destructive.

(b) The trapping process is severely affected by a low-frequency tune ripple. These results were obtained for a ripple amplitude of 10%.

Figure 6.49. Dependency of the splitting efficiencies for the islands (squares) and the core (circles) on the amplitude and the frequency of the ripple.

Static simulation studies to evaluate the secondary frequencies The secondary frequencies of particles in the islands were determined by performing static simulation studies with PTC. At several instants during the splitting process, the locations of the stable and unstable fixed points in the horizontal plane were identified based on particle tracking. The phase space of the islands was then probed by tracking of 20 particles for more than 10000 turns, which was required to provide sufficient resolution for a subsequent frequency analysis. The initial conditions for those particles were determined by spacing the distance between the SFP and the UFP into equal parts. Figure 6.50 illustrates the definition of these initial conditions and shows the increase of the surface of the islands during the MTE process.

To evaluate the secondary frequencies, a stroboscopic analysis is applied to the motion of particles: in case of the fourth order resonance under study, only particle coordinates of every fourth turn are considered. Thereby, the fact that particles move from one island to the next on consecutive turns is suppressed, which allows to study the motion within a single island. This analysis was applied to simulation results performed at five different timings along the cycle, as mentioned and shown in Fig. 6.50 (b). In Fig. 6.51, an example of this type of analysis for two particles is depicted. Close to the SFP, the motion is almost harmonic, which is no longer the case for a particle moving at the border of the island. The motion slows down significantly and almost adopts the shape of a square wave. Hence, a frequency analysis reveals a multitude of peaks for a particle at this amplitude.

The main oscillation frequency of a particle close to the SFP is found to be around 2.5 kHz and the spectrum also contains several higher harmonics. In Fig. 6.52, the frequency analysis for all 20 particles at the various timings is depicted. The resulting amplitude-dependent secondary frequency is shown, where the invariant of motion ε_0 for each particle, i.e. its single particle emittance in the horizontal phase space, was determined as measure of the particle amplitude. This was done by numerically computing the surface enclosed by its trajectory applying the Shoelace formula [94]

$$\varepsilon_0 = \frac{1}{2}\left|\sum_{i=1}^{n-1}\chi_i\chi'_{i+1} + \chi_n\chi'_1 - \sum_{i=1}^{n-1}\chi_{i+1}\chi'_i - \chi_1\chi'_n\right|, \tag{6.18}$$

where χ_i and χ'_i represent the coordinates of the horizontal phase space centred at the SFPs of the islands.

The outcome of this investigation is fully in line with the previously presented findings based on the PyORBIT simulations. Shortly after resonance crossing, the islands are very close to the central SFP and the secondary frequencies of the particles are found to be extremely small, as the most significant peaks returned by the analysis only cover the region up to 500 Hz. With increasing surface and separation of the islands, also the frequencies increase towards larger values. At the end of the splitting process, particles close to the centre of the islands oscillate at 2.5 kHz, but especially also the second harmonic at a frequency of 5 kHz importantly contributes

to the spectrum. So far, only on-momentum particles have been considered. By including particles with non-zero δ, the situation is further modified, as the spectrum represented by the beam broadens.

All these observations lead to the conclusion that the depopulation of the islands in the presence of a low-frequency tune ripple occurs due to an overlap of the external excitation frequency with the natural frequency of motion of the particles during the splitting process. For frequencies below 5 kHz, extremely small population of the islands was observed, which is due to the fact that this overlap of frequencies takes place throughout the whole splitting process. As expected, the interaction between the particles and the external driving force is especially important during the early part of the splitting process, where the island formation takes place. Considering instead a ripple at 10 kHz, the various spectra in Fig. 6.52 show the presence of only little energy at this frequency. Furthermore, an overlap occurs rather towards the end of the splitting process, where the islands have already been properly populated. Therefore, the splitting itself is almost unaffected by such a high-frequency ripple.
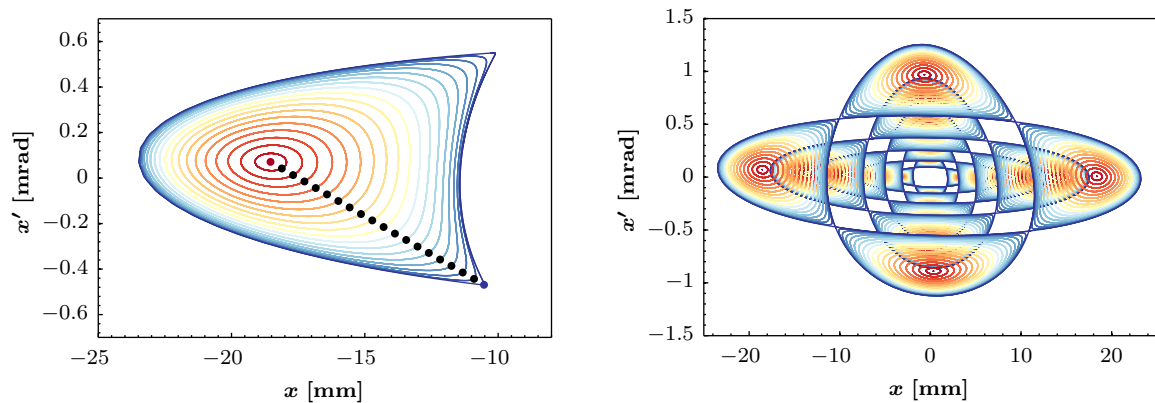
(a) Innermost island at 800 ms. The central red dot corresponds to the SFP, while the blue one indicates the location of the UFP. The black dots in-between correspond to the initial conditions for the other 18 particles and were obtained by equally spacing the distance from the centre to the separatrix of the island.

(b) Islands at 765, 770, 780, 790 and 800 ms superimposed. For each time step, the initial conditions of the tracked particles were determined according to (a).

Figure 6.50. Tracking of 20 particles to explore the phase space of the islands and to provide the simulation results to compute the secondary frequencies.
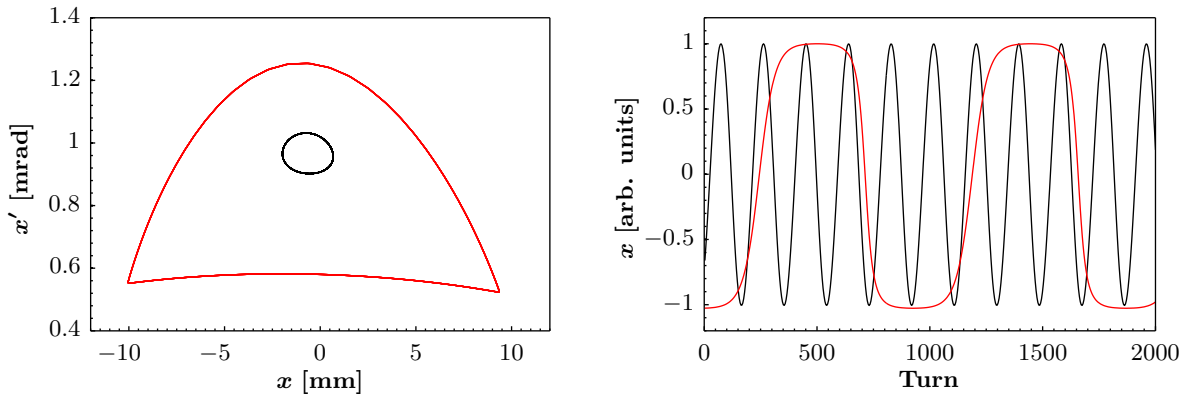
(a) Trajectories in the horizontal phase space for two particles. Only in the close vicinity of the SFP the trajectories are elliptic.

(b) Oscillation of the horizontal positions of the particles shown in (a). To improve visibility, the coordinates were normalized to their respective maximum. Close to the separatrix (red curve), the motion is no longer harmonic.
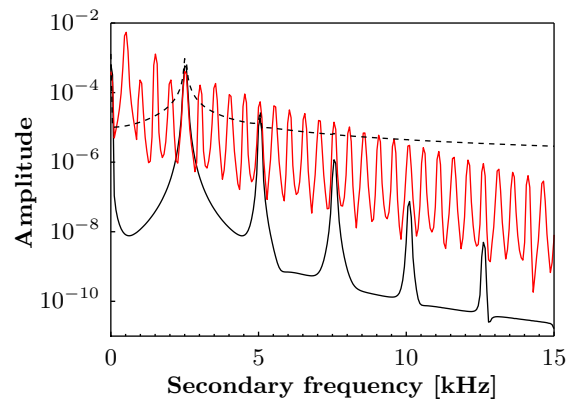
(c) Frequency spectrum of the particles following the black and red trajectories in (a). The dashed line corresponds to a FFT without window, whereas a Hann window function was applied to the simulation results in the case of the solid lines. The spectrum of the central particle contains frequencies at multiples of 2.5 kHz.

Figure 6.51. Analysis of the particle motion inside an island at a cycle time of 800 ms.

(a) Situation at 765 ms and $\delta = 0$.

(b) Situation at 770 ms and $\delta = 0$.

(c) Situation at 780 ms and $\delta = 0$.

(d) Situation at 790 ms and $\delta = 0$.

(e) Situation at 800 ms and $\delta = 0$.

(f) Situation at 800 ms and $\delta = 5 \times 10^{-4}$.

Figure 6.52. Evolution of the secondary frequency for particles inside the islands at various timings along the cycle. The red lines are spaced by 2.5 kHz.

6.2.1.4 Proposed measures to further improve the stability of the MTE process
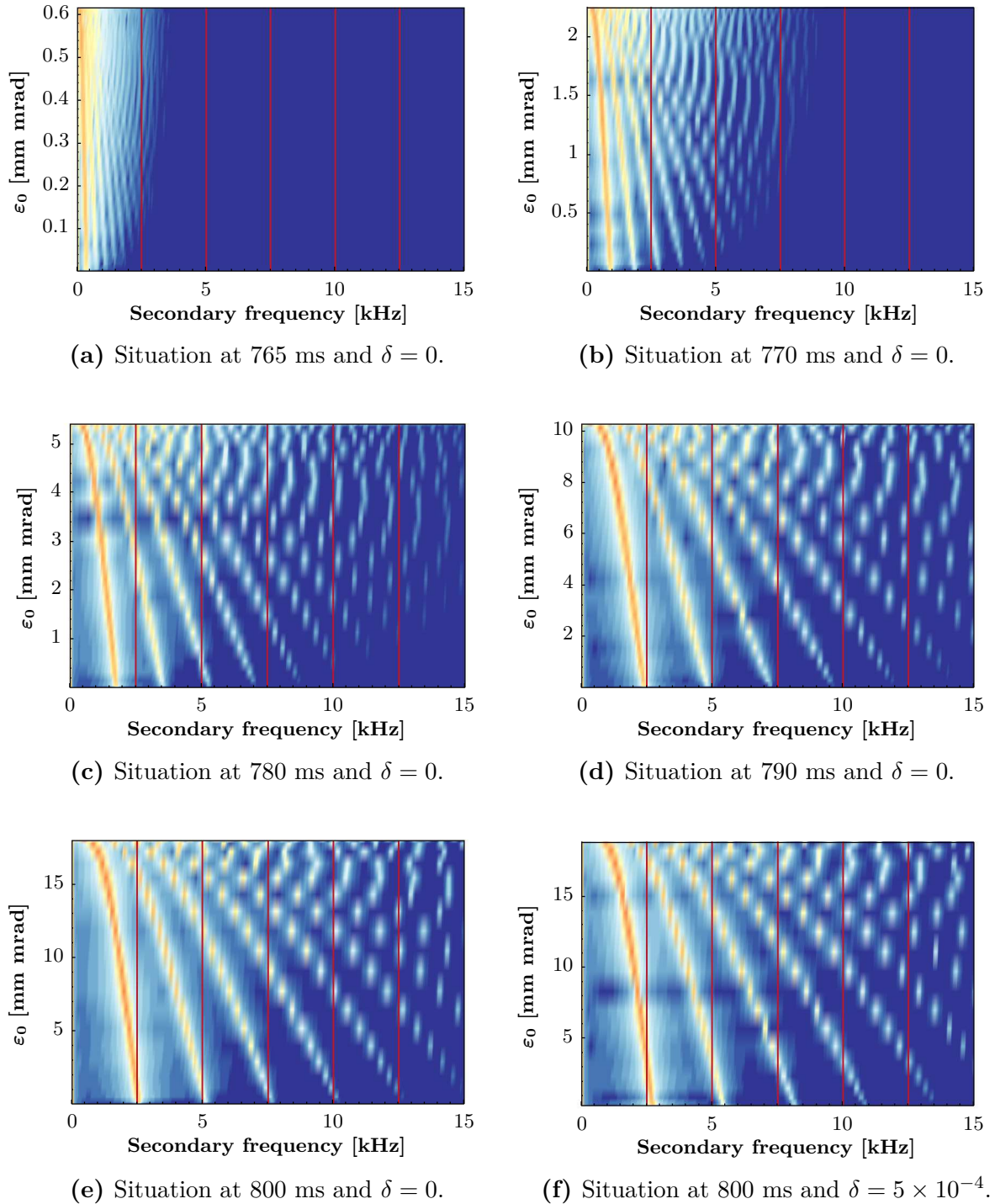
Based on the results presented on the previous pages, the magnetic stability of the various accelerator elements is clearly of crucial importance for the MTE process. Ideally, the frequencies of all PCs operating in switch-mode should be in the order of 10 kHz to reduce any interplay with the natural secondary frequencies of particles inside the islands. However, due to the load represented by certain circuits (such as the F8L), this is technically not always possible. Fortunately, the ripple caused by the PC of the F8L appears to be negligibly small and is furthermore constant in time. Therefore, the splitting process is currently not affected by this circuit, but one needs to ensure that this remains valid also in case of future upgrades to the circuit.

The situation was shown to be clearly different for the remaining PCs of the PFW. On the one hand, the feasibility of synchronizing the clocks controlling the switching of the different PCs clearly needs to be investigated. Once implemented, the splitting process would still be affected, but this effect would no longer vary with time. On the other hand, each PC of the PFW actually consists of two modules, and the switching is supposed to occur with a phase difference of π to actually cancel the frequency component at 5 kHz and a ripple at 10 kHz should be the only residual. However, even though the 5 kHz ripple was significantly reduced by resolving the cabling error, it has not been fully suppressed (see Fig. 6.41). Therefore, the phase difference between the modules within each PC should be carefully optimized, which will additionally benefit the magnetic stability of the machine.

In order to even further improve the splitting efficiency, the frequencies of the various PCs (especially those of the FW and DW circuit) could be de-tuned within the bounds of possibility. More precisely, one PC could be operated at a frequency f_1, which is either smaller or higher than the other one, which remains to be controlled at $f_2 = 5$ kHz. Simulation results, which justify this approach, are depicted in Fig. 6.53. Interference between the ripples of the two circuits leads to the shown beating signal and the overall effective ripple amplitude is reduced. As expected based on the results presented in this section, the splitting efficiency is decreased by going to lower frequencies, i.e. positive values of $f_{\text{beat}} = f_1 - f_2$. Accordingly, the efficiency is improved by programming negative values and a small gain of η_{MTE} on the sub-percent level seems achievable. Obviously, this approach requires careful tuning of the hardware as well as an experimental verification of this proposal.

Lastly, controlling the secondary frequencies in order to keeping them small during the whole splitting process could be imagined. Thus, the overlap of the beam spectrum with that of the PCs would be reduced. However, as the secondary frequencies depend on the size of the islands and their distance from the centre [78], this type of advanced splitting control requires a detailed investigation and optimization of the configuration of the non-linear elements.
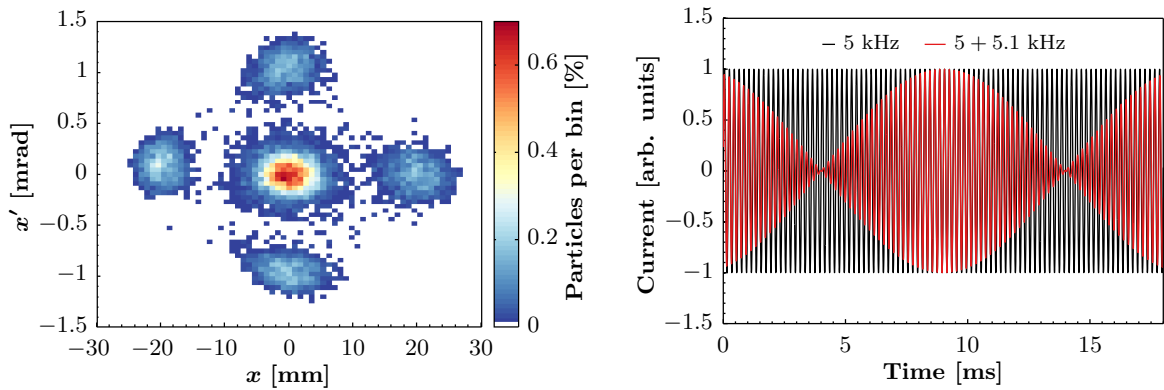
(a) Horizontal phase space at 800 ms. A 10% tune ripple according to the red curve shown in (b) ($f_{\text{beat}} = -100$ Hz) was applied. Compared to Fig. 6.48 (c), the splitting process is improved.

(b) Interference between two similar frequencies creates the beating signal shown in red. Compared to a pure 5 kHz oscillation, the effective ripple amplitude is reduced.
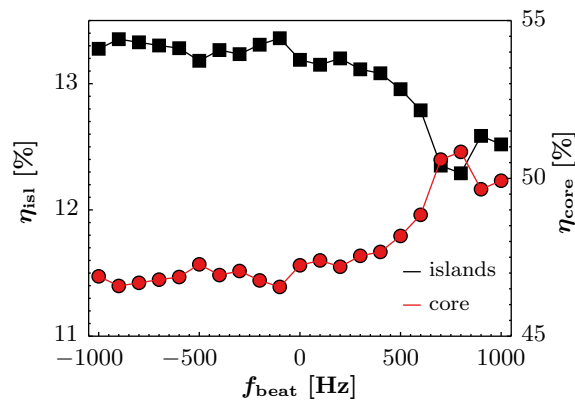
(c) Dependency of the splitting efficiency on the beating frequency f_{beat}. The case $f_{\text{beat}} = 0$ Hz corresponds to that shown in Fig. 6.48 (c). For $f_{\text{beat}} < 0$ the splitting process is improved.

Figure 6.53. Effect of a tune ripple composed of two different frequencies on the splitting process. Compared to a purely monochromatic ripple at 5 kHz, η_{MTE} is slightly improved by applying negative beating frequencies.

6.2.2 Development of a new extraction bump

The complexity of the MTE technique originates not only from the transverse splitting process, but also from the difficulty of properly extracting the horizontally split beam. The installation of TPS15 further complicated the extraction process, as this device constitutes an aperture restriction for the circulating beam, while, in order to shadow SMH16 during the rise of the extraction kickers, the extracted beam is required to pass on the external side of this passive absorber.

Therefore, a new slow extraction bump was developed and proposed in the TPS15 DR [16], which is very different from the previously used one (see Fig. 6.18). The underlying idea is to approach as closely as possible the two septa in SS15 and SS16. To achieve the necessary additional kick in SS15, it was suggested to use the high energy orbit corrector DHZ05 to open the slow bump already in SS05. The difference between this proposal and the old extraction bump is depicted in Fig. 6.54 (a). This enlarged slow bump clearly has the advantage of increasing the particle amplitude at TPS15; however, it also comes with one significant drawback: during the 6 ms long rise of the extraction bump, which follows the shape of a quarter sine wave, the particle motion is influenced by magnetic feed-down effects created by the non-linear fields of the PFW. This especially affects the positions of the islands, as the sextupolar and octupolar components of the PFW generate a quadrupolar component by feed-down, while higher-order fields cause a minor change of the islands' size and the shape.

Experimentally, the resulting tune-shift was observed to be undesirably strong. This caused the islands to be lost at SMH16, as they were transported to high amplitudes already before the maximum value of the slow bump was achieved. Therefore, a dynamic compensation of the tune during the rise time of the bump, which aims at keeping the distance between the islands and the core constant, was concluded to be inevitable.

Operational experience demonstrated that the tune compensation required by the new enlarged bump is extremely cumbersome to achieve. Any optimization of the bump settings, which has to occur on a regular basis to account for unavoidable drifts of the setup, was found to result in a large movement of the islands, likely to be accompanied by unintentional beam loss.

Therefore, a different concept of determining the tune-shift caused by the feed-down effects was pursued in the framework of this thesis. This was rendered possible on the basis of the gained confidence in the model of the machine, which is a result of the activities presented throughout the previous sections. The new approach consists of computing the lattice parameters for various given configurations using PTC, and subsequent comparison of the obtained values. Considering again the two configurations shown in Fig. 6.54 (a), the respective tune-shifts and changes of linear chromaticity during the rise time of the slow extraction bump are depicted in Fig. 6.54 (b). In agreement with experimental observations, the horizontal tune-shift ΔQ_x during the rise of the bump is found to be positive, which causes the islands to be transported towards higher amplitudes. For the old operational bump a maximum tune-shift of $\Delta Q_{x,\mathrm{max}} = 1.9 \times 10^{-3}$ is
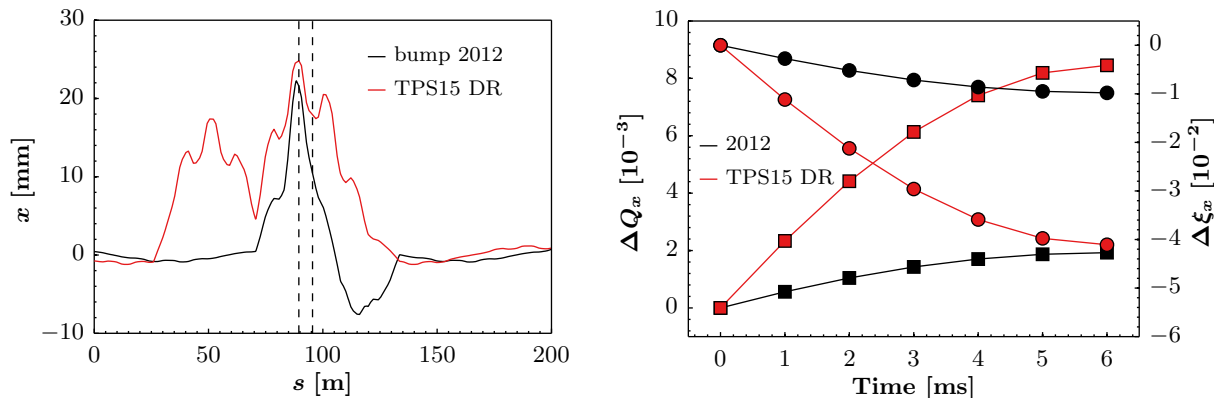
(a) Horizontal excursion of a particle at maximum bump amplitude. The dashed lines indicate the positions of TPS15 and SMH16. Some residual oscillation outside the extraction region remains.

(b) Horizontal detuning (squares) and change of linear chromaticity (circles) during the rise time of the bump.

Figure 6.54. Comparison between the old operational slow bump and the one proposed in the TPS15 DR.

obtained, whereas this value is already achieved after 1 ms rise time of the new proposal. To illustrate the resulting movement of the SFPs during these 6 ms before extraction, Fig. 6.55 shows the horizontal phase space in SS55 of the PS. This section of the machine is ideally suited for such an investigation, as the β_x-function is maximum and, as the SFPs are aligned as an upright cross, the external island moves almost purely along the position axis. Considering first
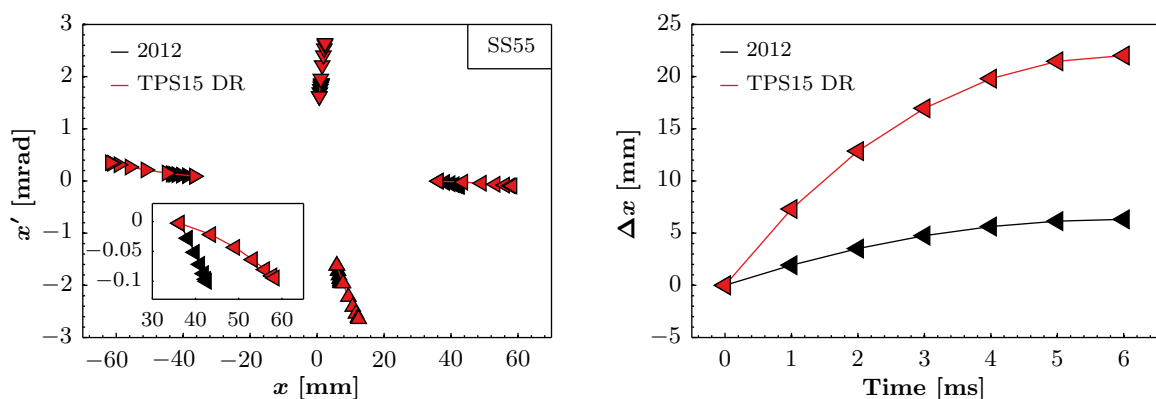
(a) Horizontal phase space. The close-up depicts the movement of the external beamlet.

(b) Change of the horizontal position of the external beamlet.

Figure 6.55. Evolution of the SFPs at the beginning of SS55 during the rise of the slow bump.

the old version of the bump, this outermost beamlet is observed to move by $\Delta x_{\max} \approx 6$ mm. Even though this value is non-negligible, it can still be accommodated within the available aperture and hence, even without any tune correction, beam loss is unlikely. Looking at the results using the bump from the TPS15 DR, the situation is drastically different. As already shown in Fig. 6.54 (b), within the first millisecond of the rise of the bump, the additional amplitude exceeds the maximum value of the other bump quoted above. Once the maximum amplitude of the enlarged bump has been reached, the tune-shift has even caused the island to be displaced by $\Delta x_{\max} \approx 22$ mm. This does not immediately lead to beam loss in this specific section; however, it significantly reduces the clearance between the beam and the machine aperture and, due to the existence of various aperture restrictions distributed along the ring (see Fig. 6.18, notably the various injection and extraction septa), may cause beam loss elsewhere.

On the other hand, the observed variations of linear chromaticity on the particle distribution are deemed to be much less important. In any case, changes of ξ_z in the order of 10^{-2} cannot be reproducibly controlled using the PFW, and correspond to the order of magnitude caused by unavoidable shot-to-shot variations.

Furthermore, space charge effects were reported to cause a positive horizontal tune-shift, apparently dominated by the contribution of the image currents, which also influences the positions of the SFPs [80]. For beam intensities of $N_p = 2 \times 10^{13}$ p, a rather small resulting tune-shift of $\Delta Q_x^{\mathrm{SC}} = 4 \times 10^{-4}$ was observed. In the absence of any extraction bump, the application of an additional single particle tune-shift was found to be sufficient in order to compensate this space charge induced effect. During the rise of the bump, however, the distance between the beamlets and the vacuum chamber is modified, which will also change the indirect space charge tune-shift. Therefore, the actual total horizontal tune-shift is likely to be larger than presented in Fig. 6.55; a fact, which has to be considered when experimentally implementing the tune compensation.

The explanations set forth above substantiate the operational difficulties, which were experienced when trying to identify a proper tune compensation scheme for the enlarged extraction bump. The systematic approach of performing tune measurements at various points during the rise time of the extraction bump suffers from two conflicting disadvantages. To reduce the error of the tune measurement, turn-by-turn data of at least 2 ms (corresponding to 950 turns) should be recorded (see also Section 3.2). However, during this time span, the tune has already changed quite importantly, resulting in the mere measurement of an average tune value. If, on the other hand, the measurement window is sufficiently reduced to more precisely follow the evolution of the tune-shift, the required resolution of $\Delta Q_x \approx 10^{-3}$ is no longer achievable.

Therefore, it was decided to consider the tune-shift obtained by simulations as figure of merit for the development of a new slow bump, which has to fulfil the requirements of approaching both TPS15 and SMH16, while minimizing the need for a tune compensation scheme. Based on the results presented in Fig. 6.58, it became clear that natural self-compensation of the tune-shift can be obtained by combining positive and negative bump amplitudes. Thereby, if properly designed, the tune-shift experienced during the first part of the bump is cancelled by the negative

particle excursion in the second part. This approach simplifies the operability of the bump and renders the extraction process more robust, as small variations of the settings only cause minor movement of the positions of the islands.

The subsequently created fast extraction bump is then supposed to send the beamlets to the external sides of both septa. In contrast to the adiabatic rise of the slow bump, which provides sufficient time for the beamlets to follow the movement of the SFPs caused by the experienced tune-shift, the fast kicks represent a discontinuity in time. As the islands remain in the machine only for up to four additional turns, no state of equilibrium will be reached and their resulting movement during this time is negligible.

The different steps to design a completely new extraction bump fulfilling all of the above requirements, which has successfully been operationally deployed in June 2015, are set forth on the following pages.

6.2.2.1 Extraction bump using BSW12-20

A simple-minded approach to extracting the MTE beam consists of applying a π-bump created by the dipole magnets BSW12 and BSW20. In order to determine the required amplitude of the slow bump, the closed orbit of the beamlets prior to the rise of the bump has to be evaluated in the first place. This is indispensable to understand the movement of the islands especially in the extraction region. The respective situation, together with the horizontal phase space at the entrance of SMH16, is shown in Fig. 6.56.

For all considerations regarding the extraction bump the shown horizontal envelopes are computed assuming the same parameters as in Fig. 6.15, which reveals a certain discrepancy when comparing these envelopes to the projections of the beamlets' surfaces obtained via particle tracking over hundreds of turns (see Fig. 6.56 (b)). Due to the non-linear nature of the motion inside the islands and the resulting distorted phase space trajectories, the logical approach of applying the coordinates of the envelopes as initial tracking conditions fails to correctly predict the equivalent surface of the islands. This becomes especially clear when looking at the internal and external islands in Fig. 6.56 (b), where the projection of the trajectory leads to an envelope, which is asymmetric with respect to the position of the fixed point. However, this does not imply a problem, as the envelopes extending to $\Delta x_{\mathrm{env}} = \pm\sqrt{(3\sigma_x)^2 + (2\sigma_s)^2}$ represent a conservative estimate of the beam size, especially when considering the beamlet close to the septum blade. Therefore, all assumptions concerning the design of the extraction bump made in the following are based on Δx_{env}, which should provide some additional safety margin for the actual operational implementation. It is worth mentioning that in any case, a final experimental optimization of the parameters, while closely monitoring beam loss in the extraction region, is inevitable (see Section 6.2.2.4).

Applying the above considerations, the required amplitude of the slow bump can finally be de-
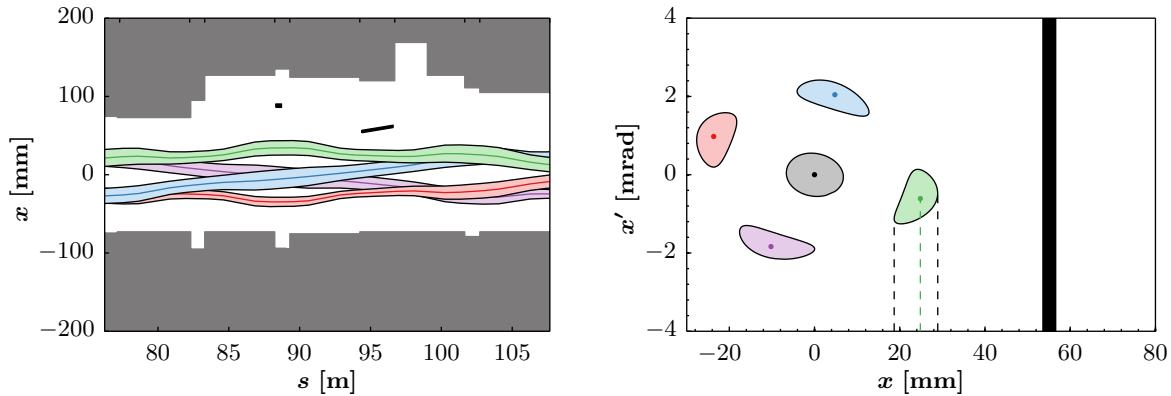
(a) Orbit of the islands between SS13 and SS18. TPS15 is indicated at its nominal settings of 86 mm/0 mrad and SMH16 at 55.5 mm/3 mrad (see also Fig. 6.57).

(b) Phase space at the entrance of SMH16. The surfaces of the islands are based on PTC tracking results and the resulting horizontal envelope of the external island is asymmetric with respect to the position of the SFP.

Figure 6.56. Horizontal closed orbit of the islands after their final rotation has taken place. The maximum aperture requirements are in the order of 80 mm.
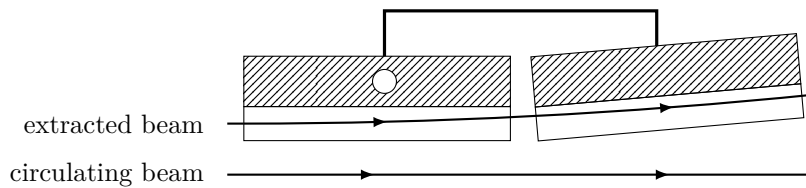

Figure 6.57. Schematic drawing of SMH16. Both elements of the septum are rotated as one rigid unit around the point of rotation indicated by the white circle, which is located 624 mm downstream of the device entrance [95]. Any setting quoted in the text actually describes the distance of the blade from the ideal orbit, measured at the longitudinal position of the rotating point. If the septum is inclined at a positive angle, the clearance between the entrance of the device and the circulating beam is further reduced.

termined. At maximum amplitude, the external island is supposed to closely approach SMH16, without actually provoking beam loss on the septum blade. Considering again the results of the closed orbit simulations depicted in Fig. 6.56 (a), the particle amplitude needs to be increased by 20.5 mm at the entrance of SMH16. This is easily achievable by powering BSW12 and BSW20 at 243.20 A. The resulting slow bump for a central particle is shown in Fig. 6.58. A certain leakage outside the extraction region is unavoidable, as the phase advance between BSW12 and BSW20 is short of π by 2%. Given the optics of the machine, the particle amplitude is obviously higher in SS15 than in SS16. The corresponding beam envelopes and the phase space portrait at SMH16 are shown in Fig. 6.59. Using this setup, the beam is correctly positioned at SMH16;

(a) Horizontal orbit of a core particle at maximum bump amplitude.

(b) Zoom around the extraction region. The dashed lines indicate the positions of TPS15 and SMH16.
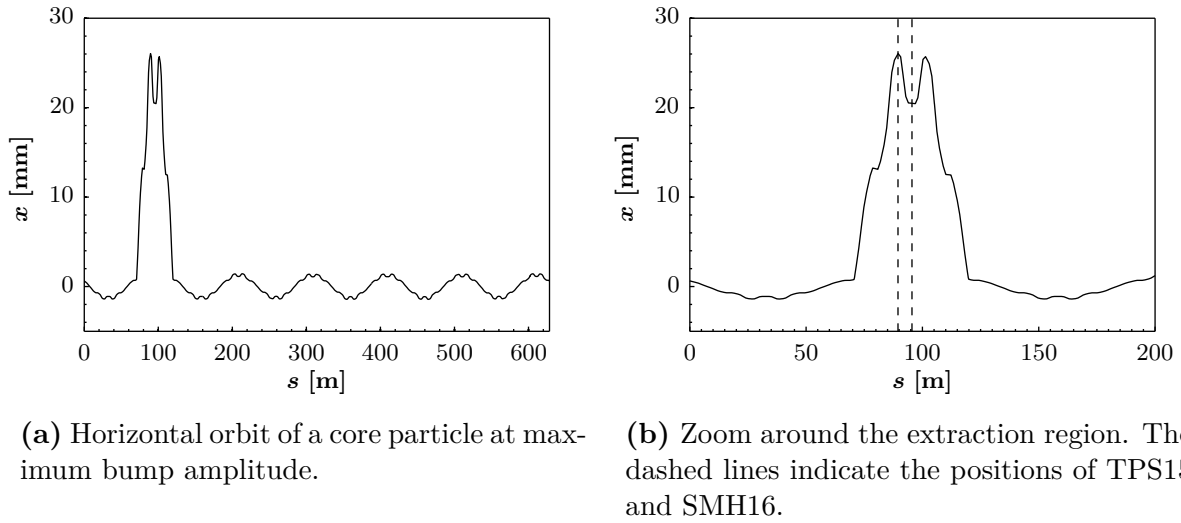
Figure 6.58. Slow bump between SS12 and SS20.

(a) Beam envelopes between SS13 and SS18. With this bump, TPS15 cannot be closely approached.

(b) At SMH16, the beamlets are correctly positioned in the horizontal phase space.
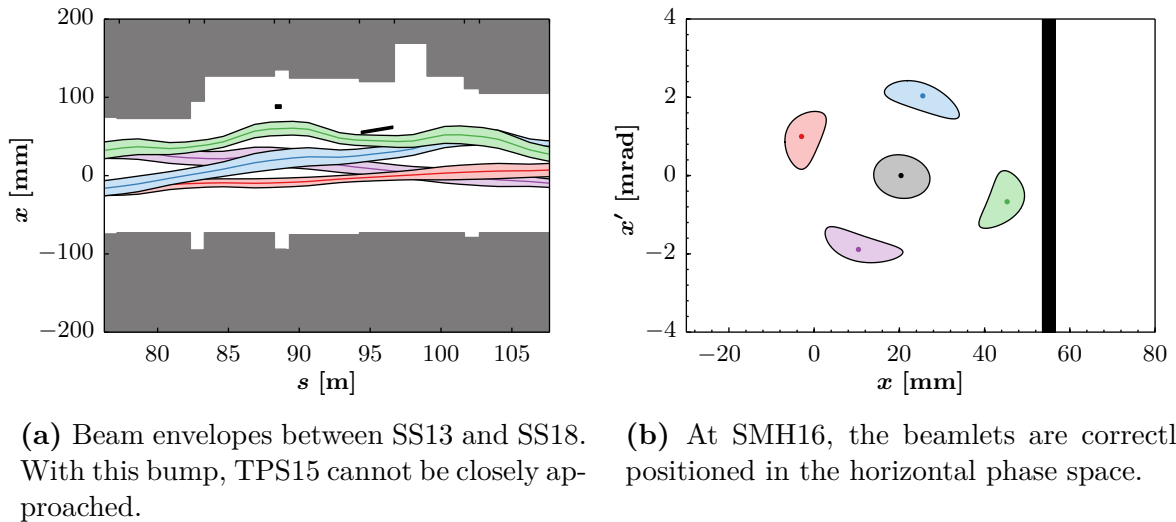
Figure 6.59. Orbit of the islands at maximum amplitude of the slow bump. The tune-shift was corrected to again achieve $Q_x = 6.255$.

however, the resulting distance to TPS15 is rather large and amounts to 17 mm. Furthermore, this kind of slow bump causes only a positive excursion of the circulating beam and, therefore, no natural self-compensation of the induced tune-shift, as it is the case for the black curve in Fig. 6.54, is observed. Instead, the horizontal tune is modified by $\Delta Q_x = 5 \times 10^{-3}$, leading up to 15 mm displacement of the external island in an odd section with large β_x−function and requiring compensation.

In order to actually extract the beam from the machine, the five-turn long fast bump created by

the kickers KFA13 and KFA21 has to be activated. This leads to an additional deflection on top of the excursion caused by the slow bump and the combined extraction bump, applying 50 kV to each of the kickers, is depicted in Fig. 6.60. The beamlets' envelopes and the phase space portraits at the septa are then shown in Fig. 6.61. It is immediately obvious that these settings do not allow to send the beam to the external side of TPS15, which is caused by the insufficient amplitude of the slow bump at this location. Even though the beam could be extracted, TPS15 cannot provide shadowing of SMH16 using this configuration. In addition, another aperture bottleneck is created as the horizontal position in SS17 becomes extremely large.

In summary, the considerations presented in this section lead to the understanding that a simple π-bump fails to comply with the requirements to properly extract the MTE beam. This conclusion is based on the necessary tune compensation on one hand, but, more importantly, on the fact that a bump created by BSW12 and BSW20 provides insufficient amplitude to send the beamlets to the other side of TPS15. Therefore, a different slow bump, which accounts for these shortcomings, is presented in the following section.

6.2.2.2 Extraction bump using BSW12-20 and BSW14-22

In order to set up a proper extraction scheme for the MTE beam, the slow bump explained on the previous pages requires significant improvement. This especially consists of increasing the amplitude at TPS15 without changing it at SMH16. A total of four dipole magnets, i.e. BSW12, 14, 20 and 22, are available to shape the slow bump, and with these elements one can actually superpose two independent π-bumps, as also BSW14 and BSW22 are separated by a phase advance of almost π. To simplify further investigations, a single strength value was assigned to each pair of dipole magnets. Therefore, the notation B12 and B14 will be used in the following to describe the bumps BSW12-BSW20 and BSW14-BSW22, respectively.

Having identified the important elements to continue the development of the extraction bump, the model was used to determine the 2×2 orbit response matrix (ORM) $\mathbf{M}_{\mathrm{ORM}}$, which describes the response of the orbit Δx_i at the locations of TPS15 and SMH16 to an excitation with B12 and B14 at a certain current ΔI_j:

$$\begin{pmatrix} \Delta x_{\mathrm{TPS15}} \\ \Delta x_{\mathrm{SMH16}} \end{pmatrix} = \mathbf{M}_{\mathrm{ORM}} \begin{pmatrix} \Delta I_{\mathrm{B12}} \\ \Delta I_{\mathrm{B14}} \end{pmatrix}. \tag{6.19}$$

The matrix elements were determined to be

$$\mathbf{M}_{\mathrm{ORM}} = \begin{pmatrix} m_{\mathrm{B12}}^{\mathrm{TPS15}} & m_{\mathrm{B14}}^{\mathrm{TPS15}} \\ m_{\mathrm{B12}}^{\mathrm{SMH16}} & m_{\mathrm{B14}}^{\mathrm{SMH16}} \end{pmatrix} = \begin{pmatrix} 0.1060 & 0.0366 \\ 0.0852 & 0.0572 \end{pmatrix} \tag{6.20}$$

in simulations, with the unit of m_j^i being mm/A.

The inverse of this matrix can then be applied to compute the required currents to push the
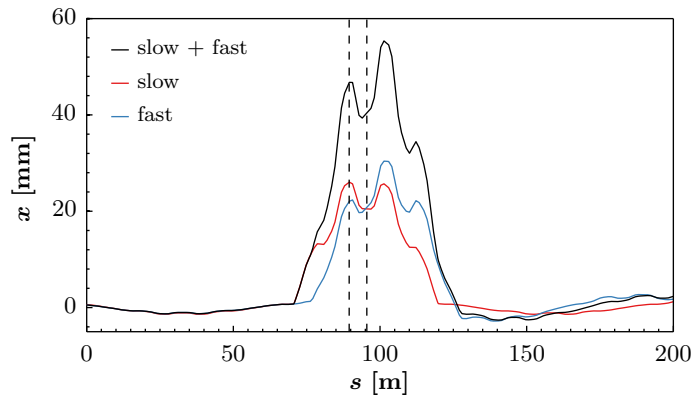
Figure 6.60. Summation of the slow and the fast extraction bump. The dashed lines indicate the positions of TPS15 and SMH16.
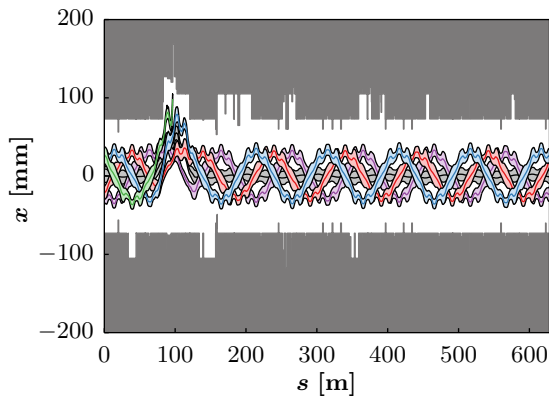
(a) Only three islands remain in the machine after extraction of the green one.
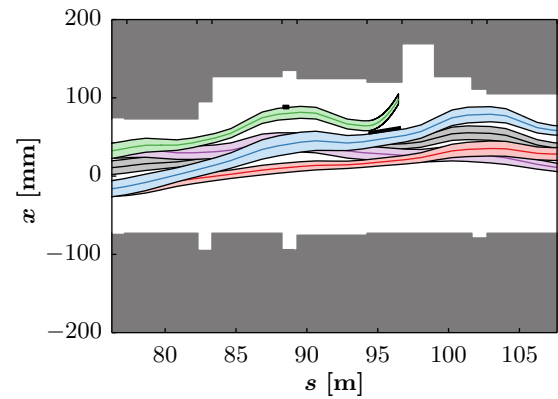
(b) The first island is properly extracted at SMH16; however, it remains on the internal side of TPS15.
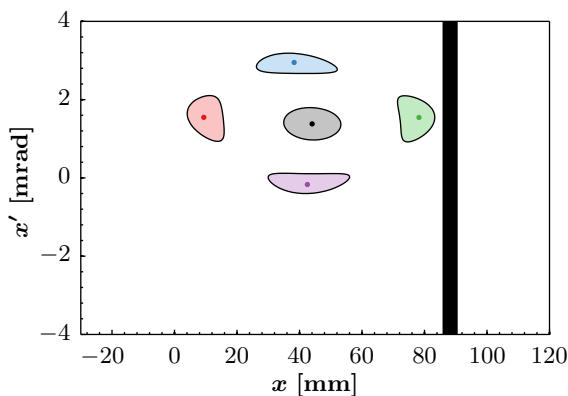
(c) Phase space portrait at TPS15.
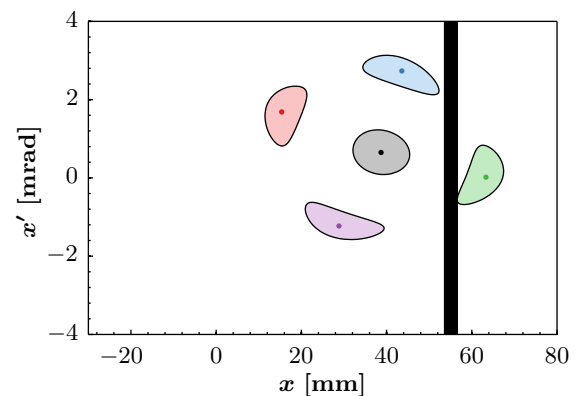
(d) Phase space portrait at SMH16.

Figure 6.61. Trajectories of the islands and phase space portraits during the first turn after firing the extraction kickers.

bump amplitude either at TPS15 or at SMH16:

$$\mathbf{M}_{\mathrm{ORM}}^{-1} \begin{pmatrix} \Delta x_{\mathrm{TPS15}} \\ \Delta x_{\mathrm{SMH16}} \end{pmatrix} = \begin{pmatrix} \Delta I_{\mathrm{B12}} \\ \Delta I_{\mathrm{B14}} \end{pmatrix}, \tag{6.21}$$

with the actual values being

$$\mathbf{M}_{\mathrm{ORM}}^{-1} \begin{pmatrix} 1 \text{ mm} \\ 0 \text{ mm} \end{pmatrix} = \begin{pmatrix} 19.41 \text{ A} \\ -28.91 \text{ A} \end{pmatrix} \tag{6.22}$$

and

$$\mathbf{M}_{\mathrm{ORM}}^{-1} \begin{pmatrix} 0 \text{ mm} \\ 1 \text{ mm} \end{pmatrix} = \begin{pmatrix} -12.42 \text{ A} \\ 35.98 \text{ A} \end{pmatrix}. \tag{6.23}$$

In Fig. 6.62, the orbit response to an excitation at the currents mentioned in Eq. (6.22) is depicted. By construction, the orbit at SMH16 remains at 0 mm, while the amplitude at TPS15 reaches 1 mm. Moreover, an important negative peak at the beginning of MU19 appears, creating an additional aperture restriction at this location. However, this negative excursion also comes with the advantage of a negative tune-shift $\Delta Q_x = -2.3 \times 10^{-4}$. Therefore, applying B12 using the settings presented in the previous section in combination with increasing the amplitude in SS15 according to Eq. (6.22) leads to an overall reduction of the tune-shift, which improves the operability of the extraction bump.

A first iteration using B12 and B14 to approach TPS15 is presented in Fig. 6.63. The results shown in Fig. 6.59 indicate 40 mm of available aperture in MU19, which, considering 2 mm of safety margin, allows to increase the bump amplitude at TPS15 by the required 17 mm.
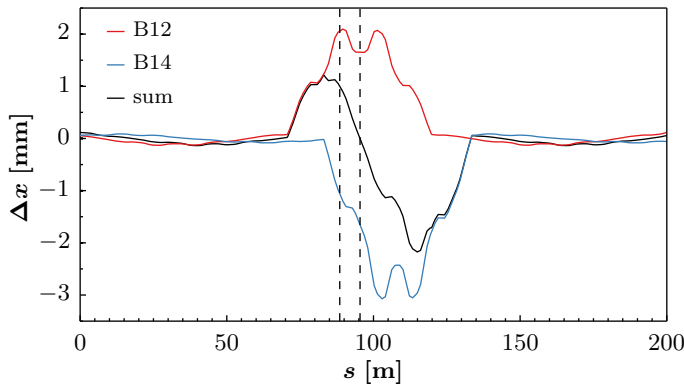

Figure 6.62.   Simulated orbit response to an excitation with B12 and B14 according to Eq. (6.22). The dashed lines indicate the positions of TPS15 and SMH16 and the amplitude at the former septum is increased by 1 mm without any modification at the latter one.

Considering the phase space portrait, it becomes clear that, due to the peculiar shape of the islands, the actual distance to the septa is larger than suggested by the envelope, which provides some additional safety margin. Overall, this slow bump causes a reduction of the horizontal tune by $\Delta Q_x = -4 \times 10^{-4}$, as the large negative amplitude in MU19 leads to a self-compensation of the tune-shift due to the feed-down effects. Therefore, the islands' distance from the core is slightly reduced at maximum bump amplitude and only minor tune correction is required to account for this effect.

Further optimization of the extraction bump is required to minimize beam loss during the fast bump. Therefore, sufficient separation between the extracted and the circulating beam has to be provided, which can be achieved by acting on the slow bump and the horizontal tune at the same time. To retain the external islands' position while increasing its distance from the core, the amplitude of the bump can be reduced by multiplying both B12 and B14 with a factor between zero and one, whereas Q_x requires an increase. Especially the operational implementation of this approach is an iterative process, as the various BLMs in the extraction region have to be precisely monitored to avoid any beam loss at the different aperture restrictions during the slow bump.

Such an additional iteration is depicted in Fig. 6.64, where the bump amplitude was reduced by 20% to $I_{B12} = 458.21$ A and $I_{B14} = -420.70$ A and the horizontal tune was increased to 0.257. By doing so, the position of the external beamlet remains unmodified with respect to the septa, but increased separation between the green and the blue islands is obtained. This provides additional space to position the septa in-between these beamlets when firing the extraction
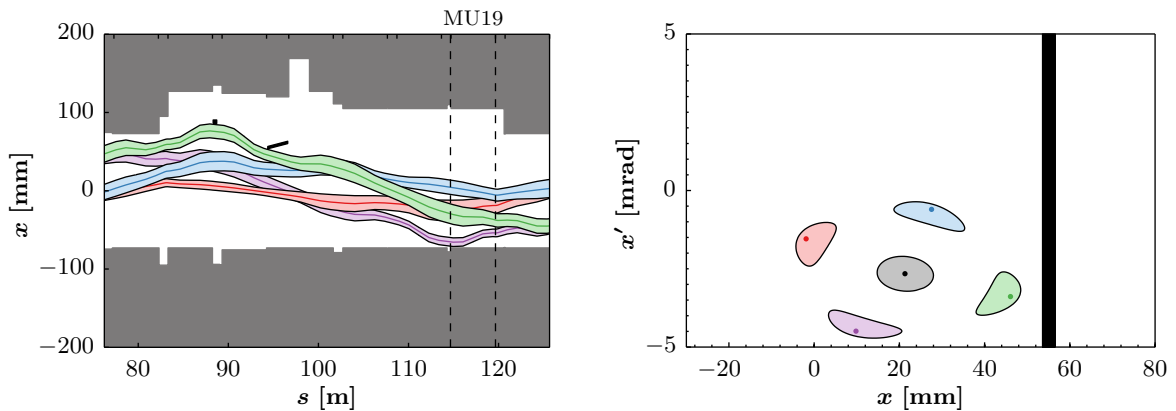
(a) The external island can be positioned close to both septa using this approach. The dashed lines indicate the beginning and end of MU19.

(b) Phase space at the beginning of SMH16.

Figure 6.63. Slow bump using B12 and B14 at 572.79 A and -525.87 A, respectively. The maximum achievable amplitude at TPS15 is constrained by the aperture in MU19.

KFAs, especially in SS16.

Lastly, Figs. 6.65-6.67 depict the actual extraction of the beamlets after activation of the fast kickers KFA13, KFA21 and, during the last turn, KFA71. As foreseen, the modified bump explained in this section is capable of sending the beam to the external side of TPS15. However, as visualized in the corresponding phase space portraits in Fig. 6.66, this is only achievable by further inserting TPS15 from its nominal position of 86 mm to the minimum of 80.5 mm.

As mentioned in the introduction to this chapter, the optics functions of all four extracted islands are in agreement. However, the DFA242 and the DFA254 in TT2 need to be used to correct the turn-by-turn variations of their trajectories, which are in the order of 1 mm. During the last turn, the core of the MTE beam is then extracted by pulsing KFA71. By definition, the extraction conditions of the core are different than those of the islands and, therefore, KFA04 can be additionally used to match angle and position of the core to the values of the islands. This requires again an operational optimization process, as the beam positions have to be measured at TPS15 as well as in the downstream transfer line.

In all presented considerations, the finite momentum spread of the beam has not been taken into account. This approach is justified as the spread is kept small by minimizing the RF voltage before the final debunching, and by the fact that a correction of the islands' positions can be achieved by slightly trimming the horizontal tune.

In conclusion, it is worth mentioning that, prior to the successful experimental verification of the proposed extraction scheme, a major hardware intervention was required, as the unipolar PC of BSW14 had previously only provided positive current. Therefore, this device had to be replaced by a bipolar spare PC, which allowed to test this extraction bump without perturbing the other users. Before discussing experimental results, the important role of the closed orbit in

(a) Phase space portrait at TPS15. **(b)** Phase space portrait at SMH16.
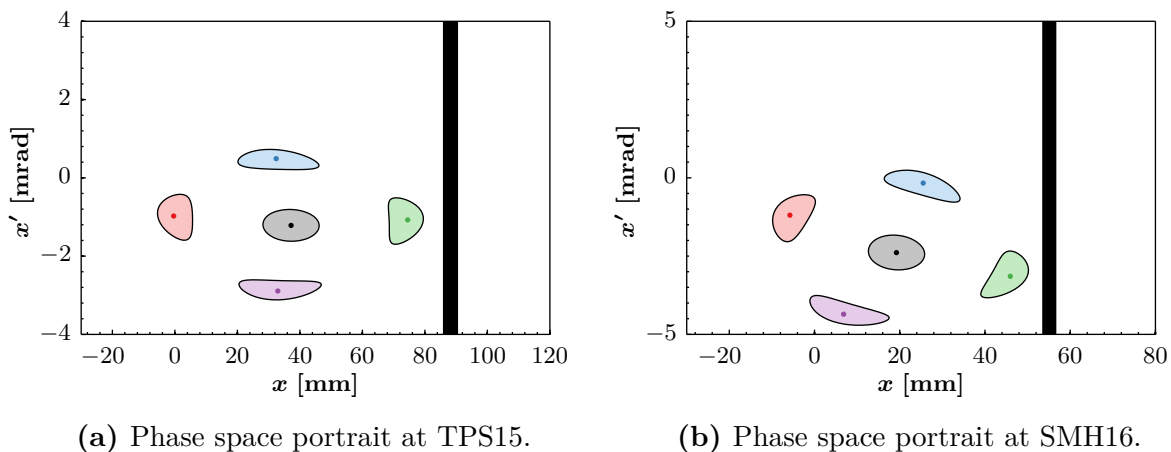
Figure 6.64. Result of applying a reduction factor of 0.8 to the currents of B12 and B14 mentioned in Fig. 6.63, while increasing the tune to $Q_x = 0.257$. This provides additional separation between the core and the islands.

(a) Extraction of the first island.

(b) Extraction of the second island.

(c) Extraction of the third island.

(d) Extraction of the fourth island.

Figure 6.65. Trajectories of the beamlets during the first four turns of the fast bump. The core (plotted in grey) remains in the machine for an additional turn.

(a) Phase space portrait at TPS15.

(b) Phase space portrait at SMH16.

Figure 6.66. Fast bump sending the beamlets to the external sides of the extraction septa.

(a) The large oscillation towards the end of the machine is due to the additional kick by KFA71, which finally extracts the remaining part of the beam from the machine.

(b) Close-up of the region SS01-SS20 showing how the additional kick sends the core to the other side of the septa.

Figure 6.67. Trajectory of the core during the last two turns of the fast bump.

the whole extraction process is briefly explained in the next section.

6.2.2.3 Importance of the closed orbit

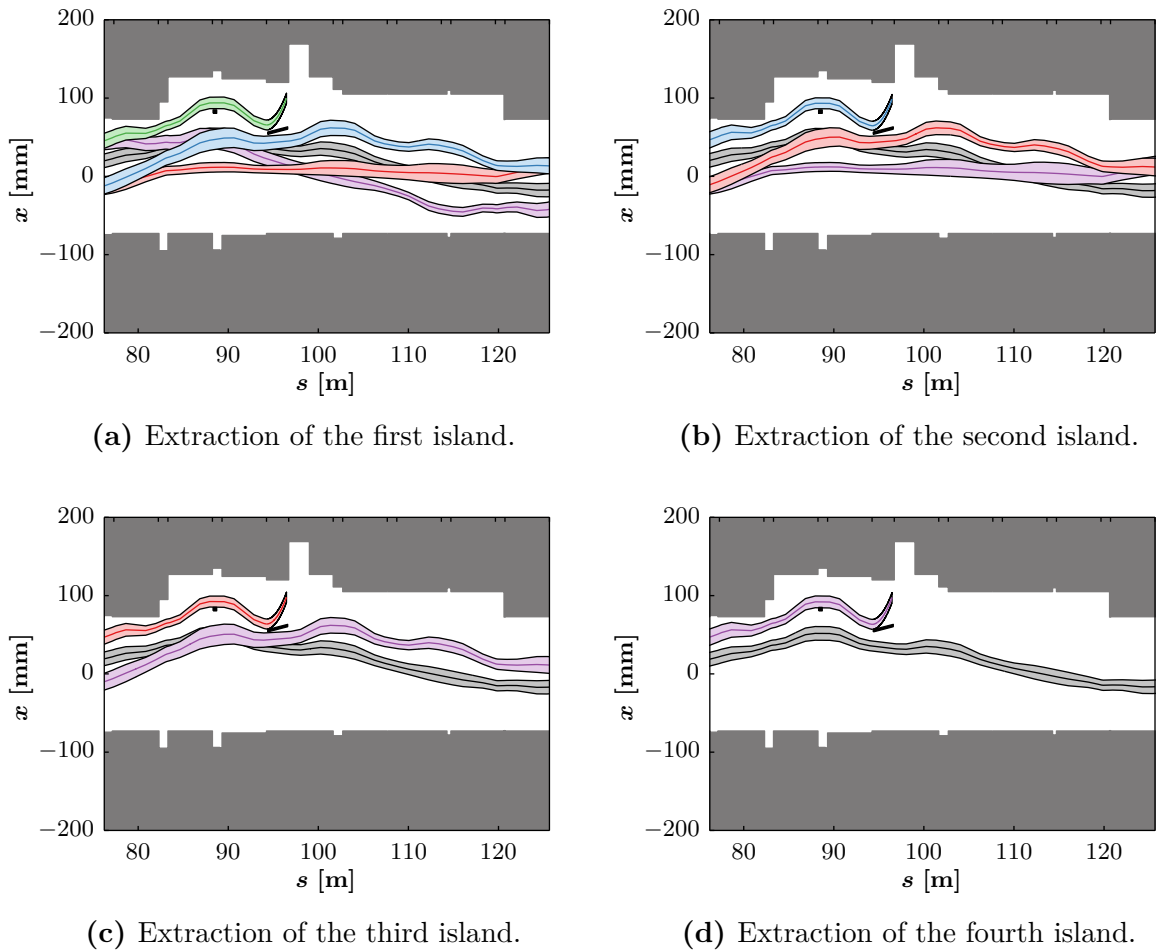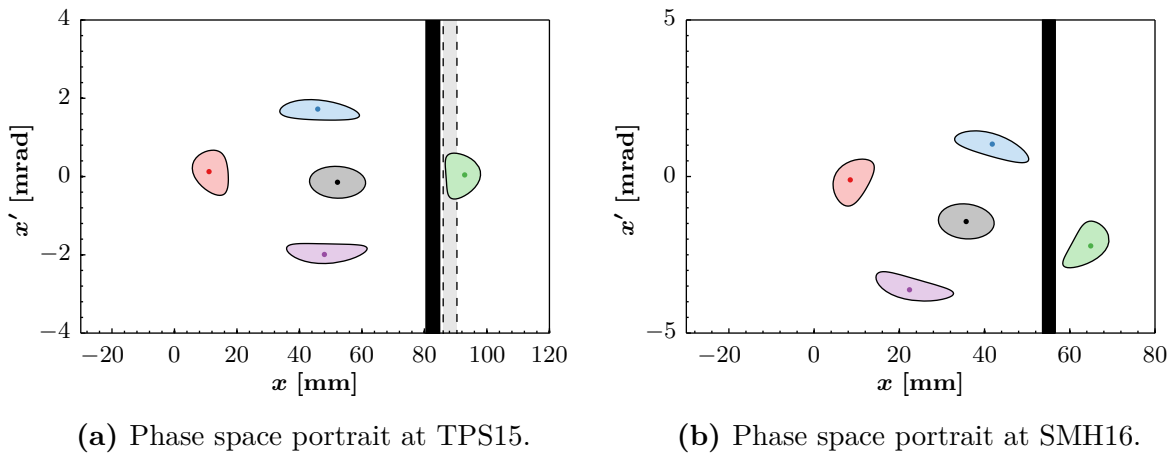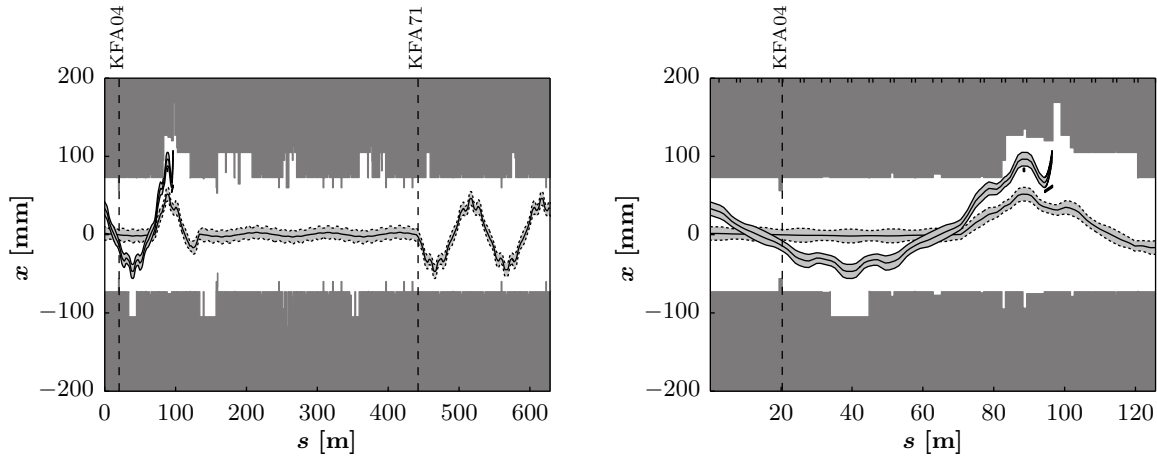The design of the extraction bump can be further improved by incorporating the actual closed orbit into the model. A corresponding measurement is depicted in Fig. 6.68 (a), which reveals a significant problem in the extraction region. The alignment of the MUs and the intrinsic magnetic errors lead to a rather large RMS value of the horizontal orbit of $x_{\mathrm{RMS}} = 3.1$ mm and, more importantly, a negative excursion of $x \approx -10$ mm at the location of TPS15. This is obviously undesired, as the extraction process is already largely constrained assuming ideal conditions. Therefore, an orbit correction scheme was indispensable, but this approach comes with an additional disadvantage: only three correctors (DHZ05, DHZ18 and DHZ60) are available to shape the orbit at high energy. To nevertheless achieve proper orbit correction at least around the extraction region, an online application available in the control room was used [96]. At first, an ORM using the three correctors was established and in several subsequent iterations the orbit was flattened in the extraction region. The resulting closed orbit is shown in Fig. 6.68 (b), where it becomes apparent that, due to the small number of correctors, the correction around SS15 occurs at the expense of the RMS orbit, which increases to $x_{\mathrm{RMS}} = 3.9$ mm.

Figure 6.68 furthermore shows the modelled closed orbit, which is achieved by introducing a dipolar kick at the centre of each MU. The kick strengths were determined with the singular

value decomposition (SVD)-based closed orbit correction algorithm of MAD-X, using the position measurements at the locations of the 43 PUs as input. Even though the simulation results might not be unique solutions, they are deemed to be sufficient to improve the extraction bump proposed in the previous section.

Another fact that has to be considered when incorporating such a closed orbit into the simulations, is the tune-shift caused by feed-down effects. Previously only discussed for the extraction bump itself, the tune-shift becomes also important for a non-zero closed orbit. Figure 6.69 shows a comparison between the initial, the corrected and zero closed orbit. In order to keep a horizontal tune of $Q_x = 6.255$ also in the presence of a non-zero closed orbit, the LEQ have to be adjusted to account for the tune-shift and to establish simulation conditions, which closely represent the reality.

The envelopes of the islands using the corrected closed orbit are shown in Fig. 6.70. The large excursions of the orbit especially in SS03 and towards the end of the ring constitute an additional complication for the extraction process. Using the same approach as set forth in the previous section, the maximum amplitude of the slow bump for a tune of $Q_x = 6.255$ is determined by the aperture bottleneck in MU19, and the respective currents were found to be 497 A for B12 and -510 A for B14. However, to increase the separation between the beamlets an improved setting was obtained by reducing these values by 20% and increasing Q_x to 6.257. The resulting trajectories during the fast bump (using 65 kV for KFA13 and KFA21) are also depicted in Fig. 6.70. Overall, the space constraints are rather demanding and only little space between the
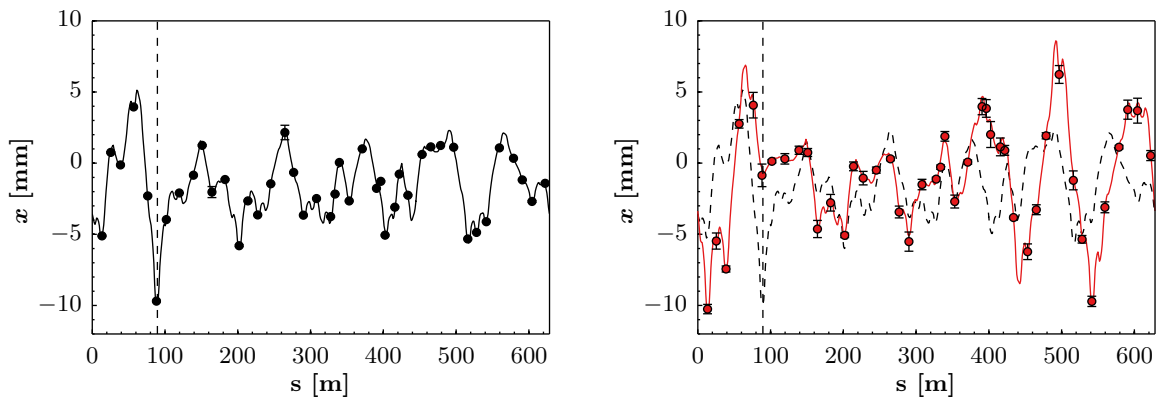
(a) Closed orbit before correction. The large negative excursion in SS15 is especially noticeable.

(b) Closed orbit after correction. The black dashed orbit represents the initial situation as shown in (a).

Figure 6.68. Comparison between the closed orbit before and after correction. The markers and the error bars represent an average value of twenty consecutive measurements and their standard deviation, respectively, and the solid lines are PTC simulation results. The straight dashed line indicates the position of TPS15.
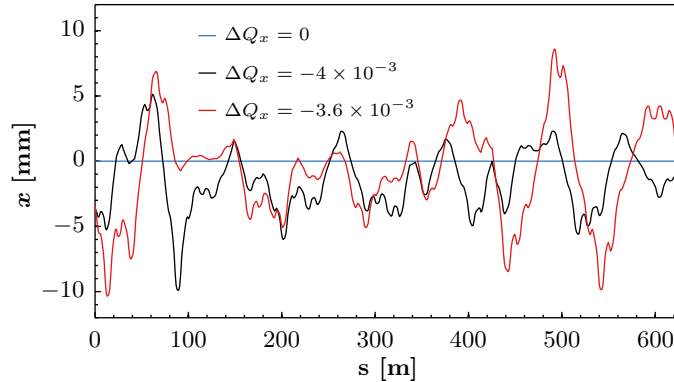
Figure 6.69. Feed-down effects modify the horizontal tune in the presence of a non-zero closed orbit. The black and red curves correspond to those shown in Fig. 6.68.

beamlets at SMH16 is achievable. Furthermore, the horizontal position of the external island slightly reduces during the four turns, causing the envelope to touch both septa during the last turn. However, no correctors are available, which could account for that fact on this short time scale.

In a final step, the settings of the extraction septa to shadow SMH16 during the rise time of the fast kickers have to be determined. Based on the considerations presented on the previous pages, it has become clear that TPS15 needs to be inserted as much as possible, i.e. to 80.5 mm. The resulting shadowing configuration, which is achieved when a particle that would otherwise centrally impinge on SMH16, is actually absorbed by TPS15, is shown in Fig. 6.71. According to the simulation results, the position of SMH16 has to be slightly increased to 56 mm (keeping the angle of 3 mrad) to fulfil the shadowing criteria.

Following the considerations presented in this section, it was possible, after some experimental fine tuning, to properly extract the MTE beam and the corresponding experimental results are summarized in the following section.

6.2.2.4 Experimental results

After the installation of the bipolar PC for BSW14, the newly developed setup of the extraction bump could be experimentally tested. First, a low-intensity beam was used to verify the setup and avoid unnecessary high beam loss during this initial phase. The settings of the slow bump were programmed according to Fig. 6.68 (b) and an intensity measurement as well as the slow BLM signals are depicted in Fig. 6.72. If properly tuned, the whole MTE process occurs completely loss-free until the activation of the fast extraction bump during the last five turns. However, the BLM signals in SS16 and SS19 started to already increase about 1 ms prior to
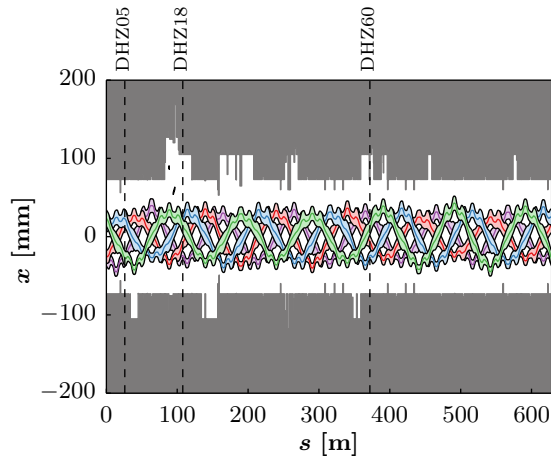
(a) Envelopes around the closed orbit after correction.
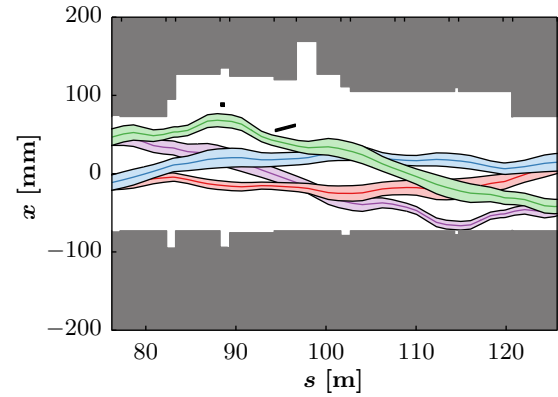
(b) Slow bump using B12 and B14 at 80% of 497 A and -510 A, respectively.
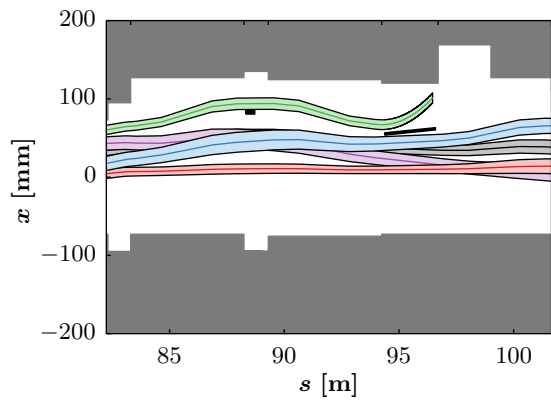
(c) Extraction of the first island. Shown are SS14-SS17.
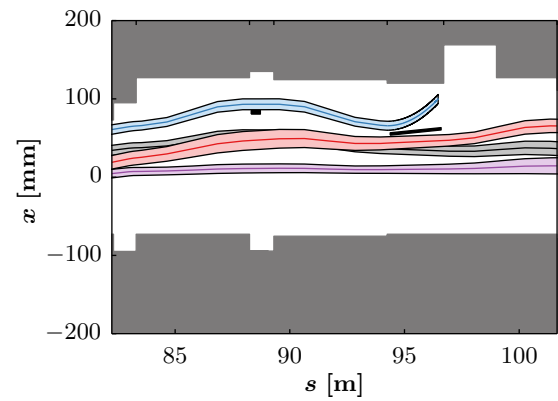
(d) Extraction of the second island.
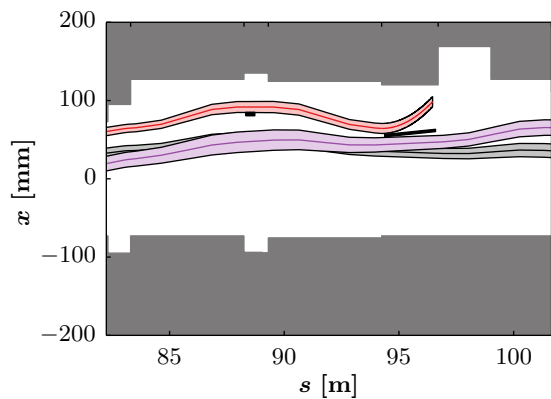
(e) Extraction of the third island.
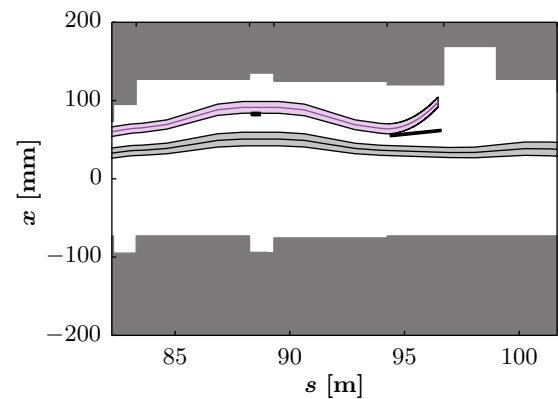
(f) Extraction of the fourth island.

Figure 6.70. Closed orbit, slow and fast bump applying the orbit correction shown in Fig. 6.68 (b). To improve the clearance between the beamlets at SMH16, the amplitude of the slow bump mentioned in the text was reduced by 20%, while the tune was increased to $Q_x = 6.257$.
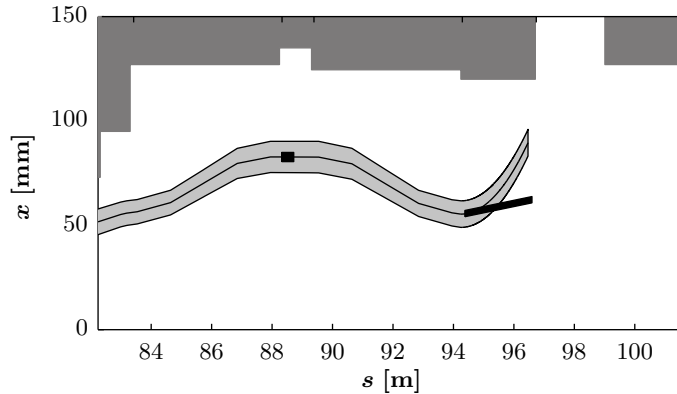
Figure 6.71. With TPS15 at 80.5 mm/0 mrad, the simulations suggest to move SMH16 to 56 mm/3 mrad to provide shadowing.
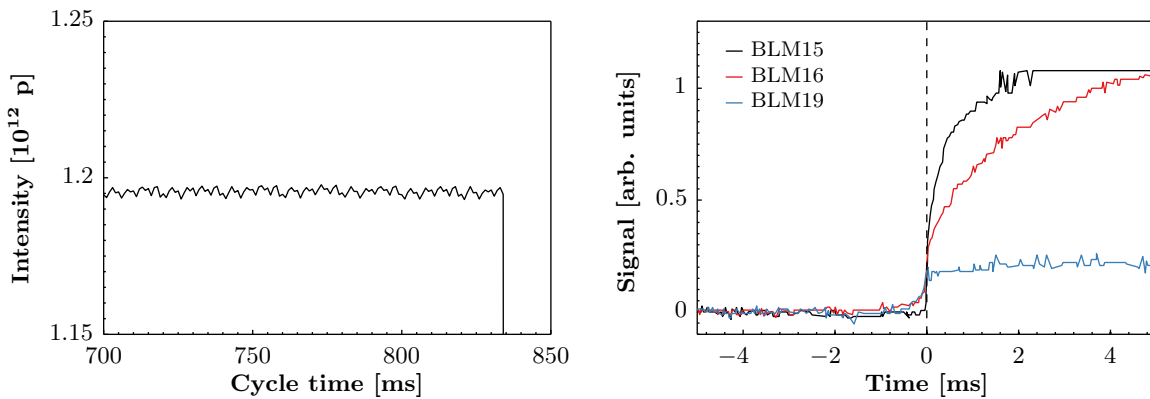
(a) BCT measurement at the end of the cycle. The intensity used during this test was more than ten times smaller than the operational requirement.

(b) Signals of the slow BLMs in the extraction region. The dashed line corresponds to the extraction timing. Some beam loss is observed before the maximum of the slow bump is reached.

Figure 6.72. Low-intensity test to verify the feasibility of the new extraction bump.

extraction, i.e. before the slow bump had reached its maximum. This could have been corrected by reducing the maximum amplitude of the slow bump, but was considered of marginal importance at this time, as the main aim was to proof the extraction principle. The subsequent increase of BLM15 and BLM16 is however unavoidable and, especially in SS15, also intended. Main beam loss is expected to occur in this well-shielded region, which is in line with the shown saturated BLM signal. Once shadowing conditions have been established, the losses in SS16 will be further reduced.

The only way to verify whether the islands are actually sent to the external side of TPS15 by
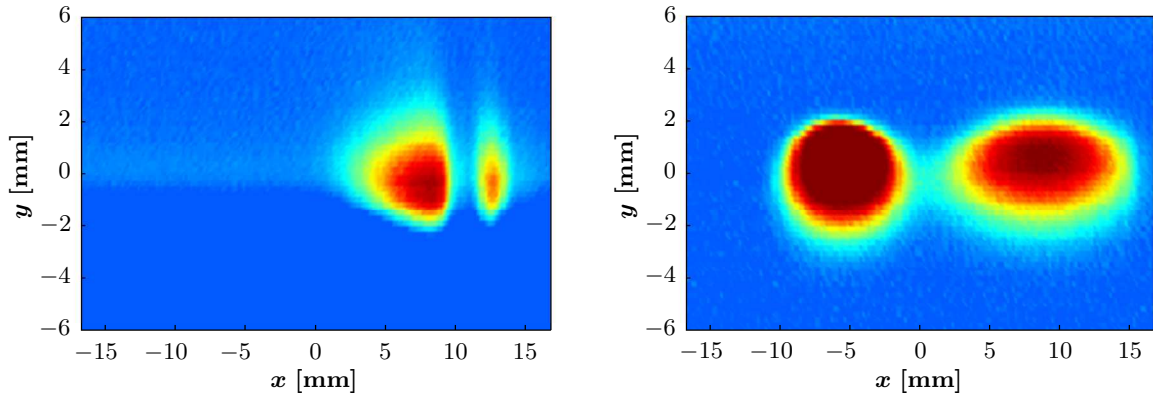
(a) For TPS15 at 86 mm, the islands are only partially extracted. The right spot corresponds to an optical reflection on the septum blade.

(b) Reducing the position of TPS15 to 80.5 mm allows to completely extract the islands on the external side of the septum. The left spot corresponds to the core, which was deliberately displaced for the purpose of illustration.

Figure 6.73. Measurements with the screen of TPS15.

the fast bump, is based on an observation system using a radiation resistant camera, a 90 degree mirror and an aluminium screen. The screen can be moved into the beam and the light created by the impact of the beam allows to reconstruct the transverse dimensions [16]. For two different positions of TPS15, measurements with this system are depicted in Fig. 6.73. As indicated by the simulations, positioning TPS15 at 86 mm provided insufficient aperture to properly extract the islands. The recorded screen image shows that a substantial fraction of the beam had been absorbed by the septum blade, leading to the remaining triangular distribution. Subsequent insertion of the blade to its minimum position provided sufficient space to correctly send the beam to the extraction channel. The respective measurement moreover shows the significantly different optics between the islands and the core. As 80% of the beam is captured in the islands, if the horizontal splitting has occurred within specifications, the optics matching to the downstream transfer line TT2 is based on the optics of these four beamlets. A certain optics mismatch is tolerated for the core, as it only contains the remaining 20% of the particles [97].

After this initial test phase the beam intensity was gradually increased, and the settings of the non-linear elements were modified to improve the adiabaticity of the splitting process. Crossing the resonance was brought forward by 40 ms compared to the settings shown in Fig. 6.44, and the arrival of the currents to their final values was rounded off to improve the rotation taking place in the horizontal phase space prior to extraction. Furthermore, it was understood and corrected that the magnets ONO39 and ONO55 were saturating at maximum current [98] (see Fig. 6.74).

These improvements provided the foundation for a first comparison between MTE and CT.

Looking at the pattern of beam loss along the PS ring shown in Fig. 6.75, the number of hot spots is reduced to a single one around SMH16. It is noteworthy that TPS15 had to be retracted to its parking position (120 mm), as it would have otherwise caused unacceptably high loss for the other operational beams. This issue was overcome at a later stage, when also the extraction schemes for the other users were redesigned [99]. By comparing losses for MTE to the CT case (see also Fig. 6.4), the benefit of extracting high-intensity beams using the MTE technique becomes immediately obvious. Instead of multiple saturated BLM signals in the CT case, only BLM16 (and occasionally BLM17) are found to saturate for MTE. As shown in Sec. 6.2.3, losses in SS17 could be reduced by improving the horizontal splitting in order to decrease the number of particles trapped between the islands and the core. These intermediate particles experience a certain deflection at SMH16 and are subsequently lost in SS17. Therefore, only BLM15 and possibly also BLM16 are expected to be saturated, once TPS15 is eventually aligned to shadow SMH16.

The mitigation of the effect of the PC ripple on the splitting process together with the new extraction bump allowed for the first time to continuously extract the MTE beam according to specification over an extended period of time, constituting a major milestone for the project. However, a comparison between the MTE and CT performances, where the data sets represent about 2.5 hours of statistics, showed that, even for significantly lower MTE intensity, the CT extraction efficiency was about 3% higher and fluctuating much less (see Fig. 6.76). This was rather unexpected, especially as TPS15 was kept at 120 mm to not perturb the CT extraction. These observations together with the emittance blow-up during the final rotation, which was observed in simulations (see Fig. 6.46 (d)), and the fact that the large negative horizontal angle of the external island at SMH16 (see e.g. Fig. 6.66 (b)) reduces the clearance between the beam and the septum blade during the fast bump, triggered further investigations to improve the
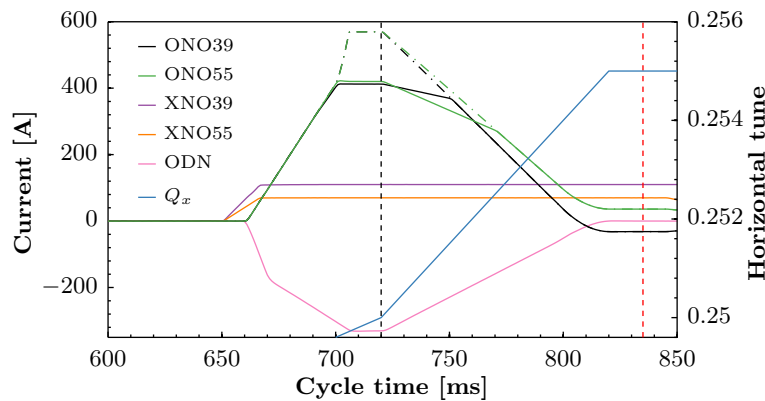
Figure 6.74. Configuration of the dedicated non-linear elements and the horizontal tune on the flat top used for the measurements depicted in Figs. 6.75 and 6.76. Resonance crossing and extraction are indicated by the dashed lines, while the dash-dotted lines correspond to the saturated octupole settings.
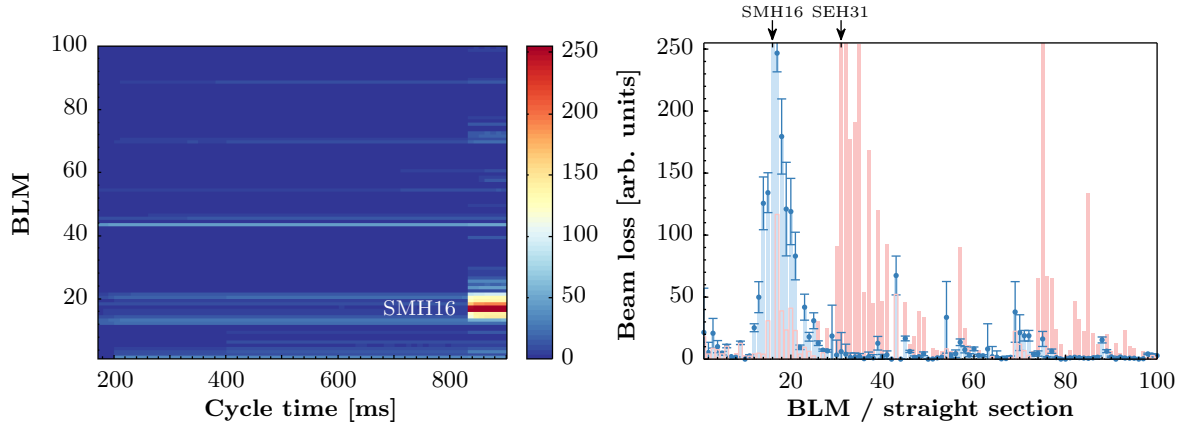
(a) Evolution of the beam losses all along the cycle. Maximum loss occurs during extraction around SS16. Minor losses at injection are apparent in SS42.

(b) Integrated beam losses after extraction. For comparison, the CT case is shown in red. The locations of the septa are indicated on the top and error bars correspond to the standard deviation of 300 consecutive measurements.

Figure 6.75. Measured beam loss on the MTE cycle in the PS ($N_p = 1.45 \times 10^{13}$ just before extraction).
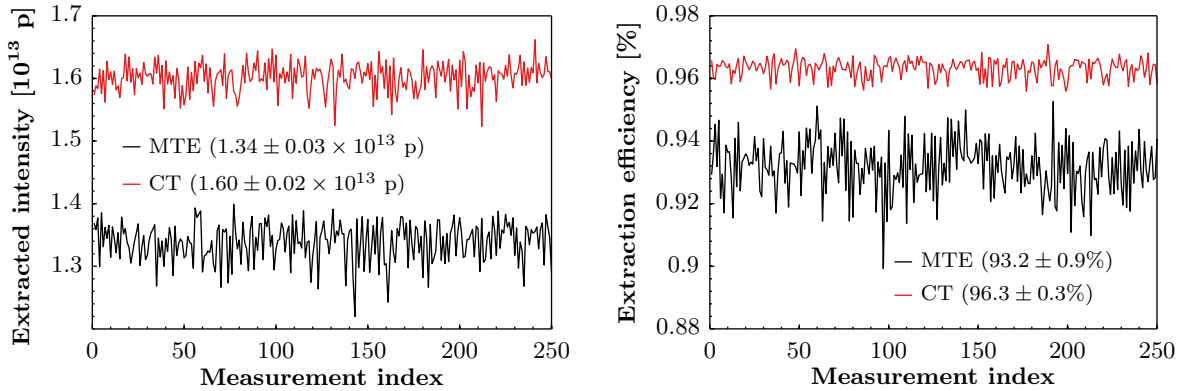
(a) MTE was extracted with 16% less intensity on average.

(b) Despite the higher intensity, the CT extraction efficiency was significantly better.

Figure 6.76. Comparison between MTE and CT in terms of extracted intensity (measured with BCT372 in TT2) and extraction efficiency recorded on 3 July 2015. The mean values and standard deviations over the 250 measurements are mentioned in the legends. The measurements took place with TPS15 in parking position.

MTE process. These additional steps are presented in the following.

6.2.3 Optimization of the rotation of the islands

After successfully splitting the beam in the horizontal phase space, the positions of the beamlets have to be rotated in order to prepare the MTE beam for extraction in SS16. Following the remarks in Section 6.2.1.2 and given the operational settings of the multipoles, this rotation process was observed to occur very quickly and, therefore, non-adiabatically. Eventually, this results in filamentation and emittance blow-up, as the particles captured inside the islands are not able to follow the rapid movement of the SFPs.

A first improvement of this situation consisted of rounding off the arrival of the multipole functions to their extraction values (see Fig. 6.77). Figure 6.78 confronts time-dependent simulation results with and without the application of this smoothing. Using the setup shown in Fig. 6.77, the whole rotation process takes only about 5 ms. During this time, the islands experience not only the rotation, but also a certain elongation. Furthermore, a small fraction of particles is expelled from the islands and remains trapped in-between the islands and the core. This is unfavourable for the subsequent extraction process, as these particles are lost during the rise of the fast bump, which reduces the overall extraction efficiency and increases the activation of the extraction region. In Fig. 6.78 (e) the horizontal phase space at the end of a rotation without any smoothing is demonstrated. The filamentation inside the islands is still ongoing at the chosen point in time, but the emittance increase with respect to Fig. 6.78 (d) is already clearly visible.

In Fig. 6.79, static simulation results of the horizontal phase space of the external island at SMH16 are illustrated during the time span of the rotation (indicated by the grey band in Fig. 6.77). At a timing of 809 ms, the beamlet is found to be perfectly positioned and reduced
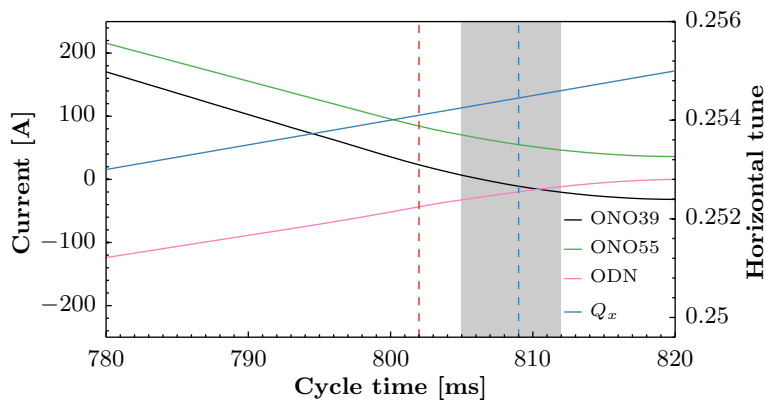
Figure 6.77. Improved setting of the octupoles by rounding off their arrival to the extraction values. The sextupole currents remained unmodified with respect to Fig. 6.74. The rotation occurs during the time indicated by the grey area and the dashed blue line corresponds to the optimum rotation angle at SMH16 (see also Fig. 6.79). The dashed red line illustrates the settings at 802 ms.

(a) Horizontal phase space at 805 ms.

(b) Horizontal phase space at 807 ms.

(c) Horizontal phase space at 809 ms.

(d) Horizontal phase space at 812 ms.

(e) Horizontal phase space at 810 ms.
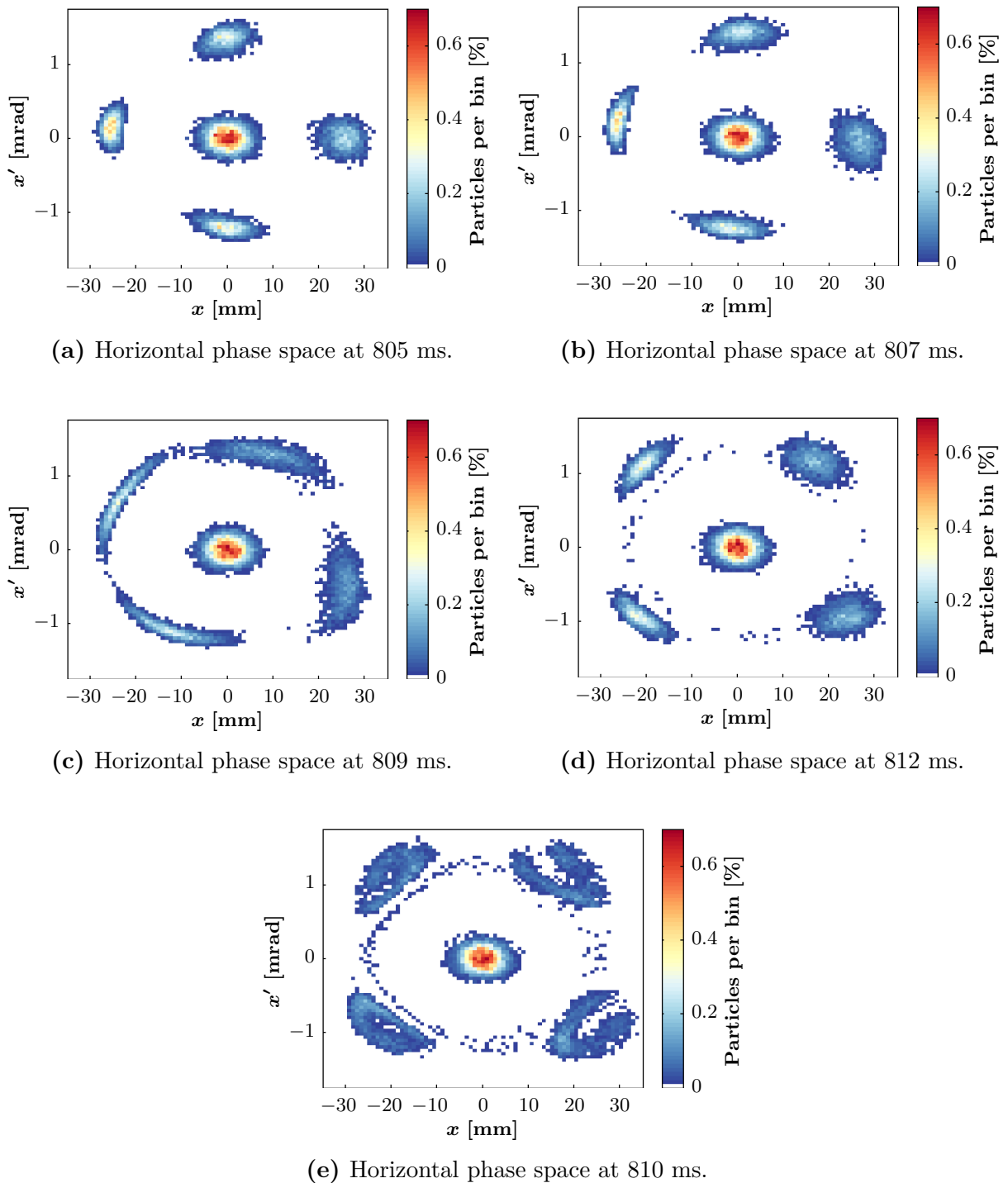
Figure 6.78. Time-dependent simulation results showing several snapshots during the final rotation. (a)-(d) correspond to the case with smoothing, while (e) corresponds to that without. Especially the benefit of rounding off the arrival of the octupole functions to their extraction values is visible, as the islands' emittances are better preserved and less particles are trapped between the islands and the core.

in size. If the rotation occurred adiabatically and could be frozen at this instant, minimum extraction losses would be expected for such a configuration. This is based on the fact that for an adiabatic rotation, no particles remain in-between the islands and the core and, furthermore, the clearance between the beam and the extraction septum is increased by reducing the beamlets' sizes. Even though the islands' phase space topology is rather distorted, the β_x−function is a representative measure of the beam size in the close vicinity of the SFP. Its behaviour for the external island is shown in Fig. 6.79 (d), and the rotation is found to be accompanied by a kind of discontinuity in the function.

The presented results led to the understanding that (i) the rotation has to occur significantly
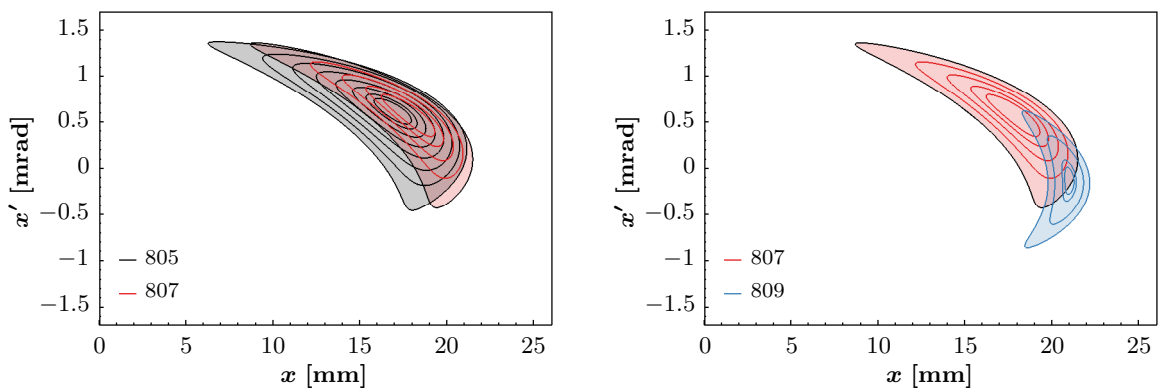
(a) Initially, the island experiences a squeeze.

(b) The main part of the rotation occurs within these 2 ms.
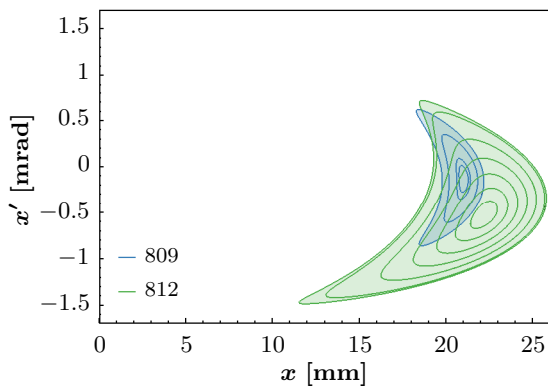
(c) At the end of the rotation, the beamlet increases again in size.
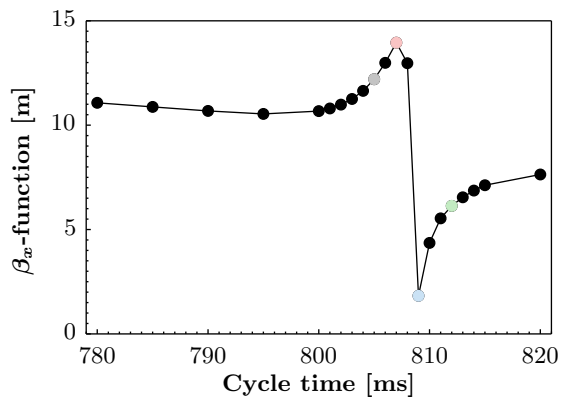
(d) Evolution of the β_x−function. The coloured markers correspond to the situations in (a)-(c).

Figure 6.79. Behaviour of the external island at the entrance to SMH16 during the final rotation (settings according to Fig. 6.77). As indicated by the time-dependent simulation results, the island is actually squeezed and rotated. To reduce losses at SMH16, the optimum position of this beamlet would correspond to the situation at 809 ms.

slower to preserve the splitting efficiency η_{MTE}, and (ii) the surface of the islands can be reduced by properly choosing the multipolar configuration. Nevertheless, it has to be considered that the reduction of the surface is always accompanied by a certain probability of de-trapping.

In a first step, it was decided to separate the splitting process from the rotation by choosing the final currents of the octupolar functions at values, which completely avoid the phase space rotation. The resulting configuration, which corresponds to the settings at 802 ms (indicated by the red dashed line in Fig. 6.77), applies the following currents:

$$I_{\mathrm{ONO39}} = 22.3\,\mathrm{A}, \quad I_{\mathrm{ONO55}} = 82.1\,\mathrm{A}, \quad I_{\mathrm{XNO39}} = 110\,\mathrm{A}, \quad I_{\mathrm{XNO55}} = 70\,\mathrm{A}, \quad I_{\mathrm{ODN}} = -43.9\,\mathrm{A}.$$

$$(6.24)$$

Secondly, it was desired to use only one out of the four ONOs and XNOs to perform an adiabatic rotation in a simple and controlled way. Therefore, simulations were performed to investigate the susceptibility of the positions of the SFPs to changes of the settings of these elements.

In Fig. 6.80, the response of the SFPs at TPS15 and SMH16 to variations of I_{XNO55} are demonstrated. To provide proper extraction conditions, $x'_{\mathrm{SMH16}} \approx 0$ mrad is sought for the outermost island, which can be achieved for a setting of $I_{\mathrm{XNO55}} = 160$ A. Additional simulations showed that such a configuration is also achievable by using ONO55 (see Fig. 6.81). Regarding the evolution of the β_x−functions during both scans (shown in Fig. 6.82), a similarity to Fig. 6.79 (d) is observed: close to the optimum settings, β_x experiences a significant jump, which can be exploited to reduce the island's size. Comparison of both scans additionally revealed that using ONO55 increases the particle amplitude more significantly. Therefore, it was chosen to perform the adiabatic rotation with XNO55, and to achieve the required final separation of the beamlets by carefully adjusting the horizontal tune. Scans with the remaining elements XNO39 and ONO39 were also conducted and revealed similar movement of the islands, but are not shown here for the sake of brevity.

In Fig. 6.83, the multipole settings to optimize the final rotation are depicted. As previously explained, the currents of ONO39 and ONO55 are kept constant from 802 ms onwards. Additionally, the strength of XNO55 is slowly increased until it reaches the required 160 A. The corresponding time-dependent simulation results are presented in Fig. 6.84 and the islands are shown to slowly adapt to the new configuration. Thereby, they are elongated and the external one is reduced in horizontal size, which provides additional margin for the proper extraction process.

Finally, the setup of the extraction bumps had to be verified using these new multipole currents. As discussed in the previous sections, the maximum slow bump amplitude is constrained by the available aperture in MU19 and, as shown by the phase space portraits in Fig. 6.85, the tune can be increased up to $Q_x = 6.262$ in order to achieve maximum separation of the beamlets. It has to be noted that the amplitude excursion due to the slow bump does not only generate a quadrupolar feed-down, but includes also higher-order effects. This becomes especially visible

(a) Situation at TPS15.

(b) Situation at SMH16.
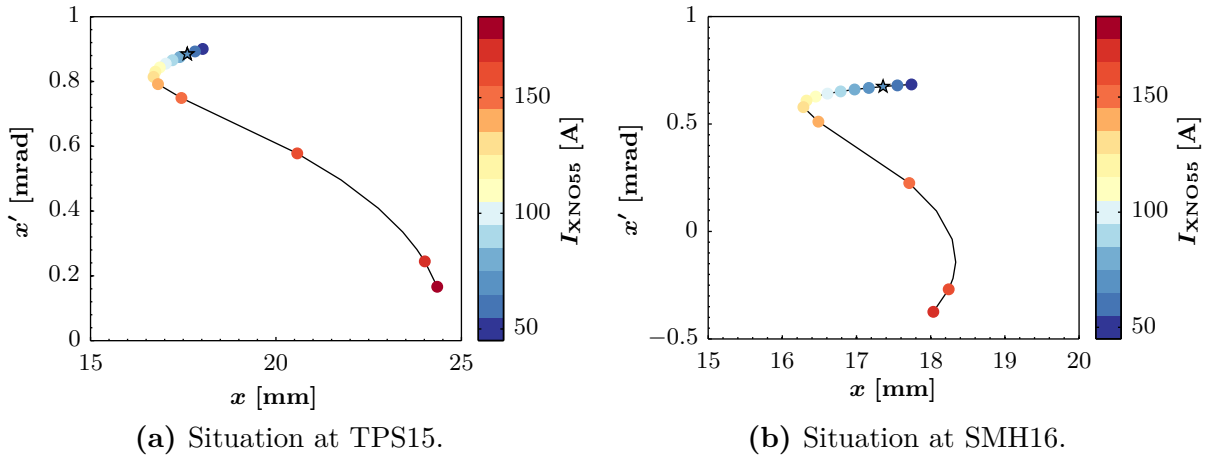
Figure 6.80. Dependency of the SFP of the external island on the strength of XNO55. The stars indicate the initial positions according to Eq. (6.24) and the tune was kept at $Q_x = 6.255$ for all cases.

(a) Situation at TPS15.

(b) Situation at SMH16.
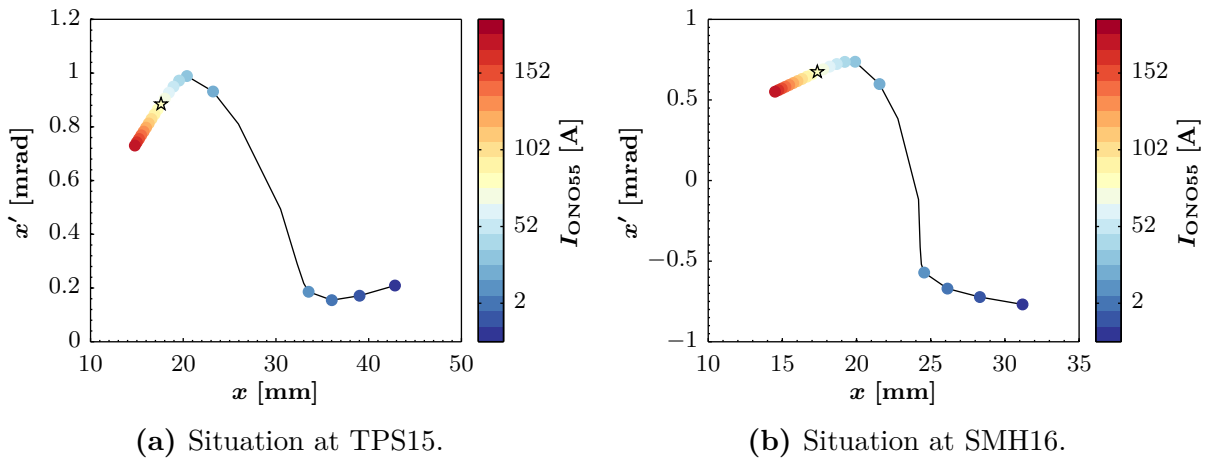
Figure 6.81. Dependency of the SFP of the external island on the strength of ONO55. The stars indicate the initial positions according to Eq. (6.24) and the tune was kept at $Q_x = 6.255$ for all cases.

(a) Scan with XNO55.

(b) Scan with ONO55.
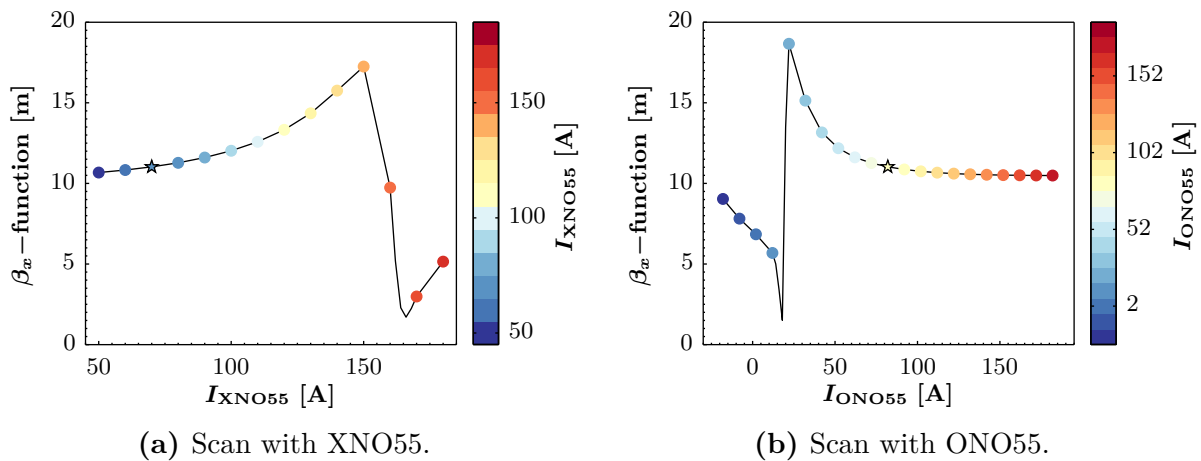
Figure 6.82. Variation of the β_x−functions during the scans with XNO55 and ONO55. The stars indicate the initial values according to Eq. (6.24).
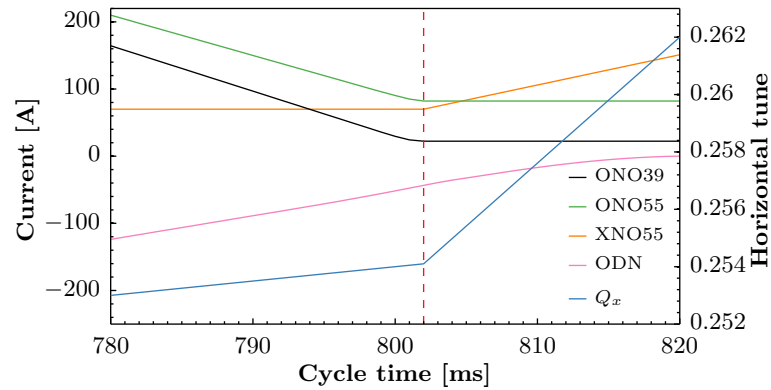
Figure 6.83. Multipole settings used to perform an adiabatic rotation with XNO55. The ramp-down of the octupoles is stopped at 802 ms (red dashed line), and XNO55 starts to increase at the same time. To achieve proper final separation of the islands, the tune is increased to $Q_x = 0.262$. All functions are kept constant after 820 ms. XNO39 remains unmodified at 110 A during the whole process.

(a) Situation at 810 ms.

(b) Situation at 815 ms.

(c) Situation at 820 ms.
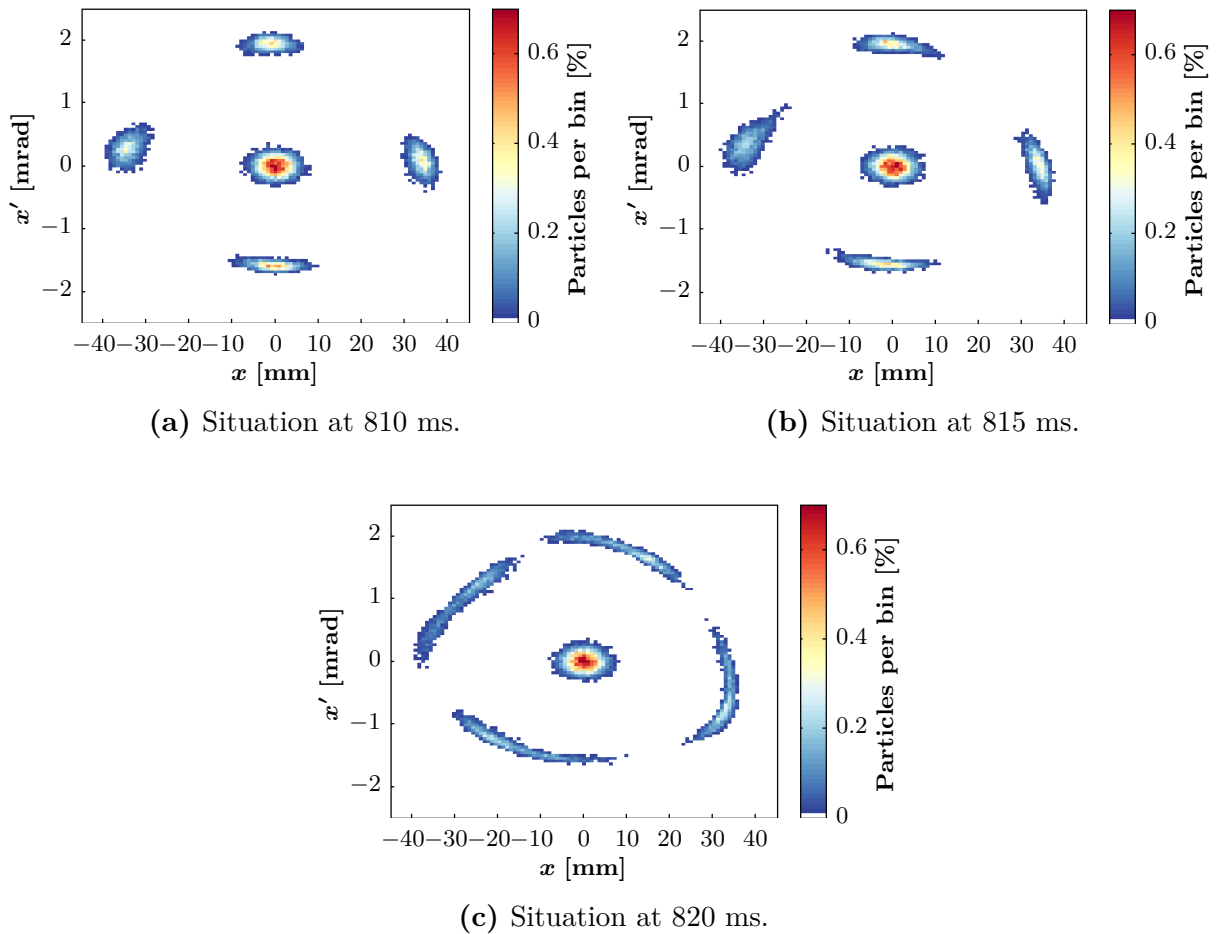
Figure 6.84. Phase space portraits in SS01 during an adiabatically performed rotation. The applied settings correspond almost to those of Fig. 6.83, with the final tune being only $Q_x = 6.255$ instead of 6.262.

(a) Horizontal phase space at TPS15.

(b) Horizontal phase space at SMH16.

(c) Horizontal phase space at MU19.
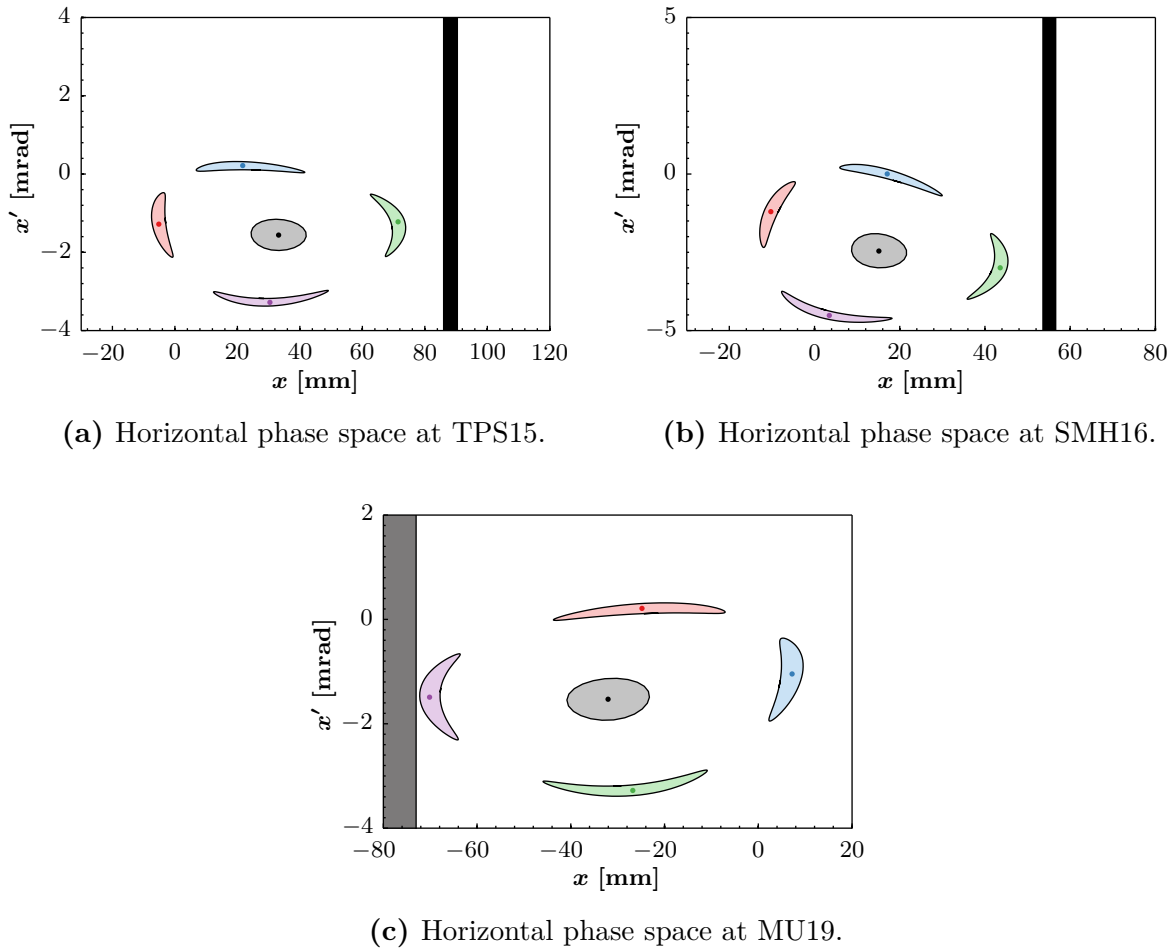
Figure 6.85. Phase space portraits at the maximum slow bump amplitude, applying $Q_x = 6.262$, $I_{B12} = 497$ A and $I_{B14} = -510$ A.

when comparing the position of the external island at SMH16 in Figs. 6.80 and 6.85, as the SFP appears even further rotated in the latter one. Overall, this setup allows to position the beamlets in a very similar way as it was obtained in Sections 6.2.2.2 and 6.2.2.3. The subsequent activation of the fast extraction kickers KFA13 and KFA21 then sends the beam to the external sides of TPS15 and SMH16 as intended. In Fig. 6.86 the second beneficial effect of the presented approach, besides the adiabatic rotation, is illustrated: the compression of the islands provides additional clearance between the beam and the blades of the septa and only particles in the tails of the island's distribution are likely to be absorbed. Moreover, the value of the dispersion function of the external island at SMH16 is significantly reduced from $D_x = 4.52$ m to $D_x = 0.11$ m, which is another justification for not considering the dispersive contribution during the design of this extraction bump. Therefore, the combination of the adiabatic rotation, which significantly reduces the number of particles captured between the islands and the core, and the small beam size at extraction, is expected to further increase the efficiency of the MTE process.

(a) Horizontal phase space at TPS15.

(b) Horizontal phase space at SMH16.
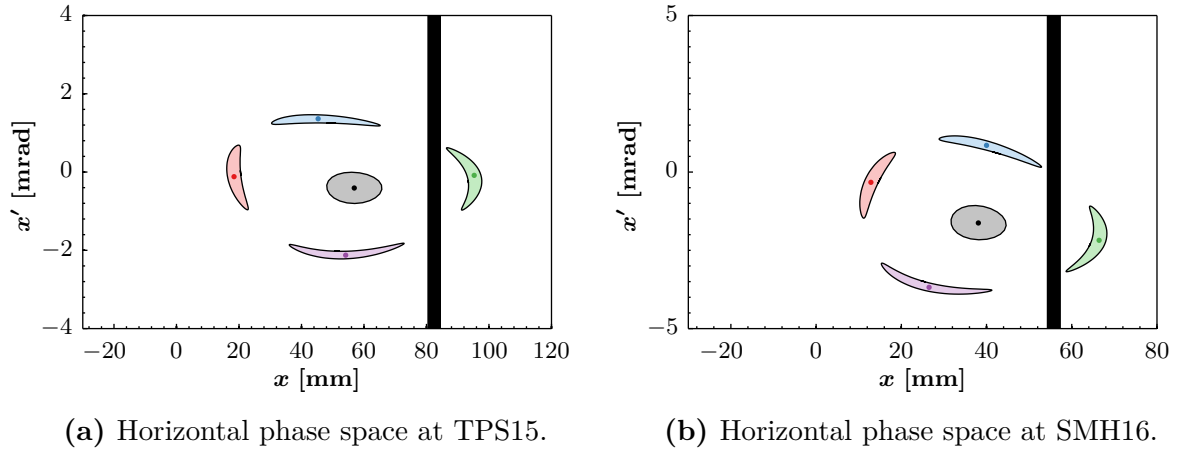
Figure 6.86. Fast extraction bump using KFA13 and KFA21 at 60 kV.
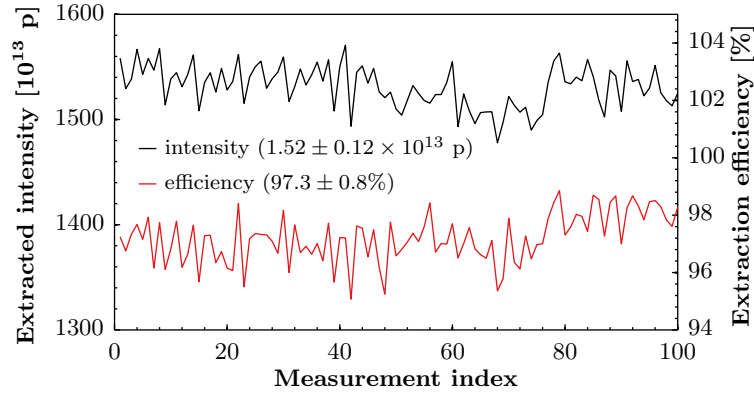
Figure 6.87. Experimental verification of the beneficial impact of the adiabatic rotation on the extraction efficiency.

The multipole settings proposed in this section were experimentally implemented and an the expected gain in extraction efficiency was indeed observed. Figure 6.87 presents the corresponding measured results, which show an improvement of about 4% with respect to the values mentioned in Fig. 6.76.

However, it should be remembered that the dedicated sextupoles in SS39 and SS55 are applied for chromaticity correction. For the case under discussion, the horizontal chromaticity becomes actually slightly negative by increasing XNO55 to 160 A, which is obviously undesired as MTE operation takes place above the transition energy. For the intensities, which are presently being operationally used, however, no instabilities have been observed. One the one hand, this is based on the fact that the whole process of rotating the phase space takes place only 6 ms prior to debunching and 15 ms prior to extraction, which restricts the available time for an instability to develop. On the other hand, the intensity per beamlet is rather small due to the transverse splitting.

The final step pursued in the framework of this thesis to further increase the extraction efficiency, i.e. positioning SMH16 in the shadow of TPS15, is presented in the next section.

6.2.4   Shadowing

The last objective in order to make MTE an operational replacement of CT was the establishment of shadowing conditions. One should recall that TPS15 was installed to reduce the activation of SMH16 by relocating the losses from SS16 to the well-shielded SS15. As set forth throughout Section 6.2.2, the position and angle of TPS15 had to be fixed to the values of 80.5 mm and 0 mrad, respectively, in order to provide sufficient separation between the beam and the septum blade during the extraction process. Therefore, the only remaining degrees of freedom corresponded to the position and angle of SMH16 and a fine scan of these parameters was experimentally conducted to determine the settings, which position SMH16 in the shadow of TPS15 and, therefore, minimize beam loss in SS16.

The essential component of the applied measurement procedure is the fast BLM16, which allows to resolve beam loss on a time scale shorter than one turn. Hence, losses occurring during the extraction of the islands can be distinguished from those created during the final turn. In Fig. 6.88 a typical beam loss pattern during the last five turns, corresponding to 10.5 μs, is shown. The first peak is proportional to losses occurring during the rise time of KFA13 and KFA21 (360 ns between 10-90% of the maximum strength), while the second, smaller, peak describes beam loss caused by the rise of KFA71 (70 ns between 10-90% of the maximum strength) [16]. To evaluate the shadowing efficiency, the sum of the amplitudes of both peaks was considered as figure of merit and the dependency of this value on the position (Fig. 6.88) and angle (Fig. 6.89) of SMH16 was investigated. For an angle of 0 mrad, beam loss was observed to be a quadratic function of the position, with a minimum located at 58.65 mm. The losses measured at this position corresponded to a reduction by about a factor three compared to the value obtained for the settings of TPS15 and SMH16, which were considered operational at the time these measurements were conducted (82.5 mm/0 mrad and 55.5 mm/3 mrad, respectively). Regarding the extraction efficiency, an additional increase of about 1% with respect to the data shown in Fig. 6.87 was obtained; however, the statistical fluctuation appeared to be rather large. Therefore, an investigation as explained in Section 6.2.1 was carried out, by measuring the cycle-by-cycle variation of the frequency component at 5 kHz of the main magnetic field and comparing it to the signal of the slow BLM16. In Fig. 6.88 (d), both signals are shown to oscillate in a correlated manner, which led to the conclusion that the noise of the PCs of the PFW still affected the MTE process, even though the ripple amplitude had been significantly reduced (see Fig. 6.41). The effect is actually twofold: on the one hand, the splitting process itself is affected, causing particles to be expelled from the islands and, on the other hand, the islands' positions are modulated. Both effects contribute to the observed cycle-by-cycle variation of the losses in SS16 and, hence, the extraction efficiency.

Based on the results of the position and angle scans, it was decided to choose the following settings as new operational configuration: TPS15 at 80.5 mm/0 mrad, SMH16 at 57.5 mm/1 mrad. Even though these values do not correspond to the observed optimum, they constitute an ac-
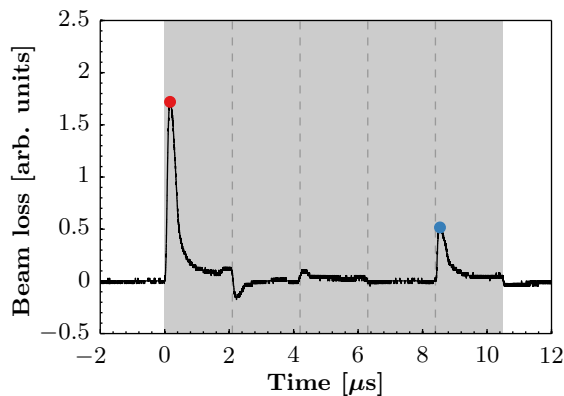
(a) Signal of the fast BLM16. The grey area indicates a duration of five turns, with the dashed lines being separated by one turn. The red and the blue circles correspond to the maximum beam loss occurring during the extraction of the islands and the core, respectively.
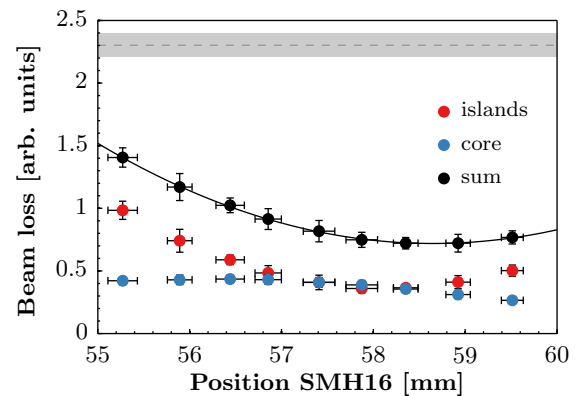
(b) Dependency of beam loss on the position of SMH16 for an angle of 0 mrad. Red and blue circles correspond to the losses of the islands and the core as described in (a), and the black circles represent their sum. Error bars describe the standard deviation obtained over 10 consecutive measurements. The parabolic fit (solid black line) $0.72 + 0.06(x - 58.65)^2$, reveals a global minimum at 58.65 mm. The dashed line and the grey band indicate mean value and standard deviation of losses for the nominal septa settings.
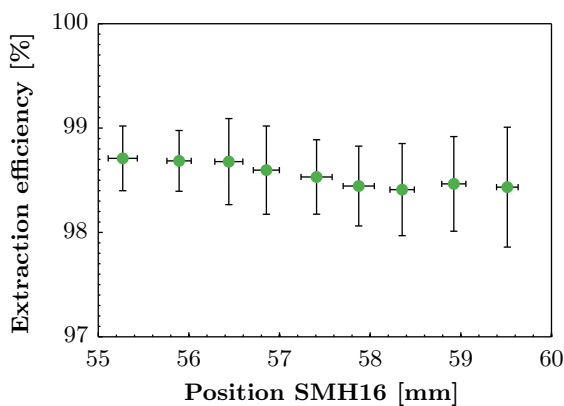
(c) Dependency of the extraction efficiency on the position of SMH16.
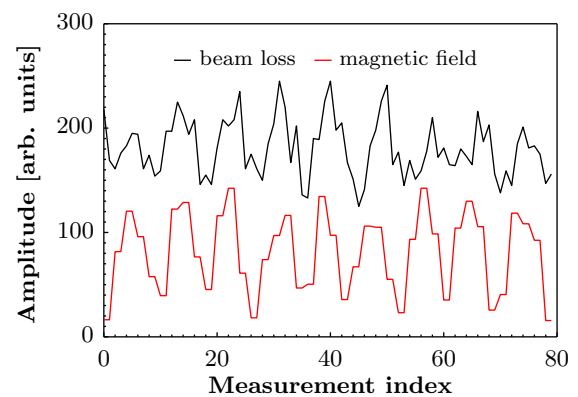
(d) Correlation between the signal of the slow BLM16 and the amplitude variation of the 5 kHz component of the main magnetic field (TPS15 at 80.5 mm/0 mrad, SMH16 at 57.5 mm/1 mrad).

Figure 6.88. Scan of the position of SMH16.

(a) Dependency of the losses measured with the fast BLM16 on the angle. The grey band indicates again the values for nominal septa settings.

(b) Extraction efficiency.
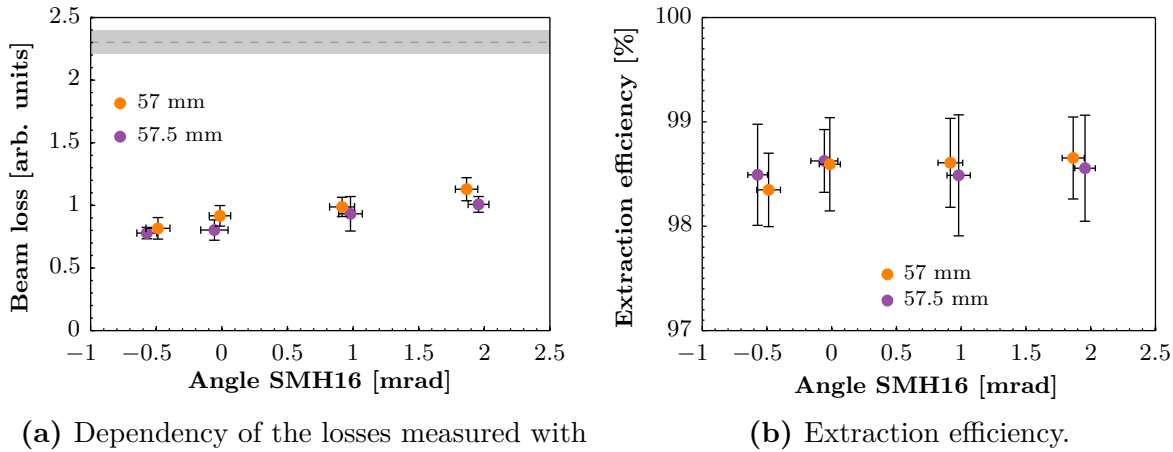
Figure 6.89. Scan of the angle of SMH16 for the two positions indicated in the legend.

ceptable compromise for both MTE and the other operational users, for which a redesign of the optics was inevitable in order to overcome the obstacle represented by this reduced extraction channel [99].

Measurements with the slow BLMs, which are presented in Fig. 6.90, confirmed the intended reduction of losses in SS16. BLM15 was found to be the only remaining saturating device.
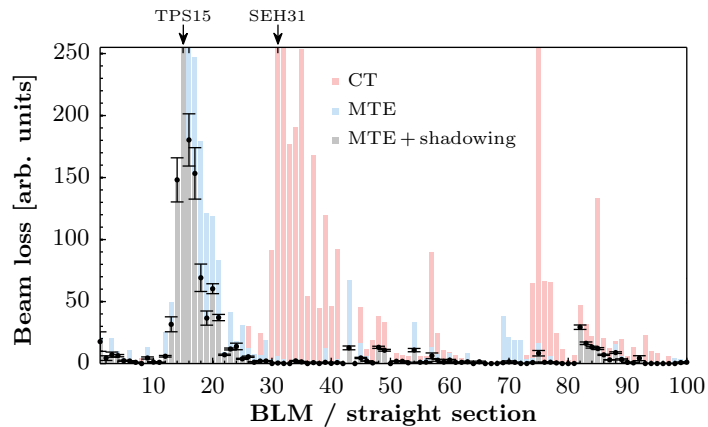
Figure 6.90. Integrated beam loss measured after extraction on the MTE cycle using TPS15 and SMH16 in shadowing configuration ($N_p = 1.55 \times 10^{13}$ just before extraction). Only BLM15 is saturated, and beam loss at the adjacent SMH16 is significantly reduced. For comparison, the MTE case with TPS15 in parking position and the CT case are shown. Error bars correspond to the standard deviation of 500 consecutive measurements.

6.3   Investigation of the longitudinal dynamics for MTE

6.3.1   Effect of the longitudinal motion on the splitting efficiency

Coupling between the horizontal and the longitudinal plane via the chromaticity and the dispersion can lead to a significant reduction of the splitting efficiency η_{MTE}. Therefore, the magnetic setup of the machine aims at reducing the chromatic tune spread by setting the chromaticity to small positive values (see Fig. 6.9), and at minimizing the RF voltage to obtain bunches with small energy spread. In this section the effect of the longitudinal motion on the islands' formation is studied in more detail and simulations are presented, which illustrate the effect of the longitudinal on the horizontal motion. Furthermore, a simple scaling law describing the dependency of η_{MTE} on δ is inferred from time-dependent simulation results.

In the first instance, the impact of the longitudinal motion on the phase space trajectories of a single particle was investigated. In Fig. 6.91, the movement of a core particle and its dependency on the longitudinal amplitude is illustrated. If the particle moves close to the centre of the longitudinal distribution, it experiences only a small energy variation caused by its synchrotron oscillations. Via the dispersion function, this leads to a small but continuous modulation of the particle's trajectory in the horizontal phase space. With increasing longitudinal amplitude, this modulation increases as well, and the change of the horizontal oscillation amplitude follows the well-known dispersion relation

$$\Delta x = D_x \, \delta. \tag{6.25}$$

In Fig. 6.91 (d) a longitudinally matched distribution of 20000 particles is displayed in order to visualize the longitudinal density in the vicinity of the chosen trajectories. Less than 1% of the distribution is situated close to the separatrix, i.e. outside the black trajectory, and, therefore, only very few particles experience the important horizontal modulation shown in Fig. 6.91 (c). Furthermore, it has to be borne in mind that a realistic longitudinal distribution of a proton bunch is more parabolic than Gaussian, which decreases the large-amplitude density even further.

Figure 6.92 presents the variation of the horizontal trajectory of a particle in the islands. The shown situation corresponds to that before the final rotation, and the surface of each island is found to be modulated differently, as the SFPs and UFPs move differently depending on the respective value of D_x. Considering that the value of D_x of the external island at SMH16 was significantly reduced by implementing the adiabatic rotation with XCT55, another reason for the improved extraction efficiency (see Section 6.2.3) of this new scheme is clearly illustrated: as the modulation of the horizontal position is almost eliminated, close to no particles will be interacting with the septum blade.

Synchrotron motion can also result in an even more important change of horizontal amplitude, which is illustrated in Fig. 6.93. On the one hand, core particles can follow the islands' sepa-

(a) Horizontal phase space trajectory of a particle with $\delta_{\max} = 0.2 \times 10^{-3}$.

(b) Horizontal phase space trajectory of a particle with $\delta_{\max} = 0.5 \times 10^{-3}$.

(c) Horizontal phase space trajectory of a particle with $\delta_{\max} = 1.2 \times 10^{-3}$.

(d) Longitudinal phase space trajectories at different amplitudes. The separatrix applying the operational MTE settings ($V_{\mathrm{RF}} = 12$ kV, $h = 16$) is shown by the black dashed line. The legend states the maximum value of δ for each trajectory and the coloured background illustrates a bi-Gaussian matched distribution ($\delta = 0.5 \times 10^{-3}$) as used for time-dependent simulation studies.

Figure 6.91. Effect of synchrotron motion on the horizontal phase space trajectory of a core particle. The red dashed lines represent pure horizontal motion, while the other trajectories are obtained using 6D tracking. The colours of the solid lines in (a)-(c) describe the particle's amplitude in the longitudinal phase space according to (d). The shown situation corresponds to resonance crossing, i.e. maximum octupole current and $Q_x = 6.25$. The value of the horizontal dispersion function at the chosen location (SS01) is $D_x = 3.04$ m.

(a) Horizontal phase space trajectory of a particle with $\delta_{\mathrm{max}} = 0.2 \times 10^{-3}$.

(b) Horizontal phase space trajectory of a particle with $\delta_{\mathrm{max}} = 0.5 \times 10^{-3}$.

(c) Horizontal phase space trajectory of a particle with $\delta_{\mathrm{max}} = 1.2 \times 10^{-3}$.

Figure 6.92. Effect of synchrotron motion on the horizontal phase space trajectory of a particle inside the islands. The magnetic settings of the machine correspond to those at 800 ms in Fig. 6.77 and the applied colour code indicates the longitudinal particle amplitude according to Fig. 6.91 (d).

ratrices just to finally end up circulating around the islands. Thereby, the particle's amplitude experiences a large change. On the other hand, large amplitude particles can be trapped inside the islands increasing their population. In contrast to purely transverse motion, synchrotron oscillations induce a periodic crossing of the resonance, which can result not only in trapping, but also in de-trapping [100].

Based on the above considerations it becomes clear that longitudinal motion plays an important role in the MTE process. Especially during the first milliseconds after resonance crossing, when the formation of the islands takes place, the spitting process is prone to be affected by the longitudinal dynamics. To further investigate this phenomenon, several time-dependent simulation
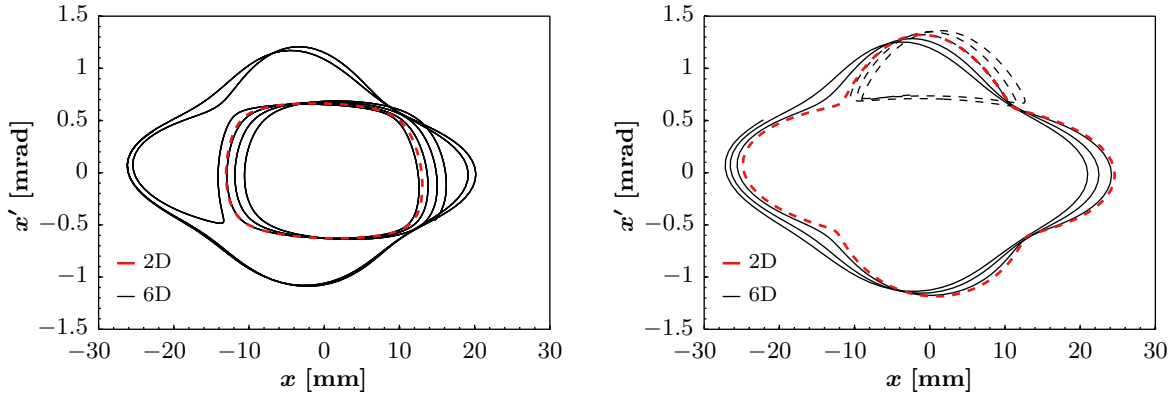
(a) Transport of a core particle to large amplitude via trapping inside the islands.

(b) Trapping of a large amplitude particle inside the islands.

Figure 6.93. Examples of significant changes in horizontal amplitude caused by a particle's energy modulation.

studies using different initial longitudinal distributions were conducted. By changing the RF voltage while keeping the bunch length constant, it was possible to create distributions that differ only in terms of δ. The respective simulation results are presented in Fig. 6.94. For very low RF voltage (see Fig. 6.94 (a)), high splitting efficiency of $\eta_{\mathrm{MTE}} \approx 17\%$ was observed, and the size and shape of the four islands appear to be almost equivalent in the corresponding phase space plot. This is insofar understandable, as the dispersive contribution to the beam size is almost suppressed by achieving such a low momentum spread of the beam. However, in practice this RF setup is unusable and, therefore, the minimum achievable voltage of $V_{\mathrm{RF}} = 12$ kV, which is required to keep the radial position of the beam under control, is applied during operation. Figure 6.94 (b) presents simulation results with this voltage and the effect of the dispersion becomes clearly visible as the size of the islands varies significantly. Starting at the external island and continuing clockwise, the following values of the horizontal dispersion function are obtained at the beginning of the simulated lattice:

$$D_x^{\mathrm{isl1}} = 5.14 \text{ m}, \ D_x^{\mathrm{isl2}} = 2.88 \text{ m}, \ D_x^{\mathrm{isl3}} = 0.87 \text{ m}, \ D_x^{\mathrm{isl4}} = 3.01 \text{ m}. \tag{6.26}$$

Increasing the RF voltage further results in a reduction of the number of particles captured in the islands and, once the momentum spread reaches values corresponding to about three times the operational configuration, the islands are barely distinguishable from the core and form a broad cloud of particles.

These simulations confirmed the importance of decoupling the longitudinal and transverse dynamics, which had been experimentally observed before. Depending on their longitudinal amplitude, particle trajectories are continuously modified throughout the splitting process, and do

(a) $V_{\mathrm{RF}} = 2$ kV, $\delta = 0.14 \times 10^{-3}$.

(b) $V_{\mathrm{RF}} = 12$ kV, $\delta = 0.49 \times 10^{-3}$ (operational situation).

(c) $V_{\mathrm{RF}} = 50$ kV, $\delta = 1.01 \times 10^{-3}$.

(d) $V_{\mathrm{RF}} = 100$ kV, $\delta = 1.42 \times 10^{-3}$.
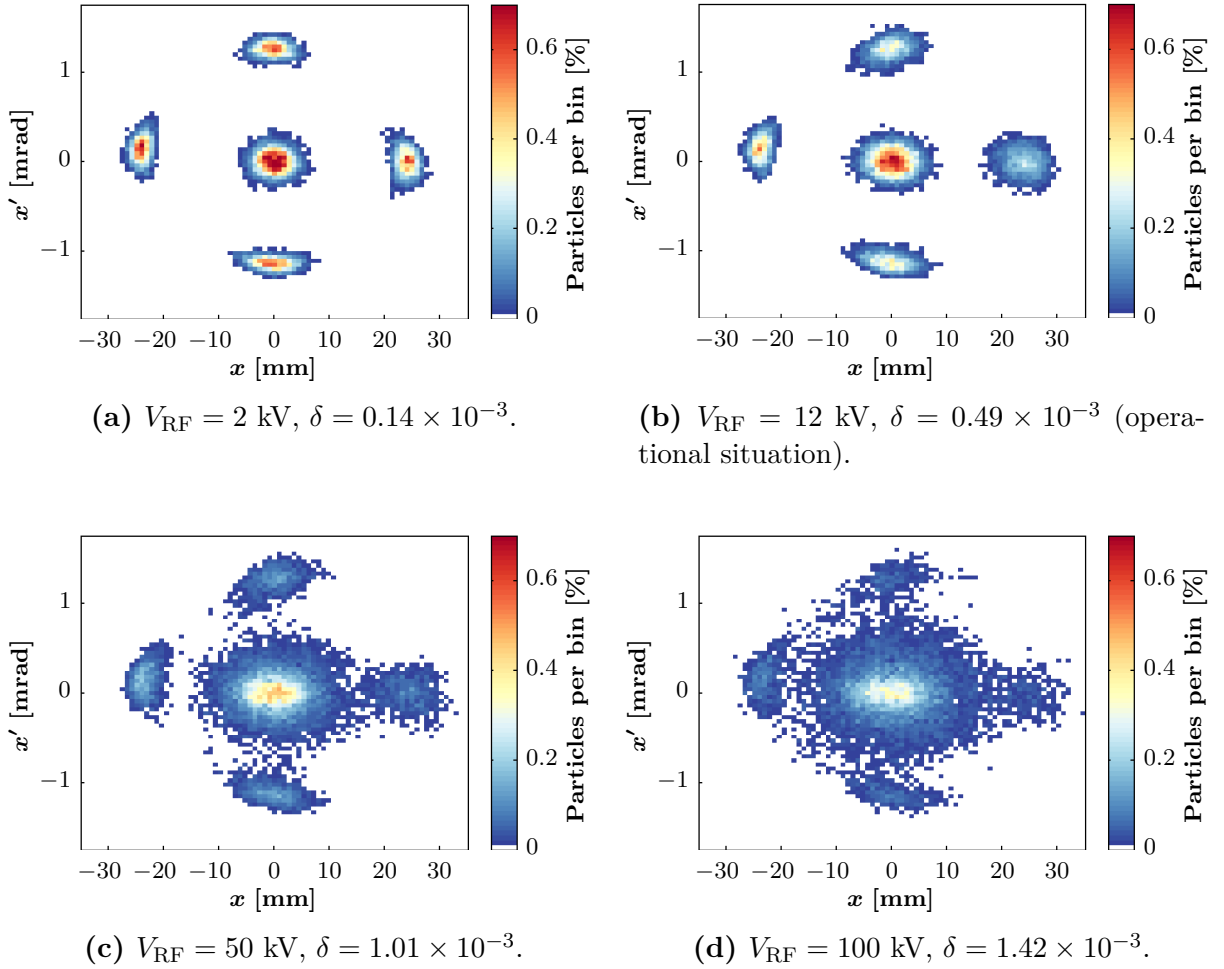
Figure 6.94. Comparison of time-dependent simulation results for different settings of the RF voltage. For high values of δ, less particles are captured in the islands.

no longer agree with the expectations based on pure 2D motion. If a system following the principles of linear dynamics were considered, this would simply lead to an increase of the beam size. However, the presence of additional SFPs complicates the situation and results in the observed reduction of η_{MTE} if the positions of these SFPs experience a significant modulation.

On the basis of the previously presented results, the dependency of the splitting efficiency on the momentum spread of the beam was investigated. First, it was verified that the momentum spread of the different longitudinal distributions used for the simulations is indeed proportional to the square root of the RF voltage. In Fig. 6.95(a), this well-known relation is confirmed and the obtained best fit is

$$\delta = (0.149\sqrt{V_{\mathrm{RF}}} - 0.038) \times 10^{-3}, \tag{6.27}$$

for V_{RF} in kV. In the next step, the splitting efficiency η_{MTE} was determined by considering only particles with a horizontal amplitude of less than 15 mm. Thereby, identifying the number of particles captured in the islands was simplified, as D_x is minimum for this beamlet. The obtained quadratic dependency of the form

$$\eta_{\mathrm{MTE}} = 17.32 - 4.56\,\delta - 3.74\,\delta^2, \tag{6.28}$$

which is valid for δ in units of 10^{-3}, is depicted in Fig. 6.95 (b). The decrease of the splitting efficiency with increasing momentum spread of the beam is clearly visible.

Benchmarking of these simulation results with experimental data has not yet been performed in great detail; however, the implementation of an offset in the above formula is expected to be required in order to account for the absence of the transverse damper in the model.

6.3.2 Implications of a non-linear momentum compaction factor

In view of the upcoming CNGS operation, the transmission and the longitudinal structure of the MTE beam in the SPS were studied in 2008. The results of these tests are described in [101], and significant differences between the longitudinal bunch profiles of the islands and the core were described. Furthermore, a bunch-by-bunch intensity variation of the islands was observed (see Fig. 6.96). As explained in Section 6.1.2.2, the beam in the PS is debunched a few milliseconds before extraction and partially recaptured using a 200 MHz RF system. This approach is necessary to reduce longitudinal losses in the SPS by adapting the bunch structure to the frequency
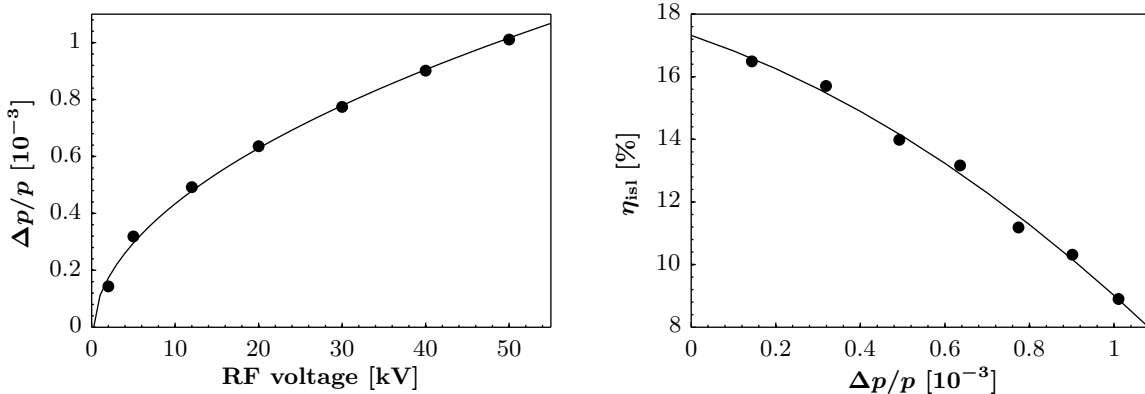
(a) Dependency of the momentum spread on the RF voltage.

(b) Dependency of the splitting efficiency on the momentum spread.

Figure 6.95. Simulation-based scaling laws describing the longitudinal dynamics and the splitting efficiency. The solid lines represent the best fit based on a non-linear least square method.
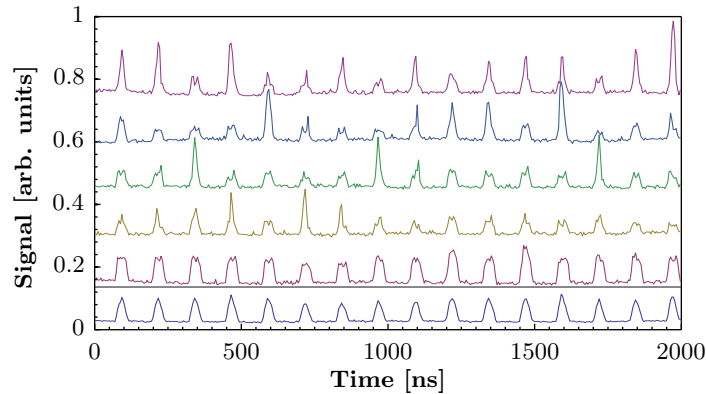
Figure 6.96. Longitudinal bunch structure observed in the SPS in 2008 [101]. The first four lines correspond to the signals of the islands, the fifth one to the core and the last one to the sum of all signals divided by five. Important amplitude variations and intra-bunch motion are observed for bunches originating from the islands, but the sum signal shows a rather conventional distribution.

of the SPS RF system. However, the modulation of the beam at 200 MHz could be excluded as possible cause of the peculiar bunch structure and, therefore, additional studies aiming at an explanation of the observed phenomenon were carried out and are presented in the following.

In a first approach, the results of the time-dependent simulations presented in the previous section were used to examine the longitudinal distributions of the islands. It was investigated whether the horizontal splitting is accompanied by a longitudinal selection process, which could explain the peculiar bunch structure. Figure 6.97 presents the projections of the islands' longitudinal distributions in s and δ for the case $V_{\mathrm{RF}} = 12$ kV. No significant differences between the distributions are observed. Even though not displayed, also the distribution of the core is very similar to those of the islands; however, the amplitude of the projection is higher by about a factor four, which is due to the higher intensity of this beamlet. Therefore, these findings are unable to explain the SPS bunch structure and a different approach was pursued.

This second procedure consisted of analytically evaluating the effect of the non-linearities required for the MTE process on the longitudinal motion. Therefore, the non-linear extension of the momentum compaction factor α_c, which was introduced in Eq. (2.18), was determined. This allowed to obtain expressions for the different orders of the slip factor η, according to

$$\eta(\delta) = \eta_0 + \eta_1\delta + \eta_2\delta^2 + \eta_3\delta^3 \ldots . \tag{6.29}$$

The non-linear terms become especially important close to the transition energy, where the linear part η_0 vanishes. Depending on the strengths of the non-linearities, the buckets can experience an important distortion or, above a certain threshold (see Eq. (6.48)), completely change their shape and adapt an α-like form (see Fig. 6.98). These α-buckets can be exploited at light sources
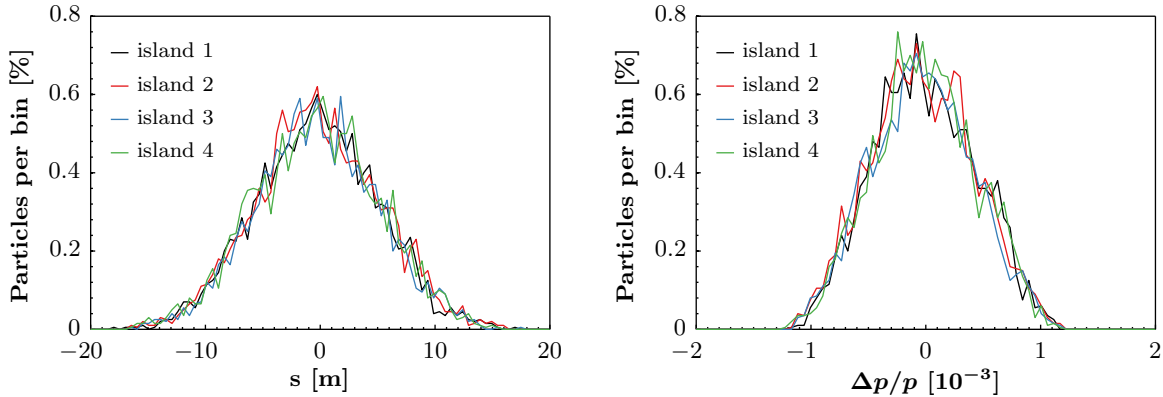
(a) Projections of the distributions along s. **(b)** Projections of the distributions along $\Delta p/p$.

Figure 6.97. Comparison of the longitudinal distributions of the four islands for the case $V_{\mathrm{RF}} = 12$ kV. No meaningful differences between the beamlets are observed.

to create extremely short electron bunches and, more recently, studies on the effect of the non-linear momentum compaction factor in the SIS 100, a heavy ion machine under construction, were presented [102]. Clearly, the presence of such α-buckets for the MTE case was excluded by the previously discussed 6D time-dependent simulation studies. However, even though the MTE extraction energy is quite far from transition ($\gamma_{\mathrm{MTE}} = 14.95$ compared to $\gamma_{\mathrm{tr}} = 6.12$), the analytical approach was pursued to evaluate at which point the MTE non-linearities might become important enough to influence the synchrotron motion.

The derivation of $\eta(\delta)$ was based on [18, 103] and the expression

$$\frac{fR}{f_0 R_0} = \frac{\beta}{\beta_0}, \tag{6.30}$$

where f describes the revolution frequency of a particle, β its relativistic parameter, R the radius of its orbit and the index 0 refers to the synchronous particle, was considered as a starting point. Inserting the relation $f = \Delta f + f_0$ leads to

$$\frac{\Delta f R}{f_0 R_0} + \frac{f_0 R}{f_0 R_0} = \frac{\beta}{\beta_0}, \tag{6.31}$$

which can be related to the slip factor after an additional manipulation:

$$\frac{\Delta f}{f_0} = \frac{\beta R_0}{\beta_0 R} - 1 \equiv -\eta(\delta)\delta. \tag{6.32}$$

Using the dependency of the path length on a particle's momentum deviation, the expression

$$R = R_0(1 + \alpha_0 \delta + \alpha_1 \delta^2 + \alpha_2 \delta^3 + \alpha_3 \delta^4 + \dots), \tag{6.33}$$

is obtained, which results in the following definition of the non-linear momentum compaction factor

$$\alpha_c = \frac{d\left(\frac{\Delta R}{R}\right)}{d\delta} = \alpha_0 + 2\alpha_1\delta + 3\alpha_2\delta^2 + 4\alpha_3\delta^3 + \ldots \equiv \frac{1}{\sqrt{\gamma_T}}. \tag{6.34}$$

Applying the definition of the relativistic momentum $p_0 = mc\beta_0\gamma_0$, the relation $\Delta p = p - p_0$, and the expressions

$$\delta = \frac{\beta\gamma}{\beta_0\gamma_0} - 1 \tag{6.35}$$

and

$$\frac{\gamma}{\gamma_0} = \sqrt{\frac{1 - 1 + \gamma^2}{\gamma_0^2}} = \sqrt{\frac{1 + \gamma^2\left(1 - \frac{1}{\gamma^2}\right)}{\gamma_0^2}} = \sqrt{\frac{1 + \gamma^2\beta^2}{\gamma_0^2}} = \sqrt{\frac{1}{\gamma_0^2} + \frac{\gamma^2\beta^2}{\gamma_0^2}} =$$

$$= \sqrt{1 - \beta_0^2 + \frac{\gamma^2\beta^2}{\gamma_0^2}} \overset{\text{Eq. (6.35)}}{=\!=\!=} \sqrt{1 - \beta_0^2 + \beta^2(\delta+1)^2\frac{\beta_0^2}{\beta^2}} = \sqrt{1 + 2\beta_0^2\delta + \beta_0^2\delta^2}, \tag{6.36}$$

the ratio between the particle velocities is obtained:

$$\frac{\beta}{\beta_0} = (1+\delta)\frac{\gamma_0}{\gamma} = \frac{1+\delta}{\sqrt{1 + 2\beta_0^2\delta + \beta_0^2\delta^2}} =$$

$$= (1+\delta)(1 - \beta_0^2\delta - \frac{1}{2}\beta_0^2\delta^2 + \frac{3}{2}\beta_0^4\delta^2 + \frac{3}{2}\beta_0^4\delta^3 + \frac{3}{8}\beta_0^4\delta^4 - \frac{5}{2}\beta_0^6\delta^3 - \frac{15}{4}\beta_0^6\delta^4 + \ldots +$$

$$+ \frac{35}{8}\beta_0^8\delta^4 + \ldots) =$$

$$= 1 - \beta_0^2\delta - \frac{1}{2}\beta_0^2\delta^2 + \frac{3}{2}\beta_0^4\delta^2 + \frac{3}{2}\beta_0^4\delta^3 + \frac{3}{8}\beta_0^4\delta^4 - \frac{5}{2}\beta_0^6\delta^6 - \frac{15}{4}\beta_0^6\delta^4 + \delta - \beta_0^2\delta^2 - \tag{6.37}$$

$$- \frac{1}{2}\beta_0^2\delta^3 + \frac{3}{2}\beta_0^4\delta^3 + \frac{3}{2}\beta_0^4\delta^4 + \frac{3}{8}\beta_0^4\delta^5 - \frac{5}{2}\beta_0^6\delta^4 - \frac{15}{4}\beta_0^6\delta^5 + \frac{35}{8}\beta_0^8\delta^4 + \ldots \approx$$

$$\approx 1 + (1 - \beta_0^2)\delta + \left(\frac{3}{2}\beta_0^4 - \frac{3}{2}\beta_0^2\right)\delta^2 + \left(3\beta_0^4 - \frac{1}{2}\beta_0^2 - \frac{5}{2}\beta_0^6\right)\delta^3 + \left(\frac{15}{8}\beta_0^4 - \frac{25}{4}\beta_0^6 + \right.$$

$$\left. + \frac{35}{8}\beta_0^8\right)\delta^4.$$

Only terms up to fourth order in δ are considered. The last expression can then be further simplified to

$$\frac{\beta}{\beta_0} \approx 1 + \frac{1}{\gamma_0^2}\delta - \frac{3}{2}\frac{\beta_0^2}{\gamma_0^2}\delta^2 + \frac{1}{2}\frac{\beta_0^2}{\gamma_0^2}\left(5\beta_0^2 - 1\right)\delta^3 + \frac{5}{4}\beta_0^4\left(\frac{3}{2} - 5\beta_0^2 + \frac{7}{2}\beta_0^4\right)\delta^4. \tag{6.38}$$

In order to determine the relationship between $\eta(\delta)$ and α_c, Eqs. (6.33) and (6.38) are inserted into Eq. (6.32), which leads to the expression

$$
\begin{aligned}
\frac{\Delta f}{f_0} &\approx \frac{1 + \frac{1}{\gamma_0^2}\delta - \frac{3}{2}\frac{\beta_0^2}{\gamma_0^2}\delta^2 + \frac{1}{2}\frac{\beta_0^2}{\gamma_0^2}\left(5\beta_0^2 - 1\right)\delta^3 + \frac{5}{4}\beta_0^4\left(\frac{3}{2} - 5\beta_0^2 + \frac{7}{2}\beta_0^4\right)\delta^4}{1 + \alpha_0\delta + \alpha_1\delta^2 + \alpha_2\delta^3 + \alpha_3\delta^4} - 1 = \\
&= \left[1 + \frac{1}{\gamma_0^2}\delta - \frac{3}{2}\frac{\beta_0^2}{\gamma_0^2}\delta^2 + \frac{1}{2}\frac{\beta_0^2}{\gamma_0^2}\left(5\beta_0^2 - 1\right)\delta^3 + \frac{5}{4}\beta_0^4\left(\frac{3}{2} - 5\beta_0^2 + \frac{7}{2}\beta_0^4\right)\delta^4\right] \cdot \\
&\quad \cdot \left(1 - \alpha_0\delta - \alpha_1\delta^2 - \alpha_2\delta^3 - \alpha_3\delta^4 + \alpha_0^2\delta^2 + 2\alpha_0\alpha_1\delta^3 + \alpha_1^2\delta^4 + 2\alpha_0\alpha_2\delta^4 + \ldots - \right. \\
&\quad \left. -\alpha_0^3\delta^3 - 3\alpha_0^2\alpha_1\delta^4 + \ldots + \alpha_0^4\delta^4 + \ldots\right) - 1 \approx \\
&\approx \left(\frac{1}{\gamma_0^2} - \alpha_0\right)\delta + \left(\alpha_0^2 - \frac{\alpha_0}{\gamma_0^2} - \alpha_1 - \frac{3}{2}\frac{\beta_0^2}{\gamma_0^2}\right)\delta^2 + \left(\frac{\alpha_0^2}{\gamma_0^2} - \alpha_0^3 + 2\alpha_0\alpha_1 - \alpha_2 - \frac{\alpha_1}{\gamma_0^2} + \right. \\
&\quad \left. +\frac{3}{2}\frac{\beta_0^2\alpha_0}{\gamma_0^2} + \frac{1}{2}\frac{\beta_0^2}{\gamma_0^2}\left(5\beta_0^2 - 1\right)\right)\delta^3 + \left[\alpha_0^4 - \frac{\alpha_0^3}{\gamma_0^2} - \alpha_3 + 2\alpha_0\alpha_2 - 3\alpha_0^2\alpha_1 - \frac{\alpha_2}{\gamma_0^2} + \right. \\
&\quad +2\frac{\alpha_0\alpha_1}{\gamma_0^2} + \alpha_1^2 + \frac{3}{2}\frac{\beta_0^2\alpha_1}{\gamma_0^2} - \frac{3}{2}\frac{\beta_0^2\alpha_0^2}{\gamma_0^2} - \frac{1}{2}\frac{\beta_0^2\alpha_0}{\gamma_0^2}\left(5\beta_0^2 - 1\right) + \frac{5}{4}\beta_0^4\left(\frac{3}{2} - 5\beta_0^2 + \right. \\
&\quad \left. \left. +\frac{7}{2}\beta_0^4\right)\right]\delta^4.
\end{aligned}
\tag{6.39}
$$

Comparing this result to Eq. (6.32), the expressions for the different orders of the slip factor read

$$
\eta_0 = \alpha_0 - \frac{1}{\gamma_0^2},
\tag{6.40}
$$

$$
\eta_1 = \alpha_0\eta_0 + \alpha_1 + \frac{3\beta_0^2}{2\gamma_0^2},
\tag{6.41}
$$

$$
\eta_2 = -\alpha_0^2\eta_0 - 2\alpha_0\alpha_1 + \alpha_2 + \frac{\alpha_1}{\gamma_0^2} - \frac{\beta_0^2(5\beta_0^2 - 1)}{2\gamma_0^2} - \frac{3\beta_0^2\alpha_0}{2\gamma_0^2},
\tag{6.42}
$$

$$
\eta_3 = \alpha_0^3\eta_0 - \alpha_1^2 + \alpha_3 - 2\alpha_0\alpha_2 + 3\alpha_0^2\alpha_1 + \frac{\alpha_2}{\gamma_0^2} - 2\frac{\alpha_0\alpha_1}{\gamma_0^2} -
\tag{6.43}
$$

$$
-\frac{3}{2}\frac{\beta_0^2\alpha_1}{\gamma_0^2} + \frac{3}{2}\frac{\beta_0^2\alpha_0^2}{\gamma_0^2} + \frac{1}{2}\frac{\beta_0^2\alpha_0}{\gamma_0^2}\left(5\beta_0^2 - 1\right) - \frac{5}{4}\beta_0^4\left(\frac{3}{2} - 5\beta_0^2 + \frac{7}{2}\beta_0^4\right).
$$

To study the effect of the non-linear terms on the synchrotron motion, the equations of motion were solved considering the δ-dependency of η. Therefore, Eqs. (6.40)-(6.43) were inserted into the synchrotron Hamiltonian $\mathcal{H}_{sy}$ defined in Eq. (2.19), and the resulting phase space dynamics is discussed in the following.

6.3.2.1 Truncation of the slip factor to first order

Considering the expansion of the slip factor up to first order, the Hamiltonian reads

$$\mathcal{H}_{\mathrm{sy}}(\phi,\,\delta) = \frac{1}{2}h\omega_0\left(\eta_0 + \frac{2}{3}\eta_1\delta\right)\delta^2 + \frac{\omega_0 eV}{2\pi\beta_0^2 E_0}\left[\cos\phi - \cos\phi_s + (\phi - \phi_s)\sin\phi_s\right], \tag{6.44}$$

leading to the following equations of motion

$$\dot{\phi} = h\omega_0\left(\eta_0 + \eta_1\delta\right)\delta$$

$$\dot{\delta} = \frac{\omega_0}{2\pi\beta_0^2 E_0}eV(\sin\phi - \sin\phi_s). \tag{6.45}$$

In addition to the common fixed points obtained in Section 2.2, two fixed points are introduced by the higher order term:

$$\left(\phi_s,\,-\frac{\eta_0}{\eta_1}\right) \qquad\qquad \text{unstable fixed point,}$$

$$\left(\pi - \phi_s,\,-\frac{\eta_0}{\eta_1}\right) \qquad\qquad \text{stable fixed point.}$$

The presence of the non-linear term leads to a second layer of buckets in the longitudinal phase space, which is well separated from the initial one, as long as η_1 remains small. However, increasing the first order term of the slip factor causes the separatrices of the respective buckets to approach until they start to merge at a certain value $\eta_{1,\mathrm{equal}}$. To calculate it, the fact that the Hamiltonian values of the separatrices of both layers have to be equal, can be exploited:

$$\mathcal{H}_{\mathrm{sy}}(\pi - \phi_s,\,0) = \mathcal{H}_{\mathrm{sy}}\left(\phi_s,\,-\frac{\eta_0}{\eta_1}\right). \tag{6.46}$$

This leads to

$$\frac{eV}{\pi\beta_0^2 E_0} = \frac{1}{6}h\frac{\eta_0^3}{\eta_{1,\mathrm{equal}}^2} \tag{6.47}$$

and

$$\eta_{1,\mathrm{equal}} = \sqrt{\frac{h\left|\eta_0^3\right|\pi\beta_0^2 E_0}{6eV}} = \frac{\eta_0^2 h}{\sqrt{12}Q_s}. \tag{6.48}$$

For values of $\eta_1 > \eta_{1,\mathrm{equal}}$, the dynamics enters the aforementioned regime of α-buckets. Figure 6.98 illustrates the longitudinal phase space for different values of η_1.
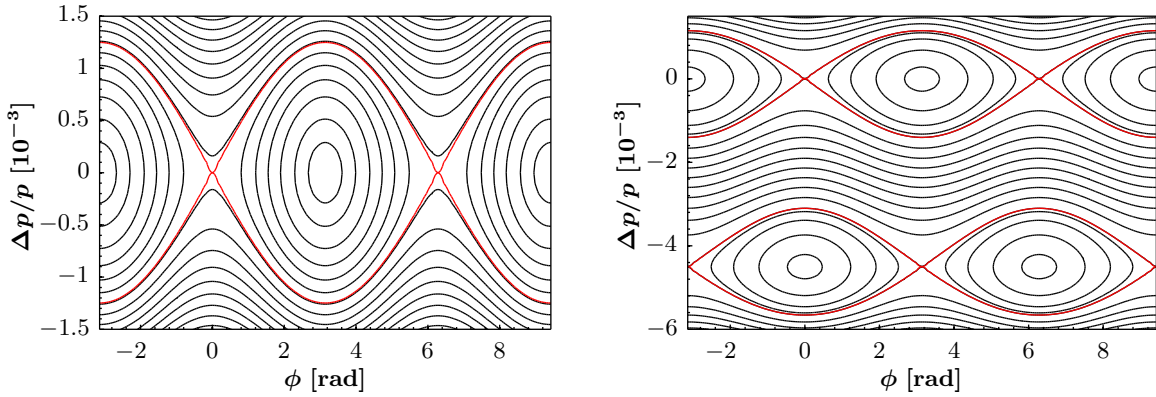
(a) $\eta_1 = 0$. Classical situation, where only one layer of buckets at $\delta = 0$ exists.

(b) $\eta_1 = 5$. A second layer of stable motion appears at $\delta = -4.5 \times 10^{-3}$. The motion around the initial SFPs remains almost undistorted.
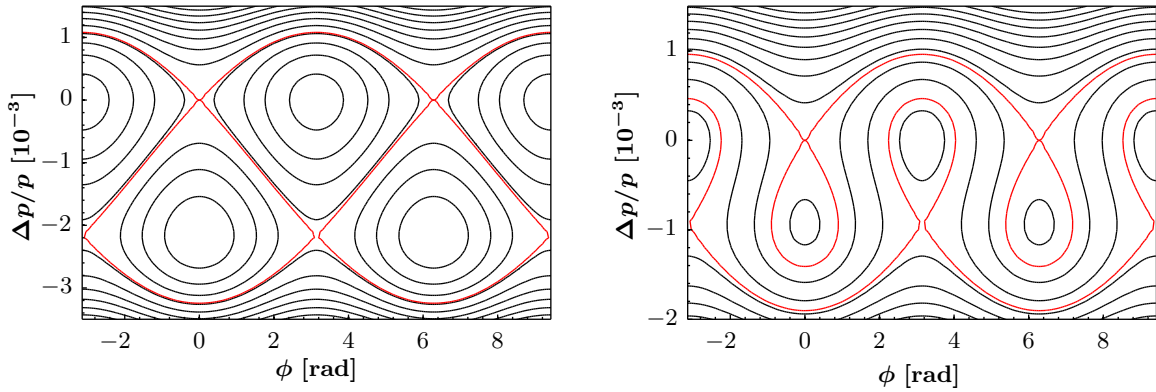
(c) $\eta_1 = 10.4 \equiv \eta_{1,\mathrm{equal}}$. Situation of overlapping separatrices, just prior to merging of the two layers. Trajectories around the SFPs are clearly distorted.

(d) $\eta_1 = 24$. The buckets are rotated by $90°$ and adopt an $\alpha-$like shape. The acceptance and the maximum bunch length are significantly reduced.

Figure 6.98. Phase space portraits illustrating the effect of the first order term of the nonlinear momentum compaction factor on the longitudinal dynamics. The applied RF settings correspond to those for MTE. The red lines correspond to the separatrices.

6.3.2.2 Truncation of the slip factor to second order

Including the second order term of the slip factor the Hamiltonian becomes

$$\mathcal{H}\mathrm{sy}(\phi, \delta) = \frac{1}{2} h\omega_0 \left(\eta_0 + \frac{2}{3}\eta_1\delta + \frac{1}{2}\eta_2\delta^2 \right) \delta^2 + \frac{\omega_0 eV}{2\pi\beta_0^2 E_0} \left[\cos\phi - \cos\phi_s + (\phi - \phi_s)\sin\phi_s \right], \quad (6.49)$$

and the corresponding equations of motion are

$$\dot{\phi} = h\omega_0 \left(\eta_0 + \eta_1\delta + \eta_2\delta^2 \right) \delta,$$

$$\dot{\delta} = \frac{\omega_0}{2\pi\beta_0^2 E_0} eV(\sin\phi - \sin\phi_s).$$

(6.50)

In addition to the classical fixed points at $\delta_1 = 0$, two layers of stability arise at

$$\delta_{2,3} = -\frac{\eta_1}{2\eta_2} \pm \sqrt{\frac{\eta_1^2}{4\eta_2^2} - \frac{\eta_0}{\eta_2}},$$

(6.51)

with the fixed points being located at

$$(\phi_s, \delta_2) \text{ and } (\phi_s, \delta_3) \qquad \text{unstable fixed point}$$
$$(\pi - \phi_s, \delta_2) \text{ and } (\pi - \phi_s, \delta_3) \qquad \text{stable fixed point.}$$

In Fig. 6.99, two of these layers are shown to merge, while the third one is still clearly separated. For high values of η_2, merging occurs at values of η_1 for which the two layers of stable motion presented in Fig. 6.98 were still significantly separated.

6.3.2.3 Application of the formalism to MTE

In the figures presented on the previous pages, the values of the different orders of the slip factor were chosen arbitrarily, in order to obtain meaningful illustrations of the phase space. To quantify a possible distortion of the longitudinal phase space during the MTE process, a more rigorous approach was applied. Based on the confidence in the model, the non-linear momentum
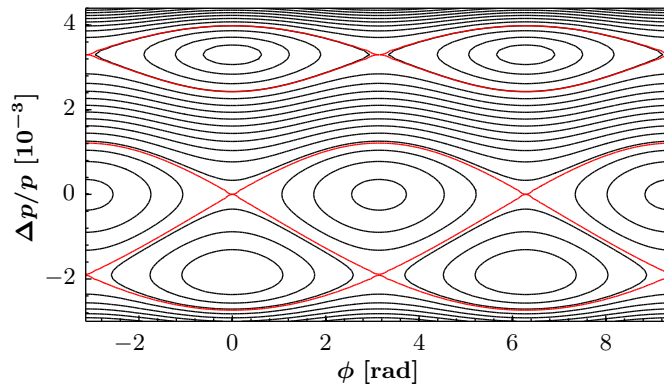
Figure 6.99. Illustration of the longitudinal phase space considering the non-linear slip factor up to second order ($\eta_1 = 5$, $\eta_2 = -3570.$). A third layer of stability is created.

compaction factor was computed with PTC. However, attention had to be paid as no multipolar components of higher order than octupolar are actually included in the simulations (see also Fig. 6.9). Therefore, the considerations presented in the following take into account non-linear terms of α_c up to second order in δ, as α_1 and α_2 are mainly created by sextupolar and octupolar contributions, respectively.

The evolution of these terms during the MTE process is shown in Fig. 6.100. α_c was found to be maximum just after resonance crossing, when the formation of the islands is still ongoing. The respective momentum compaction factors for the core and the islands read

$$\alpha_{c,730}^{\text{core}} = 0.02669 + 0.00943 \cdot \delta + \ 3.05036 \cdot \delta^2 + \dots, \tag{6.52}$$

$$\alpha_{c,730}^{\text{islands}} = 0.02669 + 0.04987 \cdot \delta - 28.70925 \cdot \delta^2 + \dots, \tag{6.53}$$

and subsequent solution of the equations of motion in Eq. (6.50) reveals

$$\delta_{2,730}^{\text{core}} = (-2.70 + 85.40\, i) \times 10^{-3} \qquad \delta_{3,730}^{\text{core}} = (-2.70 - 85.40\, i) \times 10^{-3}, \tag{6.54}$$

$$\delta_{2,730}^{\text{islands}} = 28.8 \times 10^{-3} \qquad\qquad \delta_{3,730}^{\text{islands}} = -26.8 \times 10^{-3}, \tag{6.55}$$

where i is the imaginary unit. For the core, no real solution is obtained and, therefore, the classical layer of stable motion at $\delta = 0$ remains the only solution. On the other hand, additional buckets are created considering the momentum compaction factor of the islands; however, compared to the half bucket height of $\delta_{\text{bucket}} = 1.25 \times 10^{-3}$, these additional layers are largely outside the momentum aperture of the accelerator. In order to observe a measurable effect, the
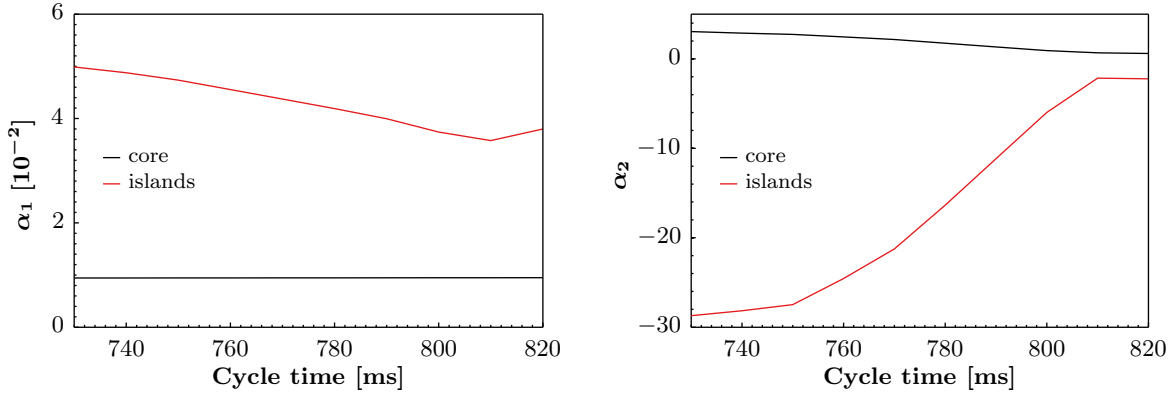
(a) First order, driven by sextupoles.   **(b)** Second order, driven by octupoles.

Figure 6.100. Evolution of the first and second order of the momentum compaction factor for the core and the islands during the MTE process. In absolute terms, values are maximum just after resonance crossing, which occurs at 720 ms (not shown in the figures), when the SFPs of the islands are still close to the centre of the machine.

sextupolar or octupolar components of the lattice would have to be increased by more than a factor 100, while keeping all other parameters constant.

These observations confirmed the understanding that the longitudinal motion during the MTE process is completely unaffected by the relatively high non-linearities. The presented analytic results are in agreement with the simulations results discussed in the beginning of this section as well as in Section 6.3.1, where neither a distortion of the bucket nor a difference between the longitudinal motion for particles in the core or in the islands was observed. This is also understandable as the MTE flat top energy is quite far from transition ($\gamma_{\mathrm{MTE}}/\gamma_{\mathrm{tr}} = 2.44$), where the effect of the non-linearities becomes maximum due to vanishing η_0.

Based on the aforementioned conclusions, the SPS observations presented in Fig. 6.96 cannot be explained by a distortion of the longitudinal motion driven by non-linear transverse fields. In the recent past, it has not been possible to further investigate this peculiar bunch structure experimentally, as it has not been observed again. This leaves the open question of whether a hardware issue might have distorted the measurement itself or of a possible malfunctioning of the PS transverse damper during the experimental studies. Further explanations could be based on direct or indirect space charge, or collective effects. Currently, no additional data is available and, therefore, the subject might require further attention in the future.

6.4 Conclusions and outlook

The MTE technique was proposed in 2001 as replacement of the CT extraction. The latter, which had been reliably used to extract beams designated for the SPS fixed target experimental programme from the PS for several decades, was understood to be not suited for high-intensity beam operation with high duty cycle. This is based on the integral part of the CT mechanism, namely the mechanic beam splitting using an electrostatic septum, which leads to high beam loss and, consequently, radioactive activation of a large fraction of the PS ring.

In the course of the MTE commissioning, several obstacles were encountered. The main issues concerned severe fluctuations of the efficiency of the transverse splitting process and unacceptably high beam loss occurring at the magnetic septum during the fast extraction bump. Due to the second problem, the commissioning of high-intensity MTE beams could only be continued after the completion of the design and the installation of a passive absorber to protect the extraction septum.

The research conducted in the framework of this thesis significantly contributed to deepening knowledge of this novel resonant extraction scheme, which is based on a stable fourth order resonance. Various experimental and simulation studies rendered the successful conclusion of the commissioning and the operational deployment of the MTE beam for SPS fixed target physics possible in September 2015. After several years of commissioning, this corresponded to an important milestone for the MTE project.

Essential ingredients for this achievement were studies which allowed the explanation and mitigation of the observed oscillations of the splitting efficiency. Magnetic and beam-based measurements revealed a significant correlation between the population of the MTE islands and an oscillation of the magnetic field at a frequency of 5 kHz. Subsequently, a current ripple on the wide circuits of the PFW, which exceeded the PC specifications, was observed and understood to degrade the MTE process. On the basis of simulation studies, this phenomenon was explained, as the natural oscillation frequencies around the SFPs of the islands were determined to be also located in the low-kHz regime. These investigations highlighted the sensibility of the transverse splitting to external perturbations.

Furthermore, the installation of the dummy septum as protection of the magnetic septum required a complete redesign of the extraction bump. Considering the feed-down effects, which are able to significantly change the positions of the SFPs during the rise of the extraction bump, an improved setting was determined and experimentally validated. Given the tight aperture constraints in the extraction region, the proposed bump turned out to be extremely robust, as it provides simple means to control the positions in SS15 and SS16. However, the extraction efficiency was measured to be only around 93%, which motivated the search for additional improvements.

By conducting 6D time-dependent tracking simulations of the splitting process, the rotation of the phase space, which is required to correctly position the beamlets at the extraction septum,

was found to occur non-adiabatically. Consequently, the islands could not follow the movement of the SFPs, causing emittance blow up and a reduction of the splitting efficiency by de-trapping. These particles, which remained trapped between the islands and the core, then contributed to the extraction losses. In order to improve this rotation, a new non-linear optics scheme was developed. Its advantage is twofold: first, the rotation is slowed down and, more importantly, the surface of the islands at the extraction septum is significantly reduced. Once the magnetic extraction septum was properly aligned to be in the shadow of the dummy septum, the extraction losses were determined to be as low as 1.5%, which agrees with the MTE design values. More specifically, these losses occurred exclusively in the extraction region, which constitutes an enormous improvement compared to the CT extraction. Due to the shadowing configuration, it was indeed possible to reduce beam loss in SS16, an important ingredient to keeping this location accessible for interventions in case of a failure of the magnetic septum.

The aforementioned conclusions indicate that the MTE technique became reliable enough to start optimizing the vast MTE parameter space. A first approach in this direction is discussed in [72], where settings of the dedicated multipoles were presented, which improved the extraction efficiency to more than 99% for an intensity of 1.5×10^{13} p. This clearly indicates the necessity for systematic studies of the multipolar settings. The optimization should also concern the reduction of the non-linear coupling between the transverse planes and, therefore, the settings of the ODN.

Moreover, the effect of negative chromaticity induced by the increased sextupole current during the final rotation should be investigated in order to determine an intensity threshold for instabilities. If this study suggests that future parameters will drive the beam unstable, a rotation scheme applying the MTE octupoles instead of the sextupoles could be envisaged.

Additional improvements concerning the PCs of the PFW are also foreseen, such as new electronics, which are expected to improve the stability of the splitting process by reducing the current ripple at 5 kHz even further.

The transverse damper system is another indispensable ingredient for proper functioning of the MTE scheme. The parameter space of this device should also undergo an optimization process, which could potentially lead to improved MTE stability and efficiency.

Performing the horizontal phase space manipulations at higher energy could also be envisaged, and the constraints in terms of beam size at the extraction septum would be further relaxed. However, it needs to be clarified if the PS extraction kickers, the orbit correctors and the LEQ provide sufficient strength, and if this approach is acceptable for the SPS.

Furthermore, research on the topic of longitudinal dynamics in the context of the MTE process was conducted. Experimental observations, which showed a dependency of the splitting efficiency on the momentum spread of the beam, were verified via simulation studies. Another study concerned investigations of the effect of non-linear momentum compaction on the longitudinal dynamics. No distortion of the longitudinal phase space was observed; however, this interesting subject could be exploited as a way of benchmarking the simulated longitudinal dy-

namics in a non-classical regime. Therefore, the dynamics close to the transition energy should be studied, where the available non-linear elements are expected to provide sufficient strengths to influence the longitudinal phase space. Experimentally, a magnetic flat top close to the transition energy - preferably below it in order to avoid transition crossing itself - could then be created to measure the effect on the bunch profiles.

References

[1] O. Brüning, P. Collier, P. Lebrun, S. Myers, R. Ostojic, J. Poole, and P. Proudlock, eds., *LHC Design Report*, CERN-2004-003-V-1 (CERN, Geneva, 2004), [https://cds.cern.ch/record/782076].

[2] CERN, European Organization for Nuclear Research, [http://home.cern].

[3] G. Aad et al., "Observation of a New Particle in the Search for the Standard Model Higgs Boson with the ATLAS Detector at the LHC", Physics Letters B **716**, 1, ISSN: 0370-2693 (2012).

[4] S. Chatrchyan et al., "Observation of a New Boson at a Mass of 125 GeV with the CMS Experiment at the LHC", Physics Letters B **716**, 30, ISSN: 0370-2693 (2012).

[5] F. Englert and R. Brout, "Broken symmetry and the mass of gauge vector mesons", Phys. Rev. Lett. **13**, 321 (1964).

[6] P. W. Higgs, "Broken symmetries and the masses of gauge bosons", Phys. Rev. Lett. **13**, 508 (1964).

[7] G. S. Guralnik, C. R. Hagen, and T. W. B. Kibble, "Global conservation laws and massless particles", Phys. Rev. Lett. **13**, 585 (1964).

[8] E. Kugler, "The ISOLDE Facility", Hyperfine Interactions **129**, 23, ISSN: 1572-9540.

[9] E. Radermacher, ed., "Neutron TOF Facility (PS213): Technical Design Report", CERN-INTC-2000-04 (2000) [http://cds.cern.ch/record/429174].

[10] K. Elsener, ed., "The CERN Neutrino Beam to Gran Sasso (NGS)", CERN-SL-99-034-DI. INFN-AE-99-05, Addendum to report CERN 98-02, INFN-AE-98-05 (Geneva, June 1999) [http://cds.cern.ch/record/390779].

[11] G. D. Lellis, "Search for Hidden Particles (SHiP): A New Experiment Proposal", Nucl. Part. Phys. **263-264**, 71, ISSN: 2405-6014 (2015).

[12] S. Gilardoni et al., "The High Intensity/High Brightness Upgrade Program at CERN: Status and Challenges", in *Proceedings of the 52nd ICFA Advanced Beam Dynamics Workshop on High-Intensity and High-Brightness Hadron Beams*, edited by N. Zhao, J. Chrin, D. Ji, C. Petit-Jean-Genaz, V. R. W. Schaa, and H. Yan (IHEP, Bejing, 2012), p. 226 [http://accelconf.web.cern.ch/AccelConf/HB2012/papers/tuo1a01.pdf].

[13]   H. Damerau, A. Funken, R. Garoby, S. Gilardoni, B. Goddard, K. Hanke, A. Lombardi,
       D. Manglunki, M. Meddahi, B. Mikulec, G. Rumolo, E. Shaposhnikova, M. Vretenar,
       and J. Coupard, "LHC Injectors Upgrade, Technical Design Report, Vol. I: Protons",
       CERN-ACC-2014-0337 (Geneva, Dec. 2014) [https://cds.cern.ch/record/1976692].

[14]   C. Bovet, D. Fiander, L. Henny, A. Krusche, and G. Plass, "The Fast Shaving Ejection
       for Beam Transfer from the CPS to the CERN 300 GeV Machine", IEEE Trans. Nucl.
       Sci. **20**, 438 (1973).

[15]   R. Cappi and M. Giovannozzi, "Novel method for multiturn extraction: trapping charged
       particles in islands of phase space", Phys. Rev. Lett. **88**, 104801 (2002).

[16]   C. Bertone, J. Borburgh, D. Bodart, R. Brown, S. Burger, S. Damjanovic, P. Demarest,
       R. Fernandez Ortega, J. Ferreira Somoza, D. Gerard, S. Gibson, S. Gilardoni, M. Giovan-
       nozzi, G. Le Godec, C. Hernalsteens, M. Hourican, N. Jurado, J. M. Lacroix, S. Mataguez,
       G. Métral, C. Pasquino, E. Perez-Duenas, S. Persichelli, B. Salvant, R. Steerenberg, and
       P. Van Trappen, "Studies and Implementation of the PS dummy Septum to Mitigate
       Irradiation of Magnetic Septum in Straight Section 16", CERN-ACC-2014-0043 (Geneva,
       Apr. 2014) [https://cds.cern.ch/record/1697680].

[17]   E. Courant and H. Snyder, "Theory of the Alternating-Gradient Synchrotron", Annals
       of Physics **3**, 1, ISSN: 0003-4916 (1958).

[18]   S. Y. Lee, *Accelerator Physics*, 3rd edition (World Scientific, Singapore, 2012), ISBN:
       9789814374941, [http://www.worldscientific.com/worldscibooks/10.1142/8335].

[19]   H. Wiedemann, *Particle Accelerator Physics*, 3rd edition (Springer, Berlin, Heidelberg,
       New York, 2007), ISBN: 9783540490436, [http://www.springer.com/us/book/9783540490456].

[20]   A. W. Chao, *Physics of Collective Beam Instabilities in High Energy Accelerators* (John
       Wiley & Sons Inc, New York, 1993), ISBN: 978-0471551843.

[21]   K. Y. Ng, *Physics of Intensity Dependent Beam Instabilities* (World Scientific, Singapore,
       2006), ISBN: 9812563423, [http://www.worldscientific.com/worldscibooks/10.1142/5835].

[22]   G. Rumolo, "Beam Instabilities", in *Proceedings of the CAS - CERN Accelerator School:
       Advanced Accelerator Physics Course*, edited by W. Herr (Trondheim, Norway, 2013)
       [https://cds.cern.ch/record/1982422].

[23]   E. Métral, T. Argyropoulos, H. Bartosik, N. Biancacci, X. Buffat, J. F. E. Muller, W.
       Herr, G. Iadarola, A. Lasheen, K. Li, A. Oeftiger, T. Pieloni, D. Quartullo, G. Rumolo,
       B. Salvant, M. Schenk, E. Shaposhnikova, C. Tambasco, H. Timko, C. Zannini, A. Burov,
       D. Banfi, J. Barranco, N. Mounet, O. Boine-Frankenheim, U. Niedermayer, V. Kornilov,
       and S. White, "Beam instabilities in hadron synchrotrons", IEEE Transactions on Nuclear
       Science **63**, 1001, ISSN: 0018-9499 (2016).

[24]   V. I. Veksler, "A new method of accelerating relativistic particles", Compt. Rend. Acad.
       Sci. USSR **43**, 329 (1944).

[25]   E. M. McMillan, "The synchrotron - a proposed high energy particle accelerator", Phys.
       Rev. **68**, 143 (1945).

[26]   E. Regenstreif, *The CERN Proton Synchrotron, pt.1* (CERN, Geneva, 1959), [http://
       cds.cern.ch/record/214352].

[27]   S. Gilardoni and D. Manglunki, eds., *Fifty Years of the CERN Proton Synchrotron: Vol-
       ume 1*, CERN-2011-004 (CERN, Geneva, 2011), [http://cds.cern.ch/record/1359959].

[28]   M. Juchno, "Magnetic Model of the CERN Proton Synchrotron", PhD thesis, EPFL,
       Lausanne (2013) [http://cds.cern.ch/record/2129023].

[29] P. Freyermuth, D. Cotte, M. Delrieux, H. Genoud, S. Gilardoni, K. Hanke, O. Hans, S. Mataguez, G. Metral, F. Peters, R. Steerenberg, and B. Vandorpe, "CERN Proton Synchrotron Working Point Matrix for Extended Pole Face Winding Powering Scheme", in *Proceedings of the First International Particle Accelerator Conference*, edited by A. Noda, C. Petit-Jean-Genaz, V. R. W. Schaa, T. Shirai, and A. Shirakawa (Kyoto, Japan, 2010), pp. 4551–4553 [http://accelconf.web.cern.ch/AccelConf/IPAC10/papers/THPE019.pdf].

[30] A. Huschauer, "Working Point and Resonance Studies at the CERN Proton Synchrotron", MA thesis, University of Technology, Vienna (2012) [http://cds.cern.ch/record/1501943].

[31] D. Belohrad, "Fast Beam Intensity Measurements for the LHC", PhD thesis, Czech Technical University, Prague (2010) [http://cds.cern.ch/record/1301517].

[32] R. Bartolini, A. Bazzani, M. Giovannozzi, W. Scandale, and E. Todesco, "Tune evaluation in simulations and experiments", Part. Accel. **52**, 147 (1995).

[33] R. Bartolini, A. Bazzani, M. Giovannozzi, E. Todesco, and W. Scandale, "Algorithms for a Precise Determination of the Betatron Tune", in *Proceedings of the Fifth European Particle Accelerator Conference*, edited by S. Myers, A. Pacheco, C. Petit-Jean-Genaz, R. Pascual, and J. Poole (Sitges, Spain, 1996), pp. 1329–1331 [http://accelconf.web.cern.ch/AccelConf/e96/PAPERS/TUPG/TUP018G.PDF].

[34] M. Gasior and R. Jones, "The principle and first results of betatron tune measurement by direct diode detection", CERN-LHC-Project-Report-853 (Geneva, Aug. 2005) [http://cds.cern.ch/record/883298].

[35] C. Steinbach, "Emittance measurements with the CERN PS wire scanner", in *Proceedings of the International Workshop on Particle Dynamics in Accelerators*, edited by S. Machida and K. Hirata, CERN-PS-95-04-OP (Tsukuba, Japan, 1995), p. 285 [https://cds.cern.ch/record/275924].

[36] S. Hancock, P. Knaus, M. Lindroos, and M. Metcalf, "Tomographic Measurements of Longitudinal Phase Space Density", Computer Physics Communications **121-122**, 648, ISSN: 0010-4655 (1999).

[37] V. Agoritsas, F. Beck, G. Benincasa, and J. Bovigny, "A microprocessor-based system for continuous monitoring of radiation levels around the CERN PS and PSB accelerators", Nucl. Instrum. Methods Phys. Res. A. **247**, 44, ISSN: 0168-9002 (1986).

[38] S. S. Gilardoni, S. Aumon, E. Effinger, J. Gil-Flores, and U. Wienands, "Beam Loss Monitors Comparison at the CERN Proton Synchrotron", in *Proceedings of the Second International Particle Accelerator Conference*, edited by A. Blanco, I. Etxebarria, F. Perez, C. Petit-Jean-Genaz, A. Wolski, and V. R. W. Schaa (San Sebastian, Spain, 2011), p. 1341 [http://accelconf.web.cern.ch/AccelConf/IPAC2011/papers/TUPC135.pdf].

[39] MAD Web Page, [http://mad.web.cern.ch/mad] (visited on 04/25/2016).

[40] H. Grote, F. Schmidt, L. Deniau, and G. Roy, "User's Reference Manual", Apr. 2016 [http://madx.web.cern.ch/madx/releases/last-dev/madxuguide.pdf].

[41] W. Herr and F. Schmidt, "A MAD-X Primer", CERN-AB-2004-027-ABP (June 2004) [https://cds.cern.ch/record/744163].

[42] F. Schmidt, E. Forest, and E. McIntosh, "Introduction to the Polymorphic Tracking Code: Fibre Bundles, Polymorphic Taylor Types and "Exact Tracking"" (Geneva, July 2002) [https://cds.cern.ch/record/573082].

[43] M. Giovannozzi, "CERN experience: MTE", Presentation at the PTC 1/2 day, CERN, Geneva, Switzerland (November 2011) [https://indico.cern.ch/event/162516/].

[44] J. Holmes, S. Cousineau, V. Danilov, S. Henderson, A. Shishlo, Y. Sato, W. Chou, L. Michelotti, and F. Ostiguy, "ORBIT: Beam Dynamics Calculations for High-Intensity Rings", in *ICFA Beam Dynamics Newsletter No. 30*, edited by J. Wei and L. Merminga (2003), p. 100 [http://icfa-usa.jlab.org/archive/newsletter/icfa_bd_nl_30.pdf].

[45] A. Shishlo, T. Gorlov, and J. Holmes, *The Python Shell for the ORBIT Code*, edited by J. Chew, San Francisco, USA, 2009, [http://accelconf.web.cern.ch/AccelConf/ICAP2009/papers/thpsc052.pdf].

[46] H. Bartosik, S. Cousineau, J. Holmes, M. Kowalska, and A. Shishlo, "Status of PyORBIT in View of CERN's needs", Presentation at Space-Charge 2015, Trinity College, Oxford, United Kingdom (March 2015) [https://eventbooking.stfc.ac.uk/uploads/spacecharge15/bartosik20150326sc2015.pdf].

[47] A. Molodozhentsev and E. Forest, "PTC-ORBIT Notes" [https://frs.web.cern.ch/frs/Source/space_charge/PTC-ORBIT/Tips_and_Tricks/PTC-ORBIT-v2.pdf].

[48] G. Rumolo and F. Zimmermann, "Practical User Guide for HEADTAIL", SL-Note-2002-036-AP (Geneva, Nov. 2002) [http://cds.cern.ch/record/702717].

[49] N. Mounet, "The LHC Transverse Coupled-Bunch Instability", PhD thesis, EPFL, Lausanne (2012), CERN-THESIS-2012-055 [http://cds.cern.ch/record/1451296].

[50] G. Métral, private communication (2014).

[51] R. Cappi, M. Giovannozzi, S. Hancock, E. Métral, G. Métral, and R. Steerenberg, "High-intensity and high-density beams in the PS", PS Performance Committee meeting, CERN, Geneva, Switzerland (December 2001) p.7 [http://psdoc.web.cern.ch/PSdoc/ppc/ppc011207/emetral.pdf].

[52] A. Blas, S. Gilardoni, and G. Sterbini, "Beam Tests and Plans for the CERN PS Transverse Damper System", in *Proceedings of the Fourth International Particle Accelerator Conference*, edited by Z. Dai, C. Petit-Jean-Genaz, V. R. W. Schaa, and C. Zhang (SINAP, Shanghai and IHEP, Bejing, 2012), p. 2947 [http://accelconf.web.cern.ch/AccelConf/IPAC2013/papers/wepme011.pdf].

[53] S. Gilardoni and D. Manglunki, eds., *Fifty Years of the CERN Proton Synchrotron: Volume 2*, CERN-2013-005 (CERN, Geneva, 2013), [http://cds.cern.ch/record/1597087].

[54] S. Aumon, "High Intensity Beam Issues in the CERN Proton Synchrotron", PhD thesis, EPFL, Lausanne (2012), CERN-THESIS-2012-261 [http://cds.cern.ch/record/1517412].

[55] C. Yu, "Optimization of Beam Envelope in the Injection Region of PS", LIU-PS meeting, CERN, Geneva, Switzerland (March 2012) [http://cern.ch/go/CC7k].

[56] J. Bellemann, "The PS Wideband Electrostatic Pick-Up" [http://cern.ch/go/9KXz].

[57] H. Burkhardt and G. Rumolo and F. Zimmermann, "Investigation of space charge effects in the SPS", in *Proceedings of the 20th Particle Accelerator Conference*, edited by J. Chew (Portland, USA, May 2003), 3041–3043 [http://accelconf.web.cern.ch/AccelConf/e04/PAPERS/WEPLT013.PDF].

[58] E. Métral, G. Rumolo, B. Salvant, and R. Steerenberg, in *Proceedings of the Twenty-Second Particle Accelerator Conference*, edited by I. Andrian, C. Carli, J. Chrin, M. Comyn, A. Espinosa, C. Eyberger, S. Hardage, C. Horak, M. Kuzin, L. Liljeby, M. Marx, A. Mauri, C. Petit-Jean-Genaz, L. Piazza, J. Poole, J. Qintana-Valdez, L. Salas, V. R. W. Schaa, H. Tanaka, and J. Thomson (LANL, Los Alamos, 2007), 4210 [http://accelconf.web.cern.ch/AccelConf/p07/PAPERS/FRPMN074.PDF].

[59] G. Sterbini, private communication (2013).

[60] S. Hancock and E. Métral, "Ghost Bunches and Blow-up Losses with High-Intensity Beams", PS/RF Note 2002-198 (2002) [http://cds.cern.ch/record/960430].

[61] C. A. Brewer, [http://www.ColorBrewer.org] (visited on 08/2015).

[62] C. Pellegrini, "On a New Instability in Electron-Positron Storage Rings (the Head-Tail Effect).", Nuovo Cim. **A64**, 447 (1969).

[63] M. Sands, "The Head-Tail Effect: An Instability Mechanism in Storage Rings ", SLAC-TN-69-8 (Mar. 1969) [http://www.slac.stanford.edu/pubs/slactns/tn01/slac-tn-69-008.pdf].

[64] M. Sands, "Head-Tail Effect II: From a Resistive-Wall Wake", SLAC-TN-69-10 (Apr. 1969) [http://www.slac.stanford.edu/cgi-wrap/getdoc/slac-tn-69-010.pdf].

[65] K. Yokoya, "Resistive Wall Impedance of Beam Pipes of General Cross Section", Part. Accel. **41**, 221 (1993).

[66] H. Damerau, R. Garoby, S. Gilardoni, B. Goddard, K. Hanke, A. Lombardi, M. Meddahi, B. Mikulec, E. Shaposhnikova, and M. Vretenar, "Upgrade Plans for the LHC Injector Complex", in *Proceedings of the Third International Particle Accelerator Conference*, edited by J. Corbett, C. Eyberger, K. Morris, C. Petit-Jean-Genaz, T. Satogata, and V. R. W. Schaa (Lousiana State University, 2012), p. 1010 [http://accelconf.web.cern.ch/AccelConf/IPAC2012/papers/tuxa02.pdf].

[67] H. Bartosik, W. Hofle, G. Iadarola, Y. Papaphilippou, and G. Rumolo, "Benchmarking HEADTAIL with Electron Cloud Instabilities Observed in the LHC", in *Proceedings of the Joint INFN-CERN-EuCARD-AccNet Workshop on Electron-Cloud Effects*, edited by R. Cimino, G. Rumolo, and F. Zimmermann (La Biodola, Italy, 2012), p. 211 [https://cds.cern.ch/record/1603289].

[68] R. Bartolini and F. Schmidt, "A Computer Code for Frequency Analysis of Non-Linear Betatron Motion", SL-Note-98-017-AP (Geneva, Feb. 1998) [http://cds.cern.ch/record/702438].

[69] A. Oeftiger, H. Bartosik, A. Findlay, S. Hancock, and G. Rumolo, Flat Bunches with a Hollow Distribution for Space Charge Mitigation, in *Proceedings of the Seventh International Particle Accelerator Conference* (Busan, Korea, 2016), MOPOR023, to be published.

[70] M. Serluca, "Optics Studies and Space Charge Effects during the 2 GeV Injection Process at the CERN PS", Presentation at the eighth Hadron Syncrotrons Incoherent effects section meeting, CERN, Geneva, Switzerland (April 2016) [https://indico.cern.ch/event/523666/].

[71] S. Persichelli, "The Beam Coupling Impedance Model of CERN Proton Synchrotron", PhD thesis, Sapienza, Rome (2015), CERN-THESIS-2015-076 [http://cds.cern.ch/record/2027523].

[72] J. Borburgh, S. Damjanovic, S. Gilardoni, M. Giovannozzi, C. Hernalsteens, M. Hourican, A. Huschauer, K. Kahle, G. Le Godec, O. Michels, and G. Sterbini, "First Implementation of Transversely Split Proton Beams in the CERN Proton Synchrotron for the Fixed-Target Physics Programme", EPL **113**, 34001 (2016).

[73] J. Barranco García and S. Gilardoni, "Simulation and Optimization of Beam Losses During Continuous Transfer Extraction at the CERN Proton Synchrotron", Phys. Rev. ST Accel. Beams **14**, 030101 (2011).

[74] M. Giovannozzi, M. J. Barnes, O. E. Berrig, A. Beuret, J. Borburgh, P. Bourquin, R. Brown, J. P. Burnet, F. Caspers, J. M. Cravero, T. Dobers, T. Fowler, S. S. Gilardoni, M. Hourican, W. Kalbreier, T. Kroyer, F. Di Maio, M. Martini, V. Mertens, E. Métral, K. D. Metzmacher, C. Rossi, J. P. Royer, L. Sermeus, R. Steerenberg, G. Villiger, and T. Zickler, *The CERN PS Multi-Turn Extraction Based on Beam Splittting in Stable Islands of Transverse Phase Space: Design Report* (CERN, Geneva, 2006), [https://cds.cern.ch/record/987493].

[75] L. R. Evans, "A Phase Plane Exchange Section for the SPS antiproton Injection Beam-Line", CERN-SPS-DI-MST-80-2 (Geneva, 1980) [https://cds.cern.ch/record/122753].

[76] M. Giovannozzi, D. Quatraro, and G. Turchetti, "Generating unstable resonances for extraction schemes based on transverse splitting", Phys. Rev. ST Accel. Beams **12**, 024003 (2009).

[77] M. Hénon, "Numerical study of quadratic area-preserving mappings", Quart. Appl. Math. **27**, 291 (1969).

[78] A. Bazzani, G. Servizi, E. Todesco, and G. Turchetti, *A Normal Form Approach to the Theory of Nonlinear Betatronic Motion* (CERN, Geneva, 1994), [https://cds.cern.ch/record/262179].

[79] M. Giovannozzi and P. Scaramuzzi, "Nonlinear Dynamics Studies at the CERN Proton Synchrotron: Precise Measurements of Islands Parameters for the Novel Multi-turn Extraction", in *Proceedings of the ninth European Particle Accelerator Conference*, edited by J. Chrin, C. Petit-Jean-Genaz, J. Poole, C. Prior, and H.-A. Synal (Lucerne, Switzerland, 2004), pp. 1861–1863 [http://accelconf.web.cern.ch/accelconf/e04/PAPERS/WEPLT018.PDF].

[80] S. Gilardoni, M. Giovannozzi, and C. Hernalsteens, "First observations of intensity-dependent effects for transversely split beams during multiturn extraction studies at the cern proton synchrotron", Phys. Rev. ST Accel. Beams **16**, 051001 (2013).

[81] H. Damerau, "Longitudinal Coupled Bunch Instabilities with MTE", Presentation at the Machine Studies Working Group meeting, CERN, Geneva, Switzerland (March 2010) [https://espace.cern.ch/be-dep/MSWG/Presentations%202010/MTECoupledBunchMSWG.ppt].

[82] S. Gilardoni, "Status of Commissioning with Beam", Presentation at the MTE Workshop, CERN, Geneva, Switzerland (September 2010) [https://indico.cern.ch/event/105961/].

[83] M. Giovannozzi, "Status of MTE", Presentation at the LHC Injectors and Experimental Facilities Committee (IEFC) meeting, CERN, Geneva, Switzerland (12 May 2010).

[84] H. Bartosik, D. Bodart, J. Borburgh, R. Brown, S. Damjanovic, S. Gilardoni, M. Giovannozzi, B. Goddard, C. Hernalsteens, M. Hourican, and M. Widorski, "Proposal of a Dummy Septum to Mitigate Ring Irradiation for the CERN PS Multi-Turn Extraction", in *Proceedings of the Third International Particle Accelerator Conference*, edited by J. Corbett, C. Eyberger, K. Morris, C. Petit-Jean-Genaz, T. Satogata, and V. R. W. Schaa (New Orleans, Louisiana, USA, 2012), p. 499 [http://accelconf.web.cern.ch/accelconf/ipac2012/papers/moppd059.pdf].

[85] L. Bruno, S. Gilardoni, M. Nonis, T. Otto, R. Steerenberg, H. Vincke, P. Vojtyla, and M. Widorski, "Final Report of the PS Radiation Working Group", CERN-ATS-2011-007 (Geneva, Mar. 2011) [https://cds.cern.ch/record/1344814].

[86] O. Hans and B. Vandorpe, "Observations from the OP side", Presentation at the Mini-workshop on PS Main Magnet Field issues, CERN, Geneva, Switzerland (February 2012) [http://indico.cern.ch/event/176553/timetable/].

[87] J. P. Burnet and O. Michels, "Projet de Consolidation des Convertisseurs PFW", Note Technique AB-PO No. 10 (Geneva, Apr. 2005) [https://edms.cern.ch/document/585302/2].

[88] S. Gilardoni, private communication (2015).

[89] M. Buzio, A. Beaumont, P. Galbraith, G. Golluccio, D. Giloteaux, S. Gilardoni, C. Petrone, and L. Walckiers, "Development of Upgraded Magnetic Instrumentation for CERN Real-Time Reference Field Measurement Systems", in *Proceedings of the First International Particle Accelerator Conference*, edited by A. Noda, C. Petit-Jean-Genaz, V. R. W. Schaa, T. Shirai, and A. Shirakawa (Kyoto, Japan, 2010), pp. 310–312 [http://accelconf.web.cern.ch/AccelConf/IPAC10/papers/MOPEB016.pdf].

[90] A. Beaumont, private communication (2015).

[91] O. Michels, private communication (2015).

[92] S. Gilardoni and M. Giovannozzi, "MTE Setting-Up", Presentation at the Machine Studies Working Group meeting, CERN, Geneva, Switzerland (March 2010) [https://espace.cern.ch/be-dep/MSWG/Presentations%202010/MTE_2010_MSWG.pdf].

[93] S. Pittet, "Operational Specification of the PS Low Energy Correctors (CBE)", 773856 V1 (Geneva, Mar. 2011) [https://edms.cern.ch/ui/file/773856/1/773856_V1_ABPO_A4.pdf].

[94] Shoelace formula, [https://en.wikipedia.org/wiki/Shoelace_formula] (visited on 03/08/2016).

[95] J. Borburgh, private communication (2015).

[96] D. Gamba, private communication (2015).

[97] E. Benedetto, G. Arduini, S. C. Cave, F. Follin, S. Gilardoni, M. Giovannozzi, and F. Roncarolo, "Optics Measurements and Transfer Line Matching for the SPS Injection of the CERN Multi-Turn Extraction Beam", in *Proceedings of the First International Particle Accelerator Conference*, edited by A. Noda, C. Petit-Jean-Genaz, V. R. W. Schaa, T. Shirai, and A. Shirakawa (Kyoto, Japan, 2010), pp. 3888–3890 [http://accelconf.web.cern.ch/AccelConf/IPAC10/papers/thpeb006.pdf].

[98] G. Le Godec, private communication (2015).

[99] C. Hernalsteens, "Review of PS Fast Extractions", Presentation at the MTE internal review, CERN, Geneva, Switzerland (October 2015) [https://indico.cern.ch/event/440851/].

[100] G. Franchetti and I. Hofmann, "Particle Trapping by Nonlinear Resonances and Space Charge", Nucl. Instrum. Methods Phys. Res. A. **561**, 195, ISSN: 0168-9002 (2006).

[101] T. Bohl, "Low Intensity MTE Beam in the SPS", CERN-BE-Note-2009-015 (2009) [http://cds.cern.ch/record/1168013].

[102] S. Sorge, "Simulation Study on Beam Loss in the Alpha Bucket Regime during SIS-100 Proton Operation", in *Proceedings of the Fifth International Particle Accelerator Conference*, edited by G. Arduini, P. Michel, C. Petit-Jean-Genaz, and V. R. W. Schaa (Dresden, Germany, 2014), p. 3008 [http://accelconf.web.cern.ch/AccelConf/IPAC2014/papers/thpro059.pdf].

[103] J. Wei, "Longitudinal Dynamics of the Non-Adiabatic Regime on Alternating-Gradient Synchrotrons", PhD thesis, SUNY, Stony Brook (1990), UMI-90-23931.

Curriculum vitae

Alexander Huschauer

Address:	141A rue Pierraz Frettaz	E-mail:	alexander.huschauer@cern.ch
	01710 Thoiry, France	Date of birth:	29 August 1986
Mobile phone:	+41 75 411 8132	Nationality:	Austrian

Work experience

01/2016 - present	**CERN, European Organization for Nuclear Research, Geneva, Switzerland** Fellow in the BE-ABP-HSI section Investigation of performance limitations in the Low Energy Ion Ring (LEIR)
01/2013 - 12/2015	**CERN, European Organization for Nuclear Research, Geneva, Switzerland** Doctoral Student in the BE-ABP-HSC section under the supervision of Dr. Simone Gilardoni Investigation of performance limitations for high-intensity beams in the Proton Synchrotron (PS)
03/2011 - 12/2012	**CERN, European Organization for Nuclear Research, Geneva, Switzerland** Internship, User and Technical Student in BE-OP-PS section under the supervision of Rende Steerenberg Identification of betatron resonances in the PS and improvement of the working point control
05/2006 - 10/2010	**KML Linear Motion Technology GmbH, Vienna, Austria** Part-time mechanical design engineer for high-precision positioning and movement systems

Education

10/2012 - present	**Vienna University of Technology, Austria** Doctoral programme in Engineering Sciences (Field: Technical Physics) Research carried out as Doctoral Student in the BE-ABP-HSC section at CERN

Thesis title: *Beam dynamics studies for high-intensity beams at the CERN Proton Synchrotron*
Supervisors: Dr. Michael Benedikt, Dr. Simone Gilardoni

10/2009 - 10/2012	**Vienna University of Technology, Austria** Master's programme in Technical Physics Degree awarded with distinction on 10 October 2012 Research carried out as Technical Student in the BE-OP-PS section at CERN Thesis title: *Working point and resonance studies at the CERN Proton Synchrotron* Supervisors: Dr. Michael Benedikt, Rende Steerenberg
10/2006 - 07/2009	**Vienna University of Technology, Austria** Bachelor's programme in Technical Physics Degree awarded with distinction on 13 July 2009 Research carried out as Technical Student in the BE-OP-PS section at CERN Thesis title: *Specific reaction measurements at nTOF at CERN* Supervisor: Prof. Helmut Leeb

Academic activities

09/2013	**CERN Open Days, Geneva, Switzerland** Participating as volunteer to present an introduction to particle accelerators to the general public
10/2010 - 06/2011	**TUtheTOP, Vienna University of Technology, Austria** Participating in this High Potential Programme to develop professional and personal skills by interaction with various Austrian companies
10/2009 - 05/2010	**Institute of Theoretical Physics, Vienna University of Technology, Austria** Tutor for Statistical Physics and Quantum Mechanics

Languages and computer skills

Languages:	German (native) English (full professional proficiency) French (fluent in speaking, intermediate in writing)
Simulation tools:	MAD-X/PTC, PyORBIT, PyHEADTAIL
Programming:	C, C++, Matlab, Python